Polymer Induced Solvation Effects on Liquid Phase Catalytic Hydrogenations

Pengcheng Huang

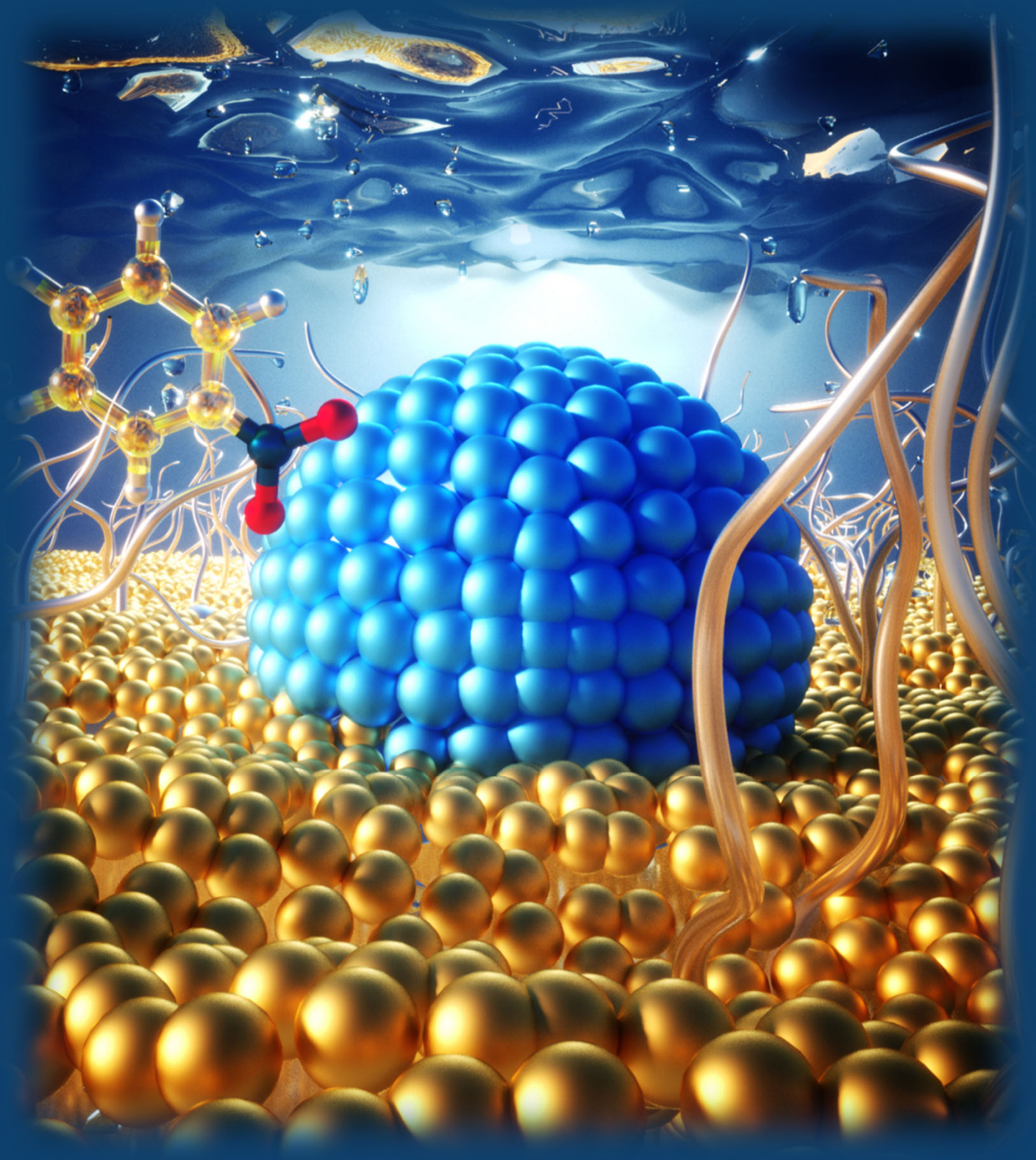

POLYMER INDUCED SOLVATION EFFECTS ON LIQUID PHASE CATALYTIC HYDROGENATIONS

Pengcheng Huang

POLYMER INDUCED SOLVATION EFFECTS ON LIQUID PHASE CATALYTIC HYDROGENATIONS

DISSERTATION

to obtain
the degree of doctor at the Universiteit Twente,
on the authority of the rector magnificus,
prof. dr. ir. A. Veldkamp,
on account of the decision of the Doctorate Board
to be publicly defended
on Friday 16 December 2022 at 16.45 hours

by

Pengcheng Huang

born on the 10th of September, 1990
in Henan, China

This dissertation has been approved by:

Supervisor
prof. dr. ir. L. Lefferts

Co-supervisor
dr. J.A. Faria Albanese

The research described in this thesis was carried out at the *Catalytic Processes and Materials* (CPM) group of the University of Twente, The Netherlands. I acknowledge the financial support for my PhD study from *China Scholarship Council* (CSC).

Cover design: Ella Marushchenko & Pengcheng Huang
Printed by: Gildeprint
Lay-out: Pengcheng Huang
ISBN: 978-90-365-5501-2
DOI: 10.3990/1.9789036555012

Graduation Committee:

Chair / secretary:	prof.dr. J.L. Herek
Supervisor:	prof.dr.ir. L. Lefferts Universiteit Twente, TNW, Catalytic Processes and Materials
Co-supervisor:	dr. J.A. Faria Albanese Universiteit Twente, TNW, Catalytic Processes and Materials
Committee Members:	prof.dr.ir. R.G.H. Lammertink Universiteit Twente, TNW, Soft matter, Fluidics and Interfaces
	prof.dr. G. Mul Universiteit Twente, TNW, Photocatalytic Synthesis
	prof. dr. D.E. Resasco The University of Oklahoma, Chemical, Biological and Materials Engineering
	prof. dr. ir. H.J. Heeres Rijksuniversiteit Groningen, Faculty of Science and Engineering
	dr. ir. M.F. Neira D'Angelo Eindhoven University of Technology, Chemical Engineering and Chemistry

Table of Content

Chapter 1

Introduction

1. Motivation

When heterogeneous catalysts are employed in the presence of solvents one must carefully consider the potential interactions between the solvent molecules and the reacting species as they can alter mass transfer rates, reaction kinetics, product selectivity, and catalyst stability.[1] For this reason, solvents must (1) ensure solubilization of reactants while promoting separation of products, (2) be thermally and chemically stable at the operating conditions, (3) favor the formation of the desired product, (4) safeguard the stability of the catalyst, (5) interact weakly with the catalytic active site to avoid competitive chemisorption, and (6) provide sufficient molecular mobility to minimize mass transport limitations.[2] Finding the perfect "marriage" between the solvent, reactants, and catalyst is rather difficult as only few solvents can deliver the desired performance. In addition, these solvents are often toxic, flammable, and fossil-based, increasing the environmental risks when employed in large-scale processes. An attractive proposition is to decouple the role of the solvent in stabilizing reactants and products in the bulk of the liquid from the more complex interactions that take place near the active site. In this concept, the catalyst employed is rendered with functionalities that modify the chemical environment surrounding the reacting species on the catalyst surface, mimicking the coordination pocket of enzymes in nature.

To create these micro-solvation environments one could leverage organic surface functionalization techniques, which offer exquisite control over the chemistry and the co-localization of active sites and solvation modifier moieties. In this context, the development of bio-inspired materials has become increasingly relevant thanks to the recent advancements in stimulus-responsive nano-materials and molecular actuators where large physical-chemical transitions cued by small environmental changes are translated into mechanical actuation.[3–5] The concept of combining catalytic materials with responsive polymeric systems to create catalytic nano-reactors that respond to external stimulus has been demonstrated as a tool to control the solubility of organo-metallic and encapsulated catalysts depending on externally induced changes in the reaction environment.[3,4,6–9] To create these materials catalytic nanoparticles and/or organo-metallic complexes are functionalized with so-called "*stimulus-responsive*" polymers, hydrogels, and/or gels.[10,11] These soft materials undergo large conformational transitions from solvated to aggregated states upon reaching a critical solubility limit, which is triggered by temperature, pH, magnetic field, and/or light, resulting in the formation of a dense polymer layer that limits the access of molecules to the active site and facilitates particle-particle agglomeration and separation. Strikingly, in these reports, the

response of the polymer-coated catalyst has been used exclusively to induce reversible mass-transport limitations to control the activity.[12] While the mechanism of actuation of catalysts coated with stimulus-responsive polymers is well understood in the context of reversible mass transport effects, there are very few reports on the study of the solvation effects that can be induced by these polymers on kinetically relevant surface reaction intermediates.

The purpose of this thesis is to leverage the solvation effects that stimulus-responsive polymers, covalently bonded to the catalyst surface, can exert on surface reaction intermediates to manipulate the activity, selectivity, and stability of the catalyst. The underlying hypothesis is that tethering the chemistry of the solvation layer close to the active sites, without inducing mass transport effects, should enable precise control over the surface coverage and apparent reaction barriers of catalytic reactions. To address this question, detailed reaction kinetics and physicochemical characterization have been conducted on model palladium catalysts supported on nonporous silica spheres containing poly-isopropylacrylamide (p-NIPAM) grown from the surface using atom transfer radical polymerization (ATRP). These thermo-responsive polymer brushes have a characteristic transition from swollen to collapsed state in water media when the temperature is above 32 °C (Lower Critical Solution Temperature – LCST) that allows precise control over the extent of interactions between the polar reactive species and both the polymer and the water molecules in the liquid media in the vicinity of the active sites. To unravel these effects the polymer-coated catalyst was employed to study the reduction of -NO_2 containing molecules (nitrite ions and nitrobenzene) with the aim of establishing fundamentally relevant structure-activity relationships that can set the basis for creating supported solvents for heterogeneous catalysis.

2. Reaction kinetics and mechanistic studies in liquid phase

The following section briefly examines the fundamentals of Langmuir-Hinshelwood-Hougen-Watson (LHHW) [13,14] reaction kinetics also referred as Langmuir-Hinshelwood kinetics, which is key in developing a mechanistic understanding of reactions activated by heterogeneous catalysts. Then, the degree of rate control analysis is being introduced to distinguish the rate controlling steps and study how the reaction conditions influence the rate controlling steps.

2.1 Langmuir-Hinshelwood-Hougen-Watson (LHHW) kinetics

In heterogeneous catalysis, it is possible to develop physically meaningful kinetic models following the "Langmuir-Hinshelwood-Hougen-Watson (LHHW) mechanism". The model was initially suggested by Irving Langmuir in 1921 and further developed by Cyril Hinshelwood in 1926.[15] This model builds on the description for the adsorption of molecules on surfaces, which includes the following assumptions (1) all the active sites on the surface are identical, (2) adsorbate-adsorbate interactions are negligible to the extent that the heat of adsorption is independent of the surface coverage, and (3) the adsorbing molecule binds to a single surface site. Next, it is assumed that the net reaction rate in the steady state will be equal to the rate of the slowest step in the process and that all the preceding steps are quasi-equilibrated. This is often referred as the rate-determining step (RDS). Considering that on heterogeneous catalysts the nature of the active site is difficult to restrict to a single type, it is often accepted that the number of active sites and the number of turnovers per site per unit of time is simply an approximation to the most relevant active site and product formation rate.[14,16] Here, one could imagine a simplified system in which two molecules (e.g. A and B) react on the surface of the catalyst to form a product C. This mechanism assumes a bimolecular reaction involving two adjacent molecules on the surface, which are both adsorbed (Figure 1). The process consists of the following sequence of steps: (1) adsorption from the gas or liquid phase, (2) dissociation of the molecules on the surface, (3) an irreversible reaction between the adsorbed molecules, and (4) desorption to the gas or liquid phase.

$$A + * \rightleftharpoons A* \quad (1)$$

$$B + * \rightleftharpoons B* \quad (2)$$

$$A* + B* \rightarrow C(l) + 2* \quad \text{(RDS)} \quad (3)$$

Here, A and B are the reactants, * is the unoccupied active site. In this case, k_1, k_{-1}, k_2, k_{-2} and k_3 are the rate constants for adsorption/desorption of A and B, and the reaction to form the product (C), respectively. The assumption here is that the surface coverage of C is low, its desorption is fast, and the equilibrium is towards the formation of C. The equilibrium for the adsorption of the different species is a function of its thermodynamic chemical potential or chemical activity.

In the case of a liquid one could express the activity of a specie i as $a_i = \gamma_i[i]$, where γ_i is the activity coefficient and $[i]$ is the concentration of the specie i in the system. For gas phase reactions, the chemical potential can be expressed as the fugacity of the specie i in the system

as $f_i = \varphi_i P_i$, where φ_i is its fugacity coefficient and P_i is its partial pressure. If one operates at low concentrations in the liquid phase, then it is often possible to approximate the activity to the concentration of that specie in the liquid phase. Here, one must be vigilant of the impact of this approximation in the development of reaction kinetics as this can lead to substantial changes in the reaction kinetics. These effects are addressed in the subsequent section of this chapter on solvation effects (**Section 4**). Having said that, if the system forms an ideal liquid solution, then one obtains the equations (4)-(7).

$$\theta_A = K_1[A]\theta^* \quad (4)$$

$$\theta_B = K_2[B]\theta^* \quad (5)$$

$$1 = \theta_A + \theta_B + \theta^* \quad (6)$$

$$\theta^* = \frac{1}{1 + K_1[A] + K_2[B]} \quad (7)$$

Since in this case, the formation of the product C* on the surface is the rate-determining step (RDS), the rate equation can be written as follows:

$$r = k_3\theta_A\theta_B = k_3K_1K_2[A][B]\theta^{*2} = \frac{k_3K_1K_2[A][B]}{(1 + K_1[A] + K_2[B])^2} \quad (8)$$

Here, it is assumed that all the preceding steps are quasi-equilibrated (QE). Thus, a balance of all the active sites can be written as [L] = [*] + [A*] + [B*]. This provides an expression for the turnover frequency ($\frac{r}{[L]} = TOF$). Here, L is the total number of active sites on the catalyst surface that are available for the reaction:

$$\frac{r}{[L]} = \frac{k_3K_1K_2[A][B]}{(1 + K_1[A] + K_2[B])^2} \quad (9)$$

The LHHW kinetic model can be employed to predict the reaction rate outside the operational window employed to develop the reaction kinetics, as long as the rate-determining step does not change. This basic requirement, however, is often not achieved in realistic catalysts as the rate-determining step can shift to early or later steps in the reaction sequence with changing operating conditions. For this reason, the next section explores the concept of the degree of rate control.

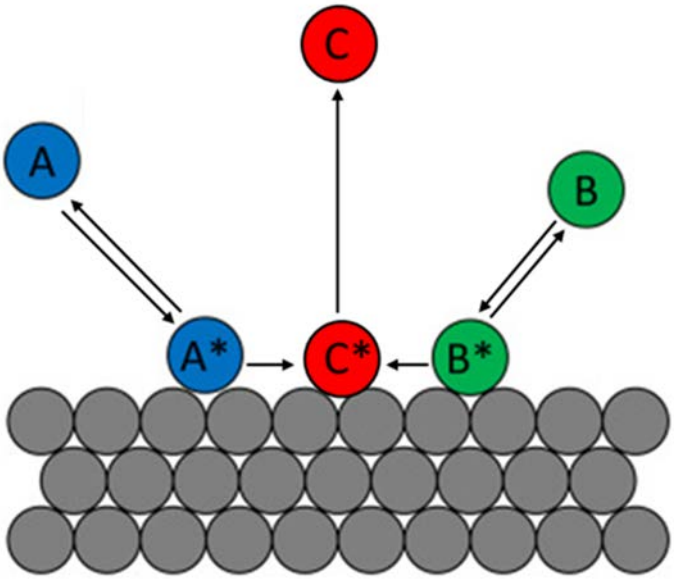

Figure 1. Schematic representation of the Langmuir–Hinshelwood-Hougen-Watson (LHHW) mechanism.[17]

2.2 Degree of rate control analysis

The degree of rate control (DRC) is a mathematical approach for analyzing multistep reaction mechanisms. It can be used to identify the "rate-controlling transition states and intermediates" in the sequence and predict its change as a function of the operating conditions employed (e.g. temperature and pressure) and the chemical potential of the reactive species. For example, when there is a single "rate-determining step", the DRC for its transition state (TS) is 1, while for the other steps, the DRC is smaller than 1. This simple yet powerful approach enables the identification of "tipping points" in which the control of the reaction kinetics can shift from one step to another, which can ultimately support the development of more robust reaction kinetics. Inspired by the work from Prof. C. Campbell, one can derive the DRC (X_{RC}) for an elementary step, *i*, as it is shown in equation 10.[18,19]

$$X_{RC,i} = \frac{k_i}{r}\left(\frac{\partial r}{\partial k_i}\right)_{k_{j\neq i},K_i} \qquad (10)$$

Where *r* is the net reaction rate to the product, and the partial derivative is taken holding constant the rate constant, k_i, for all other steps $j \neq i$ and the equilibrium constant, K_i, for step *i*. Note that keeping K_i constant means that the forward and reverse rate constants for step i, k_i, and k_{-i}, both must be varied by equal factors so that their ratio remains constant. The reaction conditions (e.g., temperature, concentrations) are also held constant here.

From the definition of the degree of rate control (*vide supra*), one can recognize that the larger the numeric value of $X_{RC,i}$ is for a given step, the bigger its influence on the rate constant on the overall reaction rate.

3. Mass transfer in three phase catalytic reactions

When catalytic reactions are conducted in a three-phase environment (i.e. gas-liquid-solid system), the molecules in the gas phase (e.g. H_2) have to diffuse from the gas phase to the liquid phase, and then transfer from the liquid to the catalyst surface in order to reach the active sites where the reaction takes place (Figure 2). Considering that reactions are driven by the chemical potential on the catalyst surface, one must ensure that sufficiently high rates of transport are achieved to sustain the kinetic control of the reaction.

The challenge, however, is that often the rates of transport in the liquid phase are insufficient to match the rate of the catalytic reaction, especially when considering the solubility of the gaseous reactant is low in the liquid phase. As a result, the reactant concentration on the external surface of the catalyst or inside the catalyst is significantly lower than that of the bulk of the fluid. In this case, mass transfer limitations become rate controlling. In other words, if the mass transfer rate is slower than the reaction rate, then the observed reaction rate will be dominated by mass transfer rather than the intrinsic activity of the catalyst. Therefore, the activity and selectivity will be significantly influenced by the rates of transfer.[20]

For the gas-liquid-solid three-phase reaction, the dissolution of the gas in the liquid may be limiting, this is often referred as gas-liquid mass transfer limitations. Here, increasing the gas-liquid interfacial area is key to maximize the transport rate. Next, the molecules from the bulk of the liquid must reach the external surface of the catalyst. In this case, it is important to check the liquid-solid mass transfer limitations. These so-called external mass transfer limitations can be reduced by increasing the mixing inside the reactor and reducing the thickness of the stagnant layer of fluid around the catalyst particle.

Finally, the last step involves the diffusion of the molecules inside the pores of the catalyst. These internal mass transport limitations can be mitigated by reducing the diffusional path of the molecules using core-shell catalysts or with smaller particle sizes. In addition, one could use catalysts with pores of low tortuosity (i.e. straight channels).

Clearly, it is essential to determine the extent of gas-liquid, liquid-solid, and internal mass transfer control over the reaction kinetics in order to develop fundamentally meaningful kinetic models. In practice, it is very challenging to accurately quantify the mass transport and reaction processes occurring inside a catalyst particle. Instead, semiquantitative methods including the Mears criterion, and Weisz-Prater, can be employed to quickly identify the potential role of mass transport in the observed catalytic performance and develop measurements to mitigate them.

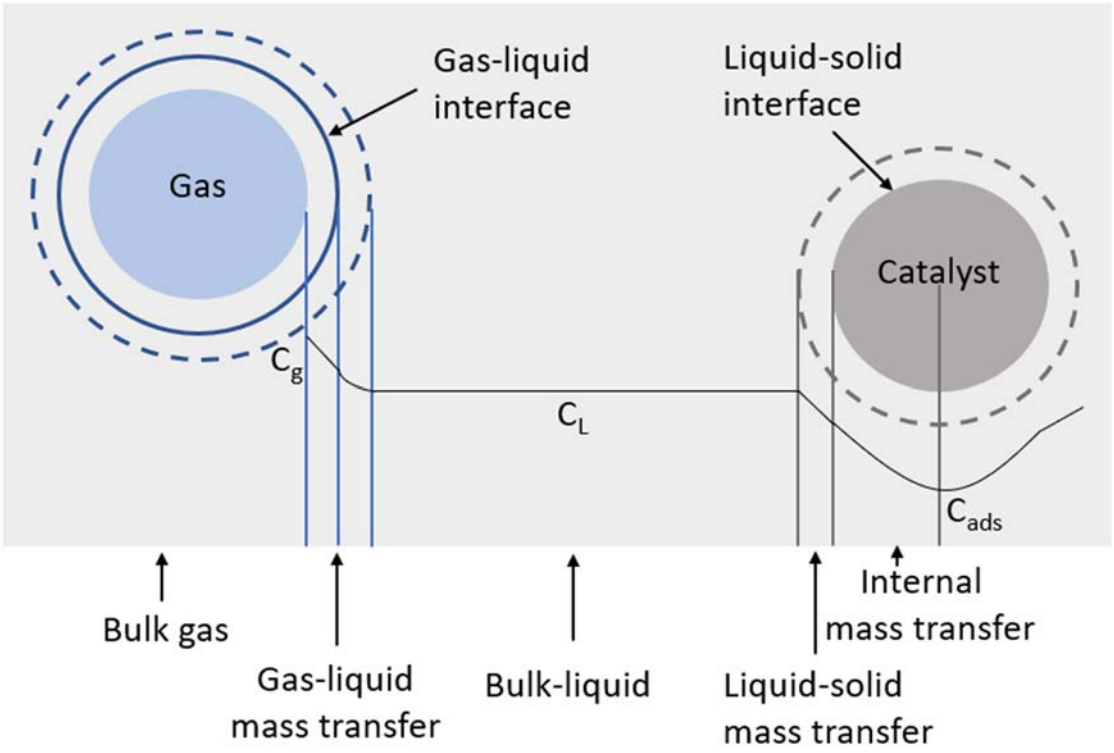

Figure 2. Schematic representation of mass transfer process in a three phase catalytic reaction.

3.1 External mass transfer

In a three-phase catalytic system, the concentration of reactants on both sides of the interface, including the gas-liquid and liquid-solid interface, drives the mass transfer of the reactants. While in the case of the reactants that are in the liquid phase the only mass transport resistances to overcome are the liquid to solid and the intra-particles transfer, for the gaseous reactants an additional resistance must be overcome at the gas-liquid interface (Figure 2). The next section revises some of the equations that are employed to estimate the external mass transport limitations in liquid-solid and combined gas-liquid-solid steps.

(1) External mass transfer analysis for the L-S step

The liquid-solid mass transfer limitations can be assessed by comparing the liquid-solid mass transfer rate and reaction rate. If the former is much larger than the latter as shown below, then no liquid-solid mass transfer limitations are expected.[21]

$$Rate_{l-s} \gg Rate_{obs} \quad (11)$$

Here, $Rate_{obs}$ is the observed reaction rate from the experiment, $Rate_{l-s}$ is the maximal liquid-solid mass transfer rate that can be calculated for the equation below.

$$Rate_{l-s} = k_{ls} * a_s * C_s \quad (12)$$

Here, C_s is the bulk concentration (mol*m^{-3}) and k_{ls} is the liquid-solid mass transfer coefficient, which can be calculated by the following equation.

$$k_{ls} = \frac{D_{AB} * Sh}{d_h} \quad (13)$$

Where D_{AB} is the diffusion coefficient of the reactant A in the solvent B (m^2*s^{-1}), d_h is the hydrodynamic size of the catalyst (m), Sh is the Sherwood number. In a slurry reactor, the micron-sized particles move along with the liquid very efficiently, i.e. with limited shear losses at the particle surface. Thus, the value of Sh is similar to the value of a particle in a stagnant liquid (Sh=2).

The geometric surface area of the catalyst per volume of solution is defined as a_s.

$$a_s = \frac{A_p * m}{\rho_c * V_p * V_R} \quad (14)$$

Here, ρ_p is the average density of the catalyst, V_p and V_R are the volumes of one catalyst particle (m^3) and reaction solution (m^3), respectively. The A_p is the geometric surface area of one catalyst particle (m^2) and m is the mass of the catalyst (kg).

If the calculated $Rate_{l-s}$ is significantly larger than the observed $Rate_{obs}$, then the liquid-solid mass transfer is not limiting.

(2) External mass transfer for the combined G-L and L-S steps

The external mass transfer limitations at both gas-liquid and liquid-solid interfaces can be semi-quantitively evaluated by the Mears criterion shown below.[22]

$$\frac{-\mathrm{r_{obs}}\rho_\mathrm{b} d_p \mathrm{n}}{\mathrm{K_c C_s}} < 0.15 \qquad (15)$$

Here, $-r_{obs}$ is the observed rate per unit of catalyst (mol*kg*s^{-1}), ρ_b is the bulk density of the catalyst (kg*m^{-3}), d_p is the radius of the catalyst particle (m), n is the reaction order, and K_c is the mass transfer coefficient (m/s). If the calculated value is smaller than 0.15, then the external mass transfer limitation can be neglected.

3.2 Internal mass transfer

The Weisz-Prater criterion (C_{wp}, Equation 16) is often used to evaluate the influence of pore diffusion resistances on the reaction rate.[23] One of the main advantages of this approach is that it can be employed to identify the potential effect of internal mass transport effects without knowing the true reaction order and kinetic constant of the reaction. The main drawback is that it can only provide a semi-quantitative measurement of the impact of intraparticle mass transport on the reaction kinetics.

$$C_{wp} = \frac{R_{obv} \times L^2 \times \rho_{Cat}}{C_s \times D_{eff}} \qquad (16)$$

Where L is the characteristic length of spherical catalyst particle (m), ρ_{Cat} is the density of the catalyst particles (kg*m^{-3}), R_{obv} is the reaction rate per mass of catalyst (mol*s^{-1}*kg^{-1}), D_{eff} is the effective diffusivity (m^2*s^{-1}), and Cs is the reactant concentration at the particle surface (mol*m^{-3}). When the calculated C_{wp} value is much small than 1 (e.g. C_{wp} < 0.3), the effect of internal mass transfer limitations can be ignored. On the contrary, when the value is larger than 1, the internal mass transfer effects must be considered in the modeling of the reaction kinetics.

In the studies conducted in the present work the effect of the pores on the mass transport was neglected as the catalyst, in this case, Pd-metal clusters, was supported on the surface of nonporous silica spheres. This model catalyst system facilitated the acquisition of kinetically relevant data. Even when the polymer coating was included in the system as a potential porous layer surrounding the metal clusters, the effect of diffusional limitations was negligible as the thickness of these layers was nano-metric. This was possible thanks to the fast rates of transport of the reactive species within such a short diffusional path.

4. Solvent effects

Solvents are ubiquitous in the chemical industry as they allow the intimate contact of reactive species and catalysts during the reaction while allowing precise control over the reaction kinetics and selectivity.[1] These effects can be induced by (1) competing with the reactants for the catalyst active sites, (2) participating directly in the reaction steps and creating alternative reaction pathways, (3) changing the transition state of a reaction and influencing the relative stabilization of the reactants and activated complex leading to changes in the apparent entropy and enthalpy of activation, (5) changing intra-pore diffusion characteristics of a porous catalyst, (6) Inhibiting undesired reactions or changing the product selectivity, and (7) changing the solubility of different components in a reaction mixture. Hence, the solvent effect has strong research significance for a liquid phase reaction. The full list of solvent effects on product selectivity and activity is shown in Figure 3.

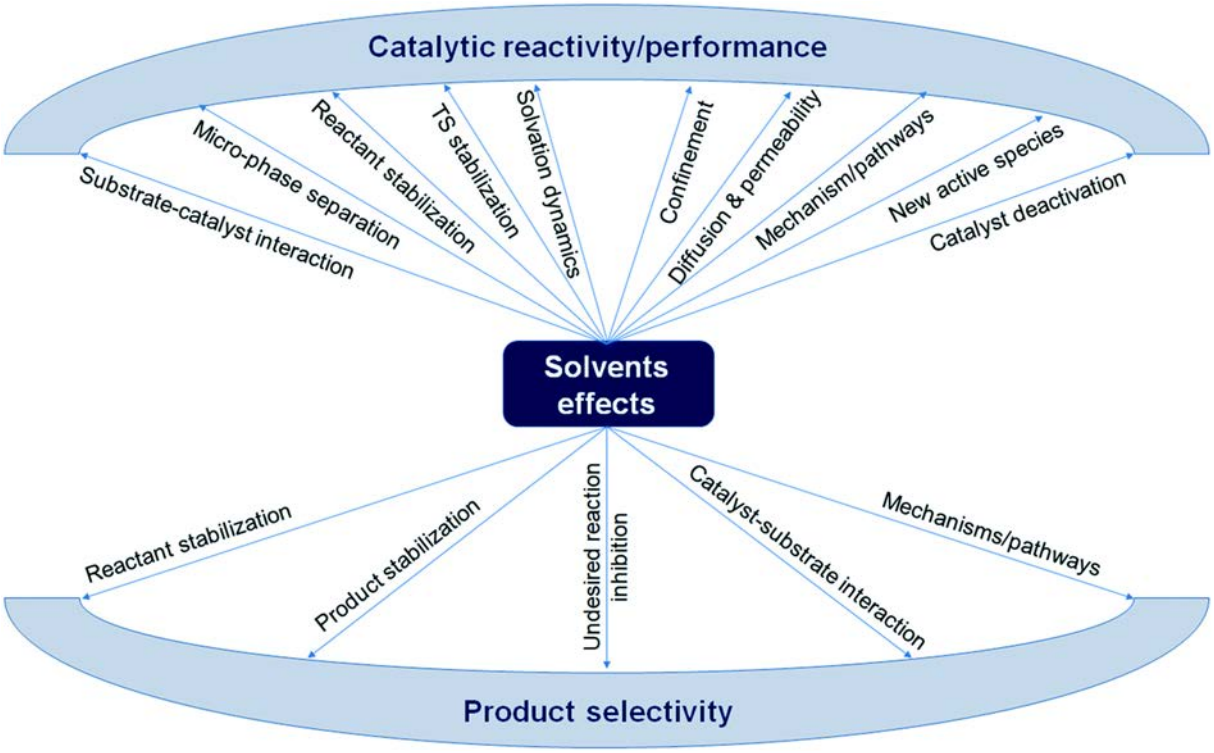

Figure 3. Representation of the key solvent effects in catalysis, categorized as the intrinsic factors responsible for the change in reactivity/performance of catalytic reactions as well as those influence product selectivity/distribution.[1]

4.1 Solvation effects

The solvation effects describe the interaction between a dissolved solute and solvent. This interaction can influence many properties of the solute (e.g. reactivity, and solubility) and the solvent (e.g. density and viscosity).[2] In the process of solvation, the solute is surrounded by a concentric solvent shell, which reorganizes the solute and solvent molecules into solvation complexes where van der Waals forces, Coulombic, and hydrogen bonding interactions play a key role in determining the extent of solvation. This complex array of inter-molecular interactions can lead to significant effects on the chemical activity of the reactants and products in the reaction media, which leads to changes in the reaction rate and selectivity.

In section 2, the detailed derivation of the LHHW equation for a reaction involving two reactants A and B was presented (Equation 9). In that case, it was assumed that the activity coefficients of all species were equal to unity. As a result, the reaction rate was a function of the concentration of A and B. Here, we were inspired by the derivations provided by Prof. D. E. Resasco [24] and Prof. D. Flaherty[25] on the transition state theory of reactions in liquid phases to establish the connection between the LHHW surface reaction kinetics and the solvation effects. For this purpose, one can apply transition state theory (TST) treatments,[26] and assume that the surface coverage is low (i.e., $1 \gg K_1[A] + K_2[B]$) to simplify equation 9 to the following expression.

$$\frac{r}{[L]} = k_3 K_1 K_2 [A][B] \qquad (17)$$

An apparent rate constant k_{app} can be defined and substituted into the rate expression leading to equation 18.

$$k_{app} = k_3 K_1 K_2 = \frac{k_b T}{h} K^{\ddagger} K_1 K_2 = \frac{k_b T}{h} \exp\left(-\frac{\Delta G_{app}^{\ddagger}}{RT}\right) \qquad (18)$$

Here, $K^{\ddagger}$ is the equilibrium constant between the transition state and reference state, k_b is the Boltzmann constant, h is the Planck constant, T is thermodynamic temperature, $\Delta G_{app}^{\ddagger}$ is the apparent free energy barrier for the transition state, which is equal to the difference between the free energies of the transition state and the molecules in the liquid. On one hand, the Gibbs free energy of the transition state includes the free energy of the activated complex in the reference state ($G^{0,\ddagger}$) and the corresponding excess of Gibbs free energy $G^{\varepsilon,\ddagger}$ induced by its solvation layer. On the other hand, the Gibbs free energy of the reactive species in the liquid

includes the free energy of the molecule in the reference state (G_i^0) and its excess free energy in the solvent (G_i^{ε}).[25]

$$\Delta G_{app}^{\ddagger} = (G^{0,\ddagger} + G^{\varepsilon,\ddagger}) - (G_i^0 + G_i^{\varepsilon}) \qquad (19)$$

The excess free energy (G^{ε}) quantifies the impact of solvent interactions on the free energy of each component. Here, one can notice that the activity coefficients of reactive species can be related to excess Gibbs free-energy contributions as follows:

$$\gamma_i = \exp\left(\frac{G_i^{\varepsilon}}{RT}\right) \qquad (20)$$

By applying equations 20, 19, and 18 to our case involving A and B one can rewrite equation 18 into a rate expression that includes the activity coefficients.

$$\frac{r}{L} = \frac{k_b T}{h} \exp\left(-\frac{G^{0,\ddagger} - G_A^0 - G_B^0}{RT}\right) * \frac{\gamma_A \gamma_B}{\gamma_{\ddagger}} [A][B] \qquad (21)$$

This leads to a new apparent rate expression that contains the excess Gibbs free energy and standard Gibbs free energy.

$$\frac{r}{L} = \frac{k_b T}{h} \exp\left(-\frac{\Delta G_{app}^{0,\ddagger} + \Delta G_{app}^{\varepsilon,\ddagger}}{RT}\right) [A][B] \qquad (22)$$

Since the quantity ($\Delta G_{app}^{0,\ddagger}$) is independent of the solvent employed one could use experimental measurements of the reaction rate in different solvents to determine the $\Delta G_{app}^{\varepsilon,\ddagger}$. This is often referred as the change in the apparent Gibbs free energy of activation ($\Delta G_{app}^{\ddagger}$).[27] The beauty of this approach is that one can extract information about the extent of solvation induced by specific solvents using only the reaction kinetics.

4.3 Polymer induced solvation effects

For the synthesis of heterogeneous catalysts, nanoparticles (NPs) have been widely used as catalyst supports in both industry and academia owing to the large surface areas, high mechanical resistance, and thermal stability, allowing the stabilization of a large number of active sites per unit of volume. Recently, the utilization of polymers to stabilize NPs has gained more attention as these materials can allow fine control over the NPs morphology, topology, and crystallinity, which ultimately alters the reactivity of the NPs surface.[28]

Previous research has shown that polymer-derived microenvironments can act as pseudo-solvents that alter the catalytic properties of supported metal catalysts. This generalizable methodology can be employed to modify metal catalysts for reactions in liquid phase, e.g. biomass conversion, and environmental pollution control.[29][30] J.A. Dumesic et al. [31] have recently demonstrated that surrounding bimetallic Pd/Au nanoparticles with a poly(vinyl alcohol) derived microenvironment can prevent the poisoning effect of biogenic impurities present in the spent fermentation medium. This polymer-derived microenvironments, generated either by intentional post-synthetic modification of pre-formed catalysts,[31][32] or as a side effect of polymer encapsulation of homogeneous catalysts,[33] can modify the active sites of the parent catalysts and improve their selectivity, stability, and activity.

More recently, a new series of polymer-coated catalyst systems are emerging leveraging the stimulus-responsive behavior of certain types of polymers (see Figure 4). Here, the metal nanoparticles (NPs) are embedded in a polymer gel that can react to external stimuli. When using the catalyst in a solution, the reactant diffusion within the polymer gel can be manipulated by external stimuli, e.g. pH or temperature. In these systems the polymer undergoes a fully reversible phase transition from swollen to coagulated or collapsed state as the signal threshold for the transition is achieved. In the collapsed state, the polymers form a dense layer that delays the molecular transport leading to low reaction kinetics. One of the most well-studied systems is poly(N-isopropylacrylamide or p-NIPAM). This thermo-responsive polymer undergoes a reversible transition from the solvated state at temperatures below its lower critical solution temperature (LCST) of 32 °C to collapsed state at higher temperatures in the aqueous phase. In the low-temperature regime, the polymer-water interaction is enthalpically driven by the formation of hydrogen bonds between the water molecules and the amide moieties in the polymer. As the temperature increases the hydrogen bonds are destabilized and the Gibbs free energy is controlled by the entropic contributions, leading to the polymer collapse on itself.

Notably, the utilization of these polymers to modify the catalytic activity and selectivity of a certain catalytic reaction has been recently demonstrated for poly(N-isopropylacrylamide).[34] The underlying mechanism of actuation, however, is still under debate.

Here, we report one of the first attempts to use poly(N-isopropylacrylamide) coated palladium catalysts (Pd/SiO_2-p-NIPAM) for the activation of N-O bonds in nitrites and nitrobenzene hydrogenation (Figure 4). The underlaying goal is to develop a framework for the development of polymer-coatings for catalysis that can widen the degrees of freedom in the design of new more stable, active, and selective catalysts.

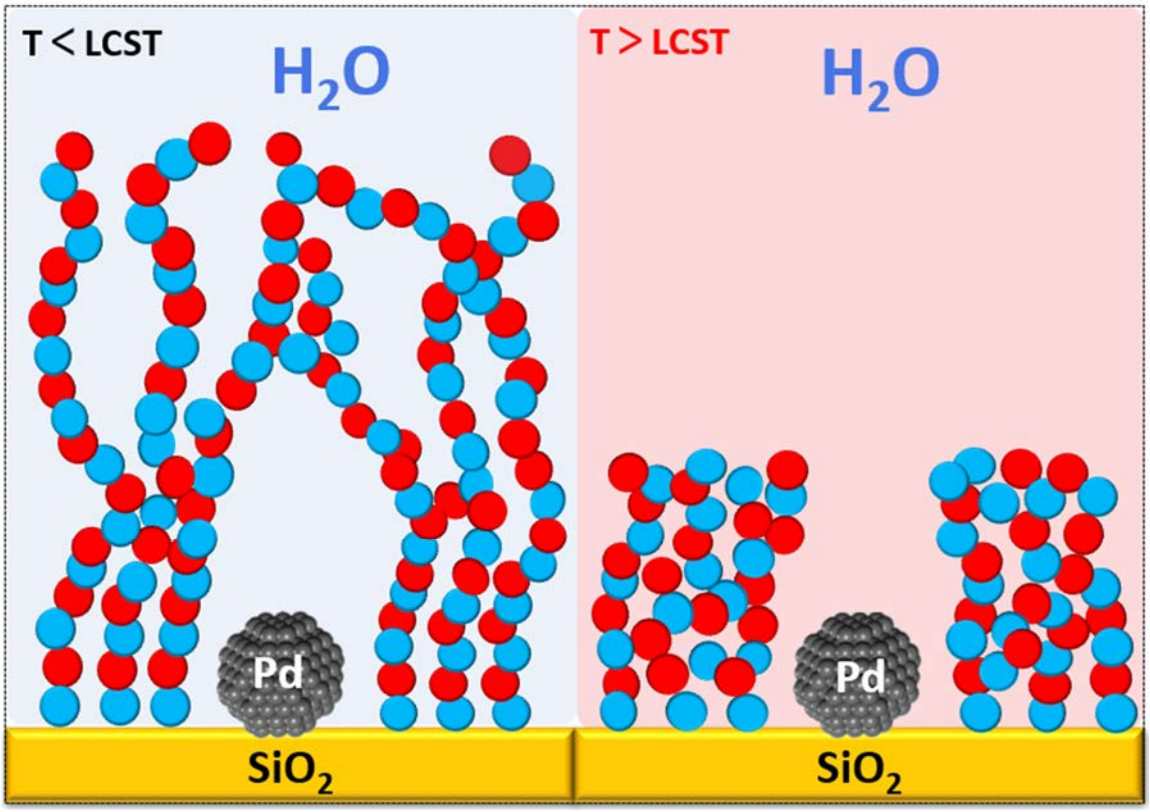

Figure 4. Illustration of the polymer structure of the Pd/SiO_2-p-NIPAM catalyst at different temperatures.

5. Selection of model reactions

To study the impact of the stimulus-responsive polymers on the performance of metal-supported catalysts it was decided to use the nitrite and nitrobenzene hydrogenation reactions as probe chemistries in the present thesis. The two reactions are catalyzed in aqueous environments and are known to be sensitive to changes in the liquid phase composition, pH, and catalyst chemistry. Furthermore, both of these reactions can be conducted even at room temperature, which facilitates the study of the effect of the p-NIPAM polymer on the reaction kinetics at temperatures above and below the LCST. Finally, the two reactions involve N-O bond activation, which is a critical reaction in the production of special chemicals, removal of pollutants in drinking water, and production of fuels from biomass-derived feedstocks. In the next section, we briefly discuss the nitrite and nitrobenzene hydrogenation reactions and the interplay between the operating conditions and the activity and selectivity of the catalyst.

5.1. Nitrite hydrogenation

The groundwater pollution by nitrate, nitrite, and ammonia can directly or indirectly cause a series of diseases (blue baby syndrome, cancer, and hypertension) in healthy individuals.[35] According to the World Health Organization (WHO), the maximum allowable levels of nitrate, nitrite, and ammonia concentration in drinking water are 50 mg/L, 3 mg/L, and 1.5 mg/L respectively.[36] This has become a major issue in many developed countries as the utilization of fertilizers in intensive farming has led to the uncontrolled release of these nitrogen species in the subsurface aquifers. As a result, there is a renewed interest in the development of processes for the removal of nitrite, nitrate, and ammonia from ground and surface water.

Various technologies have been used to remove nitrite and nitrate, including photocatalytic reduction,[37] electrodialysis,[38] reverse osmosis,[39] ion exchange,[40] biological methods,[41] and catalytic reduction.[42][43] Among them, the most promising technology to remove nitrite and nitrate from drinking water is the heterogeneous hydrogenation over supported noble metal catalysts as it converts nitrite to harmless nitrogen gas without producing highly concentrated brine and nutrients. More importantly, this technology can convert mg/L concentration levels of nitrite, which cannot be processed by biological methods since the drinking water lacks nutrients for microorganisms.[37][44][45] After the first catalytic reduction of nitrate was published in 1993 by Tacke et al.,[46] the follow-up research has shown that nitrate can be reduced to nitrite using a Pd catalyst modified with Cu.[47] The conversion of the resulting nitrite can be accomplished using a Pd catalyst in which nitrogen or ammonia can be formed. The process involves two consecutive reactions as shown below.

$$2NO_2^- + 3H_2 + 2H^+ \rightarrow N_2 + 4H_2O \qquad (23)$$

$$NO_2^- + 3H_2 + 2H^+ \rightarrow NH_4^+ + 2H_2O \qquad (24)$$

Since the polymer herein studied can induce solvation effects of ions and polar molecules, one can employ this hydrogenation reaction to study the polymer-induced solvation effects.[29] In particular, we are interested in learning how the state of the polymer above and below the LCST affects the reaction rate and selectivity.

5.2 Nitrobenzene hydrogenation

Aniline (AN) is an important industrial chemical intermediate for the production of plastics (e.g. polyurethanes), herbicides, pharmaceuticals, pigments, dyes, and rubber. It is produced

industrially by the reduction of nitrobenzene (NB) in hydrogen. [48] In this reaction process aniline and P-aminophenol form via parallel pathways as shown in Figure 5. Harber et al.[49] proposed the first reaction mechanism in 1898 for this reaction in which nitrobenzene was converted to aniline in a three-step process via nitrosobenzene and phenylhydroxylamine intermediates. This mechanism was generally accepted until very recently. For instance, Jackson et al.[50] showed that nitrosobenzene cannot be an intermediate in the hydrogenation of nitrobenzene using kinetic isotope experiments. The authors found the most abundant surface intermediate was the phenyl nitro-hydroxyl specie (Ph–N(OH)) rather than the nitrosobenzene intermediate (Figure 5, green pathway). This new mechanism has been widely accepted and it is supported by subsequent DFT and spectroscopy studies.[51][52][53]

The product distribution of this reaction is sensitive to changes in the local environment (reactant concentration, pH, solvent, etc.). Thus, we expect that the solvation effects induced by the polymer can result in drastic changes in the product selectivity and activation energy of the NB hydrogenation reaction.

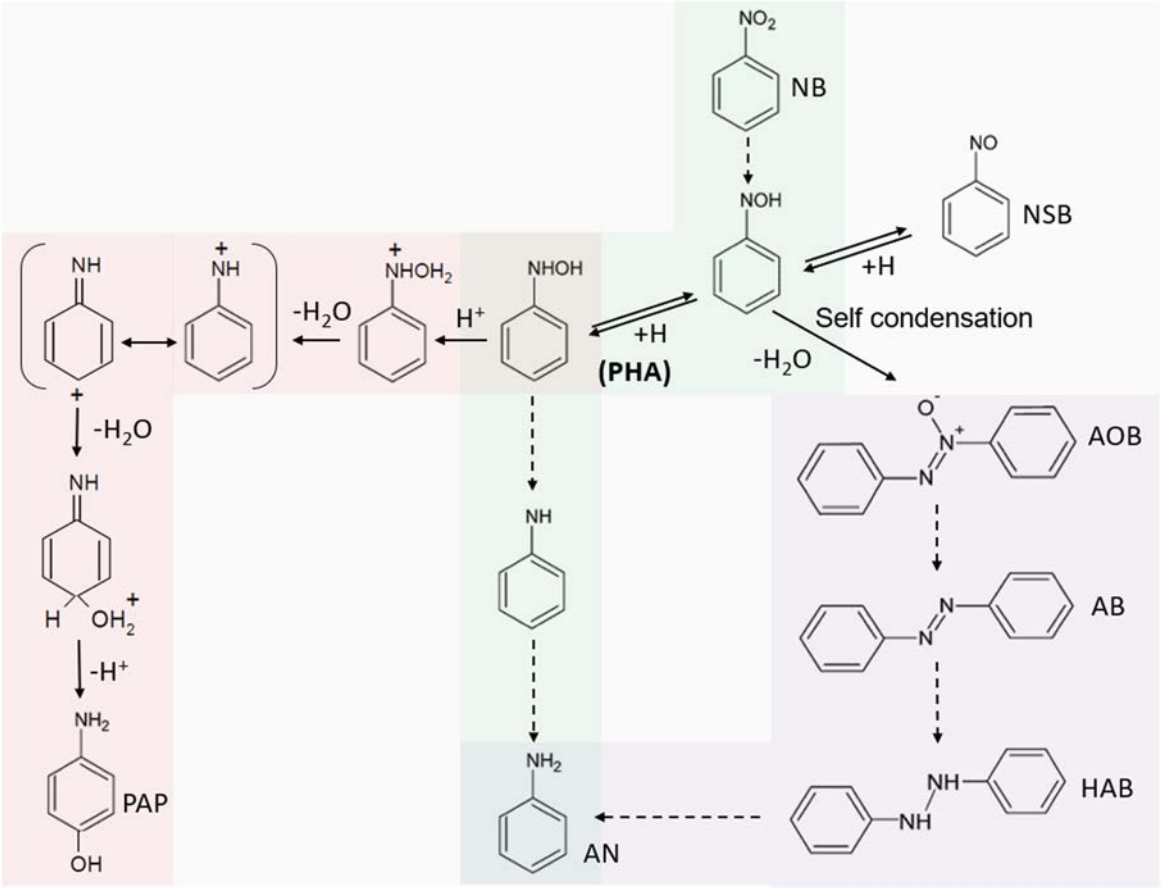

Figure 5. Reaction diagram of nitrobenzene hydrogenation reaction.

6. Scope and outline of the thesis

In this thesis, we explored the polymer-induced solvation effects via modification of the catalyst with thermally responsive polymer coatings. The aim of using a thermally responsive polymer is to manipulate the solvation environment around the active sites of the catalyst in a fully reversible manner, simply leveraging the temperature of the system. Nitrite and nitrobenzene hydrogenation reactions were employed as model reactions to study these solvation effects due to their sensitivity to the reaction media, fast kinetics at room temperature, and practical relevance in pollution control and synthesis of chemicals. For this purpose, we conducted detailed reaction kinetics and modeling studies to unravel how the polymer-coated catalyst behaves under variable operating conditions.

In **Chapter 2**, a rigorous kinetic study of nitrite hydrogenation has been conducted using the uncoated Pd/SiO_2 catalyst to develop a mechanistic model of the reaction and unravel the interplay between operating conditions, apparent activation barriers, and rate-determining step in the presence of water as a solvent. In contrast to the previous research conducted by P. Xu et al.,[54] here, we use non-porous silica support to avoid any internal mass transfer effects. Furthermore, the present work explored the effects of temperature on the apparent reaction orders and the degree of rate control. By combining the kinetic data related to the apparent reaction orders in hydrogen and nitrite, a revised mechanism has been proposed in which the hydrogenation of NO* to HNO* and subsequent hydrogenation of HNO* to HNOH* co-limits the reaction rate. This experimental observation was supported by DFT calculations that showed that the first and second hydrogenation steps of NO* have similar apparent energy barriers when the hydrogenation reaction is assisted by water molecules adjacent to the active site. In the postulated mechanism, the hydrogen dissociated on the palladium surface undergoes a separation into a proton and electron in which the proton is shuttled by the water network near the palladium surface towards either NO* or HNO*, while the electron is transferred to the reacting species via the metal. Furthermore, the degree of rate control analysis showed that the RDS shifts with the reaction conditions, which explains why the reaction orders drastically change with reactant concentration and temperature.

In **Chapter 3**, a polymer-coated catalyst was successfully synthesized consisting of Pd/SiO_2-p-NIPAM to study the polymer-induced solvation effects on nitrite hydrogenation. In addition, the influence of temperature on the behavior of a thermally responsive polymer and the corresponding induced solvation effect on a reaction has been discussed. Here, it was demonstrated for the first time that p-NIPAM polymers can induce a solvation effects that can

stabilize the transition state thus lowering the activation energy barrier of a reaction in completely reversible manner.

To study the effect of polymer-coated catalysts on uncharged molecules, the nitrobenzene hydrogenation was explored on Pd. The main goal of this study was to test the potential extrapolation of this concept to other reactions. The effect of polymer on the activation energy barrier at temperatures below and above the LCST of the p-NIPAM has been explained using the excess free energy based on the transition state theory. Furthermore, the potential interactions of the reactants and the polymer species was explored using by NMR spectroscopy. This part of the work is presented in **Chapter 4.**

The effect of solvents is crucial in catalysis due to their influence on reactivity, selectivity, and mechanism of chemical reactions. To verify the proton shuttling effects and polymer-induced solvation effects, we decided to study the impact of using aprotic solvents during the nitrobenzene hydrogenation This was accomplished by changing the solvent from pure water to mixtures with increasing concentrations of 1-methyl-2-pyrrolidone (NMP). Here, the solubility of organic compounds is greatly enhanced while the proton shuttling effect is hindered by increasing the NMP concentration. This modified the reaction selectivity and activation energy barrier of the catalyst. This part of the work is shown in **Chapter 5.**

Chapter 6 summarizes the main findings of this thesis, including the main conclusions and recommendations for future work.

References

[1] J.J. Varghese, S.H. Mushrif, Origins of complex solvent effects on chemical reactivity and computational tools to investigate them: a review, React. Chem. Eng. 4 (2019) 165–206.

[2] M. Andreev, J.J. de Pablo, A. Chremos, J.F. Douglas, Influence of ion solvation on the properties of electrolyte solutions, J. Phys. Chem. B. 122 (2018) 4029–4034.

[3] M. a C. Stuart, W.T.S. Huck, J. Genzer, M. Müller, C. Ober, M. Stamm, G.B. Sukhorukov, I. Szleifer, V. V Tsukruk, M. Urban, F. Winnik, S. Zauscher, I. Luzinov, S. Minko, Emerging applications of stimuli-responsive polymer materials., Nat. Mater. 9 (2010) 101–113. https://doi.org/10.1038/nmat2614.

[4] A. Grinthal, J. Aizenberg, Adaptive all the way down: building responsive materials from hierarchies of chemomechanical feedback., Chem. Soc. Rev. 42 (2013) 7072–85. https://doi.org/10.1039/c3cs60045a.

[5] R. Eelkema, J.H. van Esch, Catalytic control over the formation of supramolecular materials., Org. Biomol. Chem. (2014) 6292–6296. https://doi.org/10.1039/c4ob01108b.

[6] S.S. Nagarkar, A. V. Desai, S.K. Ghosh, Stimulus-responsive metal-organic frameworks, Chem. - An Asian J. 9 (2014) 2358–2376. https://doi.org/10.1002/asia.201402004.

[7] D. Díaz Díaz, D. Kühbeck, R.J. Koopmans, Stimuli-responsive gels as reaction vessels and reusable catalysts, Chem. Soc. Rev. 40 (2011) 427–448. https://doi.org/10.1039/C005401C.

[8] X. Liu, Y. Yang, M.W. Urban, Stimuli-Responsive Polymeric Nanoparticles, Macromol. Rapid Commun. 201700030 (2017) 1–20. https://doi.org/10.1002/marc.201700030.

[9] R. Roa, W.K. Kim, M. Kanduč, J. Dzubiella, S. Angioletti-Uberti, Catalyzed Bimolecular Reactions in Responsive Nanoreactors, ACS Catal. 7 (2017) 5604–5611. https://doi.org/10.1021/acscatal.7b01701.

[10] J. Pyun, K. Matyjaszewski, Synthesis of nanocomposite organic/inorganic hybrid materials using controlled/"living" radical polymerization, Chem. Mater. 13 (2001) 3436–3448. https://doi.org/10.1021/cm011065j.

[11] J.O. Zoppe, N.C. Ataman, P. Mocny, J. Wang, J. Moraes, H.A. Klok, Surface-Initiated Controlled Radical Polymerization: State-of-the-Art, Opportunities, and Challenges in

Surface and Interface Engineering with Polymer Brushes, Chem. Rev. 117 (2017) 1105–1318. https://doi.org/10.1021/acs.chemrev.6b00314.

[12] S. Wu, J. Dzubiella, J. Kaiser, M. Drechsler, X. Guo, M. Ballauff, Y. Lu, Thermosensitive Au-PNIPA yolk-shell nanoparticles with tunable selectivity for catalysis, Angew. Chemie - Int. Ed. 51 (2012) 2229–2233. https://doi.org/10.1002/anie.201106515.

[13] G.F. Froment, K.B. Bischoff, D.J. Wilde, Chemical Reactor Analysis and Design, 3rd ed., John Wiley & Sons, New York, 2011.

[14] F. Kapteijn, J.A. Moulijn, Chapter 6: Kinetics and Transport Processes, in: Handb. Heterog. Catal., 1997: pp. 1189–1261.

[15] K.J. Laidler, J.H. Meiser, Physical Chemistry (1982), (n.d.).

[16] H.-J. Freund, R.A. van Santen, M. Neurock, M. Boudart, C.B. Mullins, J.K. Norskov, P. Stoltze, K. Tamura, S. Naito, G. Jonkers, G. Ertl, Section 5: Elementary Steps and Mechanisms, Handb. Heterog. Catal. (1997) 911–1051. https://doi.org/10.1002/9783527619474.ch5a.

[17] C. Becker, From Langmuir to Ertl: The “Nobel” History of the Surface Science Approach to Heterogeneous Catalysis, (2018).

[18] C.T. Campbell, The Degree of Rate Control: A Powerful Tool for Catalysis Research, ACS Catal. 7 (2017) 2770–2779. https://doi.org/10.1021/acscatal.7b00115.

[19] Z. Mao, C.T. Campbell, The degree of rate control of catalyst-bound intermediates in catalytic reaction mechanisms: Relationship to site coverage, J. Catal. 381 (2020) 53–62. https://doi.org/10.1016/j.jcat.2019.09.044.

[20] C. Franch, R.G.H. Lammertink, L. Lefferts, Partially hydrophobized catalyst particles for aqueous nitrite hydrogenation, Appl. Catal. B Environ. 156–157 (2014) 166–172. https://doi.org/10.1016/j.apcatb.2014.03.020.

[21] A.J. Frierdich, J.R. Shapley, T.J. Strathmann, Rapid reduction of N-nitrosamine disinfection byproducts in water with hydrogen and porous nickel catalysts, Environ. Sci. Technol. 42 (2008) 262–269.

[22] D.E. Mears, Tests for Transport Limitations in Experimental Catalytic Reactors, Ind. Eng. Chem. Process Des. Dev. 10 (1971) 541–547. https://doi.org/10.1021/i260040a020.

[23] D. Shuai, J.K. Choe, J.R. Shapley, C.J. Werth, Enhanced activity and selectivity of carbon nanofiber supported Pd catalysts for nitrite reduction, Environ. Sci. Technol. 46 (2012) 2847–2855. https://doi.org/10.1021/es203200d.

[24] G. Li, B. Wang, D.E. Resasco, Solvent effects on catalytic reactions and related phenomena at liquid-solid interfaces, Surf. Sci. Rep. (2021) 100541. https://doi.org/10.1016/j.surfrep.2021.100541.

[25] D.S. Potts, D.T. Bregante, J.S. Adams, C. Torres, D.W. Flaherty, Influence of solvent structure and hydrogen bonding on catalysis at solid–liquid interfaces, Chem. Soc. Rev. 50 (2021) 12308–12337. https://doi.org/10.1039/d1cs00539a.

[26] H. Eyring, The activated complex and the absolute rate of chemical reactions., Chem. Rev. 17 (1935) 65–77.

[27] A.K. Chew, T.W. Walker, Z. Shen, B. Demir, L. Witteman, J. Euclide, G.W. Huber, J.A. Dumesic, R.C. Van Lehn, Effect of Mixed-Solvent Environments on the Selectivity of Acid-Catalyzed Dehydration Reactions, ACS Catal. 10 (2020) 1679–1691. https://doi.org/10.1021/acscatal.9b03460.

[28] Z.B. Shifrina, V.G. Matveeva, L.M. Bronstein, Role of polymer structures in catalysis by transition metal and metal oxide nanoparticle composites, Chem. Rev. 120 (2019) 1350–1396.

[29] T.J. Schwartz, T.S. Wesley, J.A. Dumesic, Modifying the Surface Properties of Heterogeneous Catalysts Using Polymer-Derived Microenvironments, Top. Catal. 59 (2016) 19–28.

[30] Y. Zhao, J.A. Baeza, N.K. Rao, L. Calvo, M.A. Gilarranz, Y.D. Li, L. Lefferts, Unsupported PVA-and PVP-stabilized Pd nanoparticles as catalyst for nitrite hydrogenation in aqueous phase, J. Catal. 318 (2014) 162–169.

[31] T.J. Schwartz, R.L. Johnson, J. Cardenas, A. Okerlund, N.A. Da Silva, K. Schmidt-Rohr, J.A. Dumesic, Engineering catalyst microenvironments for metal-catalyzed hydrogenation of biologically derived platform chemicals, Angew. Chemie - Int. Ed. 53 (2014) 12718–12722. https://doi.org/10.1002/anie.201407615.

[32] R. Alamillo, A.J. Crisci, J.M.R. Gallo, S.L. Scott, J.A. Dumesic, A tailored microenvironment for catalytic biomass conversion in inorganic–organic nanoreactors, Angew. Chemie. 125 (2013) 10539–10541.

[33] R. Akiyama, S. Kobayashi, “Microencapsulated” and related catalysts for organic chemistry and organic synthesis, Chem. Rev. 109 (2009) 594–642.

[34] Y. Lu, Y. Mei, M. Drechsler, M. Ballauff, Thermosensitive core-shell particles as carriers for Ag nanoparticles: Modulating the catalytic activity by a phase transition in networks, Angew. Chemie - Int. Ed. 45 (2006) 813–816. https://doi.org/10.1002/anie.200502731.

[35] C.S. Bruning-Fann, J.B. Kaneene, The effects of nitrate, nitrite and N-nitroso compounds on human health: a review., Vet. Hum. Toxicol. 35 (1993) 521–538.

[36] F. Edition, Guidelines for drinking-water quality, WHO Chron. 38 (2011) 104–108.

[37] K.T. Ranjit, B. Viswanathan, Photocatalytic reduction of nitrite and nitrate ions to ammonia on M/TiO2 catalysts, J. Photochem. Photobiol. A Chem. 108 (1997) 73–78. https://doi.org/10.1016/S1010-6030(96)04505-4.

[38] V.K. Indusekhar, G.S. Trivedi, B.G. Shah, Removal of nitrate by electrodialysis, Desalination. 84 (1991) 213–221.

[39] S.S. Madaeni, S. Koocheki, Influence of di-hydrogen phosphate ion on performance of polyamide reverse osmosis membrane for nitrate and nitrite removal, J. Porous Mater. 17 (2010) 163–168.

[40] A. Pintar, J. Batista, J. Levec, Integrated ion exchange/catalytic process for efficient removal of nitrates from drinking water, Chem. Eng. Sci. 56 (2001) 1551–1559.

[41] V. Matějů, S. Čižinská, J. Krejčí, T. Janoch, Biological water denitrification—a review, Enzyme Microb. Technol. 14 (1992) 170–183.

[42] H.C. Aran, J.K. Chinthaginjala, R. Groote, T. Roelofs, L. Lefferts, M. Wessling, R.G.H. Lammertink, Porous ceramic mesoreactors: A new approach for gas-liquid contacting in multiphase microreaction technology, Chem. Eng. J. 169 (2011) 239–246. https://doi.org/10.1016/j.cej.2010.11.005.

[43] A. Pintar, G. Berčič, J. Levec, Catalytic liquid-phase nitrite reduction: Kinetics and catalyst deactivation, AIChE J. 44 (1998) 2280–2292.

[44] H.C. Aran, J.K. Chinthaginjala, R. Groote, T. Roelofs, L. Lefferts, M. Wessling, R.G.H. Lammertink, Porous ceramic mesoreactors: a new approach for gas–liquid contacting in multiphase microreaction technology, Chem. Eng. J. 169 (2011) 239–246.

[45] M. Hu, Y. Liu, Z. Yao, L. Ma, X. Wang, Catalytic reduction for water treatment, Front. Environ. Sci. Eng. 12 (2018) 1–18. https://doi.org/10.1007/s11783-017-0972-0.

[46] S. Hörold, K.-D. Vorlop, T. Tacke, M. Sell, Development of catalysts for a selective nitrate and nitrite removal from drinking water, Catal. Today. 17 (1993) 21–30.

[47] Y. Yoshinaga, T. Akita, I. Mikami, T. Okuhara, Hydrogenation of nitrate in water to nitrogen over Pd–Cu supported on active carbon, J. Catal. 207 (2002) 37–45.

[48] M. Turáková, T. Salmi, K. Eränen, J. Wärnå, D.Y. Murzin, M. Králik, Liquid phase hydrogenation of nitrobenzene, Appl. Catal. A Gen. 499 (2015) 66–76.

[49] F. Haber, Über stufenweise Reduktion des Nitrobenzols mit begrenztem Kathodenpotential, Z. Elektrochem. 4 (1898) 506–514.

[50] E.A. Gelder, S.D. Jackson, C.M. Lok, The hydrogenation of nitrobenzene to aniline: a new mechanism, Chem. Commun. (2005) 522–524.

[51] L. Zhang, J. Jiang, W. Shi, S. Xia, Z. Ni, X. Xiao, Insights into the hydrogenation mechanism of nitrobenzene to aniline on Pd 3/Pt (111): a density functional theory study, RSC Adv. 5 (2015) 34319–34326.

[52] L. Zhang, Z.-J. Shao, X.-M. Cao, P. Hu, Interface-tuned selective reductive coupling of nitroarenes to aromatic azo and azoxy: a first-principles-based microkinetics study, Phys. Chem. Chem. Phys. 21 (2019) 12555–12565.

[53] L. Zhang, Z.-J. Shao, X.-M. Cao, P. Hu, Insights into different products of nitrosobenzene and nitrobenzene hydrogenation on Pd (111) under realistic reaction conditions, J. Phys. Chem. C. 122 (2018) 20337–20350.

[54] P. Xu, S. Agarwal, L. Lefferts, Mechanism of nitrite hydrogenation over Pd/γ-Al2O3 according a rigorous kinetic study, J. Catal. 383 (2020) 124–134.

Chapter 2

Proton Shuttling Flattens the Energy Landscape of Nitrite Catalytic Reduction

Abstract

Water molecules can enhance or inhibit hydrogenation reactions depending on the nature of the reactive species and active sites. In metal-catalyzed nitrite (NO_2^-) reduction the presence of protons is essential to complete the reaction in the aqueous phase. By coupling rigorous kinetics studies of nitrite hydrogenation on Pd with kinetic isotope studies and theoretical calculations we have shown that, contrary to previously proposed mechanisms of surface H-insertion on NO*, in aqueous environments the reaction proceeds via H-shuttling in which protons move via the aqueous environment while the electrons reach the NO* through the metal in a concerted fashion. This unique mechanism flattens the energy landscape, which leads to the same apparent activation energy barrier (0.6 eV) for the formation of HNO* and HNOH*. These results are consistent with the hydrogen reaction orders, kinetic isotopic experiments, and micro-kinetic modeling including co-limiting reaction steps for NO* hydrogenation to HNO* and HNOH*. This work provides new insights that will be key in developing more efficient catalysts and processes for catalytic removal of micro-pollutants, such as nitrate and nitrite, in drinking water and more broadly to hydrogenation reactions in aqueous phase.

This part of work has been published as research article: Proton Shuttling Flattens the Energy Landscape of Nitrite Catalytic Reduction. Journal of catalysis. 413 (2022): 252-263.

1. Introduction

In nature water plays a crucial role in facilitating the operation of bio-chemical redox processes like those involved in the carbon and nitrogen cycles. For instance, in nitrogen reducing, molybdenum enzymes (NR-Mo) it has been shown that four ordered water molecules located near the metal site define the binding site of nitrates.[1]This is not surprising as proton transfer reactions, that are enhanced by hydrogen bonding provided by water, are required in the reduction of nitrate to nitrite. These N oxyanions are essential in the pathway to N_2 that closes the N-cycle. When conducting these reactions in solid catalysts these localized molecular interactions, ubiquitous to aqueous environments, cannot be capture using classical solvation theories, such as those proposed by Debye and Hückel,[2] Kirkwood,[3] Kamlet and Taft,[4] as the continuum description cannot capture the complexity that arises at the solid-liquid interface. It is clearly the role of molecular water in the catalytic cycle what makes a detailed knowledge of these interactions essential in heterogeneous catalysts.[5,6]

Aqueous environments are often avoided in heterogeneous catalysis as water can be detrimental for the reaction due to either strong adsorption to the catalyst active sites inhibiting the rate, degradation of the support via hydrolysis, oxidation of metal clusters, or the lixiviation of the catalyst active phase. In many cases, however, water presence is unavoidable. This is the case of catalytic reduction of nitrate (NO_3^-) and nitrite (NO_2^-) in drinking water.[7–9] The reaction has gained renewed interest primarily due to the leakage of nitrogen-based fertilizers from intensive agricultural activities into natural aquifers.[10] These contaminants can directly or indirectly cause a series of diseases in humans, such as blue baby syndrome, cancer, and hypertension, and severely damage to the environment via eutrophication of water bodies.[11] This has resulted in strict limits of these micropollutants in drinking water. According to the World Health Organization (WHO), the maximum allowable levels of nitrate, nitrite, and ammonia concentration in drinking water are 50 mg/L, 3 mg/L, and 1.5 mg/L, respectively.[12] Depending of the reaction conditions, media, and catalyst chemistry the selectivity can be steered towards nitrogen or ammonia.[13–15] The latter, however, is an undesired product as its toxicity is even higher than that of nitrite. Considering the low concentrations of nitrates and nitrite in drinking water it is essential to use catalysts with extremely high activity and selectivity to nitrogen at near ambient conditions.[16] While the hydrogenation of nitrates to nitrite readily occurs on oxophilic Cu-based catalysts,[17,18] the reduction of the latter to dinitrogen, requires catalysts that can activate both H_2 dissociation and N-N bond formation. This is typically achieved using noble catalysts (e.g. Palladium and Rhodium).[17–21] Here,

protons, molecular hydrogen, nitrates, and nitrite actively participate in the reaction. Specifically, protons play an essential role in this reaction. For instance, on Rh catalysts it has been shown that slow reaction kinetics are obtained in acidic pH due to the strong adsorption of NO* species on the surface, which are readily formed from HNO_2.[22] Notably, deprotonation of HNO_2 at high pH led to measurable rates and high selectivity towards ammonia. This was attributed to slower dissociation rates of NO_2^- to NO* on Rh. In contrast, on Pd very fast reaction kinetics and nearly complete selectivity to nitrogen was observed at low pH.[23,24] This trait of nitrite hydrogenation makes it a perfect reaction probe for studying the role of water on the reaction activity and selectivity of metal catalysts.

The reaction mechanism of nitrite has been extensively studied in the past using experimental,[23–31] spectroscopic,[7,32–34] and computational tools.[22,29,35–37] On Pd-based catalysts detailed spectroscopic and reaction kinetic studies have shown that NO_2^- undergoes hydrogenolysis to NO* and H_2O in the presence of protons and hydrogen. [25,26,34] This critical intermediate could either dissociate into N- and O- atoms,[27] or undergo dimerization with another NO,[28] or couple with H[22,23,25,26,34] before forming N_2. Density functional theory (DFT) calculations have shown that dissociation of N-O is kinetically unfavorable with barriers of 1.46 eV.[22] Likewise, NO* dimerization reactions are considered unlikely to occur due to the increased repulsion forces caused by the dipole-dipole interaction of chemisorbed NO*.[29] In this scenario, the H-insertion on surface NO* species seems to be the most possible pathway.

In-depth analysis of the reaction kinetics of the published literature (see Table 1) reveals that significant changes in the reaction order take place with the reactant concentration. For instance, when the concentration ranges used were relatively narrow with nitrite concentrations and hydrogen pressures of 0.1-1 mM and 0.1-1 bar, respectively, the apparent reaction orders in hydrogen varied between 0 and 0.5, while the nitrite orders ranged from 0 to 1. These observations suggest that the rate limiting step involves hydrogen insertion on surface nitrosyls species (NO* and/or HNO*). Notably, when low partial pressures of hydrogen were employed the reaction order increased to ~ 2, while nitrite orders became negative. This change in the hydrogen reaction order reveals that the rate limiting step drastically shifts with surface coverage to a late step in the hydrogenation mechanism.[23] These drastic changes in the rate determining step are common in electrocatalytic processes as the surface coverages can be widely varied with the applied potential. However, in low temperature thermo-catalytic reactions such observations are difficult to rationalized as surface coverages are often low. An

alternative explanation could be that the apparent energy barriers for the different H-insertion steps start to reach similar values. That is that the energy landscape flattens. In this description, the degree of rate control can readily shift from different steps in the mechanism as a function of the surface coverage.

Considering that in heterogeneous catalysts water can exert multiple effects on reactivity, stability, and selectivity, including: (1) alteration of the energetics of bulk, surface, and activated complexes,[38–40] (2) participation in the reaction mechanism via H-bonding and proton transfer,[37,41,42] and (3) competitive adsorption with reactive species.[43] In this contribution, we have combined detailed catalyst characterization, catalytic measurements, kinetic isotope studies, density functional theory calculations, and micro-kinetics to unambiguously stablish the fundamental role of water molecules in the nitrite reduction on Pd. First, we developed a set of nonporous spherical SiO_2 particles decorated with Pd clusters with well-controlled cluster size to ensure that internal mass transport limitations can be disregarded. This rigorous approach is required because selectivity in nitrite reduction appears particular sensitive to internal concentration gradients, even when catalyst efficiency is not yet affected according the Weisz-Prater criterion.[23,44] The resulting materials shows near complete selectivity to nitrogen (>99 %) and high intrinsic activity characteristic of Pd catalysts. The concerted use of catalytic testing, kinetic isotopic effects, and DFT revealed that H-insertion is facilitated by the water molecules via proton shuttling in which the electron from the H* moves via the conduction band of the metal, while the corresponding proton is transferred via a network of water molecules. This results in facile insertion of hydrogen on NO* and HNO* surface intermediates, explaining the change of the reaction order of hydrogen from 0 to 1.5 at high and low surface coverages, respectively. This is further illustrated using the degree of rate control of these reaction steps as a function of the hydrogen partial pressures and temperature. These new insights expand our understanding of the nitrite reduction chemistry, providing additional strategies to optimize the catalyst activity and selectivity.

Table 1. Kinetics of nitrite hydrogenation at room temperature reported in the literature.

Catalyst	Reactor	pH	Hydrogen pressure (bar)	Nitrite concentration (mM)	Hydrogen order	Nitrite order
Pd/Al_2O_3 [21]	Membrane	7	0.01–1	0.24–2.4	0	N/A
$Pd/\gamma\text{-}Al_2O_3$ [30]	Slurry	4.7	0.11–1	0.11–0.65	0–0.5	0–1
Pd/Al_2O_3 [23]	Batch	5.5	0.01–0.8	0.3–10	0.3-2.3	-1-0.4
Pd/CNF [45]	Membrane	7	0.2–1	0.044–0.22	<0	N/A
Pd/AC [44]	Fixed bed	4.5-9	0.3–0.7	0.27–0.45	0.4	0.7
Pd/ACC [46]	Slurry	4.5–8	1.8–6.4	1.63	0	1

2. Experimental section

2.1 Materials

Tetraethyl orthosilicate (TEOS, 98 %), ammonium hydroxide solution (NH_4OH, 25 % (NH_3 basis)), Tetraamminepalladium(II) nitrate solution ($Pd(NH_3)_4(NO_3)_2$, 10 wt. % in H_2O, 99.99%), sodium hydroxide (NaOH, 99 %), methanol (99.9%) and ethanol (99.8%) were purchased from Sigma-Aldrich and used as received. All the aqueous solutions were prepared using ultra-purified water obtained on a water purification system (Millipore, Synergy).

2.2 Catalyst preparation

2.2.1 Synthesis of the SiO_2 spheres

SiO_2 spheres were prepared by the hydrolysis of TEOS in an ethanol solution in the presence of ammonia and water following the procedure originally described by Stöber et al.[47] The procedure can be summaries as follows. Firstly, two solutions were prepared. For the solution, 15 mL of TEOS dissolved in 200 mL of ethanol in an oven-dried beaker. For solution II, 50 ml of NH_4OH, 30 mL of water and 100 mL of ethanol were added. After that, the solution I was added to solution II and the reaction was allowed to proceed for 22 h at room temperature under

continuous stirring (400 rpm). Then, the SiO_2 spheres were rinsed with ethanol twice. After that, the particles were dried in a vacuum oven at 50 °C overnight.

2.2.2 Synthesis of Pd/SiO_2 catalyst

Pd/SiO_2 catalyst was prepared by a strong electrostatic adsorption (SEA) method.[48,49] First, the point of zero charges (PZC) of the synthesized SiO_2 spheres was investigated (Figure S1). The PZC of the synthesized SiO_2 is 2.3. Then, 2 g of SiO_2 were dispersed in 60 ml of deionized water via sonication for 5 minutes. The pH of the solution was adjusted to 10.5 by adding $NH_3.H_2O$ solution. After that, 1.12 g $Pd(NH_3)_4(NO_3)_2$ was added dropwise to the SiO_2 dispersion, and the reaction took place for 1 h at room temperature under continuous stirring (300 rpm). During the adsorption process, the pH was kept constant at 10.5 by adding the $NH_3.H_2O$ solution. The resulting solution was filtered via sequential vacuum and filtration membranes. Then, the sample was dried in a vacuum oven at 40 °C overnight. Finally, the samples were calcined at 300 °C in the air for 0.5 h and reduced H_2 for 3 h with a heating rate of 2 °C /min.

2.2.3 Catalyst characterization

Brunauer–Emmett–Teller (BET) surface area analysis was conducted using a Micromeritics Model ASAP 2400 instrument. For each study, 0.2–0.3 g of sample was degassed at 120 °C for 24 h before measurement. The transmission electron microscopy (TEM) analysis results were obtained using a Tecnai F30 field emission TEM, with an acceleration voltage of 300KV and coupled with a HAADF detector (Fischione). The Scanning Electron Microscopy (SEM) was conducted to investigate the particle size by using a JEOL, LA6010 with a resolution of 4 nm @ 20 kV. The metal loading of the Pd/SiO_2 samples were determined by X-ray fluorescence (XRF) (Bruker, S8 TIGER). The metal dispersion of the Pd/SiO_2 samples was determined by CO chemisorption at room temperature (Micromeritics, Chemisorb 2750). The samples were reduced in H_2 at room temperature for 1 h and then flushed in He for 30 min. After that, CO was introduced as pulses, and the response was recorded using a TCD detector.

2.3 Catalytic tests

The reaction was conducted using the previously reported setup from our group.[23] Catalytic activity and selectivity were measured at atmospheric pressure with a temperature range from 25-50 °C. A pH value of 5.5 is maintained by buffering continuously CO_2 at a pressure of 0.1

bar. The glass reactor (DURAN ® baffled wide mouth bottle GLS 80) has four connections on the lid used for gas-in, gas-out, thermometer and sampling with a capacity of 1 L. The reaction conditions are summarized in Table S2. For a standard experiment, 0.05 g catalyst was suspended in 0.3 L deionized (DI) water and stirred at 500 rpm under 0.8 bar hydrogen (0.1 bar CO_2, 0.1 bar He) for at least 1 h, removing dissolved oxygen and reducing the catalyst. After that, the hydrogen pressure is switched to the value of choice. The reaction was started by introducing of 3 mL $NaNO_2$ solution (100 mM) in the glass reactor. Hydrogen pressure was varied between 0.01 and 0.9 bar, and the nitrite concentration was varied between 0.5 and 5 mM. The reaction temperature is controlled by an IKA contact thermometer ETS-D5. During the catalytic reaction, the samples were collected using a 5 mL syringe (BD Plastipak) and filtered with a syringe filter (PTFE 0.2 µm, Whatman). The nitrite and ammonium concentrations were explicitly analyzed using a ion-chromatography (DIONEX, ICS 3000) equipped with an autosampler and channel for anion and cation separately that can measure the anion and cation concentration simultaneously.

The apparent reaction orders and activation barriers were determined from a broad range of nitrite concentrations (0.5-5 mM), hydrogen partial pressures (0.01-0.9 bar), and temperatures (25-50 °C), using the initial rate calculated from the slope of the nitrite concentration profile as a function of time. By considering exclusively data at conversion lower than 10% it was possible to avoid the concentration effects on the rate characteristic of batch reactor operation (Figure S4). For the activation energy investigation, the decrease of hydrogenation concentration in the solution caused by increasing the temperature is compensate by increasing the partial hydrogenation pressure according to Henry's Law. The Kinetic Isotope Effect (KIE) test was conducted by using ^{15}N-labeled $NaNO_2$ to replace the unlabeled $NaNO_2$ to investigate the influence of nitrogen atoms and by using D_2/D_2O to replace H_2/H_2O to examine the impact of hydrogen atoms. The nitrite conversion and ammonium selectivity were calculated according to equation 1 and equation 2. Since it is well known that nitrogen and ammonia are the only product.[23] So, the nitrogen selectivity was calculated based on the mass balance.

$$NO_2^- \text{ conversion}_{t1} = \frac{[NO_2^-]_{t0} - [NO_2^-]_{t1}}{[NO_2^-]_{t0}} * 100 \qquad (1)$$

$$NH_4^+ \text{ selectivity}_{t1} = \frac{[NH_4^+]_{t1}}{[NO_2^-]_{t0} - [NO_2^-]_{t1}} * 100 \qquad (2)$$

Here, $[NO_2^-]_{t0}$ is initial nitrite concentration, $[NO_2^-]_{t1}$ is the concentration of nitrite at t1, $[NH_4^+]_{t1}$

2.4. Data reconciliation and parameter estimation

The kinetic model was evaluated by determining the parameter values that minimize the objective function given in equation 3.[50]

$$\mathrm{SSE} = \sum_{i=1}^{n} \left(\log_{10}(\mathrm{TOF}_{\mathrm{EXP}_i}) - \log_{10}(\mathrm{TOF}_{\mathrm{MOD}_i})\right)^2 \quad (3)$$

The square error for any experiment ***i*** was obtained by the difference between measured Turnover Frequency (TOF) and the corresponding model prediction at the same condition. The residual sum of squares (SSE) was combined with the total sum of squares (SST, Equation 4) to obtain the determination coefficient (R^2, Equation 5) and the Akaike Information Criterion (AIC, Equation 6) for each least squares solution.[51] Especially, the AIC involves a regression for variable parameter numbers, which helps identify the over-fitting case and determine a statistically preferred model.

$$\mathrm{SST} = \sum_{i=1}^{n} \left(\log_{10}(\mathrm{TOF}_{\mathrm{EXP}_i}) - \frac{1}{n}\sum_{i=1}^{n} \log_{10}(\mathrm{TOF}_{\mathrm{EXP}_i})\right)^2 \quad (4)$$

$$R^2 = 1 - \frac{\mathrm{SSE}}{\mathrm{SST}} \quad (5)$$

$$\mathrm{AIC} = 2n_k + \ln(\mathrm{SSE}) \quad (6)$$

In equations (4)-(6), *n* is the experimental measurements numbers and n_k is the number of adjustable parameters regressed in a model.

3. Result and discussion

3.1. Nitrite hydrogenation over Pd/SiO_2 catalyst

3.1.1. Catalyst Structure

The catalysts were characterized using SEM, HR-TEM, N_2 adsorption, and CO chemisorption (Table 2). The SEM image shows that the synthesized silica support has a diameter of ~ 500 nm (Figure S2). The specific surface area of SiO_2 and Pd/SiO_2 shows a very similar value, suggesting that the structure and porosity of the support remained unaltered after metal deposition. In addition, the value is very close to that theoretically estimated for a non-porous spherical silica particle with a diameter of 500 nm (Table 2). TEM characterization shows an average metal particle size of 2.5 nm (Figure S3), which agrees with the average particle size regressed from CO-chemisorption measurements.

Table 2. Characterization data of Pd/SiO_2 and support material SiO_2.

	TEM	XRF	CO-chemisorption	N_2-physisorption		
Sample	Pd particle size (nm)	Pd loading (wt. %)	Pd dispersion (%)	Specific surface area (m^2/g)	Theoretical specific surface area (m^2/g)	Pore volume (cm^3/g)
SiO_2	-	-	-	7.5	6.4	0.002
Pd/SiO_2	2.5	0.2	55.5	7.9	6.7	0.002

3.1.2. Mass transfer effects

To discern mechanistic information we conducted rigorous analysis of role of mass transfer effects on the experimentally measure rates. Heat transport limitations were assumed to be negligible due to the high heat capacity of water (4.2 kJ kg^{-1} K^{-1}), low conversion levels employed, and diluted nitrite concentrations (0.5-5 mM). Internal diffusional limitations were negligible in this Pd/SiO_2 catalyst since the specific surface area of the silica support is very close to the theoretical specific surface area of a non-porous material (i.e. sphere of 500 nm). The external mass transport limitations were assessed by measuring the turnover frequency (TOF) as a function of the agitation rate in the baffled reactor (Figure S5), increasing the agitation to 250 rpm plateaued the TOF, indicating that external mass transfer limitations can be excluded at the conditions hereto employed. These results agree with the estimated mass transport rates for the reactants. For instance, when the nitrite concentration is 1 mM, the calculated mass transfer rate is 4.3 x 10^2 mM min^{-1}, which is five orders of magnitude larger than the highest reaction rate measured (5.0 x 10^{-3} mM min^{-1}) at the same nitrite concentration. Likewise, the Mears criterion shows that external transport of hydrogen in the G-L and/or L-S interface does not limit our measurements (Section 4.1.2 and 4.1.3 in SI). Considering that the system is free of mass transfer effects one could use the information from the apparent reaction orders to extract mechanistic insights.

3.1.3. Apparent reaction orders and activation energy

As shown in Figure 1d the apparent activation energy barrier for the nitrite reduction in aqueous phase was 29 ± 1 kJ mol^{-1}, which is within the range reported in the literature for Pd catalysts

operating at similar reaction conditions (22.6 to 35.3 kJ mol^{-1}).[24,44,52] Next, we studied the reaction orders for nitrite and hydrogen in a broad window of concentrations at low and high temperature, the overall reaction order is summarized in Table 3.The reaction order investigation presented in Figure 1a and 1b, indicates that regardless of the reaction temperature (25°C and 50°C) the nitrite apparent reaction orders varied from 0.7 to 0 at high hydrogen partial pressures (0.8 bar). Notably, reducing the partial pressure of hydrogen to 0.05 bar drastically changed the reaction order to -0.9 and -0.2 at 25°C and 50°C, respectively. Here, the large reaction orders observed at the high hydrogen partial pressures would be consistent with the molecular chemisorption of nitrite, while the strong inhibition of nitrite observed at low hydrogen partial pressures reveals that hydrogen and nitrite compete for the same active site on the Pd surface. In contrast to previously proposed mechanisms summarized by Rosca et al.[53] who claim the N-O bond breaking is the rate-determining and hydrogenation happens on the dissociated fragments, the results herein obtained would suggest that the RDS only requires one surface N-containing surface specie as the highest apparent reaction order is significantly lower than 2 even at the low nitrite concentration region. These observations are not unique to this Pd/SiO_2 catalyst. For instance, Xu et al.[23] obtained a nitrite reaction order of -1, at low hydrogen partial pressures, when studying the hydrogenation of nitrite on Pd catalysts supported on alumina at 25°C in a similar buffered reaction system.

In the case of hydrogen, the reaction orders varied between 1.4 to 1.2 at low partial pressures when the experiments conducted at 25°C and 50°C, respectively (Figure 1c). Above 0.1 bar the reaction reaches an asymptotic behavior characteristic of saturation kinetics regardless of the temperature employed. While the modest decrease of the reaction orders with increasing temperature could be explained in terms of the entropic contributions to the Gibbs free energy of adsorption ($\Delta G_{ads} = \Delta H_{ads} - T\Delta S_{ads}$) that effectively reduced the inhibition of the reaction rate caused by surface coverage, the significant changes of reaction orders of hydrogen from 1.5 to close to 0 are more difficult to rationalize. Here, one could argue these high reaction orders are associated to a late rate-determining step in which multiple pre-equilibrated hydrogenation reactions are needed before reaching the RDS. This postulate was previously proposed by Xu et al.[23] during the hydrogenation of nitrite in buffered systems over Pd/Al_2O_3. In that case, the authors obtained reaction orders for hydrogen that varied from 0.3 to 2 at 20°C. This considerable variation was attributed to the changes in the surface coverage assuming that the rate-determining step is fixed regardless of the partial pressure of hydrogen and nitrite concentration. In this rationale, it is assumed that NO* is readily formed on the Pd surface at

the pH employed in this reaction (pH ~ 5.5), which is stepwise hydrogenated to (H)NO* and $(H)_2NO$* before reaching the RDS involving the decomposition of $(H)_2NO$*. An alternative proposition is that these changes are caused by a switch in the degree of rate control of two consecutive rate-determining steps. In this scenario, at low hydrogen partial pressures the mechanism is controlled by the hydrogenation of partly hydrogenated nitro-species, e.g. (H)NO*, leading to high reaction orders, which upon increasing the pressure shifts to the preceding step in the sequence (e.g. NO* hydrogenation) with the concomitant decrease in the reaction order. To further evaluate the aforementioned postulate we conducted kinetic isotope labelling experiments.

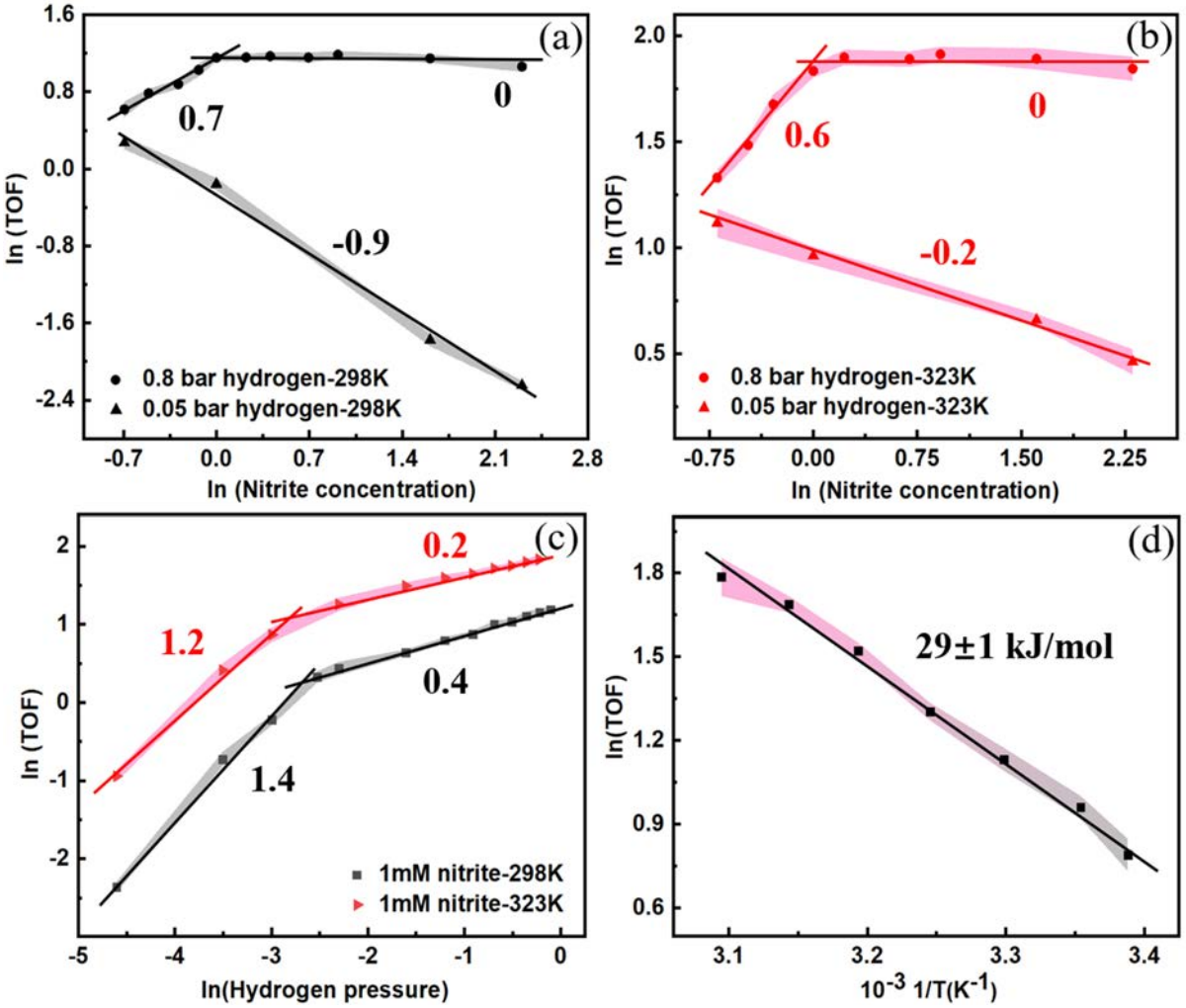

Figure 1. (a) and (b) effect of nitrite concentration on reaction rate for 0.05 and 0.8 bar hydrogen pressure at 25°C and 50°C. (c) Effect of hydrogen pressure on reaction rate for 1 mM nitrite concentration at 25°C and 50°C, (d) Temperature dependence of turnover frequency (TOF) over temperature. The shadow shows the error margin.

Table 3. Overview of the apparent reaction orders in nitrite and hydrogen information in all ranges of the nitrite and hydrogen concentrations

Temperature (°C)	Low hydrogen pressure		High hydrogen pressure	
	Hydrogen order	Nitrite order	Hydrogen order	Nitrite order
25	1.4 ± 0.1	-0.9 ± 0.1	0.4 ± 0.1	0.7± 0.1
50	1.2 ± 0.1	-0.2 ± 0.1	0.2 ± 0.1	0.6± 0.1

3.1.4. ^{15}N-labelling experiments

In these experiments, the nitrogen in $NaNO_2$ was isotopically labelled with ^{15}N while all the reaction conditions were kept constant. The observed turnover frequency (TOF=2.58 min^{-1}) for the reduction was similar to that of unlabeled $NaNO_2$ reduction (TOF=2.68 min^{-1}). The resulting kinetic isotope effect (k_{N14}/k_{N15}) was 1.04 ± 0.02 (Table 4), which is in line with previous reports on reduction of nitrite containing aromatic molecules. Considering that the maximum ratio of specific rate constants for ^{14}N to ^{15}N is 1.14 at 25°C,[54] it is clear that the small values obtained here suggest that there is no significant primary KIE. This further supports the idea that the rate determining step is not related to N-N bond formation nor N-O cleavage as previously suggested.[53]

3.1.5. Hydrogen-Deuterium isotope effect

By conducting kinetic experiments using deuterated hydrogen and water we explored the role of hydrogen insertion in the nitrite hydrogenation. Here, we obtained primary kinetic isotope effect with a K_H/K_D value of 2.4 at 25 °C. When increasing the temperature to 50 °C, the isotope effect of K_H/K_D is 1.5 (Table 4), which is consistent with the literature that deuterium reacts less readily than hydrogen at room temperature, thus increasing the temperature the value reaches of $\sqrt{2}$. [55] From the kinetic isotope effect, it is clear that the hydrogen atom is involved in the rate-determining step.

Table 4. Kinetic isotope effect.

	$KIE(K_H/K_D)^1$	$KIE(K_H/K_D)^1$	$KIE(K^{14}_N/K^{15}_N)^2$
	25℃	50℃	25℃
Pd/SiO_2	2.37 ± 0.1	1.51 ± 0.1	1.04 ± 0.02

Note: 1. using D_2/D_2O to replace H_2 and H_2O. 2.using $Na^{15}NO_2$ to replace $Na^{14}NO_2$.

3.1.6. The effect of the hydrogen pressure, nitrite concentration and kinetic isotope effect on ammonium selectivity

The selectivity of ammonium under different reaction conditions are shown in Figure 2. It shows the selectivity to ammonium increases with the hydrogen pressure (Figure2a), especially when the reaction conducted at a higher temperature, this is in agreement of the literature that the selectivity to ammonium increase with the H_2 pressure and temperature using a Pd/ Al_2O_3 catalyst.[31] Selectivity to ammonium decreases with increasing nitrite concentration (Figure2b). This is in line with the literature that using a Pd/γ-Al_2O_3 catalyst.[23] Experimental data on ammonia selectivity have a larger error margin, especially in the case of low hydrogen pressure and nitrite concentration. This is caused by the fact that ammonia concentration is relatively low at the beginning of the reaction, especially with a low concentration of reactant. So, in this case, the ammonia analysis is possible only with significant experimental scatter.

The kinetic isotope effect on the ammonium selectivity are shown in Table S1. It shows there is almost no effect on the ammonium selectivity or within the error margin. The possible reason is that to replace the N^{14} with N^{15} or to replace the H with D, the increase in atomic mass will slow down the rate determining steps, but for the other steps, the reaction rate are the same, the selectivity is not affected.

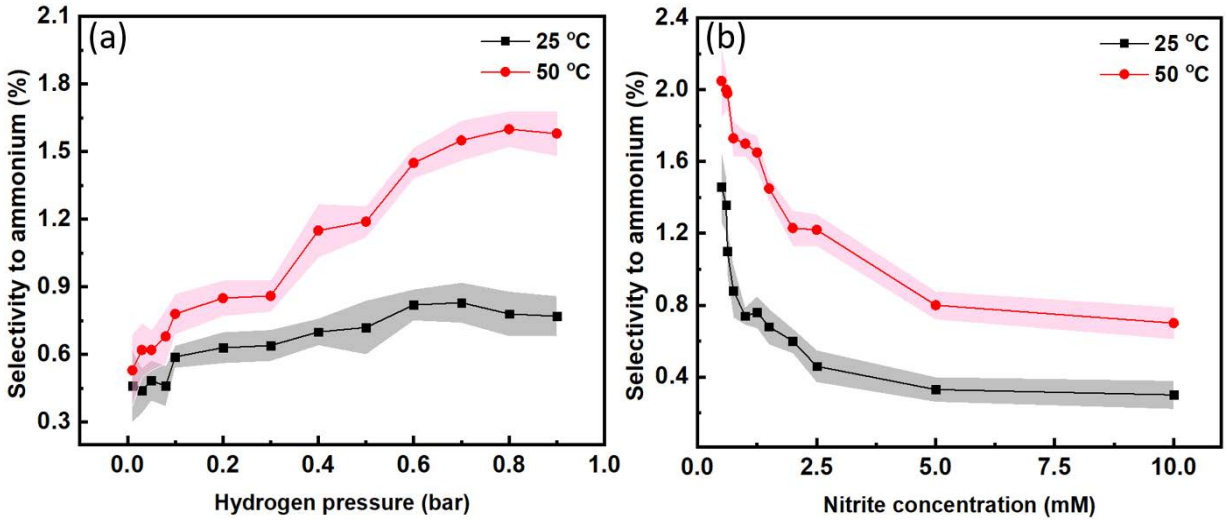

Figure 2. Selectivity to ammonium at 10% nitrite conversion level as a function of (a) hydrogen pressure, with 1mM nitrite concentration and (b) nitrite concentration, with 0.8 bar hydrogen pressure.

3.2 DFT calculation

This part is in cooperation with the University of Oklahoma in the United States of America, they have done a detailed DFT calculations considering implicit, explicit model, and proton shuttling path. It is concluded that the shuttling mechanism lowers the apparent barriers. This flattening of the energy landscape leads to similar barriers for the first two hydrogenation of NO that can match very well the observed reaction orders. Also the energy barrier for the hydrogenation steps are being calculated and used for the subsequent section. The details are show in supporting information section 5.

3.3. Langmuir-Hinshelwood-Hougen-Watson (LHHW) reaction kinetics

3.3.1. Rate expression development

As previously explained, the mechanism for nitrite hydrogenation involves barrier less formation of NO* on the palladium surface from chemisorbed NO_2^- and H_2, followed by sequential hydrogenation reactions to form HNO*, HNOH*, and HN*. As shown in the SI Section 6, the only possible mechanism that would lead to reaction orders for hydrogen that vary from 0.5 to 1.5, and thus fitting our results, is that involving co-limiting hydrogenation of NO* and HNO*. Choosing a single RDS would unavoidably lead to variations of the reaction

orders for hydrogen that vary between 0-1 for NO* hydrogenation or 0.5-1.5 for HNO* hydrogenation, which would be inconsistent with experimentally measured values. In this scenario, the elementary steps are as follows:

1. $H_2 + 2* \leftrightharpoons 2H^*$ (dissociative hydrogen adsorption, $\mathbf{K_1}$)
2. $NO_2^- + * \leftrightharpoons NO_2^{-*}$ (molecular nitrite adsorption, $\mathbf{K_2}$)
3. $NO_2^{-*} + H^* + H^+ \leftrightharpoons NO^* + H_2O + *$ (barrierless NO * formation, $\mathbf{K_3}$)
4. $NO^* + H^* \leftrightharpoons HNO^* + *$ (hydrogenation of NO *, $\mathbf{k_4}$) **TS1** RDS
5. $HNO^* + H^* \rightarrow HNOH^* + *$ (hydrogenation of HNO *, $\mathbf{k_5}$) **TS2** RDS
6. $HNOH^* + H^* \leftrightharpoons HN^* + H_2O + *$ (hydrogenation of HNOH *, $\boldsymbol{k_6}$) **TS3**

The underlaying assumption in this mechanism is that protons are readily available in this system and that chemisorbed hydrogen on Pd is required to provide the electrons for the reduction reactions. As a result, hydrogen atoms have been included in the site balance equation. This results in the following rate expression (Equation 7).

$$r_{NO_2^-} = \frac{k_5 k_4 * {K_1}^{3/2} K_2 K_3 [H_2]^{3/2} [NO_2{}^-][H^+]}{\left[k_{-4} + k_5 K_1^{\frac{1}{2}} [H_2]^{\frac{1}{2}}\right] * \left[1 + K_1^{1/2} [H_2]^{\frac{1}{2}} + K_2 [NO_2{}^-] + K_1^{1/2} K_2 K_3 [H_2]^{1/2} [NO_2{}^-][H^+] + \cdots \right]^2} \quad (7)$$
$$K_1 K_2 K_3 K_4 [H_2][NO_2{}^-][H^+]$$

If one considers that the concentration of the $[H^+]$ is low and constant (about 10^{-5} mol L^{-1}) in comparison to NO_2^- and H_2 concentrations (~ 10^{-3} mol L^{-1}), then it is possible to neglect the influence of protons in this buffered system. In this sense, the expression above can be simplified to equation 8.

$$r_{NO_2^-} = \frac{k_5 k_4 {K_1}^{3/2} K_2 K_3 [H_2]^{3/2} [NO_2{}^-]}{\left[k_{-4} + k_5 K_1^{1/2} [H_2]^{1/2}\right] * \left[1 + K_1^{1/2} [H_2]^{\frac{1}{2}} + K_2 [NO_2{}^-]\right]^2} \quad (8)$$

In this rate expression (Equation 8), one can immediately recognize that the reaction order for hydrogen and nitrite vary from 0 to 1.5 and -1 to 1, respectively.

3.4 Kinetic fitting analysis

We employed the extensive kinetic data presented in Figure 1 to evaluate the validity of the dual RDS mechanism. For this purpose, we used as input values for the error minimization algorithm the Gibbs free energies calculated by DFT for steps 4, -4, and 5. In this analysis, we

limited our fitting to the regression of the equilibrium and reaction constants. Here, it is important to mention that the optimized values of the Gibbs free energies of adsorption and activation were close to those obtained from the DFT calculation, indicating that these optimized values are physically meaningful.

Here, we observed that the model involving step 6 as RDS leads to large residual error, AIC, and low correlation coefficient at low and high temperatures (see Table S1). In contrast, when the RDS is moved earlier in the mechanism to either steps 4 or 5 the goodness of the fitting improves. We observe that when the reaction temperature is 25°C , step 4,5 both as RDS has the smallest residual error, AIC and high correlation coefficient, which means the best fitting is obtained. However, when the temperature increased to 25°C, steps 4 as RDS lead to the smallest residual error, AIC and high correlation coefficient. Essentially, this analysis suggests that as the reaction conditions are varied the system is either controlled by step 4, 5 or both. The kinetic fitting of step 4,5 as RDS are show in Figure S13.

3.5 Degree of rate control

We examined the degree of rate control of the step 4 and 5 over a large range of experimental conditions using the dual RDS model. We defined the Degree of Rate Control, X_{RC}, for elementary step, i, as described by Campbell (Equation 9).[56,57]

$$X_{RC,i} = \frac{k_i}{r}\left(\frac{\partial r}{\partial k_i}\right)_{k_{j\neq i}, K_i} \quad (9)$$

In order to assess the influence of temperature on the X_{RC} we estimated the values of the heat and entropies of adsorption using Van't Hoff equation for the equilibrium between the reactants in the liquid phase and the palladium surface, while the activation enthalpies and entropies were regressed using transition state treatments. To ensure thermodynamic consistency, we followed the criteria proposed by Vannice,[58] including: (1) heat of adsorption must be negative for adsorbing species, (2) there must be a decrease in entropy upon adsorption, and (3) the molecule cannot lose more entropy than it possesses before adsorption (see Section 7 and 8 in SI).

Our statistically optimal model predicts that, in general, both surface reactions are kinetically significant and the degree of rate control from each is sensitive to the operating conditions. As shown in Figure 3a, at 25°C the rate control lies primarily with step 5 at low hydrogen partial pressures (c.a. 0.01 bar), explaining the high reaction orders measured. Increasing the partial

pressure of hydrogen above 0.1 bar drastically led to a shift in the X_{RC} to step 4, which is consistent with the low reaction orders of hydrogen experimentally observed. Likewise, increasing the temperature shifted the rate control from step 5 to step 4 (Figure 3b) at low hydrogen partial pressure (0.01 bar). These results are in line with the slight decrease in the apparent reaction orders in hydrogen from 1.4 to 1.2 at 25°C and 50°C, respectively. Notably, at high hydrogen partial pressures (0.8 bar) the X_{RC} is dominated by step 4 of the reaction (Figure 3c). This explains the low sensitivity of the reaction orders near the saturation regime. These results illustrate the key role of the surface coverage in the large variations of the reaction orders for hydrogen in hydrogenation reactions.

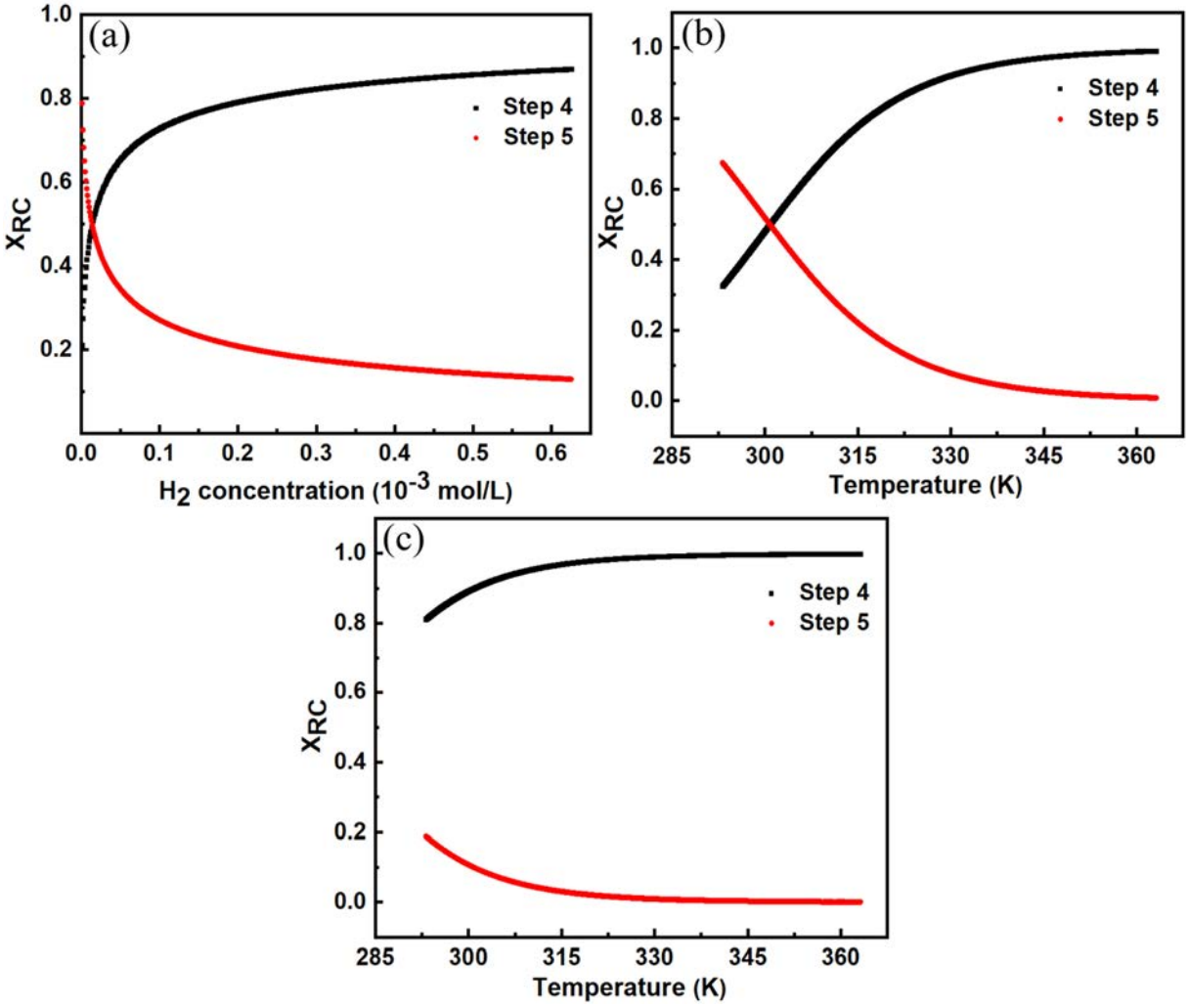

Figure 3. Degree of Rate Control as a function of hydrogen pressure (a) at 25°C. Degree of Rate Control as a function of temperature: (b) pH_2 = 0.01 bar, (c) pH_2 = 0.8 bar. Results were generated using the optimal parameter set from the kinetic fitting in section 3.4.

4. Conclusions

We have provided new experimental and theoretical insights into the reaction mechanism of nitrite hydrogenation on Pd catalysts that suggests that the large variations of the apparent reaction orders with the partial pressures of hydrogen, nitrite concentration, and temperature are correlated to a co-limiting rate limiting step. Rigorous Density Functional Theory calculations shows that the hydrogenation of NO via the nitrogen adatom is kinetically favored HNO over the NOH pathway. Furthermore, when explicit water molecules are included in the model to actively participate in the reaction via proton shuttling the activation energy barriers are reduced in comparison to non-assisted hydrogenation using implicit solvent models. This flattening of the energy landscape is in line with the observed reaction kinetics, and kinetic isotope effect measurements that suggest that NO* and HNO* hydrogenation reactions are co-limiting this reaction. Finally, the interdependence of the surface coverages and the extent of kinetic control of these two steps is clearly showcased by the LH kinetic modelling and degree of rate control analysis. Our results, reveal the importance of considering both chemical potentials of reacting species (partial pressures and surface coverages) and the Gibbs free energies of activation (rate and adsorption constants) in analyzing the seemingly simple nitrite hydrogenation reaction on palladium.

Reference

[1] W.G. Zumft, Cell biology and molecular basis of denitrification, Microbiol. Mol. Biol. Rev. 61 (1997) 533–616. https://doi.org/10.1128/mmbr.61.4.533-616.1997.

[2] P.H. Debye, E. Zur, Theorie der Elektrolyte. I. Gefrierpunktserniedrigung und verwandte Erscheinungen, Phys. Zeitschrift. 24 (1923) 185–206. https://doi.org/10.1063/1.1724503.

[3] J.G. Kirkwood, Theory of solutions of molecules containing widely separated charges with special application to zwitterions, J. Chem. Phys. 2 (1934) 351–361. https://doi.org/10.1063/1.1749489.

[4] M.J. Kamlet, J.L.M. Abboud, M.H. Abraham, R.W. Taft, Linear Solvation Energy Relationships. 23. A Comprehensive Collection of the Solvatochromic Parameters, π, α, and β, and Some Methods for Simplifying the Generalized Solvatochromic Equation, J. Org. Chem. 48 (1983) 2877–2887. https://doi.org/10.1021/jo00165a018.

[5] D.S. Potts, D.T. Bregante, J.S. Adams, C. Torres, D.W. Flaherty, Influence of solvent structure and hydrogen bonding on catalysis at solid–liquid interfaces, Chem. Soc. Rev. 50 (2021) 12308–12337. https://doi.org/10.1039/d1cs00539a.

[6] G. Li, B. Wang, D.E. Resasco, Solvent effects on catalytic reactions and related phenomena at liquid-solid interfaces, Surf. Sci. Rep. (2021) 100541. https://doi.org/10.1016/j.surfrep.2021.100541.

[7] U. Prüsse, M. Hähnlein, J. Daum, K.D. Vorlop, Improving the catalytic nitrate reduction, Catal. Today. 55 (2000) 79–90. https://doi.org/10.1016/S0920-5861(99)00228-X.

[8] K.N. Heck, S. Garcia-Segura, P. Westerhoff, M.S. Wong, Catalytic Converters for Water Treatment, Acc. Chem. Res. 52 (2019) 906–915. https://doi.org/10.1021/acs.accounts.8b00642.

[9] A. Kapoor, T. Viraraghavan, Nitrate Removal From Drinking Water—Review, J. Environ. Eng. 123 (1997) 371–380. https://doi.org/10.1061/(ASCE)0733-9372(1997)123:4(371).

[10] D.E. Canfield, A.N. Glazer, P.G. Falkowski, The evolution and future of earth's nitrogen cycle, Science (80-.). 330 (2010) 192–196. https://doi.org/10.1126/science.1186120.

[11] C.S. Bruning-Fann, J.B. Kaneene, The effects of nitrate, nitrite and N-nitroso compounds on human health: a review., Vet. Hum. Toxicol. 35 (1993) 521–538.

[12] F. Edition, Guidelines for drinking-water quality, WHO Chron. 38 (2011) 104–108.

[13] S. EBBESEN, B. MOJET, L. LEFFERTS, In Situ Attenuated Total Reflection Infrared (ATR-IR) Study of the Adsorption of NO, Langmuir. 24 (2008) 869–879.

[14] A.J. Lecloux, Chemical, biological and physical constrains in catalytic reduction processes for purification of drinking water, Catal. Today. 53 (1999) 23–34. https://doi.org/10.1016/S0920-5861(99)00100-5.

[15] M. Hu, Y. Liu, Z. Yao, L. Ma, X. Wang, Catalytic reduction for water treatment, Front. Environ. Sci. Eng. 12 (2018) 1–18. https://doi.org/10.1007/s11783-017-0972-0.

[16] V. Höller, I. Yuranov, L. Kiwi-Minsker, A. Renken, Structured multiphase reactors based on fibrous catalysts: Nitrite hydrogenation as a case study, Catal. Today. 69 (2001) 175–181. https://doi.org/10.1016/S0920-5861(01)00367-4.

[17] A. Obuchi, S. Naito, T. Onishi, K. Tamaru, Mechanism of catalytic reduction of NO by H2 or CO on a Pd foil; Role of chemisorbed nitrogen on Pd, Surf. Sci. 122 (1982) 235–255. https://doi.org/10.1016/0039-6028(82)90076-0.

[18] S. Hörold, K.-D. Vorlop, T. Tacke, M. Sell, Development of catalysts for a selective nitrate and nitrite removal from drinking water, Catal. Today. 17 (1993) 21–30.

[19] V. Matějů, S. Čižinská, J. Krejčí, T. Janoch, Biological water denitrification-A review, Enzyme Microb. Technol. 14 (1992) 170–183. https://doi.org/10.1016/0141-0229(92)90062-S.

[20] K.T. Ranjit, B. Viswanathan, Photocatalytic reduction of nitrite and nitrate ions to ammonia on M/TiO2 catalysts, J. Photochem. Photobiol. A Chem. 108 (1997) 73–78. https://doi.org/10.1016/S1010-6030(96)04505-4.

[21] H.C. Aran, J.K. Chinthaginjala, R. Groote, T. Roelofs, L. Lefferts, M. Wessling, R.G.H. Lammertink, Porous ceramic mesoreactors: A new approach for gas-liquid contacting in multiphase microreaction technology, Chem. Eng. J. 169 (2011) 239–246. https://doi.org/10.1016/j.cej.2010.11.005.

[22] C.A. Clark, C.P. Reddy, H. Xu, K.N. Heck, G. Luo, T.P. Senftle, M.S. Wong, Mechanistic insights into pH-controlled nitrite reduction to ammonia and hydrazine over rhodium, ACS Catal. 10 (2019) 494–509.

[23] P. Xu, S. Agarwal, L. Lefferts, Mechanism of nitrite hydrogenation over Pd/γ-Al2O3 according a rigorous kinetic study, J. Catal. 383 (2020) 124–134. https://doi.org/10.1016/j.jcat.2020.01.003.

[24] Z. Zhang, W. Shi, W. Wang, Y. Xu, X. Bao, R. Zhang, B. Zhang, Y. Guo, F. Cui, Interfacial electronic effects of palladium nanocatalysts on the by-product ammonia

selectivity during nitrite catalytic reduction, Environ. Sci. Nano. 5 (2018) 338–349.

[25] O.M. Ilinitch, L. V Nosova, V. V Gorodetskii, V.P. Ivanov, S.N. Trukhan, E.N. Gribov, S. V Bogdanov, F.P. Cuperus, Catalytic reduction of nitrate and nitrite ions by hydrogen: investigation of the reaction mechanism over Pd and Pd–Cu catalysts, J. Mol. Catal. A Chem. 158 (2000) 237–249.

[26] I. Mikami, Y. Sakamoto, Y. Yoshinaga, T. Okuhara, Kinetic and adsorption studies on the hydrogenation of nitrate and nitrite in water using Pd-Cu on active carbon support, Appl. Catal. B Environ. 44 (2003) 79–86.

[27] J. Wärn, I. Turunen, T. Salmi, T. Maunula, Kinetics of nitrate reduction in monolith reactor, Chem. Eng. Sci. 49 (1994) 5763–5773. https://doi.org/10.1016/0009-2509(94)00331-9.

[28] M. Duca, B. Van Der Klugt, M.A. Hasnat, M. Machida, M.T.M. Koper, Electrocatalytic reduction of nitrite on a polycrystalline rhodium electrode, J. Catal. 275 (2010) 61–69.

[29] H. Shin, S. Jung, S. Bae, W. Lee, H. Kim, Nitrite reduction mechanism on a Pd surface, Environ. Sci. Technol. 48 (2014) 12768–12774. https://doi.org/10.1021/es503772x.

[30] A. Pintar, G. Berčič, J. Levec, Catalytic liquid-phase nitrite reduction: Kinetics and catalyst deactivation, AIChE J. 44 (1998) 2280–2292.

[31] M.J.E. da Silva, L. Lefferts, J.A. Faria Albanese, N-isopropylacrylamide polymer brushes alter the micro-solvation environment during aqueous nitrite hydrogenation on Pd/Al2O3 catalyst, J. Catal. 402 (2021) 114–124. https://doi.org/10.1016/j.jcat.2021.08.003.

[32] J. Sá, T. Berger, K. Föttinger, A. Riss, J.A. Anderson, H. Vinek, Can TiO2 promote the reduction of nitrates in water?, J. Catal. 234 (2005) 282–291. https://doi.org/10.1016/j.jcat.2005.06.015.

[33] S.D. Ebbesen, B.L. Mojet, L. Lefferts, In situ attenuated total reflection infrared (ATR-IR) study of the adsorption of NO2-, NH2OH, and NH4+ on Pd/Al2O3 and Pt/Al2O3., Langmuir. 24 (2008) 869–79. https://doi.org/10.1021/la7027725.

[34] S.D. Ebbesen, B.L. Mojet, L. Lefferts, In situ ATR-IR study of nitrite hydrogenation over Pd/Al2O3, J. Catal. 256 (2008) 15–23. https://doi.org/10.1016/j.jcat.2008.02.013.

[35] L.Y. Huai, C.Z. He, H. Wang, H. Wen, W.C. Yi, J.Y. Liu, NO dissociation and reduction by H2 on Pd(1 1 1): A first-principles study, J. Catal. 322 (2015) 73–83. https://doi.org/10.1016/j.jcat.2014.11.011.

[36] S. Guo, K. Heck, S. Kasiraju, H. Qian, Z. Zhao, L.C. Grabow, J.T. Miller, M.S. Wong,

Insights into Nitrate Reduction over Indium-Decorated Palladium Nanoparticle Catalysts, ACS Catal. 8 (2018) 503–515. https://doi.org/10.1021/acscatal.7b01371.

[37] Z. Zhao, R. Bababrik, W. Xue, Y. Li, N.M. Briggs, D.-T. Nguyen, U. Nguyen, S.P. Crossley, S. Wang, B. Wang, Solvent-mediated charge separation drives alternative hydrogenation path of furanics in liquid water, Nat. Catal. 2 (2019) 431–436.

[38] M.A. Mellmer, C. Sanpitakseree, B. Demir, P. Bai, K. Ma, M. Neurock, J.A. Dumesic, Solvent-enabled control of reactivity for liquid-phase reactions of biomass-derived compounds, Nat. Catal. 1 (2018) 199–207. https://doi.org/10.1038/s41929-018-0027-3.

[39] A.K. Chew, T.W. Walker, Z. Shen, B. Demir, L. Witteman, J. Euclide, G.W. Huber, J.A. Dumesic, R.C. Van Lehn, Effect of Mixed-Solvent Environments on the Selectivity of Acid-Catalyzed Dehydration Reactions, ACS Catal. 10 (2020) 1679–1691. https://doi.org/10.1021/acscatal.9b03460.

[40] D.T. Bregante, A.M. Johnson, A.Y. Patel, E.Z. Ayla, M.J. Cordon, B.C. Bukowski, J. Greeley, R. Gounder, D.W. Flaherty, Cooperative effects between hydrophilic pores and solvents: Catalytic consequences of hydrogen bonding on alkene epoxidation in zeolites, J. Am. Chem. Soc. 141 (2019) 7302–7319. https://doi.org/10.1021/jacs.8b12861.

[41] J. Wang, S. Zeng, N. Chen, D. Shang, X. Zhang, J. Li, Research progress of ammonia adsorption materials, Guocheng Gongcheng Xuebao/The Chinese J. Process Eng. 19 (2019) 14–24. https://doi.org/10.12034/j.issn.1009-606X.218171.

[42] G. Li, B. Wang, T. Kobayashi, M. Pruski, D.E. Resasco, Optimizing the surface distribution of acid sites for cooperative catalysis in condensation reactions promoted by water, Chem Catal. 1 (2021) 1065–1087. https://doi.org/10.1016/j.checat.2021.08.005.

[43] J.S. Bates, B.C. Bukowski, J. Greeley, R. Gounder, Structure and solvation of confined water and water-ethanol clusters within microporous Brønsted acids and their effects on ethanol dehydration catalysis, Chem. Sci. 11 (2020) 7102–7122. https://doi.org/10.1039/d0sc02589e.

[44] J.K. Chinthaginjala, L. Lefferts, Support effect on selectivity of nitrite reduction in water, Appl. Catal. B Environ. 101 (2010) 144–149. https://doi.org/10.1016/j.apcatb.2010.09.023.

[45] R. Brunet Espinosa, D. Rafieian, R.S. Postma, R.G.H. Lammertink, L. Lefferts, Egg-shell membrane reactors for nitrite hydrogenation: Manipulating kinetics and selectivity, Appl. Catal. B Environ. 224 (2018) 276–282.

https://doi.org/10.1016/j.apcatb.2017.10.058.

[46] Y. Matatov-Meytal, Y. Shindler, M. Sheintuch, Cloth catalysts in water denitrification: III. pH inhibition of nitrite hydrogenation over Pd/ACC, Appl. Catal. B Environ. 45 (2003) 127–134.

[47] W. Stöber, A. Fink, E. Bohn, Controlled growth of monodisperse silica spheres in the micron size range, J. Colloid Interface Sci. 26 (1968) 62–69.

[48] X. Hao, S. Barnes, J.R. Regalbuto, A fundamental study of Pt impregnation of carbon: Adsorption equilibrium and particle synthesis, J. Catal. 279 (2011) 48–65. https://doi.org/10.1016/j.jcat.2010.12.021.

[49] M.G. Seo, D.W. Lee, S.S. Han, K.Y. Lee, Direct Synthesis of Hydrogen Peroxide from Hydrogen and Oxygen over Mesoporous Silica-Shell-Coated, Palladium-Nanocrystal-Grafted SiO2 Nanobeads, ACS Catal. 7 (2017) 3039–3048. https://doi.org/10.1021/acscatal.7b00388.

[50] X. Gao, A. Heyden, O.A. Abdelrahman, J.Q. Bond, Microkinetic analysis of acetone hydrogenation over Pt/SiO2, J. Catal. 374 (2019) 183–198.

[51] H. Akaike, A new look at the statistical model identification, IEEE Trans. Automat. Contr. 19 (1974) 716–723.

[52] V. Höller, K. Rådevik, I. Yuranov, L. Kiwi-Minsker, A. Renken, Reduction of nitrite-ions in water over Pd-supported on structured fibrous materials, Appl. Catal. B Environ. 32 (2001) 143–150. https://doi.org/10.1016/S0926-3373(01)00139-4.

[53] V. Rosca, M. Duca, M.T. de Groot, M.T.M. Koper, Nitrogen cycle electrocatalysis, Chem. Rev. 109 (2009) 2209–2244.

[54] J. Bigeleisen, M. Wolfsberg, of Isotope Effects in Chemical Kinetics In Advances in Chemical Physics, 1958.

[55] K.B. Wiberg, Ionic reactions of deuterium-containing compounds, Chem. Rev. 55 (1955) 713–743.

[56] C.T. Campbell, The Degree of Rate Control: A Powerful Tool for Catalysis Research, ACS Catal. 7 (2017) 2770–2779. https://doi.org/10.1021/acscatal.7b00115.

[57] Z. Mao, C.T. Campbell, The degree of rate control of catalyst-bound intermediates in catalytic reaction mechanisms: Relationship to site coverage, J. Catal. 381 (2020) 53–62. https://doi.org/10.1016/j.jcat.2019.09.044.

[58] A. Vannice, Kinetics of Catalytic Reactions, 1st ed., Springer, New York, 2005. https://doi.org/10.1016/S0166-9834(00)80062-7.

Supporting information

1. Characterization and theoretical calculation of the catalyst

1.1 Zeta potential curves of synthesized SiO_2 particles

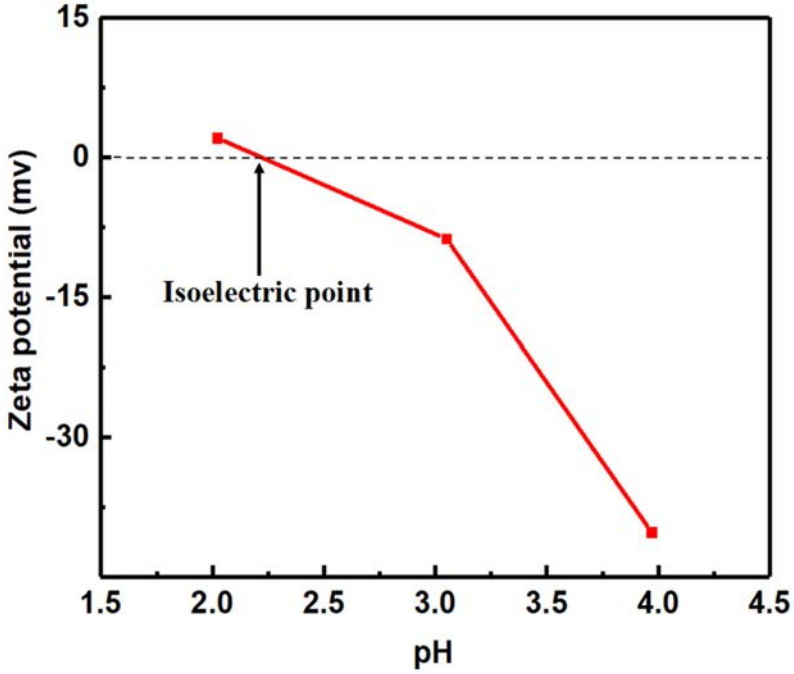

Figure S1. Zeta potential curves of synthesized SiO_2 particles.

1.2 SEM images of the synthesized SiO_2 Particles

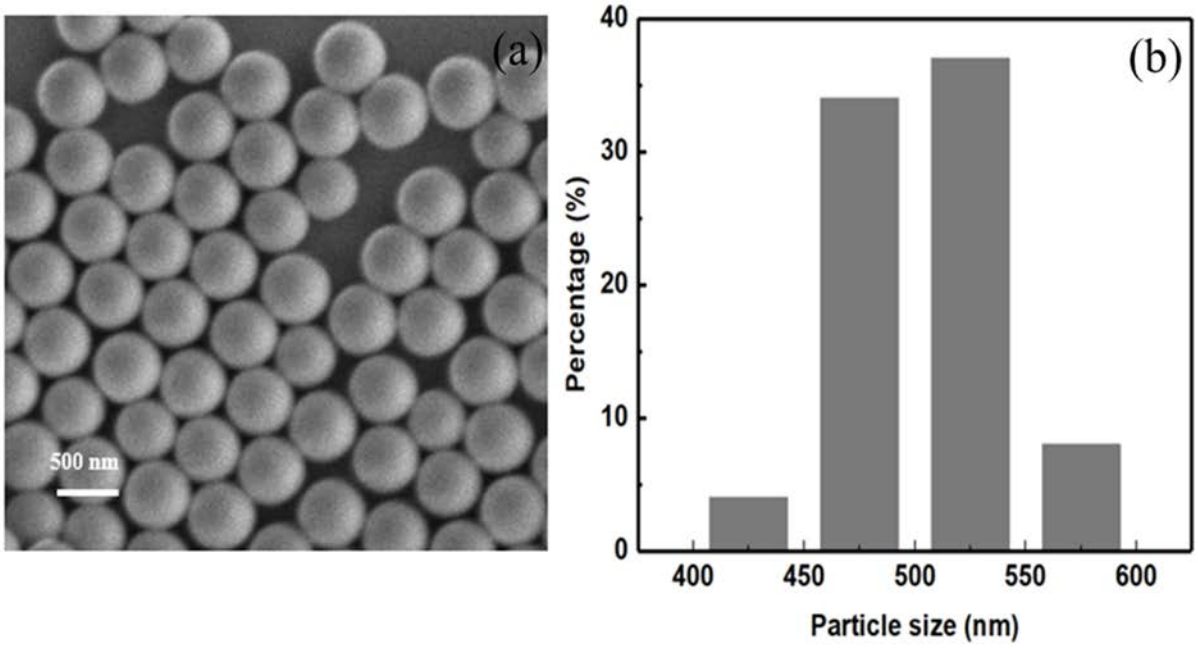

Figure S2. SEM image and particle size distribution of synthesized SiO_2 particles.

1.3 TEM-EDX images of the synthesized Pd/SiO_2 catalyst

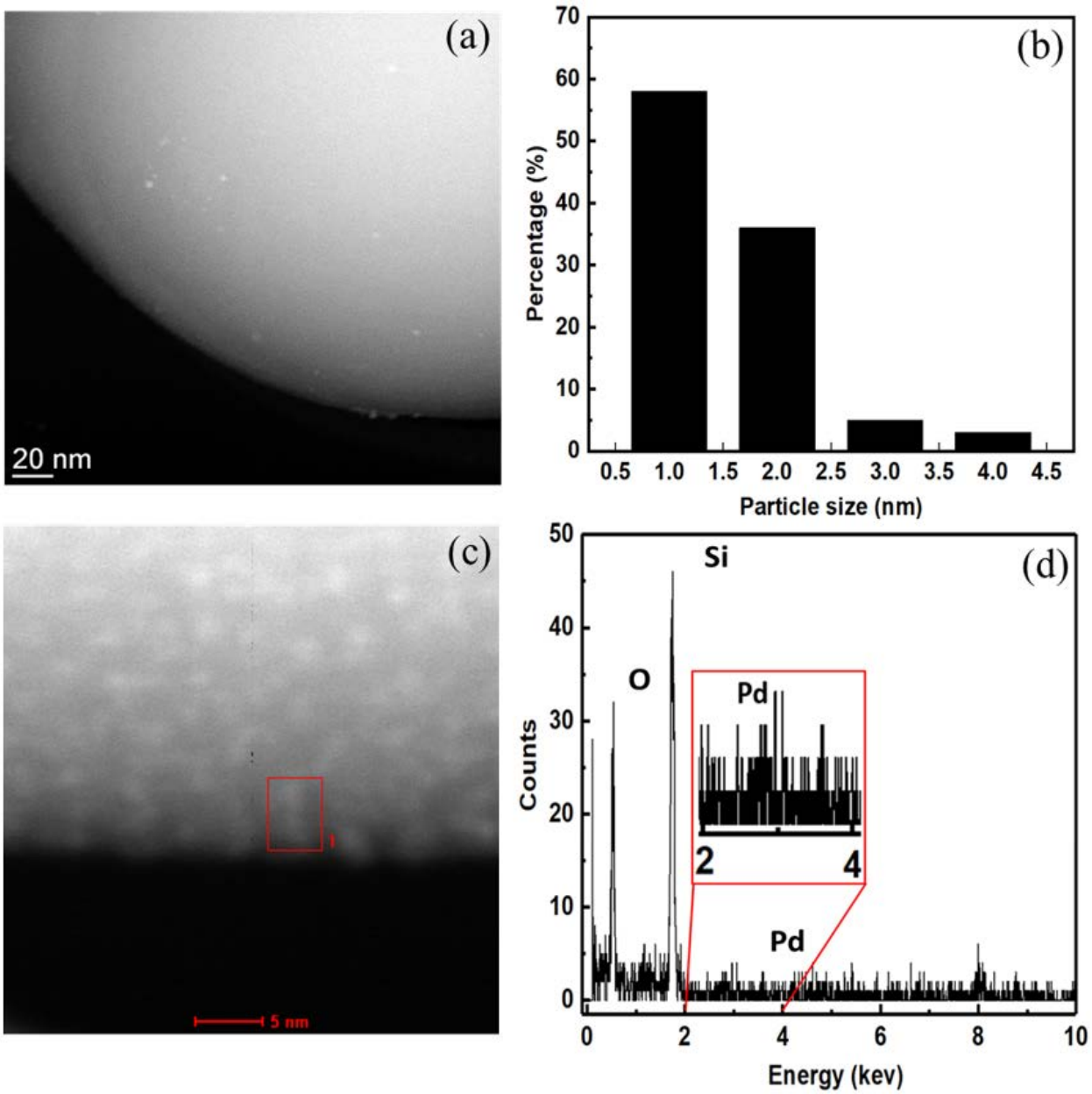

Figure S3. High resolution TEM-EDX images (a, c), metal cluster size distribution (b), and EDX characterization of Pd over the marked region (c, d) of Pd/SiO_2 catalyst.

1.4. Calculation of the theoretical surface area

1.4.1. Theoretical specific surface area of SiO_2 particles

The theoretical specific surface area of the silica particles is calculated based on the average particle size obtained from SEM. Using equation S1 and S2, where r_p is the radius of the silica

sphere (m), ρ_p is the density of a silica particle (kg/m^3), S_p is the specific surface area (m^2/g) and n is the number of silica sphere for 1 g of sample. The average diameters of the SiO_2 samples is 500 nm as shown in Figure S2, while a density of 1890 kg/m^3 is assumed.[1]

$$\frac{4}{3}\pi\ r_p{}^3 * \rho_p * n = 1 \qquad \text{(S1)}$$

$$S_p = 4\pi\, r_p{}^2 * n \qquad \text{(S2)}$$

The calculated theoretical specific surface area is 6.35 m^2/g.

1.4.2. Theoretical specific surface area of Pd/SiO_2 particles

The theoretical specific surface area of Pd/SiO_2 particles is calculated based on the average Pd particle size from TEM. Using equation S3 and S4, where r_p is the radius of the palladium particles (m), ρ_p is the density of a palladium (kg/m^3). S_p is the specific surface area (m^2/g), and n is the number of palladium particles for 1 g of sample. The average diameters Pd particles is 2.5 nm as shown in Figure S3, the Pd loading is 0.17%.

$$\frac{4}{3}\pi\ r_p{}^3 * \rho_p * n = 1 * 0.17\% \qquad \text{(S3)}$$

$$S_p = 4\pi\, r_p{}^2 * n \qquad \text{(S4)}$$

The calculated theoretical specific surface area for the palladium particle is 0.34 m^2/g. the Pd loading is only 0.17%, compared with the SiO_2 support, the contribution for the surface area is very small. So, the theoretical specific surface area for Pd/SiO_2 is 6.69 m^2/g.

2. The kinetic isotope effect on ammonium selectivity

Table S1. kinetic isotope effect on ammonium selectivity

	$NaN^{14}O_2$	$NaN^{15}O_2$	H_2/H_2O		D_2/D_2O	
Temperature (°C)	25	25	25	50	25	50
Selectivity to ammonium (%)[#]	0.79	0.80	0.86	1.56	0.88	1.49

[#]Note: Selectivity to ammonium at 10% nitrite conversion level with 0.8 bar H_2 and 1mM initial nitrite concentration.

3. Operation conditions

3.1. Nitrite and ammonium concentration profile

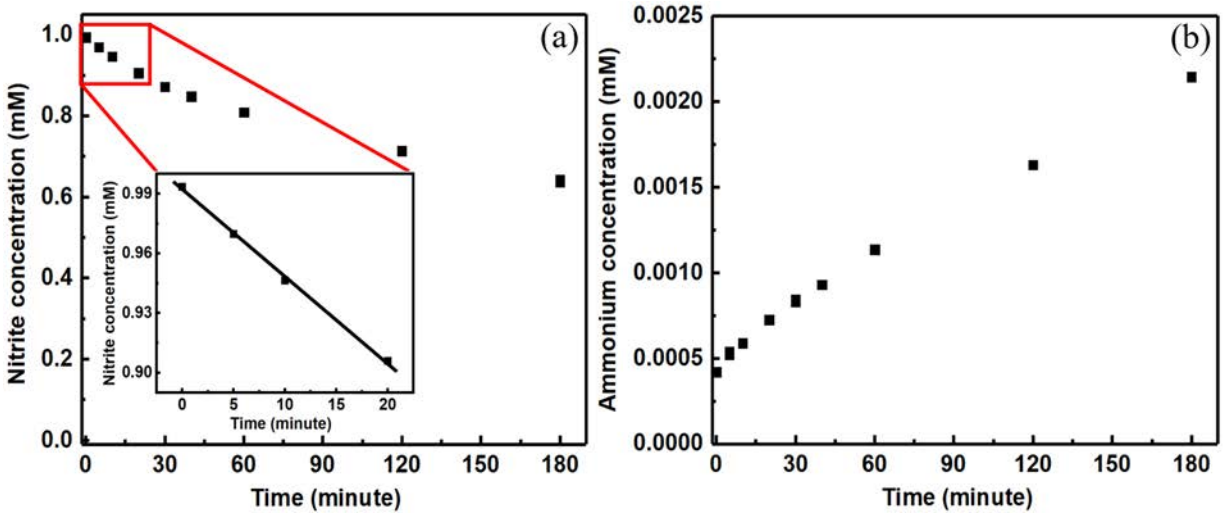

Figure S4. (a) nitrite concentration as a function of time with 1mM initial nitrite concentration and 0.8 bar hydrogen pressure, with a zoomed-in initial points that are used to obtain initial rate, (b) ammonium concentration as a function of time.

Table S2. Operating conditions of the nitrite hydrogenation in a slurry reactor

Reaction temperature, ℃	25-50
Reaction volume, L	0.3
pH of the solution	5.5
Stirring speed, rpm	500
Average catalyst particles size, nm	500
Amount of catalyst, g	0.05
Total gas flow rate, mL/min	100
Total operating pressure, bar	1
Carbon dioxide partial pressure, bar	0.1
Hydrogen partial pressure, bar	0.01–0.8
Helium partial pressure (balance), bar	0.1–0.89
Initial nitrite concentration, mM	0.5–10

4. Mass transfer

4.1. External mass transfer

4.1.1. Experimental check

Figure S5 shows the Turnover frequency of Pd/SiO_2 catalyst under different agitation speeds and temperature. As it can be noted when there is no agitation the TOF is rather small. This is indicative that at low rpms the reaction is limited by sluggish external mass transfer. When the agitation speed varies from 250 to 750 rpm, it shows a similar TOF for both temperature. Since the reaction are being conducted at 500 rpm, it can be concluded that there are no external mass transfer limitations. Meanwhile, this reaction is conducted in liquid water at diluted concentrations, external heat transfer limitations can be excluded as well.

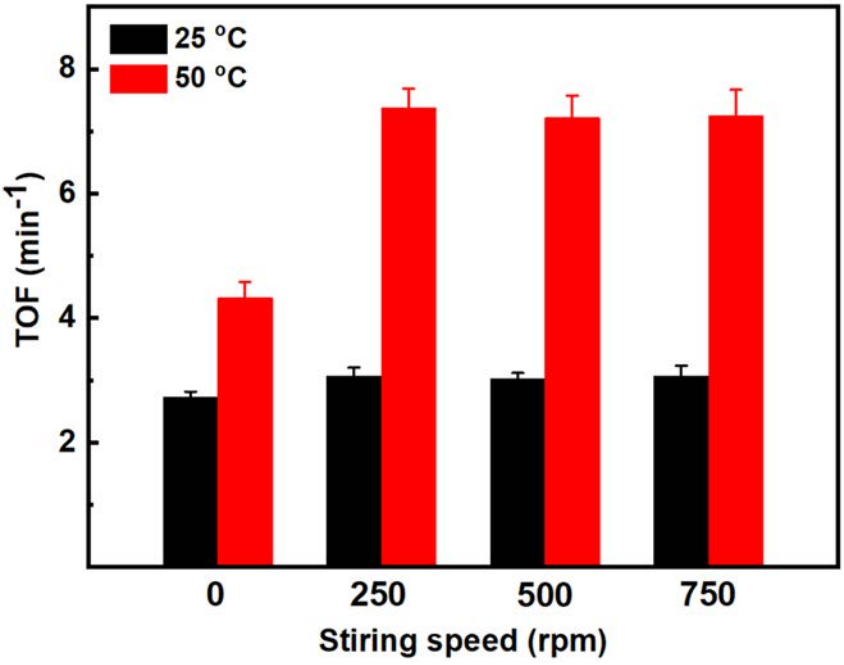

Figure S5. Turnover frequency (TOF) of the Pd/SiO_2 catalyst under different agitation speed and temperature.

4.1.2. Liquid-Solid mass transfer

The liquid-solid (L-S) mass transfer rate constant for nitrite was calculated based on the literature.[2] Slip velocity of the catalyst particles was calculated to conservatively estimate the mass transfer rate between solid and aqueous solution. Stokes' law was assumed to apply, and the particle's slip velocity was calculated by:

$$\mathcal{U}_t = \frac{g*d_p^2*(\rho_p-\rho)}{18\mu} = \frac{9.81*(5.57*10^{-7})^2*(1890-1)}{18*1.002*10^{-3}} = 3.19*10^{-7}\ \ m*s^{-1} \quad \text{(S5)}$$

Where ρ_p is average density of the catalysts (1890 kg*m^{-3}), g is the standard gravity (9.81 m*s^{-2}), ρ is water density (1 kg*m^{-3} at 20 °C, d_p is the hydrodynamic size of the catalysts 5.57*10^{-7} m) [3] and μ is absolute viscosity of water (1.002 g m^{-1} s^{-1} at 20 °C).The calculated slip velocity is 3.19 * 10^{-7} m*s^{-1}. The corresponding Reynolds number was calculated by the following expression:

$$R_e = \frac{d_p*\mathcal{U}_t}{\upsilon} = \frac{5.57*10^{-7}*3.19*10^{-7}}{1.003*10^{-6}} = 1.77*10^{-7} \quad \text{(S6)}$$

In which υ is kinematic viscosity of water (1.003 * 10^{-6} m^2*s^{-1} at 20 °C). The Reynolds number Re is $1.77*10^{-7} < 1$. This is indicative of laminar flow and Stokes law is applicable.

The Sherwood number (Sh) and Peclet number (Pe) were calculated based on the following equations:

$$Pe = \frac{d_p*\mathcal{U}_t}{D} = \frac{5.57*10^{-7}*3.19*10^{-7}}{1.9*10^{-9}} = 9.35*10^{-5} \quad \text{(S7)}$$

$$Sh = \frac{4}{Pe} * ln\left(\frac{1}{1-Pe/_2}\right) = \frac{4}{9.35*10^{-5}} * \ln\left(\frac{1}{1-\frac{1}{2}*9.35*10^{-5}}\right) = 2.0 \quad \text{(S8)}$$

In which D is the nitrite diffusion coefficient in pure water (1.9×10^{-9} m^2*s^{-1}). The obtained value of Sh is equal to the value for a particle in stagnant liquid (Sh=2), which is typical for a slurry reactor as the small particles essentially move with the liquid, with limited shear at the surface of the particles. The L-S mass transfer coefficient for nitrite is calculated according to the following expression:

$$k_{ls} = \frac{D*Sh}{d_p} = \frac{1.9*10^{-9}*2}{5.57*10^{-7}}\ m*s^{-1} = 6.82*10^{-3}\ m*s^{-1} \quad \text{(S9)}$$

The calculated k_{ls} is 6.08*10^{-3} m*s^{-1}. The geometric surface area of the catalyst per volume of solution is:

$$a_s = \frac{A_p*m}{\rho_c*V_p*V_R} \quad \text{(S10)}$$

Where m is the mass of the catalyst in the experiments (kg), A_p is the geometric surface area of one catalyst particle (m^2), V_R is the volume of reaction solution (m^{-3}) and V_p is the volume of one catalyst particle (m^3).

$$a_s = \frac{4\pi*(2.5*10^{-7}\ m)^2*5*10^{-5}\ kg}{1890\ kg*m^{-3}*\frac{4\pi}{3}*(2.5*10^{-7}\ m)^3*3*10^{-4}\ m^3} = 1058.2\ m^{-1} \quad \text{(S11)}$$

The mass transfer rate constant was calculated by multiplying the mass transfer coefficient by the geometric surface area of the catalyst per volume of solution:

$$k_{ls} * a_s = 6.82 * 10^{-3} * 1058.2\ = 7.22\ s^{-1} = 433.02\ \text{min}^{-1} \quad \text{(S12)}$$

The mass transfer is first order. So the maximum mass transfer rate at concentration C_s in the bulk of the liquid can be calculated by the following equation:

$$Max\ mass\ transfer\ rate = k_{ls} * a_s * C_s \quad \text{(S13)}$$

When using the experiment nitrite concentration (1 mM), the mass transfer rate is 433.02 mM*min^{-1}, which is significantly larger than even the highest reaction rate (0.00478 mM*min^{-1}) at the same nitrite concentration. Therefore, L-S mass transfer is not limiting.

4.1.3. External mass transfer, combined G-L and L-S.

Mears criterion is used to estimate any limitation at the G-L and/or L-S interface,[4,5] the result are shown in Table S3. External mass transfer limitations can be neglected if the Mears' criterion listed below is satisfied:

$$\frac{-r_{obs}\rho_b d_p n}{K_c C_s} < 0.15 \quad \text{(S14)}$$

Where $\boldsymbol{\rho_b}$ is bulk density of the catalyst (kg*m^{-3}), $-r_{obs}$ is the observed rate per unit mass of catalyst (mol*kg^{-1}*s^{-1}), d_p is the catalyst particle radius (m), n is the reaction order, K_c is the mass transfer coefficient (m/s) and C_s is bulk concentration (mol*m^{-3}).

According to the previous calculation in section 4.1.2, the Re number ($1.77 * 10^{-7}$) is much smaller than 1, which indicates the mass transfer coefficient can be estimated based on following equation.[5]

$$Sh = \frac{K_c*2*d_p}{D_{AB}} = 2 \quad \text{(S15)}$$

Where d_p is the catalyst particle radius (m), Sh is the Sherwood number and D_{AB} is the H_2 gas phase diffusivity (m^2*s^{-1}). The calculated diffusivity D_{AB} for H_2 is 6.3*10^{-5} m^2*s^{-1}.[4]

$$K_c = \frac{D_{AB}}{d_p} = \frac{6.3*10^{-5}\ m^2*s^{-1}}{2.5*10^{-7}\ m} = 252\ m*s^{-1} \quad \text{(S16)}$$

Table S3. value of the different parameters and the results of Mears criteria

$-r_{obs}(H_2)$	$mol*s^{-1}*kg^{-1}$	$4.78*10^{-4}$
ρ_b	$kg*m^{-3}$	1890
n	N/A	0.4
d_p	m	$2.5*10^{-7}$
C_s (H_2)	$mol*m^{-3}$	0.624
K_c (H_2)	$m*s^{-1}$	252
Mears criteria (H_2)	N/A	$5.75*10^{-10}$

Based on the above calculation, the gas-liquid and liquid-solid mass transfer limitation can be ignored.

5. DFT Calculations

5.1. Nitrite reduction mechanism on clean Pd surface

As previously mentioned, many reaction mechanisms have been proposed for nitrite reduction in aqueous solutions using Pd-based catalysts.[6–12] These reaction mechanisms commonly start with nitrite adsorption and dissociative adsorption of hydrogen to form H*, followed by hydrogenation of nitrite to form adsorbed NO*, which has been claimed as a crucial intermediate.[7,13,14] The N−O bond could dissociate directly to form N* and O*[7,15–17] or assisted by hydrogen via hydrolysis of HNO*, NOH* and HNOH* species. The NO* direct dissociation is hindered by its high activation barrier on Pd(111).[18] Instead, NO* hydrogenation is favored. The N-O dissociation barrier in HNO*, NOH*, and HNOH* were calculated to be higher than those of the sequential hydrogenation steps.[19] Therefore, in the following DFT calculations, we follow the hydrogenation of NO* to form NHOH, hydrolysis of which produces NH*, another surface dominant specie. The N-N bond could form between NH* and another surface species to form N_2. Instead, NH* can also proceed with two more hydrogenation steps to form NH_3. The free energy profile is plotted in Figure S6.

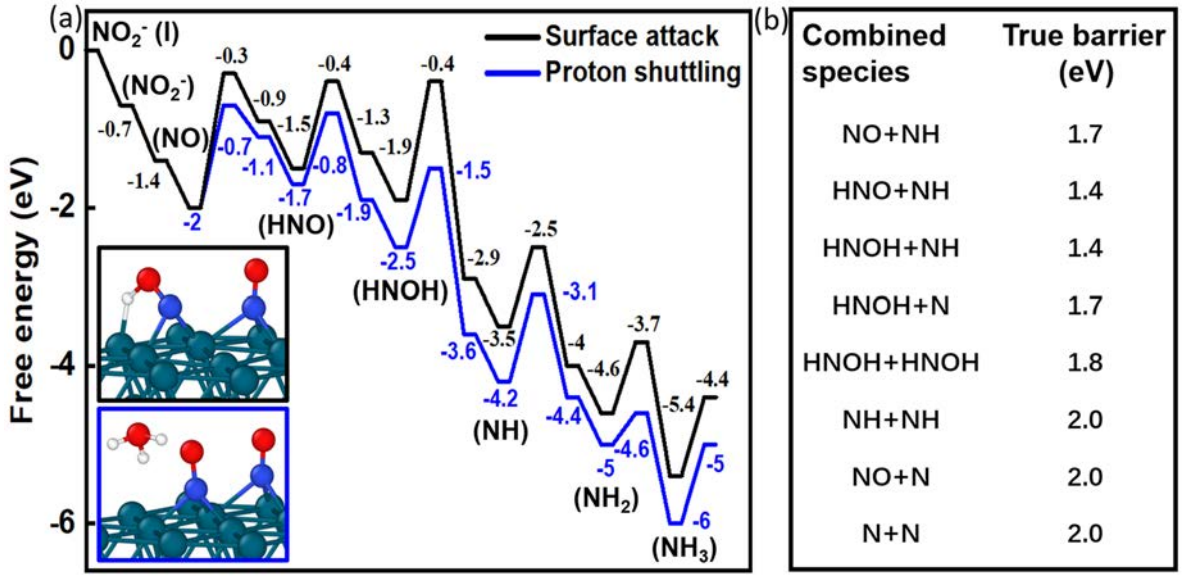

Combined species	True barrier (eV)
NO+NH	1.7
HNO+NH	1.4
HNOH+NH	1.4
HNOH+N	1.7
HNOH+HNOH	1.8
NH+NH	2.0
NO+N	2.0
N+N	2.0

Figure S6. (a) Free energy diagram of NO_2^- reduction on a Pd(111) surface. Black line: hydrogen directly attacks surface species. Blue line: proton shuttle through H_2O to the surface species illustrated in solvent effect and Figure S9. The atomic structures of transition state for the first hydrogenation reaction with and without proton shuttling are shown as insets. (b)The true barriers for possible N-N coupling species. The H adsorption is shown in each step that requires H-insertion with a free energy of c.a. 0.6 eV.

The adsorption energy of NO_2^- from liquid phase onto the Pd surface is – 0.7 eV, and its conversion to form NO* is exothermic by 0.6 eV. It suggests the NO_2^- favors the adsorption on Pd surface and converts to NO easily, agreeing with a previous report.[11] NO* adsorbs strongly on Pd with an adsorption energy of -2.8 eV, much stronger than hydrogen adsorption (-0.6 eV). This energy difference between NO* and H* suggests NO* likely covers the Pd surface and competes for sites, in line with the experimentally measured negative reaction order in nitrite at low hydrogen pressures. The first hydrogenation can happen at either the N or O in NO*. Our results shows the formation of NOH* is slightly favorable than HNO* (see comparison in Figure S6). However, the kinetic barrier of HNO* toward HNOH* is feasible by difference of 0.7 eV comparing to the barrier of NOH*. Thus, Figure S6 shows the most favorable pathway following the sequence of NO*, HNO*, HNOH*, NH* and NH_2^*. Among all the elementary steps, the transition states (TS) of the first, second, and third steps to form HNO, HNOH and NH have a similar energy with the highest values. The RDS should thus be within the first three steps. Given the polar nature of the surface species the transition state

energy of these steps will be very sensitive to the presence of water molecules via so-called "*solvation effects*".

5.2. Solvent effects on the hydrogenation and hydrogenolysis

We consider the solvent effect in two approaches: an implicit model, which includes the effect of electrostatics, cavitation, and dispersion on the interaction between a solute and reactant. Another one is the explicit model, where the actual H_2O molecules are included in the calculations. Figure S9 shows the free energy profile of NO* hydrogenation towards HNOH* using either the implicit model or the explicit model. Here, one could notice that a similar change in the free energy of the TS and chemisorbed species has been observed for the steps of NO and HNO hydrogenation in two solvent models. In the following section, we focus on the explicit solvent model to include the proton shuttling mechanism where explicit water needs to be present to participate in the reaction. Strikingly, the results indicate that the proton shuttling has a pronounced effect in promoting the first three hydrogenation/hydrogenolysis steps, i.e. lowering their intrinsic activation barriers by 0.4, 0.2, and 0.5 eV, respectively, in comparison to the explicit solvent model (Figure S6). Such an enhancement is because H_2O shortens the hydrogenation path, reducing the energy of the TS by stabilizing the positive charge at H_3O^+ (Figure S10). As a result, this shuttling mechanism lowers the apparent barriers. This flattening of the energy landscape leads to similar barriers for the first two hydrogenation steps.

The proton shuttling path was investigated with extra water molecules to test the convergence of the explicit model (Figure S7). The results with more than one H_2O molecule shows a comparable stabilization of the TS, very similar to the model with one water molecule, suggesting that the key chemistry required in this model has been captured with just one water in the proximity (Figure S11). The true barriers for each hydrogenation, listed in Figure S7, shows the most pronounced water promotion on the NOH* formation. When the O atom in NO* is targeted for hydrogenation, the true barrier of shuttling is reduced by 1.0 eV, almost independent on the number of water molecules. NO* adsorbs on Pd with N, leaving the O interfacing with the solvent. The H_2O molecules open a favorable shuttling path for the surface hydrogen to attack O as observed in other hydrogenation of oxygenates.[20] Yet, such a promotion effect is strictly limited for hydrogenation of O in HNO*, because in the tilted configuration of HNO*, the hydrogenation path from the surface is already shortened and facilitated. Different from the O hydrogenation, hydrogenation of N in NO* is promoted

moderately by 0.5 eV, because of the extra energy cost for water to approach the surface and hydrogenate the N that is strongly bonded with Pd. A similar effect is shown for hydrogenating N in NOH*; the water enhancement for hydrogenating N in NOH* is minor. While these results might indicate that H-insertion on the O of NO* should be the most preferable pathway in the explicit water model (red curve in Figure S7a i-iv), the barriers obtained for this mechanism are significantly larger than those obtained in the H-NO* pathway. Furthermore, the hydrogen addition to the O of NO* would result in reaction orders for hydrogen that vary between 1 and 1.5. That is, 1.5 hydrogen insertions have occurred on the system before the RDS. Such mechanism, however, would not explain the low reaction orders in hydrogen herein observed (Figure 1c). Instead, it is more likely that hydrogen is inserted at the nitrogen atom of NO* leading to similar apparent barriers in the two subsequent hydrogenation steps, resulting in two co-limiting rate limiting steps with reaction orders varying from 0 to 1.5 (blue curve in Figure S7a i-iv).

It is worth noting that the reactions mediated by different number of water molecules at the interface may require disruption of hydrogen bonds and displacing water molecules from the bulk to the interface, which can add an additional free energy change. We thus quantitively estimate the free energy change of water reconstruction (e.g. move a cluster of water (1-3 molecules) from the bulk to the interface) at room temperature (section 5.4.4 in SI). The enthalpy and entropy change result from breaking hydrogen bonds between the water clusters and the water bulk during the reconstruction. Previous studies showed that such disruption of hydrogen bonds could lead to a noticeable free energy cost (~1 kJ mol^{-1} per hydrogen bond), which includes the enthalpy loss and entropy gain by breaking one hydrogen bond.[21][22][23] Such a free energy cost associated with large water clusters at the interface was also discussed in olefin epoxidation, though the exact entropy change is different as in the latter case water is partitioned from organic nitrile rather than bulk water.[24] Formation of large water clusters at the interface, which requires breaking multiple hydrogen bonds, is thus less likely than the model with one interfacial water molecule.

Overall, presence of water molecules does not change the reaction mechanism as the hydrogenation of NO* still follows the HNO path. However, there is a subtle but noticeable change of the relative difference between TS1 and TS2. That is, the second hydrogenation has either a larger (by 0.2 eV) or comparable apparent barrier, as compared to the first hydrogenation. This finding is in good agreement with our further kinetic fitting analysis.

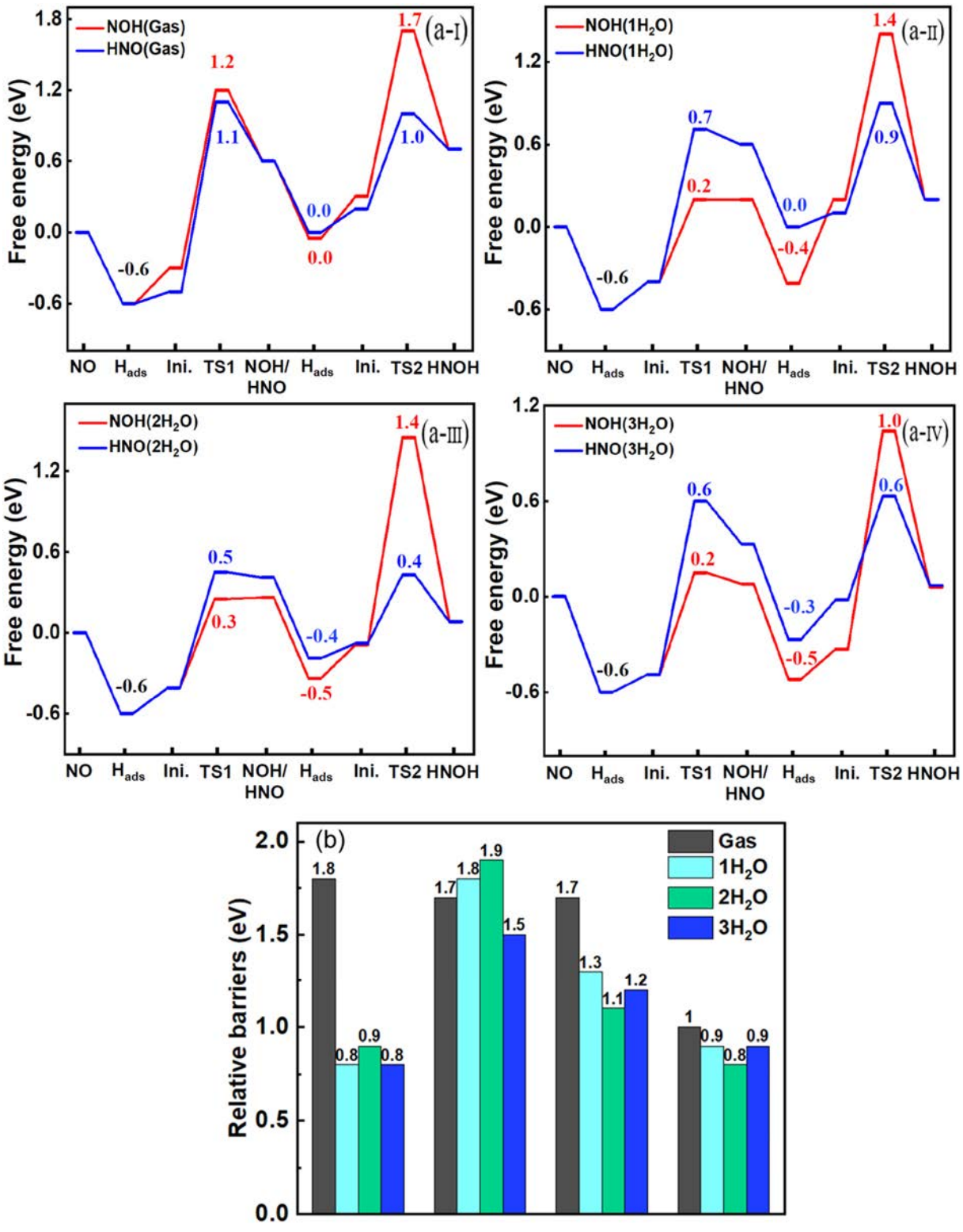

Figure S7. Free energy diagram for NO reduction on the Pd(111) surface with different molecules (a-I) Gas; (a-II) 1 H_2O; (a-III) $2H_2O$; (a-IV) $3H_2O$.(b) The relative barriers for each hydrogenation step via NOH to HNOH or via HNO to HNOH.

Finally, we want to briefly discuss the selectivity to N_2 and NH_3 based on the DFT calculations. Figure S6 suggests that the N-N coupling barriers between different surface species (N*, NO*, NH*. HNO*, HNOH*) are all higher than the corresponding hydrogenation barriers, indicating NH_3 formation to be more favorable. However, it should be notice that NO* and its reaction intermediates bind stronger with Pd than hydrogen does. The prominence of the N_2 product observed in experiments could be due to the high coverage of NO* and its intermediates on the Pd surface, which leads to a competitive coupling reaction toward N_2 over the hydrogenation. This explains the high selectivity of the catalyst towards nitrogen (> 98 %) for the different reaction conditions employed. This interpretation is in good agreement with the observation that at the end of a batch experiment, the Pd surface is almost completely covered with remarkably stable N atoms.[8]

5.3 Computational Methodology

The calculations were carried out using periodic plane-wave DFT implemented in VASP.[25–27] The Perdew-Burke-Ernzerhof (PBE) functional within the generalized gradient approximation (GGA)[28] was used for the exchange-correlation energy. Electron-ion interactions was described by the projector augmented wave (PAW) approach, and van der Waals (vdW) interaction[29] as included using the DFT-D3 method.[30] All electronic energies in calculations were converged within 10^{-5} eV, and the force on each atom was converged to below 0.02 eV $Å^{-1}$. The simulated Pd bulk has lattice constant of 3.89 Å which on agreement with measured crystallographic properties of Pd. The Pd (111) facet was optimized and used to build a close-packed 3x3 Pd(111) surface with thickness of 4 layers and a vacuum layer of 15 Å along z direction as the previous research.[31] The reactant adsorbed on Pd surface has 1 nanometer distance which is long enough to avoid the interaction from periodic surface. The 3×3×1 Monkhorst-pack k-point mesh was used to sample the first Brillouin zone during structural optimization. In calculations, two NO adsorbates were positioned on the Pd surface, equaling to 2/9 surface coverage. Two different solvation models were compared. The implicit solvation effect was computed by VASPsol.[32] The explicit model was investigated by incorporating different numbers of water molecule near the NO molecules and the most stable local configuration was used for activation barrier calculations. Total energies of several initial geometries of explicit water were compared (Figure S 10-g), and the most stable one was adopted for calculations of activation barriers and transition states. The transition state searches were performed using the dimer method[33] with the initial guesses obtained through the

nudged elastic band (NEB) method.[33,34] The transition states were further confirmed by calculating the vibrational frequencies. The adsorption energy E_{ads} was calculated by equation S17.

$$E_{ads} = (E_{slab-ads} - E_{slab} - nE_{ads-gas}) / n \quad \text{(S17)}$$

Where $E_{slab-ads}$, E_{slab}, and $E_{ads-gas}$ are the total energy of adsorbate/slab system, clean metal slab, and the isolated adsorbate in gas phase, respectively, and n is the number of adsorbates in the calculations. The adsorption free energy of liquid-phase NO_2^- on Pd surface is obtained by thermodynamic cycle discussed in SI section 5.4.1. For hydrogen adsorption calculations, the residual H entropy upon adsorption was assumed to be the value reported for adsorption of H over Pd black.[35] The discussion on H entropy is covered and shown in Figure S8 and section 5.4.2 in SI. Also in SI, section 5.4.4 and 5.4.5 validate the micro-solvation model (1,2,3 water molecules) and investigate the entropy and enthalpy contribution on activation free energies as well as loss of water entropy in proposed mechanism.

5.4. Computational details

The DFT structural information was were visualized by Software OVITO.[36]

5.4.1. The NO_2^- adsorption energy

Here we will discuss the calculation on NO_2^- adsorption energy on Pd surface using thermodynamic cycle. The total energy is referred to gaseous NO_2^- based on the following steps.

$$HNO_2(g) \rightarrow HNO_2(l) \quad \text{(S18)}$$

$$HNO_2(l) \rightarrow NO_2^- + H^+ \quad \text{(S19)}$$

$$NO_2^- + * \rightarrow NO_2* + e^- \quad \text{(S20)}$$

The adsorption of gaseous HNO_2 is described as

$$HNO_2(g) + * \rightarrow NO_2* + H^+ + e^- \quad \text{(S21)}$$

Hence, the adsorption energy of aqueous NO_2^- is obtained by adding the gaseous HNO_2 adsorption with the thermodynamic correction:

$$\Delta G_{NO_2^-*} = G_{NO_2*} + 0.5G_{H_2(g)} - G_* - G_{HNO_2(g)} + \Delta G_{correction} \quad \text{(S22)}$$

$\Delta G_{correction}$ denotes the free energy change of HNO_2 liquefaction (S17) and protonation (S18).

$$\Delta G_{correction} = \Delta G_{S17} + \Delta G_{S18} \quad \text{(S23)}$$

Where $G_{NO_2*}, G_*, G_{HNO_2(g)}$ *and* $G_{H_2(g)}$ are the calculated Gibbs free energy of NO_2^- adsorption on Pd, clean Pd substrate, HNO_2 and H_2 in vacuum, respectively. $\Delta G_{correction}$ denotes the correction term consisting of liquefaction energy in equation S18 and deprotonation energy in equation S19, both of which were obtained from the NIST Chemistry Webbook.[37]

$$HNO_2(g) + 3H_2(g) \rightarrow NH_3(g) + 2H_2O(g) \quad \text{(S24)}$$

The calculated reaction energy for S24 (ΔE_{S23}) is -5.4 eV.

$$NO_2^-(l) + H^+(l) + 3H_2(g) \rightarrow NH_3(g) + 2H_2O(g) \quad \text{(S25)}$$

ΔE_{S18} is the deprotonation of HNO_2 and is pH-dependent. We computed the ΔE_{S18} using pH of 5.5 (Experimental measurement) and the associated ionization constant pKa.[38] By summing up $\Delta E_{S23}, \Delta E_{S17}$ *and* ΔE_{S18}, we also estimated the reaction energy in the liquid phase ΔE_{S24} which is

$$\Delta E_{S24} = \Delta G_{S23} - \Delta G_{S17} + \Delta G_{S18} = -5.95\ eV \quad \text{(S26)}$$

The theory predicted nitrite reduction in liquid phase release heats equals to 574 kJ mol^{-1}.

5.4.2. The effect of H adsorption energy on NO_2^- reduction free energy diagram (Clean surface result)

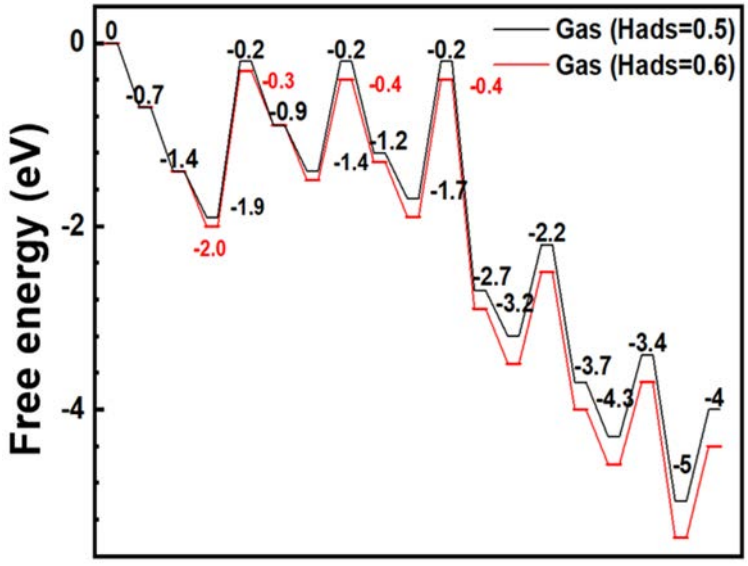

Figure S8. Free energy diagram of NO_2^- reduction. The number is displayed on black line assuming adsorption energy of -0.5 eV. The value is labelled on first three transition states along the red line when adsorption energy is -0.6 eV.

It should be noticed that the adsorption step could determine the relative value of transition state energies of the following steps. We compare adsorption energy in the same reaction diagram obtained from some assumptions. For instance. Campbell and Sellers[39] quantified the adsorption entropies of alkane on Pt(111). They suggested that the adsorption entropy loss resulted from frozen motion in the z direction, which could nearly equal to 1/3 of the original gas entropy. When H entropy loss upon adsorption was assumed in the similar case, -0.6 eV H adsorption energy were obtained. However, under reaction conditions, the surface could be covered by other species such as NO and reaction intermediates, and adsorbed H may be unable to diffuse on Pd surface. In other words, all the translational entropy of H would be lost upon adsorption. In this way, adsorption energy was determined to be -0.5 eV. A small difference is noticed in the reaction diagram due to this less exothermic adsorption. Both results are in reasonable agreement with -90 kJ mol^{-1} K^{-1} entropy loss based on experimental measurement.[35] The entropy of H lost on adsorption is thus well correlated with the surface coverage.

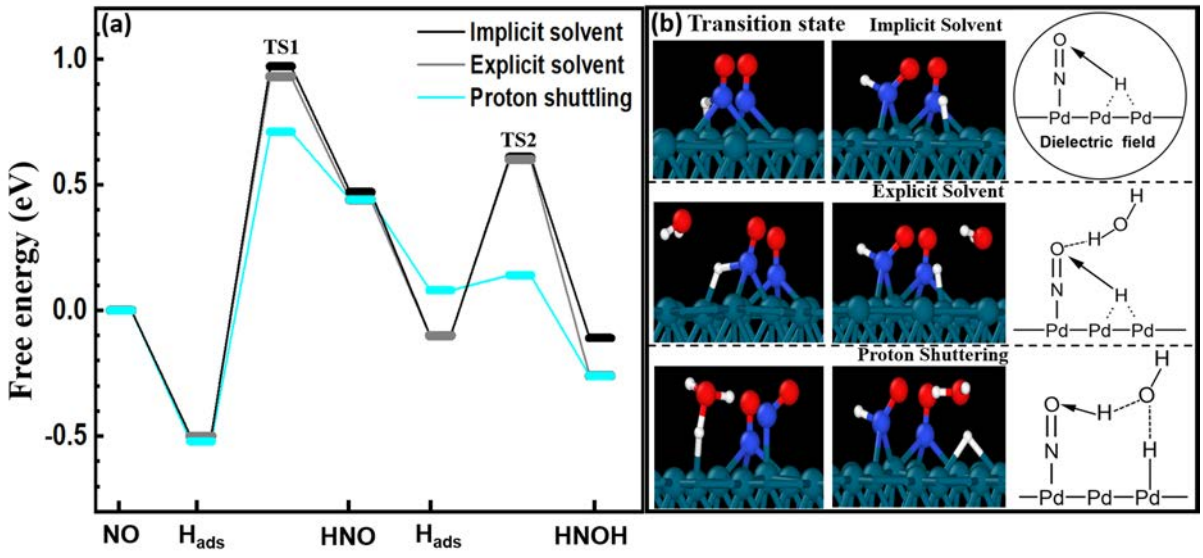

Figure S9. (a) The energy diagram comparing NO reduction toward HNO path under different solvent treatment while only 1 H_2O is considered explicitly with and without the proton shuttling scenario. (b) Transition state (TS1 and TS2) structures.

Stabilization of added water molecules (explicit solvent model) alters the energy diagram significantly. Compared with the implicit solvent, the reaction energy landscape becomes slightly less endothermic. Both the explicit and implicit models show similar barriers to the model of clean surface without solvents. Yet, when H_2O in an explicit solvent is involved in

the reaction via proton shuttling, the activation barriers are greatly reduced. This indicates that proton shuttering opens a new reaction path that makes the hydrogenation of NO to HNO and the following step to HNOH more favorable. The proton shuttling mechanism not only decreases the activation barrier on both steps, but also provides further stabilization for the HNOH species due to the formation of hydrogen bonds.

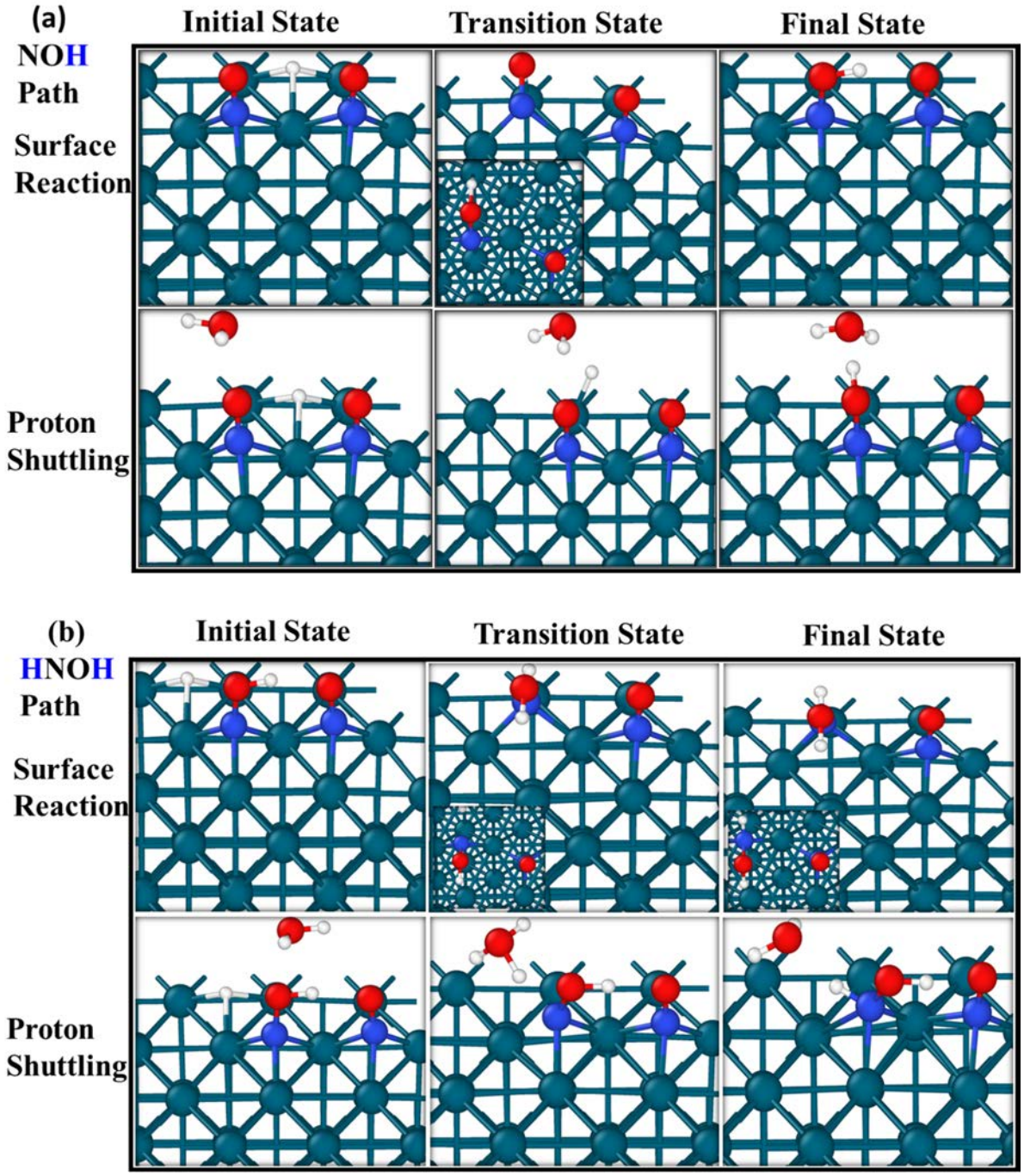

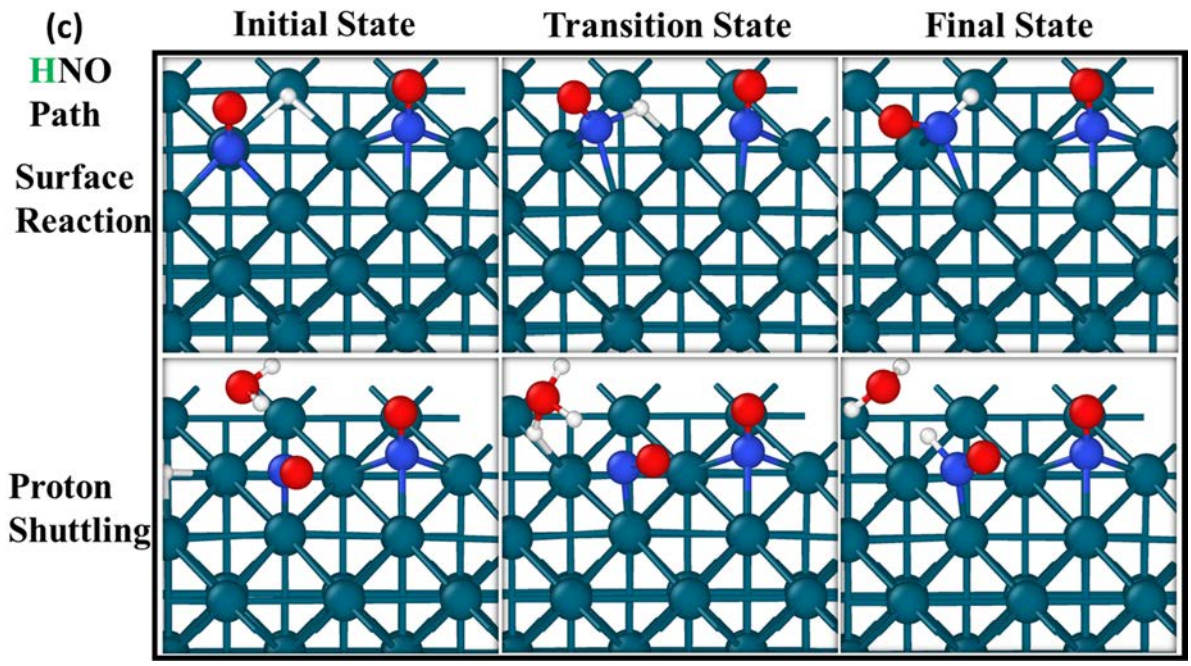
(c)
HNO
Path
Initial State
Transition State
Final State
Surface
Reaction
Proton
Shuttling

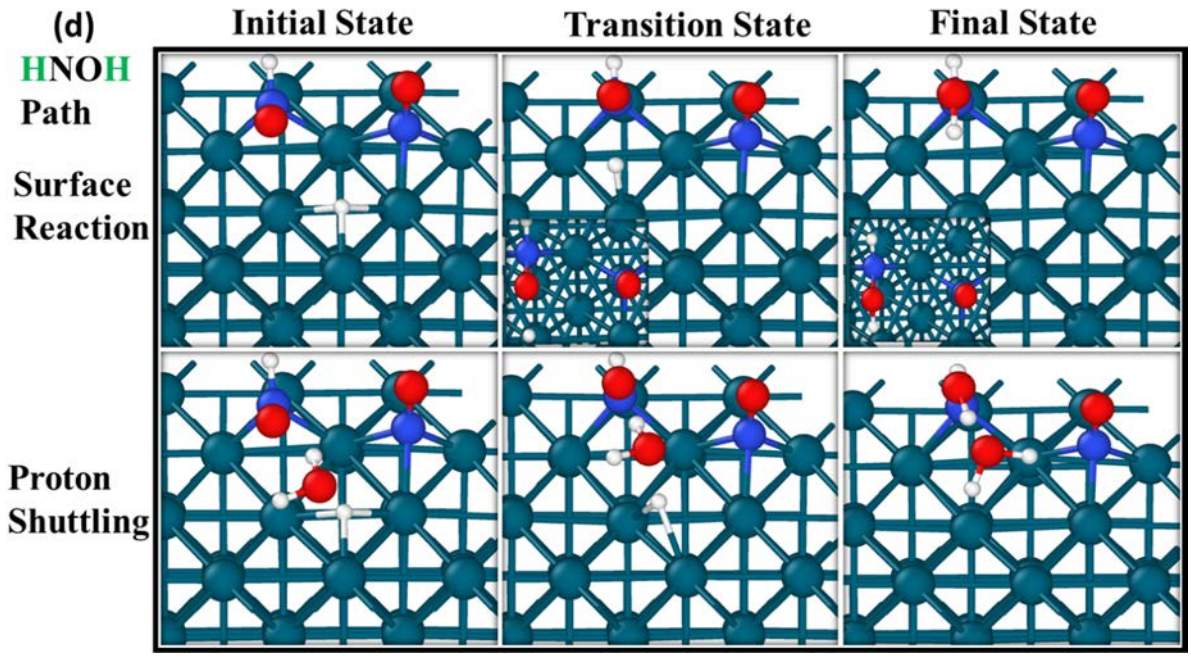
(d)
HNOH
Path
Initial State
Transition State
Final State
Surface
Reaction
Proton
Shuttling

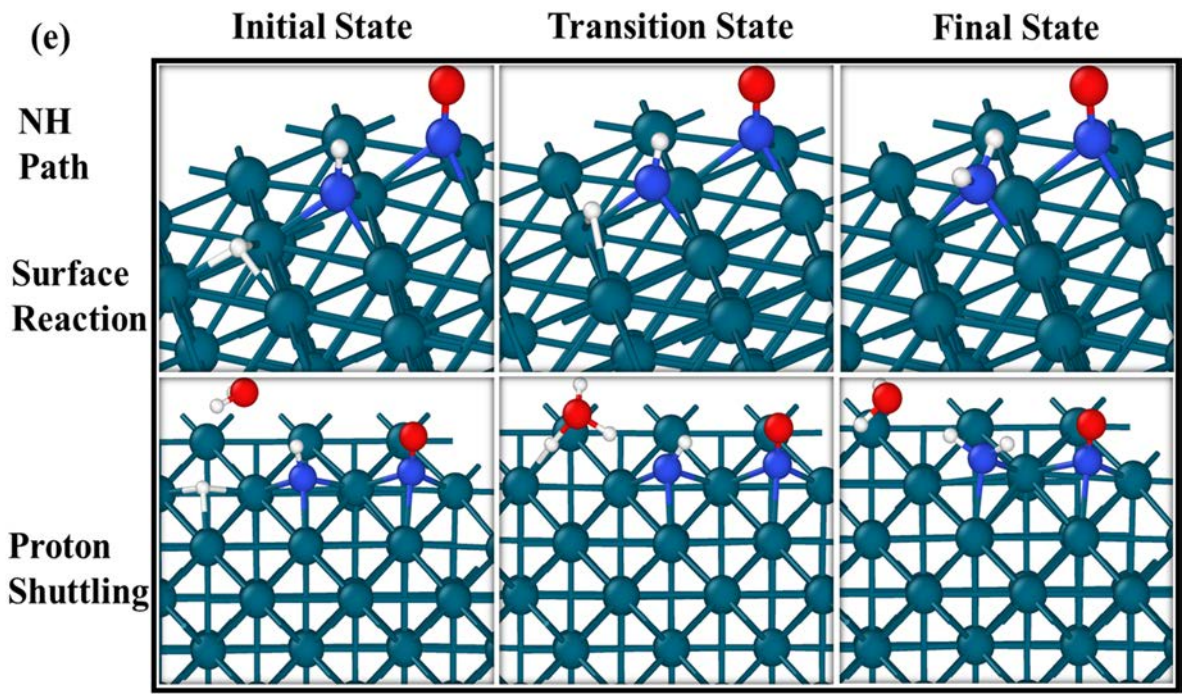
(e)
Initial State
Transition State
Final State
NH Path
Surface Reaction
Proton Shuttling

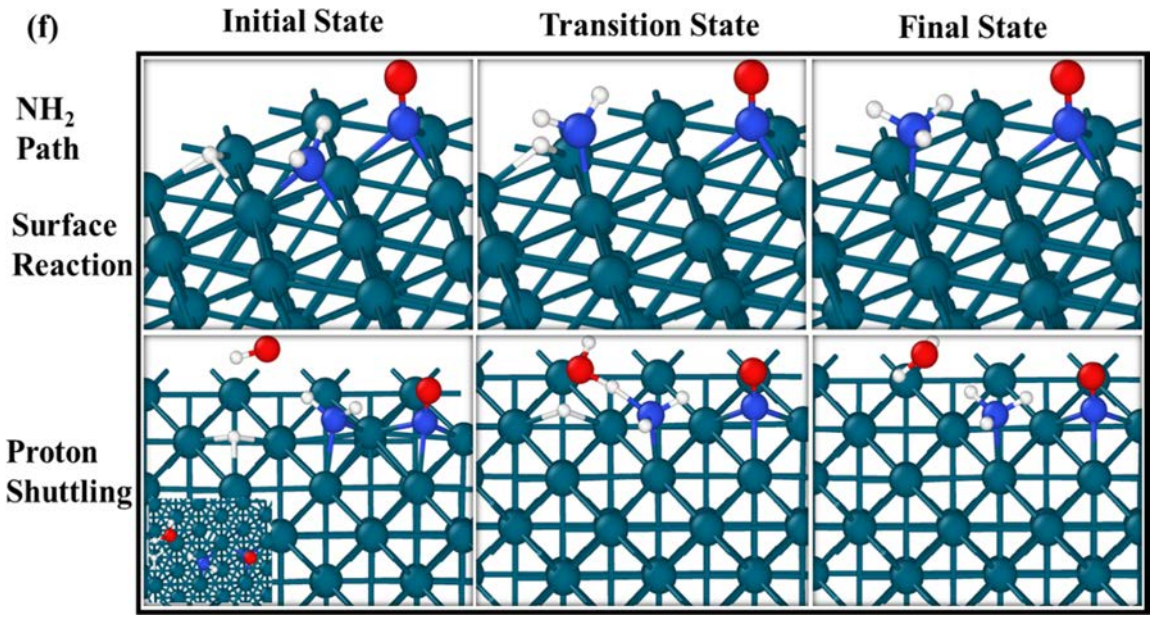
(f)
Initial State
Transition State
Final State
NH2 Path
Surface Reaction
Proton Shuttling

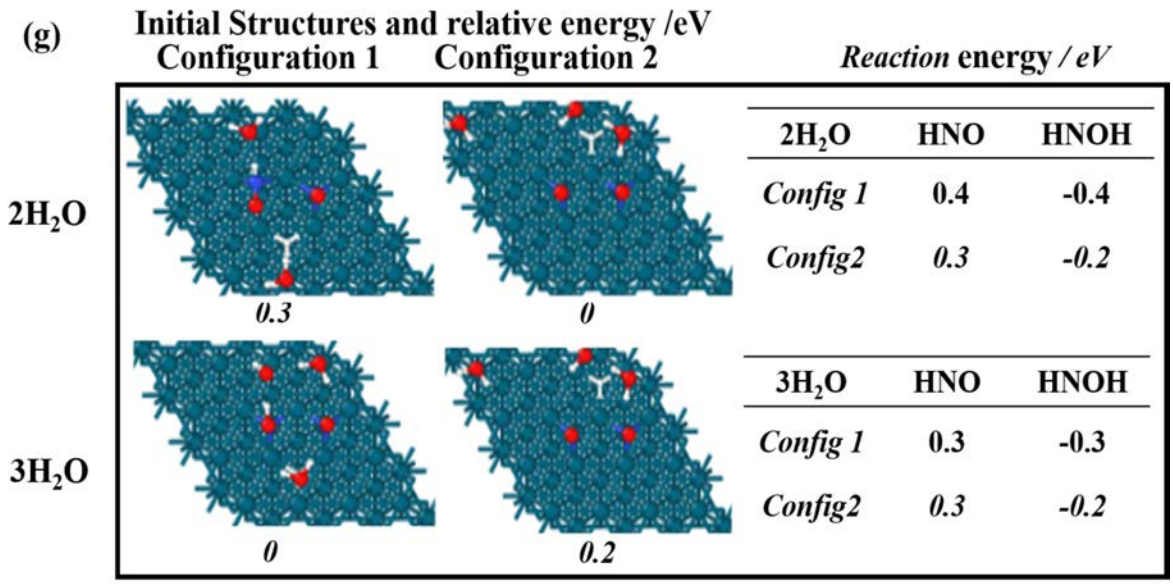

Figure S10. The calculated configurations of NO hydrogenation with proton shuttling (1H_2O included). The shuttling mechanism reveals the promotion of H_2O to the shorten the reaction path from the Pd surface to the reactant. The promotion is pronounced for O hydrogenation since water shortens the reaction path as a depository for proton transferring. Instead, the reaction path on N is intrinsically feasible due to the direct metal-NO bonding at the interface, the promotion effect of water is unrecognizable. The hydrogenation of O in HNO* is relatively easy as HNO* is tilted on the Pd surface, reducing the distance of O from the surface. Similarly, the hydrogenation path is short for NOH* and NH* since N is bound with Pd. Thus, H_2O promotion is not seen on those reactions. H_2O promotes the NH_2 hydrogenation. NH_2 transfers to the Pd top site and a proton shuttling from H_2O to pair with the unpaired electron at the N atom; in this way, water shortens the reaction path.

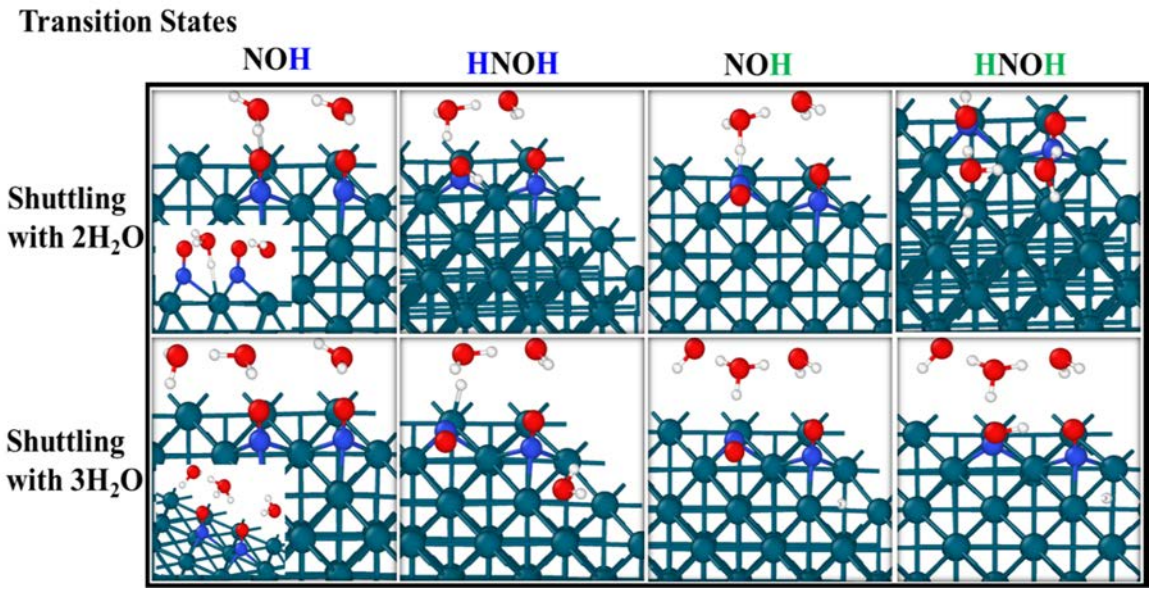

Figure S11. NO hydrogenation with shuttling mechanism (2, 3 H_2O model). Transition states for NO hydrogenation are displayed. The number of water molecules does not alter significantly the transition states or bring extra stabilization.

5.4.3 Hydrogenation sequence of NO

Depending on hydrogenation sequence, the formation of HNOH could be via two paths: NOH* path where hydrogen is added to the O atom followed by N hydrogenation, or HNO* path where N gets hydrogenated first. It is difficult to determine the hydrogenation sequence on clean Pd surface as comparable barriers are found. As shown in Figure S7, formation of NOH* and HNO* have similar activation energy (1.2 vs 1.1 eV). The HNO* path is favorable because of its feasible second hydrogenation over the clean Pd surface. This is because hydrogenation of N of HNO* has weakened interaction with surface Pd, while N in NOH* has strong binding to the surface. Also, when N is hydrogenated first, the tilted configuration facilitates surface hydrogen attack to the oxygen. Hence, the HNO path is slightly more favorable over NOH on the clean Pd surface.

By including the solvent implicitly and explicitly with the proton shuttling mechanism an energy drop is observed in the NO reduction diagram, particularly for the hydrogenation of NO at the oxygen; a clear drop in activation energy is observed (Figure S9). Our results show that NOH* path is energetically more challenging than HNO* due to the high activation energy of ~ 1.0 eV for the second hydrogenation step (Figure S7). The proton shuttling mechanism

suggests that the HNO path is more favorable since it has the lowest apparent barriers in general when compared to the NOH* path.

5.4.4 The loss of H_2O entropy in water-assisted transition states

The change in enthalpy and entropy associated with disrupting a single hydrogen bond (HB) in bulk H_2O was estimated by the Van't Hoff analysis and statistical mechanics in literature[21]. The disruption of the HBs for an average H_2O molecule to form free H_2O leads to a ΔH_{HB} of 10 kJ mol_{H2O}^{-1} and ΔS_{HB} of 22 J $mol_{H2O}^{-1}K^{-1}$ in agreement with other literature values [22][23]. Also, the change in enthalpy associated with disrupting a single hydrogen bond could be obtained by dividing ΔH_{HB} by the average number of hydrogen bonding $<N_{HB}>$. Measured in ab initio MD simulations, H_2O molecule in the bulk fluid phase possess the HBs value of 3.3.

Removing H_2O molecules from bulk phase to the Pd surface leads to disruption of HB and decrease of $<N_{HB}>$. By counting the $<N_{HB}>$ of adsorbed state, the enthalpy and entropy change for the process could be estimated. Absorbed H_2O process only one "hydrogen bonding" with water and thus result in the value of 2 of $<N_{HB}>$ loss compared with the bulk liquid phase as illustrated in Figure S12. H_2O dimer is expected to interact with each other as well as the NO* species. The $<N_{HB}>$ of $2H_2O$ system would be 4 in total and 2 per H_2O. Suggested by the water trimer geometry on Figure S11, the third H_2O could only interact with one of the H_2O molecules. Thus, $3H_2O$ would process 5 in total and 1.6 per H_2O. By multiplying the $\Delta H_{<HB>}$ by $<N_{HB}>$, ΔH is determined for micro solvation system as well as the ΔS. Thus, the $\Delta G_{<HB>}$ at room temperature could be determined by the following equation.

$$\Delta G_{<HB>} = \Delta H_{<HB>} - T\Delta S_{<HB>} = 0.9 \text{ kJ } (mol_{H2O}\, mol_{HB})^{-1} \quad \text{(S27)}$$

For example, for a water molecule moved from the bulk phase to the interface, the lost <HB> equals to (3.3-2) $mol_{HB}\, mol_{H2O}^{-1}$. Hence, the free energy of a single water reconstruction is obtained as 1.2 kJ mol^{-1} ($\Delta G_{<HB>} \times <HB>_{lost}$ = 1.2 kJ mol^{-1}). The free energy of reconstruction for 2 and 3 H_2O molecules could be determined in a similar way shown in Table S4. To quantitively analyze the reconstruction process, we also calculated their possibility at room temperature with respect to the case where all water molecules are rested in the bulk phase.

$$P(x) = e^{-\frac{\Delta G}{RT}} \quad \text{(S28)}$$

Table S4. Free energy change for formation of water clusters of 1, 2, and 3 H_2O at the interface

System	ΔG reconstructructions kJ mol_{H2O}^{-1}	P(x)
0 H_2O	0 (reference)	1.0
1 H_2O – Pd surface	1.2	0.62
2 H_2O – Pd surface	2.3	0.40
3 H_2O – Pd surface	3.0	0.30

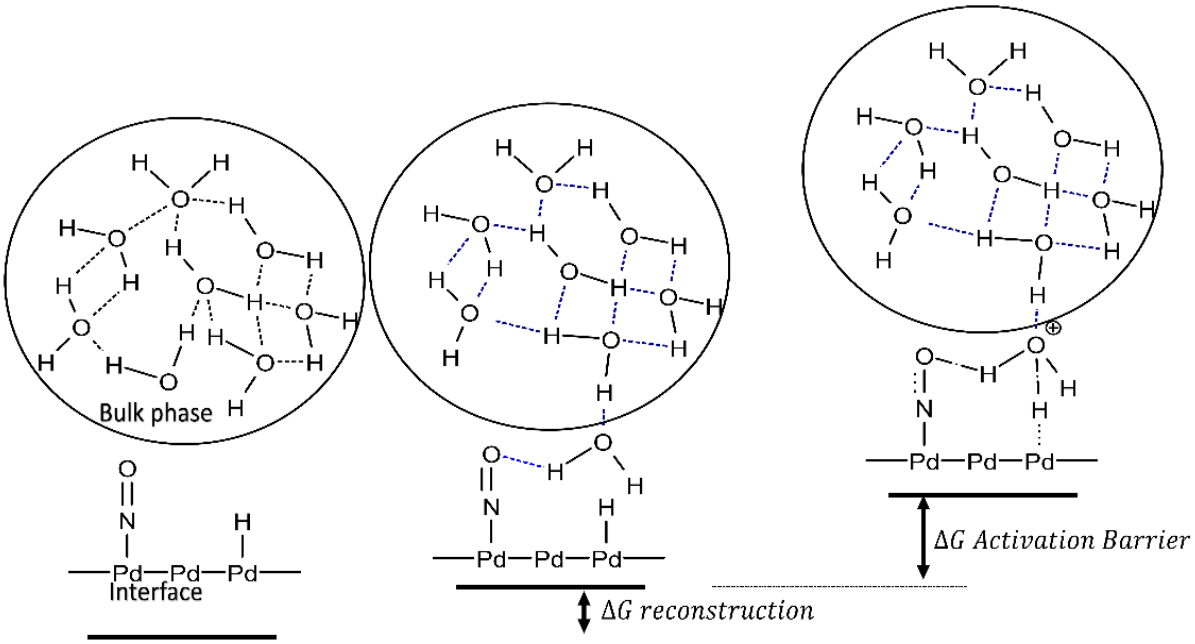

Figure S12. Diagram for free energy estimation in section 5.4.4 and 5.4.5

5.4.5. The enthalpy and entropy contribution on activation free energy

Given the transition state are of the same energy scale as the number of water varies, our result shows the activation barrier ΔG is mostly determined by the enthalpy term indicating 1 water proton shuttling is able to capture the solvation effect on the nitrite reduction energy diagram.

$$\Delta G = \Delta E + \Delta E\_H + ZPE - T\Delta S \quad \text{(S29)}$$

Where ΔG is free energy activation barrier, ΔE is the calculated energy difference between transition state and ground state, ΔE_H is enthalpy contribution, ZPE is zero point energy difference, and TΔS is entropy contribution using 50 cm^{-1} as cut-off for low frequencies.

The entropy change during adsorption and desorption are corrected using the following assumption: the entropy loss or gain of species is assumed to be one-third of the translational and rotational entropy processed by the species in gas phase. The corresponding translational and rotational entropy are determined by Sackur-Tetrode equation. Also, the vibrational entropy change along the step is determined by the vibrational frequency using 50 cm^{-1} as the cutoff. The result show in Table S5.

Table S5. The enthalpy and entropy contribution on free energy activation barrier of transition state (Apparent barrier)

$NO + H \rightarrow HNO$	ΔE (eV)	ΔE_H(eV)	ZPE (eV)	ΔS (eV/K)	ΔG(eV)
1 Water	0.7(2)	-3.7E-03	-6.3E-03	1.9E-05	0.7
2 Water	0.4(9)	-5.3E-03	-1.6E-02	3.1E-05	0.5
3 Water	0.6(0)	-1.7E-02	-1.0E-02	8.9E-05	0.6

6. Langmuir-Hinshelwood-Hougen-Watson (LHHW) derivation

To properly understand the observed reaction orders and activation barriers we conducted a detailed LHHW modelling that leverages previous research on nitrite hydrogenation conducted by L. Lefferts and co-workers.[40]

The mechanism consists of the following reaction steps:

1. $H_2 + 2* \rightleftharpoons 2H*$
2. $NO_2^- + * \rightleftharpoons NO_2^-*$
3. $NO_2^-* + H* + H^+ \rightleftharpoons NO* + * + H_2O$
4. $NO* + H* \rightleftharpoons HNO* + *$
5. $HNO* + H* \rightleftharpoons HNOH* + *$
6. $HNOH* + H* \rightleftharpoons HN* + * + H_2O$

As it can be noted, the steps that proceeded after HNOH* formation are omitted in this LH mechanism as DFT and detailed kinetic results indicate that the RDS must be between steps 4 and 5 in the reaction. Based on this mechanism one could develop the following expressions for the surface coverage of the difference reacting species:

$$\theta_H = K_1^{1/2}[H_2]^{1/2}\theta_v \quad \text{(S30)}$$

$$\theta_{NO_2^-} = K_2[NO_2^-]\theta_v \quad \text{(S31)}$$

$$\theta_{NO} = K_1^{1/2}K_2K_3[H_2]^{1/2}[NO_2^-][H^+][H_2O]^{-1}\theta_v \quad \text{(S32)}$$

$$\theta_{HNO} = K_1K_2K_3K_4[H_2][NO_2^-][H^+][H_2O]^{-1}\theta_v \quad \text{(S33)}$$

$$\theta_{HNOH} = K_1^{3/2}K_2K_3K_4K_5[H_2]^{3/2}[NO_2^-][H^+][H_2O]^{-1}\theta_v \quad \text{(S34)}$$

In this mechanism one can envision multiple possible rate determining steps that can potentially explain the observed reaction orders. In the next section we develop in more detailed those that fit best our current understanding of the nitrite reaction. That is the mechanisms that include a single rate determining step (step 4 or 5) and a dual rate determining step (4 and 5 simultaneously limiting the rate).

6.1 Single rate determining step

One could argue that steps 4-5 could be potentially rate determining steps (RDS) based on the previous observations of ATR-FTIR on surface reaction intermediates[6,13,41,42] and some of our own kinetic isotope effect experiments (Table 4).

For every possible RDS, the assumption is as follows: (1) pre-equilibration with the reaction steps, (2) fast equilibration with the subsequent steps, (3) water concentration is constant as the reactions are conducted in aqueous media, and (4) irreversibility of the RDS, thanks to the negligible concentration of products in the experiments.

6.1.1 Step 4 as RDS

If the RDS is step 4, then we can describe the rate of reaction of NO_2^- as $r_{NO_2^-} = r_4$, where r_4 is:

$$r_4 = k_4\theta_{NO}\theta_H \quad \text{(S35)}$$

$$r_4 = k_4 K_1 K_2 K_3 [H_2][NO_2^-][H^+]{\theta_v}^2 \quad \text{(S36)}$$

Assuming that the Most Abundant Surface Reaction Intermediates (MASRI) on the surface are NO*, H*, and NO_2^-* one could derive the following site balance:

$$\theta_v = \frac{1}{1+K_1^{1/2}[H_2]^{1/2}+K_2[NO_2^-]+K_1^{1/2}K_2K_3[H_2]^{1/2}[NO_2^-][H^+]} \quad \text{(S37)}$$

By substituting equation S37 on equation S36 we obtain the following expression:

$$r_4 = \frac{k_4 K_1 K_2 K_3 [H_2][NO_2^-][H^+]}{\left[1+K_1^{1/2}[H_2]^{1/2}+K_2[NO_2^-]+K_1^{1/2}K_2K_3[H_2]^{1/2}[NO_2^-][H^+]\right]^2} \quad \text{(S38)}$$

If one considers the system is maintained at constant pH due to the use of CO_2 as buffer, then the expression above can be simplified to:

$$r_4 = \frac{k_4 K_1 K_2 K_3 [H_2][NO_2^-]}{\left[1+K_1^{1/2}[H_2]^{1/2}+K_2[NO_2^-]\right]^2} \quad \text{(S39)}$$

In this rate expression S39, one can immediately recognize that the reaction order for hydrogen and nitrite vary in the following manner (Table S6):

Table S6. Reaction orders of hydrogen and nitrite derived from the expression S39

	H_2 order	NO_2^- order
High H_2 pressure, low NO_2^- concentration	0	1
Low H_2 pressure, high NO_2^- concentration	1	-1

Notably, the hydrogenation order theoretically allowed in this model cannot explain the experimentally observed values for hydrogen of 1.5. Thus, this model is expected fail at representing our results.

6.1.2 Step 5 as RDS

If the RDS is step 5, then we can describe the rate of reaction of NO_2^- as $r_{NO_2^-} = r_5$, where r_5 is:

$$r_5 = k_5 \theta_{HNO} \theta_H \quad \text{(S40)}$$

$$r_5 = k_5 {K_1}^{3/2} K_2 K_3 K_4 [H_2]^{3/2} [{NO_2}^-][H^+] {\theta_v}^2 \quad \text{(S41)}$$

Assuming that the Most Abundant Surface Reaction Intermediates (MASRI) on the surface are NO*, HNO*, H*, and NO_2^-* one could derive the following site balance:

$$\theta_v = \frac{1}{1+K_1^{1/2}[H_2]^{1/2}+K_2[{NO_2}^-]+K_1^{1/2}K_2K_3[H_2]^{1/2}[{NO_2}^-][H^+]+\cdots \atop K_1K_2K_3K_4[H_2][{NO_2}^-][H^+]} \quad \text{(S42)}$$

By substituting equation S42 on equation S41 one can obtain the following expression:

$$r_5 = \frac{k_5 {K_1}^{3/2} K_2 K_3 K_4 [H_2]^{3/2} [{NO_2}^-][H^+]}{\left[1+K_1^{1/2}[H_2]^{1/2}+K_2[{NO_2}^-]+K_1^{1/2}K_2K_3[H_2]^{1/2}[{NO_2}^-][H^+]+\cdots \atop K_1K_2K_3K_4[H_2][{NO_2}^-][H^+]\right]^2} \quad \text{(S43)}$$

If one considers the system is maintained at constant pH thanks to the use of CO_2 as buffer, then the expression above can be simplified to:

$$r_5 = \frac{k_5 {K_1}^{3/2} K_2 K_3 K_4 [H_2]^{3/2} [{NO_2}^-]}{\left[1+K_1^{1/2}[H_2]^{1/2}+K_2[{NO_2}^-]\right]^2} \quad \text{(S44)}$$

In this rate expression S44, one can immediately recognize that the reaction order for hydrogen and nitrite vary in the following manner (Table S7):

Table S7. Reaction orders of hydrogen and nitrite derived from the expression S44

	H_2 order	NO_2^- order
High H_2 pressure, low NO_2^- concentration	0.5	1
Low H_2 pressure, high NO_2^- concentration	1.5	-1

Here, it is clear that the hydrogenation orders that are theoretically possible in the model do not cover the observed hydrogen reaction order of 0 at 50 °C obtained in the experiments. Thus, this model is expected to fail at describing these results.

6.1.3 Step 6 as the RDS

If the RDS is step 6, then we can describe the rate of reaction of NO_2^- as $r_{NO_2^-} = r_6$, where r_6 is:

$$r_6 = k_6\theta_{HNOH}\theta_H \quad \text{(S45)}$$

$$r_5 = k_6 k_5 {K_1}^2 K_2 K_3 K_4 [H_2]^2 [{NO_2}^-][H^+]{\theta_v}^2 \quad \text{(S46)}$$

Assuming that the most abundant surface reaction intermediates (MASRI) on the surface are NO*, HNO*, HNOH,H*, and NO_2^-* one could derive the following site balance:

$$\theta_v = \frac{1}{\begin{matrix}1+K_1^{1/2}[H_2]^{1/2}+K_2[{NO_2}^-]+K_1^{1/2}K_2K_3[H_2]^{1/2}[{NO_2}^-][H^+]+\cdots \\ K_1K_2K_3K_4[H_2][{NO_2}^-][H^+]+K_1^{3/2}K_2K_3K_{4K_5}[H_2]^{3/2}[{NO_2}^-][H^+]\end{matrix}} \quad \text{(S47)}$$

By substituting equation S47 on equation S46 we obtain the following expression:

$$r_5 = \frac{k_6 k_5 {K_1}^2 K_2 K_3 K_4 [H_2]^2 [{NO_2}^-][H^+]}{\left[\begin{matrix}1+K_1^{1/2}[H_2]^{1/2}+K_2[{NO_2}^-]+K_1^{1/2}K_2K_3[H_2]^{1/2}[{NO_2}^-][H^+]+\cdots \\ K_1K_2K_3K_4[H_2][{NO_2}^-][H^+]+K_1^{3/2}K_2K_3K_{4K_5}[H_2]^{3/2}[{NO_2}^-][H^+]\end{matrix}\right]^2} \quad \text{(S48)}$$

If one considers the system is maintained at constant pH thanks to the use of CO_2 as buffer, then the expression above can be simplified to:

$$r_5 = \frac{k_6 k_5 {K_1}^2 K_2 K_3 K_4 [H_2]^2 [{NO_2}^-]}{\left[1+K_1^{1/2}[H_2]^{1/2}+K_2[{NO_2}^-]\right]^2} \quad \text{(S49)}$$

In this rate expression S49, one can immediately recognize that the reaction order for hydrogen and nitrite vary in the following manner (Table S8):

Table S8. Reaction orders of hydrogen and nitrite derived from the expression S49

	H_2 order	NO_2^- order
High H_2 pressure, low NO_2^- concentration	1	1
Low H_2 pressure, high NO_2^- concentration	2	-1

Here, it is clear that the hydrogenation orders that are theoretically possible in the model do not cover the observed hydrogen reaction order of 0 at 50°C obtained in the experiments. Thus, this model is expected to fail at describing these results.

6.2. Dual rate determining step

If one assumes that (1) two steps contribute to the rate (e.g. step 4 and step 5) and (2) the pseudo-steady

state approximation is valid in this system, then one could capture the experimentally observed reaction

rates as follows:

$$\frac{d(HNO)}{dt} = k_4\theta_{NO}\theta_H - k_{-4}\theta_{HNO}\theta_v - k_5\theta_{HNO}\theta_H = 0 \quad \text{(S50)}$$

$$k_4\theta_{NO}\theta_H = [k_{-4}\theta_v + k_5\theta_H]\theta_{HNO} \quad \text{(S51)}$$

$$\theta_{HNO} = \frac{k_4\theta_{NO}\theta_H}{k_{-4}\theta_v + k_5\theta_H} \quad \text{(S52)}$$

$$\theta_{HNO} = \frac{k_4K_1K_2K_3[H_2][NO_2^-][H^+]}{k_{-4}+k_5K_1^{1/2}[H_2]^{1/2}} * \theta_v \quad \text{(S53)}$$

The rate expression for the consumption of NO_2^- per catalyst site can be written as a function of the rate determining step ($r_{overall} = \frac{r_i - r_{-i}}{\sigma_i}$, σ_i is the stoichiometry of the i[th] elementary step), then (assuming that r_5 is irreversible) one can obtain the following:

$$r_{NO_2^-} = r_5 = k_5\theta_{HNO}\theta_H \quad \text{(S54)}$$

By substituting equation S53 and equation S30 on equation S54 one obtains the following rate expression:

$$r_{NO_2^-} = \left[k_5 \frac{\left[k_4{K_1}^{3/2}K_2K_3[H_2]^{3/2}[NO_2^-][H^+]\right]}{k_{-4}+k_5K_1^{\frac{1}{2}}[H_2]^{\frac{1}{2}}}\right] * {\theta_v}^2 \quad \text{(S55)}$$

Assuming that the Most Abundant Surface Reaction Intermediates (MASRI) on the surface are NO*, HNO*, H*, and NO_2^-* one could derive the equation S42.

$$\theta_v = \frac{1}{1+K_1^{1/2}*[H_2]^{1/2}+K_2*[NO_2^-]+K_1^{1/2}*K_2*K_3*[H_2]^{1/2}*[NO_2^-]*[H^+]+\cdots} \quad \text{(S42)}$$
$$K_1*K_2*K_3*K_4*[H_2]*[NO_2^-]*[H^+]$$

By substituting equation S42 on equation S55 one obtains the following rate expression:

$$r_{NO_2^-} = \frac{k_5 k_4 * {K_1}^{3/2} K_2 K_3 [H_2]^{3/2} [NO_2{}^-][H^+]}{\left[k_{-4} + k_5 K_1^{\frac{1}{2}} [H_2]^{\frac{1}{2}}\right] * \left[1 + K_1^{1/2} [H_2]^{\frac{1}{2}} + K_2 [NO_2{}^-] + K_1^{1/2} K_2 K_3 [H_2]^{1/2} [NO_2{}^-][H^+] + \cdots \right]^2} \quad \text{(S56)}$$
$$K_1 K_2 K_3 K_4 [H_2][NO_2{}^-][H^+]$$

If one considers the system is maintained at constant pH ($[H^+]$ of 10^{-5} mol L^{-1}) thanks to the use of CO_2 as buffer, then the expression above can be simplified to:

$$r_{NO_2^-} = \frac{k_5 k_4 {K_1}^{3/2} K_2 K_3 [H_2]^{3/2} [NO_2{}^-]}{\left[k_{-4} + k_5 K_1^{1/2} [H_2]^{1/2}\right] * \left[1 + K_1^{1/2} [H_2]^{\frac{1}{2}} + K_2 [NO_2{}^-]\right]^2} \quad \text{(S57a)}$$

$$r_{NO_2^-} = \frac{k_4 {K_1}^{3/2} K_2 K_3 [H_2]^{3/2} [NO_2{}^-]}{\left[\frac{k_{-4}}{k_5} + K_1^{1/2} [H_2]^{1/2}\right] * \left[1 + K_1^{1/2} [H_2]^{1/2} + K_2 [NO_2{}^-]\right]^2} \quad \text{(S57b)}$$

In this rate expression S57a, one can immediately recognize that the reaction order for hydrogen and nitrite vary in the following manner (Table S9):

Table S9. Reaction orders of hydrogen and nitrite derived from the expression S57a

	H_2 order	NO_2^- order
High H_2 pressure, low NO_2^- concentration	0	1
Low H_2 pressure, high NO_2^- concentration	1.5	-1

In this model, the hydrogen orders can cover all the experimentally observed reaction orders. Thus, it is expected that this model will be able to predict the measured rates.

The result from least squares regression for all rate control scenarios are summarized in Table S10.

Table S10. Results from least squares regression for all rate control scenarios.

Temperature (°C)	Case	Variable parameters	SSE	AIC	R^2
25	Step 4	4	0.25	-23.54	0.999
	Step 4,5	6	0.14	-32.83	0.999
	Step 5	5	1.21	14.39	0.998
	Step 6	6	2.77	35.40	0.997
50	Step 4	4	0.09	-35.77	0.999
	Step 4,5	6	0.08	-32.14	0.999
	Step 5	5	0.89	7.97	0.998
	Step 6	6	2.96	31.51	0.996

7. Kinetic modeling fitting

The model was developed using transition state theory. First, we converted all the equilibrium and reaction constants into G of activation and equilibrium $K_i = e^{\left[\frac{-G^o_{Xi*}}{RT}\right]}$ and $k_i = \frac{K_B T}{h} e^{\left[\frac{-(G^0_{TSi} - \Sigma_{i=1}^{n} G^0_{Xri})}{RT}\right]}$, respectively. For simplicity we rewrite the equation using $g_i = \frac{-G^o_{Xi*}}{RT}$.

For hydrogen $K_1 = e^{\left[\frac{-\Delta G_H}{RT}\right]}$ or $K_1 = e^{[g_H]}$ (S58)

For nitrite $K_2 = e^{\left[\frac{-\Delta G_{NO_2^-}}{RT}\right]}$ or $K_2 = e^{\left[g_{NO_2^-}\right]}$ (S59)

For NO + H $K_3 = e^{\left[\frac{-\Delta G_{NO}}{RT}\right]}$ or $K_3 = e^{[g_{*NO}]}$ (S60)

For reaction 4 $k_4 = \frac{K_B T}{h} e^{\left[\frac{-\Delta G^{\ddagger}_{TS4}}{RT}\right]}$ or $k_4 = \frac{K_B T}{h} e^{[g_{TS4}]}$ (S61)

For reaction 5 $k_5 = \frac{K_B T}{h} e^{\left[\frac{-\Delta G^{\ddagger}_{TS5}}{RT}\right]}$ or $k_5 = \frac{K_B T}{h} e^{[g_{TS5}]}$ (S62)

For the backward reaction -4 $k_{-4} = \frac{K_B T}{h} e^{\left[\frac{-\Delta G^{\ddagger}_{TS-4}}{RT}\right]}$ or $k_{-4} = \frac{K_B T}{h} e^{[g_{TS-4}]}$ (S63)

Now, we can substitute equation S58-S62 into equation S57b to get the following equations.

$$r_{NO_2^-} = \left[\frac{K_B T}{h}\right] \frac{e^{[g_{TS4}]} e^{\left[\frac{3}{2}g_H\right]} e^{\left[g_{NO_2^-}\right]} e^{[g_{NO}]} [H_2]^{3/2} [NO_2{}^-]}{\left[\frac{e^{[g_{TS-4}]}}{e^{[g_{TS5}]}} + e^{\left[\frac{1}{2}g_H\right]} [H_2]^{1/2}\right] * \left[1 + e^{\left[\frac{1}{2}g_H\right]} [H_2]^{1/2} + e^{\left[g_{NO_2^-}\right]} [NO_2{}^-]\right]^2} \quad \text{(S64a)}$$

$$r_{NO_2^-} = \left[\frac{K_B T}{h}\right] \frac{e^{\left[g_{TS4} + \frac{3}{2}g_H + g_{NO_2^-} + g_{NO}\right]} [H_2]^{3/2} [NO_2{}^-]}{\left[e^{[g_{TS-4} - g_{TS5}]} + e^{\left[\frac{1}{2}g_H\right]} [H_2]^{1/2}\right] * \left[1 + e^{\left[\frac{1}{2}g_H\right]} [H_2]^{1/2} + e^{\left[g_{NO_2^-}\right]} [NO_2{}^-]\right]^2} \quad \text{(S64b)}$$

The equation 64b is used to do the kinetic fitting with the experiment data. To this fitting the error minimization algorithm was set-up to obtain the equilibrium and kinetic constants using as starting point the calculated values obtained from the DFT model for the proton-shuttling mechanism. In this analysis, we limited our fitting to the regression of the equilibrium and reaction constants. Here, it is important to mention that the optimized values of the Gibbs free energies of adsorption and activation were close to those obtained from the DFT calculations, indicating that these values are physically meaningful (see Table S11). To ensure the thermodynamic consistency of the results, we imposed to the error minimization the following boundaries: equilibrium constants should decrease with increasing temperature, while the kinetic constant should increase with increasing temperature.

Table S11. Regressed equilibrium and kinetic constants at 25 °C and 50 °C for the nitrite hydrogenation on Palladium.

Kinetic Parameter	ln K/lnk		Gibbs Free Energy (kJ mol^{-1})		Gibbs Free Energy (eV)	
	25°C	50°C	25°C	50°C	25°C	50°C
K H_2	17.32	15.91	-42.94	-42.75	-0.45	-0.44
K NO_2^-	11.07	10.18	-27.44	-27.34	-0.28	-0.28
K NO	6.71	3.73	-16.63	-10.02	-0.17	-0.10
k TS1	-49.46	-45.18	122.61	121.39	1.27	1.26
k TS2	-39.37	-31.62	97.6	84.97	1.01	0.88
k TS-1	-36.34	-31.48	90.1	84.59	0.93	0.88

The kinetic fitting results of steps 4,5 as RDS are shown in Figure S13**.** Here, it can be noticed that there is a good agreement between the model and experimental data. This is further elaborated in Table S10 that includes the results from the least squares regression R^2, AIC, and SSE.

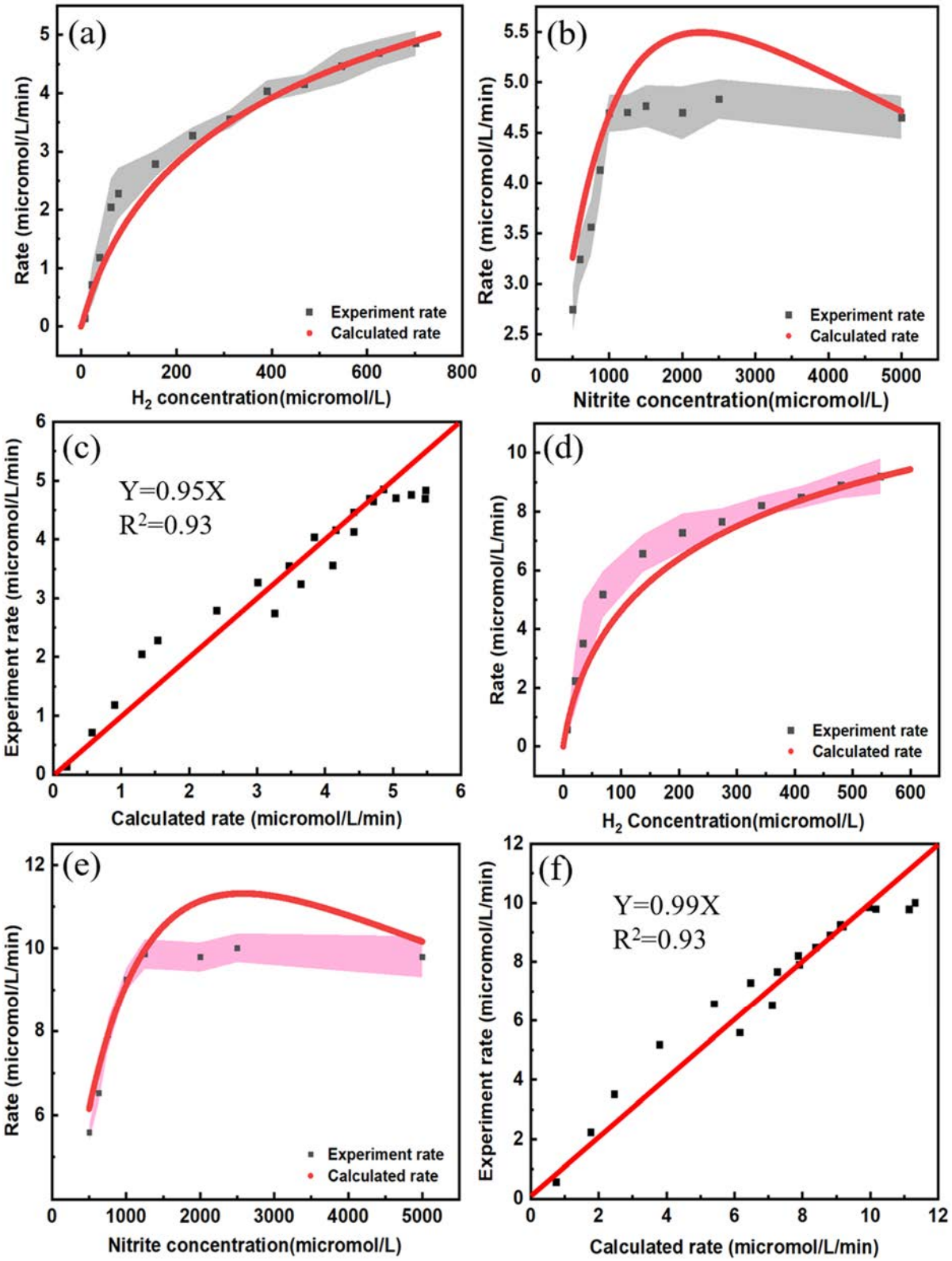

Figure S13. Kinetic fitting result at 25°C: (a) reaction rate changes with hydrogen concentration, (b) reaction rate changes with nitrite concentration, (c) Reaction rate along with the calculated rate; Kinetic fitting result at 50°C: (d) reaction rate changes with hydrogen concentration, (e) reaction rate changes with nitrite concentration, (f) Reaction rate along with the calculated rate.

8. Degree of rate control

As shown in the preceding section, it seems that the rate determining step changes with the reaction conditions. We try to understand how the reaction conditions change the rate determining steps using the method from developed by Campbell et al.[43] In this approach, the quasi equilibrated adsorption steps, the equilibrium constants K_i, can be expressed as $K_i = (-G^0_{X*}/RT)$, where $G^0_{X*}$is the standard-state Gibbs free energy of the adsorbate X* formed in Step i. Next, k_4 is the forward rate constant of Step 4. According to the transition state theory this can be expressed as $k_4 = \frac{K_B T}{h}\exp[-(G^0_{TS4} - G^0_{H_2} - G^0_{NO_2^-} - G^0_{NO})/RT]$, where G^0_{TS4} is the standard-state Gibbs free energy of the transition state in Step 4 (TS4). If all rate constants and equilibrium constants in equation 64b are expressed as functions of Gibbs free energies, equation 64b becomes:

$$r_{NO_2^-} = \left[\frac{K_B T}{h}\right] \frac{e^{\left[g_{TS4} - g_{H_2} - g_{NO_2^-} - gNO\right]} e^{\left[\frac{3}{2} g_{H_2}\right]} e^{\left[g_{NO_2^-}\right]} e^{[g_{NO}]} [H_2]^{3/2} [NO_2{}^-]}{\left[\frac{e^{[g_{TS4} - gHNO]}}{e^{[g_{TS5} - gHNO]}} + e^{\left[\frac{1}{2} g_{H_2}\right]} [H_2]^{1/2}\right] * \left[1 + e^{\left[\frac{1}{2} g_H\right]} [H_2]^{1/2} + e^{\left[g_{NO_2^-}\right]} [NO_2{}^-]\right]^2} \quad \text{(S65)}$$

Plugging equation S63 into the equation of the DRC (Equation 9), then obtain the DRCs of TS4 and TS5.

$$X_4 = \frac{\partial(lnr)}{\partial(g_{TS4})} = \frac{e^{\left[\frac{1}{2} g_{H_2}\right]} [H_2]^{1/2}}{\left[e^{[gTS4 - gTS5]} + e^{\left[\frac{1}{2} g_{H_2}\right]} [H_2]^{1/2}\right]} \quad \text{(S66)}$$

$$X_5 = \frac{\partial(lnr)}{\partial(g_{TS5})} = \frac{e^{[gTS4 - TS5]}}{\left[e^{[gTS4 - gTS5]} + e^{\left[\frac{1}{2} g_{H_2}\right]} [H_2]^{1/2}\right]} \quad \text{(S67)}$$

Table S12. Calculated enthalpies and entropies of adsorption and activation for the nitrite hydrogenation reaction.

Step	Species involved	Slope	Y-Intercept	Enthalpy (kJ mol^{-1})	Entropy (J/mol*K^{-1})
1	H_2	5.44	-0.91	-45.21	-7.60
2	NO_2^-	3.45	-0.48	-28.64	-4.03
3	NO	11.49	-31.83	-95.53	-264.60
4	TS1	-16.48	5.81	137.01	48.31
5	TS2	-29.86	60.78	248.27	505.37
6	TS-1	-18.73	26.49	155.75	220.22

As it can be noted from Table S12 resulting enthalpies of adsorption are all negative and the corresponding absolute values of the adsorption entropies for hydrogen (7.6 J/mol*K^{-1}) and nitrite (4.0 J/mol*K^{-1}) are lower than those in the standard state with values of 131 J/mol*K^{-1} and 106 J/mol*K^{-1}, respectively, which is in compliance with the thermodynamic guidelines proposed by Prof. Vannice.[44] These parameter are used for the degree of rate control analysis.

References

[1] B.A. Humphreys, E.J. Wanless, G.B. Webber, Effect of ionic strength and salt identity on poly (N-isopropylacrylamide) brush modified colloidal silica particles, J. Colloid Interface Sci. 516 (2018) 153–161.

[2] T. Ye, D.P. Durkin, M. Hu, X. Wang, N.A. Banek, M.J. Wagner, D. Shuai, Enhancement of Nitrite Reduction Kinetics on Electrospun Pd-Carbon Nanomaterial Catalysts for Water Purification, ACS Appl. Mater. Interfaces. 8 (2016) 17739–17744. https://doi.org/10.1021/acsami.6b03635.

[3] S.L. Greasley, S.J. Page, S. Sirovica, S. Chen, R.A. Martin, A. Riveiro, J. V. Hanna, A.E. Porter, J.R. Jones, Controlling particle size in the Stöber process and incorporation of calcium, J. Colloid Interface Sci. 469 (2016) 213–223. https://doi.org/10.1016/j.jcis.2016.01.065.

[4] W.S. Lee, Z. Wang, W. Zheng, D.G. Vlachos, A. Bhan, Vapor phase hydrodeoxygenation of furfural to 2-methylfuran on molybdenum carbide catalysts, Catal. Sci. Technol. 4 (2014) 2340–2352. https://doi.org/10.1039/c4cy00286e.

[5] D.E. Mears, Tests for Transport Limitations in Experimental Catalytic Reactors, Ind. Eng. Chem. Process Des. Dev. 10 (1971) 541–547. https://doi.org/10.1021/i260040a020.

[6] S.D. Ebbesen, B.L. Mojet, L. Lefferts, Mechanistic Investigation of the Heterogeneous Hydrogenation of Nitrite over Pt/Al 2 O 3 by Attenuated Total Reflection Infrared Spectroscopy, J. Phys. Chem. C. 113 (2009) 2503–2511. https://doi.org/10.1021/jp8081886.

[7] R. Zhang, D. Shuai, K.A. Guy, J.R. Shapley, T.J. Strathmann, C.J. Werth, Elucidation of Nitrate Reduction Mechanisms on a Pd-In Bimetallic Catalyst using Isotope Labeled Nitrogen Species, ChemCatChem. 5 (2013) 313–321. https://doi.org/10.1002/cctc.201200457.

[8] Y. Zhao, N. Koteswara Rao, L. Lefferts, Adsorbed species on Pd catalyst during nitrite hydrogenation approaching complete conversion, J. Catal. 337 (2016) 102–110. https://doi.org/10.1016/j.jcat.2016.02.007.

[9] C.P. Theologides, G.G. Olympiou, P.G. Savva, K. Kapnisis, A. Anayiotos, C.N. Costa, Mechanistic aspects (SSITKA-DRIFTS) of the catalytic denitrification of water with hydrogen on Pd-Cu supported catalysts, Appl. Catal. B Environ. 205 (2017) 443–454. https://doi.org/10.1016/j.apcatb.2016.12.055.

[10] X. Huo, D.J. Van Hoomissen, J. Liu, S. Vyas, T.J. Strathmann, Hydrogenation of aqueous nitrate and nitrite with ruthenium catalysts, Appl. Catal. B Environ. 211 (2017) 188–198. https://doi.org/10.1016/j.apcatb.2017.04.045.

[11] H. Shin, S. Jung, S. Bae, W. Lee, H. Kim, Nitrite reduction mechanism on a Pd surface, Environ. Sci. Technol. 48 (2014) 12768–12774. https://doi.org/10.1021/es503772x.

[12] V. Höller, K. Rådevik, I. Yuranov, L. Kiwi-Minsker, A. Renken, Reduction of nitrite-ions in water over Pd-supported on structured fibrous materials, Appl. Catal. B Environ. 32 (2001) 143–150. https://doi.org/10.1016/S0926-3373(01)00139-4.

[13] S.D. Ebbesen, B.L. Mojet, L. Lefferts, Effect of pH on the Nitrite Hydrogenation Mechanism over Pd/Al2O3 and Pt/Al2O3: Details Obtained with ATR-IR Spectroscopy, J. Phys. Chem. C. (2011) 1186–1194. https://doi.org/10.1021/jp106521t.

[14] Y.B. Yin, S. Guo, K.N. Heck, C.A. Clark, C.L. Conrad, M.S. Wong, Treating Water by Degrading Oxyanions Using Metallic Nanostructures, ACS Sustain. Chem. Eng. 6 (2018) 11160–11175. https://doi.org/10.1021/acssuschemeng.8b02070.

[15] X. Fan, C. Franch, E. Palomares, A.A. Lapkin, Simulation of catalytic reduction of nitrates based on a mechanistic model, Chem. Eng. J. 175 (2011) 458–467. https://doi.org/10.1016/j.cej.2011.09.069.

[16] I. Mikami, Y. Sakamoto, Y. Yoshinaga, T. Okuhara, Kinetic and adsorption studies on the hydrogenation of nitrate and nitrite in water using Pd-Cu on active carbon support, Appl. Catal. B Environ. 44 (2003) 79–86.

[17] J. Wärn, I. Turunen, T. Salmi, T. Maunula, Kinetics of nitrate reduction in monolith reactor, Chem. Eng. Sci. 49 (1994) 5763–5773. https://doi.org/10.1016/0009-2509(94)00331-9.

[18] L.Y. Huai, C.Z. He, H. Wang, H. Wen, W.C. Yi, J.Y. Liu, NO dissociation and reduction by H2 on Pd(1 1 1): A first-principles study, J. Catal. 322 (2015) 73–83. https://doi.org/10.1016/j.jcat.2014.11.011.

[19] S. Guo, K. Heck, S. Kasiraju, H. Qian, Z. Zhao, L.C. Grabow, J.T. Miller, M.S. Wong, Insights into Nitrate Reduction over Indium-Decorated Palladium Nanoparticle Catalysts, ACS Catal. 8 (2018) 503–515. https://doi.org/10.1021/acscatal.7b01371.

[20] Z. Zhao, R. Bababrik, W. Xue, Y. Li, N.M. Briggs, D.-T. Nguyen, U. Nguyen, S.P. Crossley, S. Wang, B. Wang, Solvent-mediated charge separation drives alternative hydrogenation path of furanics in liquid water, Nat. Catal. 2 (2019) 431–436.

[21] D.T. Bregante, M.C. Chan, J.Z. Tan, E.Z. Ayla, C.P. Nicholas, D. Shukla, D.W. Flaherty, The shape of water in zeolites and its impact on epoxidation catalysis, Nat.

Catal. 4 (2021) 797–808. https://doi.org/10.1038/s41929-021-00672-4.

[22] K.A.T. Silverstein, A.D.J. Haymet, K.A. Dill, The strength of hydrogen bonds in liquid water and around nonpolar solutes, J. Am. Chem. Soc. 122 (2000) 8037–8041.

[23] G.E. Walrafen, Y.C. Chu, Shear viscosity, heat capacity, and fluctuations of liquid water, all at constant molal volume, J. Phys. Chem. 95 (1991) 8909–8921.

[24] B.R. Goldsmith, T. Hwang, S. Seritan, B. Peters, S.L. Scott, Rate-enhancing roles of water molecules in methyltrioxorhenium-catalyzed olefin epoxidation by hydrogen peroxide, J. Am. Chem. Soc. 137 (2015) 9604–9616.

[25] R.A.V. Hernández, Bayesian Optimization for Calibrating and Selecting Hybrid-Density Functional Models, J. Phys. Chem. A. 124 (2020) 4053–4061.

[26] G. Kresse, J. Furthmüller, Efficiency of ab-initio total energy calculations for metals and semiconductors using a plane-wave basis set, Comput. Mater. Sci. 6 (1996) 15–50.

[27] G. Kresse, J. Hafner, Ab initio molecular-dynamics simulation of the liquid-metal–amorphous-semiconductor transition in germanium, Phys. Rev. B. 49 (1994) 14251.

[28] P.E. Blöchl, Projector augmented-wave method, Phys. Rev. B. 50 (1994) 17953–17979. https://doi.org/10.1103/PhysRevB.50.17953.

[29] G. Kresse, D. Joubert, From ultrasoft pseudopotentials to the projector augmented-wave method, Phys. Rev. B. 59 (1999) 1758.

[30] S. Grimme, J. Antony, S. Ehrlich, H. Krieg, A consistent and accurate ab initio parametrization of density functional dispersion correction (DFT-D) for the 94 elements H-Pu, J. Chem. Phys. 132 (2010) 154104.

[31] M. Chen, Y. Yan, M. Gebre, C. Ordonez, F. Liu, L. Qi, A. Lamkins, D. Jing, K. Dolge, B. Zhang, P. Heintz, D.P. Shoemaker, B. Wang, W. Huang, Thermal Unequilibrium of PdSn Intermetallic Nanocatalysts: From In Situ Tailored Synthesis to Unexpected Hydrogenation Selectivity, Angew. Chemie Int. Ed. 60 (2021) 18309–18317. https://doi.org/https://doi.org/10.1002/anie.202106515.

[32] K. Mathew, R. Sundararaman, K. Letchworth-Weaver, T.A. Arias, R.G. Hennig, Implicit solvation model for density-functional study of nanocrystal surfaces and reaction pathways, J. Chem. Phys. 140 (2014) 1–8. https://doi.org/10.1063/1.4865107.

[33] A. Heyden, A.T. Bell, F.J. Keil, Efficient methods for finding transition states in chemical reactions: Comparison of improved dimer method and partitioned rational function optimization method, J. Chem. Phys. 123 (2005) 224101.

[34] G. Henkelman, B.P. Uberuaga, H. Jónsson, A climbing image nudged elastic band method for finding saddle points and minimum energy paths, J. Chem. Phys. 113

(2000) 9901–9904.

[35] M. Yamauchi, R. Ikeda, H. Kitagawa, M. Takata, Nanosize effects on hydrogen storage in palladium, J. Phys. Chem. C. 112 (2008) 3294–3299. https://doi.org/10.1021/jp710447j.

[36] A. Stukowski, Visualization and analysis of atomistic simulation data with OVITO-the Open Visualization Tool, Model. Simul. Mater. Sci. Eng. 18 (2010). https://doi.org/10.1088/0965-0393/18/1/015012.

[37] E. P.J. Linstrom and W.G. Mallard, NIST Chemistry WebBook, NIST Standard Reference Database Number 69, National Institute of Standards and Technology, Gaithersburg MD, 20899, 2021. https://doi.org/https://doi.org/10.18434/T4D303.

[38] D.D. Perrin, Ionisation constants of inorganic acids and bases in aqueous solution, Elsevier, 2016.

[39] C.T. Campbell, J.R. V Sellers, The entropies of adsorbed molecules, J. Am. Chem. Soc. 134 (2012) 18109–18115.

[40] P. Xu, S. Agarwal, L. Lefferts, Mechanism of nitrite hydrogenation over Pd/γ-Al2O3 according a rigorous kinetic study, J. Catal. 383 (2020) 124–134. https://doi.org/10.1016/j.jcat.2020.01.003.

[41] S.D. Ebbesen, B.L. Mojet, L. Lefferts, In situ attenuated total reflection infrared (ATR-IR) study of the adsorption of NO2-, NH2OH, and NH4+ on Pd/Al2O3 and Pt/Al2O3., Langmuir. 24 (2008) 869–79. https://doi.org/10.1021/la7027725.

[42] S.D. Ebbesen, B.L. Mojet, L. Lefferts, In situ ATR-IR study of nitrite hydrogenation over Pd/Al2O3, J. Catal. 256 (2008) 15–23. https://doi.org/10.1016/j.jcat.2008.02.013.

[43] Z. Mao, C.T. Campbell, The degree of rate control of catalyst-bound intermediates in catalytic reaction mechanisms: Relationship to site coverage, J. Catal. 381 (2020) 53–62. https://doi.org/10.1016/j.jcat.2019.09.044.

[44] A. Vannice, Kinetics of Catalytic Reactions, 1st ed., Springer, New York, 2005. https://doi.org/10.1016/S0166-9834(00)80062-7.

Chapter 3

Controlling Solvation Effects in Pd-Catalyzed Nitrite Reduction in Water Using Stimulus-Responsive Polymer Coatings

Abstract

Conducting catalytic reactions in aqueous phases is rather challenging as mass transfer rates, catalyst stability, selectivity, and activity can be greatly compromised by the reactive nature of water molecules. In the absence of mass transport and catalyst deactivation, one can engineer the micro-solvation environment of the catalyst to increase activity and selectivity in polar aqueous phases. Here, we present a new approach to influence the selectivity and activity of the metal-catalyzed hydrogenation reaction of nitrites in the aqueous phase using a catalyst containing temperature-sensitive polymer coatings that can induce fully-reversible solvation effects on the surface reaction kinetics. The switchable micro-solvation environment facilitated the reduction of nitrites (NO_2^-), which is a relevant reaction in the removal of nitrogen pollutants from drinking water. The Pd/SiO_2 catalyst consisted of nonporous SiO_2 spheres of c.a. 500 nm decorated with Pd clusters (2-3 nm). Subsequently, atom transfer radical polymerization (ATRP) was employed to grow well-controlled polymer brushes of poly-n-isopropylacrylamide (p-NIPAM) with dry thicknesses of just 7 nm on the Pd/SiO_2 catalyst, allowing operation in the absence of mass transfer limitations. The polymer-coated catalyst showed a four-fold higher selectivity to NH_4^+ at the same conversion level when compared to the parent Pd/SiO_2 catalyst. Notably, the polymer-coated catalyst displayed two distinct apparent activation energy barriers as temperature increased. That is that when the temperature was below the lower critical solution temperature of p-NIPAM (LCST of 32 °C) the apparent activation energy barrier was reduced by a factor of three, when compared to the non-coated catalyst. Transition state treatment of the reaction kinetics revealed that the lower apparent barriers in the swollen state

of the polymer were induced by a large decrease in the excess enthalpy of apparent activation, indicative of a favorable interaction between the reactive species and activated complex with the polymer. This stabilization effect came at the expense of entropy losses explaining the lower apparent entropy of activation. This enhancement, however, vanished at temperatures above the LCST, leading to apparent barriers similar to those of the parent Pd/SiO_2 catalyst.

1. Introduction

The use of stimulus-responsive polymer gels as catalyst coatings and/or hosts of catalyst nanoparticles has been widely employed for either efficient catalyst recovery and/or regulation of mass transport towards the active sites. In the first one, the catalyst is recovered by applying an external stimulus (e.g. pH, heat, light, or magnetic fields) that triggers a change in the conformational structure of the polymer from swollen to de-swollen, initiating the flocculation and precipitation of the catalyst out of the reaction media. This in turn, facilitates the catalyst separation and recycling.[1] In the second approach, the mass transfer of molecules towards the active sites is reversibly strained as the polymer collapses onto its globular configuration due to the application of the external stimulus.[2] Removal of the external stimuli leads to the polymer swelling allowing the unrestricted conversion of molecules. Because the catalytic activity was regulated by the permeability of the molecules through the polymer, it was possible to convert molecules selectively depending on their solubility in the polymer matrix.[3–5] This enabled an unprecedented level of control over the conversion of molecules based on their interaction with the stimulus-responsive polymer above and below the critical solubility threshold.

The first kinetic model of egg-shell nano-reactors with stimulus-responsive behavior was developed by Carregal-Romero et al.[6] for the electron-transfer reaction between hexacyanoferrate(III) and borohydride ions using Au nanoparticles encapsulated on poly-isopropylacrylamide (p-NIPAM) with different extents of cross-linking. This polymer has a characteristic lower critical solution temperature limit (LCST) of 32 °C. That means that at temperatures above the LCST the solubility of the polymer in water drastically decreases due to entropic contributions to the Gibbs free energy of the system. In this case, the authors described the system using a pseudo-first-order kinetic model in which the observed kinetic constant was defined as the result of the coupling of the first-order surface reaction kinetics (k_r) and the mass transport (k_d) through the polymer layer (Equation 1) at temperatures below and above the LCST.

$$k_{obs}^{-1} = k_r^{-1} + k_d^{-1} \qquad (1)$$

In this explanation, the authors argued that at low temperatures the activation barriers measured were those corresponding to the diffusion of the reactants at infinite dilution in the aqueous media (~ 10 kJ mol^{-1}). At high temperatures (> 32 °C) the polymer density increases leading to a drop in the porosity and an increase in tortuosity that lowered the effective diffusion. The

authors explained that the observed higher activation barriers were caused by the more difficult diffusion process (~ 30 kJ mol^{-1}). Upon increasing the content of crosslinking in the polymer gel the extent of gel shrinkage upon reaching the LCST was drastically reduced, which in turn lowered the activation energies previously observed above the LCST. In a subsequent study, the groups of Prof. M. Ballauff and Prof. J. Dzubiella reported that the nature of p-NIPAM-reactant interactions exerted a remarkable influence on the observed rate of reaction, allowing hydrophobic molecules to be converted selectively at high temperatures.[5] This was attributed to a more favorable partition of the hydrophobic reactants into the polymer matrix (i.e., lower Gibbs free energy of transfer from the bulk to the polymer) above the LCST of p-NIPAM despite the constrained porosity and enhanced tortuosity. In this case, the diffusion rate of the limiting reactant through the polymer layer was derived following the Debye−Smoluchowskia theory.[3]

The theory predicts that as the p-NIPAM environment becomes more hydrophobic above the LCST the partition of molecules into the polymer matrix increases exponentially for the more hydrophobic reactants, while the opposite occurs to the hydrophilic substrates. The theory has been successfully employed to describe multi-component reaction processes occurring in stimulus-responsive nano-reactors.[2] The main drawback of this approach is that the interactions between the polymer and surface reacting species are neglected. This is because the kinetics observed in an uncoated catalyst are assumed to be equal to those measured in a polymer-containing one in the solvated state of the polymer (k_r). More recent studies have shown, however, that this oversimplification leads to important deviations between theory and experimental observations. In fact, these new results indicate that polymer-reactant interactions are key for both diffusion and reaction of molecules when catalysts are functionalized with p-NIPAM polymeric brushes.[7,8]

To challenge this model the present contribution aims at studying the interplay of the polymer-solvation effects on the surface reaction kinetics (k_r) in the absence of any mass transfer limitations (i.e. $k_d >> k_r$). For this purpose, we have developed a Pd-containing catalyst supported on nonporous SiO_2 spheres of c.a. 500 nm that contained p-NIPAM brushes grown from the -OH surface functional groups using atom transfer radical polymerization (ATRP). In these catalysts, all Pd atoms are readily available for reaction, and no internal mass transport limitations are expected as there are no pores. In addition, we employed high mixing rates (500 rpm) to ensure instantaneous equilibration of gaseous reactants in the aqueous slurry of the catalyst, thus eliminating gas-liquid and liquid-solid transport limitations. To explore this

concept, we applied the Pd/SiO_2 with and without p-NIPAM brushes for the hydrogenation of nitrites (NO_2^-), which are toxic pollutants present in drinking water contaminated by agricultural and industrial activities. By combining detailed catalyst characterization, rigorous kinetic measurements, and transition state theory treatments, we have demonstrated that stimulus-responsive polymers present next to the active site, and in the absence of any mass transport limitation, can induce solvation effects that alter the apparent reaction barriers for the nitrite hydrogenation. Furthermore, taming of these effects was possible simply by modifying the extent of swelling of the polymer p-NIPAM brushes. These results open new opportunities to tailor the micro-solvation environment of catalysts in a dynamic manner by leveraging the conformational structure of polymers and highlight the complexity of stimulus-responsive nano-reactors.

2. Experimental section

2.1 Materials

Tetraethyl orthosilicate (TEOS, 98 %), ammonium hydroxide solution (NH_4OH, 25 % - NH_3 basis), Tetraamminepalladium(II) nitrate solution ($Pd(NH_3)_4(NO_3)_2$, 10 wt. % in H_2O, 99.99%), sodium hydroxide (NaOH, 99 %), (3-aminopropyl)triethoxysilane (APTES, 99%), triethylamine (Eth_3N, 99.5%), Bromoisobutyryl bromide (BIBB, 98%), copper(II) bromide ($CuBr_2$, 99%), 1,1,4,7,10,10-hexamethyltriethylenetetramine (HMTETA,97%), L-ascorbic acid (99%), methanol (99.9%), and ethanol (99.8%) were purchased from Sigma-Aldrich and used as received. N-isopropylacrylamide (NIPAM, Sigma-Aldrich, 97%) was purified by recrystallization in n-hexane (Sigma-Aldrich, 99.1 %) and stored below 4 °C prior to use. Tetrahydrofuran (THF, Sigma-Aldrich, 99.8%) was dried for at least one day over 4 Å molecular sieves (Honeywell) before use. All the aqueous solutions were prepared using ultra-purified water obtained from a water purification system (Millipore, Synergy).

2.2 Catalyst preparation

2.2.1 Synthesis of SiO_2 spheres and Pd/SiO_2 catalyst

The SiO_2 spheres and Pd/SiO_2 were synthesized following a method published before by our group.[9] In short, The SiO_2 spheres were prepared using the method reported by Stöber et al.[10] to get dense Silica spheres. After that, the Pd/SiO_2 catalyst was prepared using the strong

electrostatic adsorption (SEA) method to load Pd on the surface of obtained SiO_2 spheres.

2.2.2 Synthesis of Pd/SiO_2-NIPAM catalyst

P-NIPAM brush modified Pd/SiO_2 particles were synthesized via surface-initiated atom transfer radical polymerization (ATRP) method.[11] The synthesis was performed on bromine functionalized silica particles and carried out in a methanol/water solvent mixture (4:1 v/v) and reagents NIPAM/$CuBr_2$/HMTETA/ascorbic acid was used in the molar ratios 900/1.5/15/10, with the monomer to solvent mass ratio being 0.058/1. The comprehensive particle preparation and brush synthesis protocol with reaction scheme are available in supporting information Section 2.

2.3 Catalyst characterization

Brunauer–Emmett–Teller (BET) surface area analysis was conducted from the nitrogen adsorption isotherms at 77 K using a Micromeritics Model ASAP 2400 instrument. For each analysis, 0.2–0.3 g of sample was degassed at 120 °C for 24 h before measurement. The transmission electron microscopy (TEM) analysis results were obtained by using a Tecnai F30 field emission TEM, with an acceleration voltage of 300 kV, and coupled with a HAADF detector (Fischione). The Scanning Electron Microscopy (SEM) was conducted by using a JEOL, LA6010 with a resolution of 4 nm @ 20 kV. The metal loading of the Pd/SiO_2 samples was determined by X-ray fluorescence (XRF) (Bruker, S8 TIGER). The metal dispersion of the Pd/SiO_2 samples was determined by CO chemisorption at room temperature (Micromeritics, Chemisorb 2750). The samples were reduced in H_2 at room temperature for one hour and then flushed in He for 30 min. After that, CO was introduced as pulses and the response was recorded using a TCD detector. The thermal Gravimetric Analysis (TGA) (Mettler-Toledo, TGA/SDTA 851) was performed from 25 to 1000 °C at a ramp rate of 10 °C min^{-1} under a constant flow of argon at 30 mL min^{-1}.

2.4. Catalytic tests

Catalytic activity and selectivity of the catalyst were measured following our previous method. [9] In short, the reaction was conducted in a 1 L batch reactor and maintained by buffering continuously CO_2 (0.1 bar) to keep a pH value of 5.5.[9] In a standard experiment, 0.05 g catalyst were suspended in 0.3 L deionized (DI) water and stirred at 500 rpm under 0.8 bar

hydrogen (0.1 bar CO_2, 0.1 bar He) for at least one hour, removing dissolved oxygen and reducing the catalyst. After that, the hydrogen pressure was changed to the value of choice. The reaction was started by introducing 3 mL $NaNO_2$ solution (100 mM) into the glass reactor. Hydrogen pressure varied between 0.01 and 0.9 bar, and the nitrite concentration varied between 0.5 and 5 mM. During the catalytic test, samples were collected using a 5 mL syringe (BD Plastipak) and filtered using a syringe filter (PTFE 0.2 μm, Whatman) to remove catalyst particles. Nitrite and ammonium concentrations were measured using ion-chromatography (DIONEX, ICS 3000) equipped with an UltiMate autosampler. The reaction rate was determined based on the initial activity at low nitrobenzene conversion (<10%) to regress the instantaneous reaction rate at time zero.[9] The turnover frequency (TOF) was calculated as the reaction rate per surface atom of palladium as determined with XRF, CO chemisorption, and TEM measurements.

3. Results and discussion

3.1 Catalyst characterization

Figure 1a illustrates the growth of p-NIPAM brushes on Pd/SiO_2 catalysts leveraging surface hydroxyl moieties of the colloidal SiO_2 particles. This structure was confirmed independently using SEM and HR-TEM. From Figure 1b i-ii it is clear that SiO_2 particles produced via the Stobër process are nonporous and spherical solids with a narrow particle size distribution of c.a. 500 nm. TEM characterization of the parent Pd/SiO_2 and coated catalyst (Pd/SiO_2-p-NIPAM) revealed that the metal clusters were c.a. 2 nm (Figures 1c,1d). A slightly decrease in the metal cluster size was observed upon functionalization of Pd/SiO_2 with p-NIPAM polymers. This drop was attributed to particle detaching during the polymerization step. Further TEM-EDX images showed that the Pd particles were well dispersed on the Pd/SiO_2-p-NIPAM catalyst (Figure S2). Upon functionalization with the p-NIPAM polymeric brushes over 22 hours it was possible to achieve a polymer dry thickness of c.a. 7 nm (Figure 1d). These observations were in line with dynamic light scattering (DLS) measurements (Figure S3). The stimulus-responsive behavior of the polymer-coated catalyst (Pd/SiO_2-p-NIPAM) was confirmed by measuring the average hydrodynamic diameter of the particles at different temperatures (25 to 50 °C). At temperatures below 30 °C, the particle size remained stable at c.a. 640 nm. Increasing the temperature above 32 °C led to a rapid drop in the particle size to c.a. 510 nm, which would indicate that the film thickness of the polymer varies from 71.9 to 6.9 nm as temperature

increases from 25 to 50 °C. Notably, the thickness of the collapsed polymer (6.9 nm) was consistent with the polymer dry measurements obtained from TEM (Figure 1d-i).

The Pd metal loading and dispersion are summarized in Table 1. For the Pd/SiO_2 catalyst, the Pd metal loading was 0.17 wt. %, while the Pd dispersion was 55.5% based on CO chemisorption, corresponding to an average Pd particle size of 2 nm. This is in good agreement with the estimated Pd particle size obtained by TEM (2.1 nm). In the case of Pd/SiO_2-p-NIPAM, the mean Pd particle size was c.a. 1.9 nm (Figure 1d-ii**)**. Surprisingly, the Pd dispersion obtained from CO chemisorption indicated a much lower value (c.a. 19.9%). This difference could be associated to the partial blockage of the Pd surface by the polymer brushes. Similar observations were reported by Zhao et al.[12] when using polyvinyl alcohol (PVA) and polyvinylpyrrolidone (PVP) to cover Pd nanoparticles for nitrite reduction. To estimate the metal dispersion, we employed the mean particle size obtained from TEM. In this case, the mean size (d_{VA}) was determined as the volume-area mean diameter ($d_{VA} = \sum n_i d_i^3 / \sum n_i d_i^2$), where d_i and n_i denote the mean size and number of the particles belonging to i^{th} range of the histograms respectively. [13] Based on the mean Pd particle size of 1.9 nm (Figure 1d-ii), the Pd dispersion for the Pd/SiO_2-p-NIPAM catalyst was c.a. 57.5 % (see supporting information section 4).

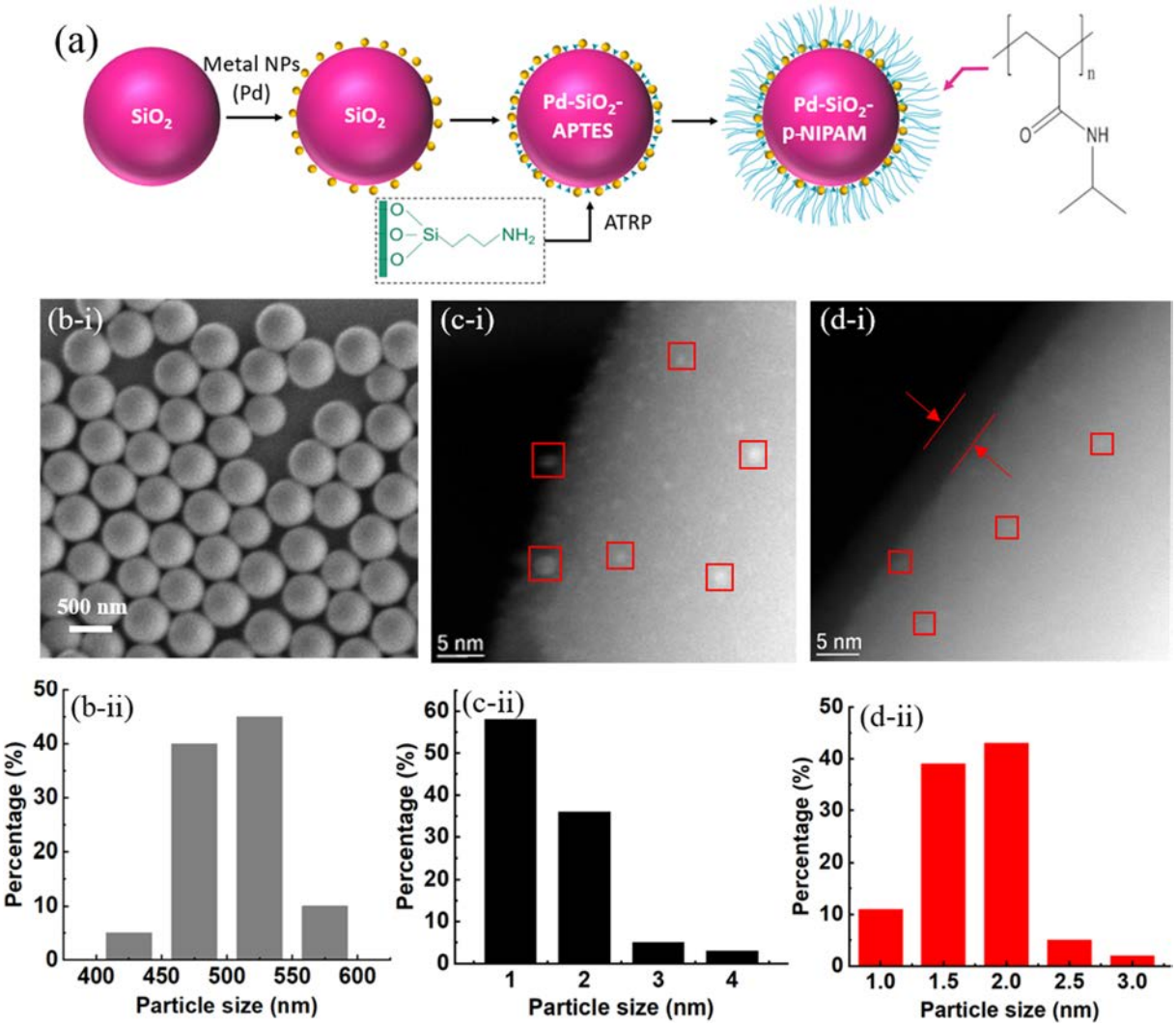

Figure 1. Synthesis strategy for the growth of p-NIPAM brushes on Pd-SiO_2 spheres (a), scanning electron microscopy (SEM) of SiO_2 spheres (b-i), high-resolution transmission electron microscopy (HR-TEM) of Pd/SiO_2 (c-i) and Pd/SiO_2-p-NIPAM (d-i) catalysts together with the particle size distribution of SiO_2 (b-ii) and Pd clusters for Pd/SiO_2 (c-ii) and Pd/SiO_2-p-NIPAM catalyst (d-ii).

Table 1. Characterization data of both parent catalyst (Pd/SiO_2), polymer coated (Pd/SiO_2-p-NIPAM), and support material (SiO_2).

Sample	SEM	XRF	CO-chemisorption	TEM		N_2 physisorption	
	Particle size (nm)	Pd loading (wt. %)	Pd dispersion (%)	Mean Pd particle size (nm)	Pd dispersion (%)	Specific surface area (m^2/g)	Theoretical specific surface area (m^2/g)
SiO_2	500	-	-	-	-	7.5	6.4
Pd/SiO_2	500	0.17	55.5	2.1	52.0	7.9	6.7
Pd/SiO_2-p-NIPAM	500	0.15	19.9	1.9	57.5	9.2	-

3.2. Catalytic performance of the p-NIPAM coated Pd/SiO_2 catalyst

The catalysts coated with a thermo-responsive polymer (p-NIPAM) are expected to perform differently when changing the temperature above and below the LCST. To study this effect, we conducted a detailed kinetic study on the reactant concentration and temperature using Pd/SiO_2 and Pd/SiO_2-p-NIPAM catalysts.

As shown in supporting information section 5, internal and external mass transfer effects have been excluded under the reaction conditions herein employed. First, we studied the impact of the polymer on the selectivity of the non-coated catalyst. Here, it was observed that, at the same conversion level (c.a. 10%), increasing temperature led to higher ammonium selectivity. This trend is in agreement with previous literature on reduction of nitrites using Pd catalyst.[14][15] Notably, in the presence of the polymer a significant enhancement in ammonia selectivity was observed (c.a. fourfold higher) regardless of the temperature employed (Figure 2). This suggests that the p-NIPAM polymer brushes promote NH_4^+ formation. These differences can be related to mass transfer limitations, particle size effects, and/or solvation effects. The detailed analysis of the potential causes is discussed in section 4.

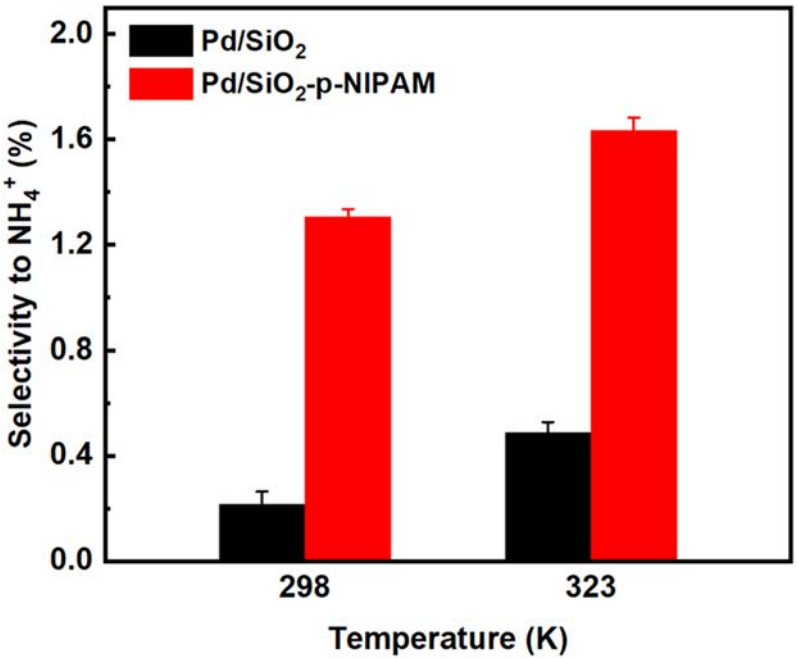

Figure 2. Influence of temperature on the selectivity to ammonium using Pd/SiO_2 and Pd/SiO_2-p-NIPAM catalyst at 10% conversion level.

3.4 Reaction order investigation

Rigorous reaction kinetics were conducted over a broad window of hydrogen and nitrites concentrations to reveal the interplay of surface coverages and reaction rates over the Pd/SiO_2 and polymer-coated Pd/SiO_2-p-NIPAM catalysts (Figure 3). For the reaction order investigation we employed two temperatures (25 °C and 50 °C) and in the case of NO_2^-, we assessed the effect of the partial pressure of hydrogen by measuring the reaction orders at 0.03 and 0.8 bar. The reaction order of nitrite on Pd/SiO_2 at high hydrogen partial pressures (0.8 bar) varied from 0.6 to 0 as the concentration increased. This trend was observed at low (25 °C) and high (50 °C) temperatures. For the Pd/SiO_2-p-NIPAM catalyst a different trend was observed when varying the temperature. At temperatures below the LCST (25 °C), first order kinetics were observed. In this case, increasing the concentration further led to saturation kinetics as indicated by the plateau of the TOF. Notably, at temperatures above the LCST, when the polymer becomes hydrophobic and collapses, there was no inflexion point and the reaction order was c.a. 0.3 across the concentration window herein explored.

Negative reaction orders of nitrite were observed on both catalysts when the reaction was conducted at a lower H_2 partial pressure (Figures 3e,3f). The negative reaction orders suggest that hydrogen and nitrite compete for the same active sites on both catalysts. Detailed inspection

of the data reveals that in the Pd/SiO_2-p-NIPAM catalyst nearly zero order dependence with nitrite concentration was observed with values of -0.2 and -0.1 at 25 and 50 °C, respectively. These higher reaction orders in the p-NIPAM coated catalysts can be attributed to weaker interaction of nitrite on palladium. The nature of the changes in the reaction orders with temperature is further addressed in section 4.

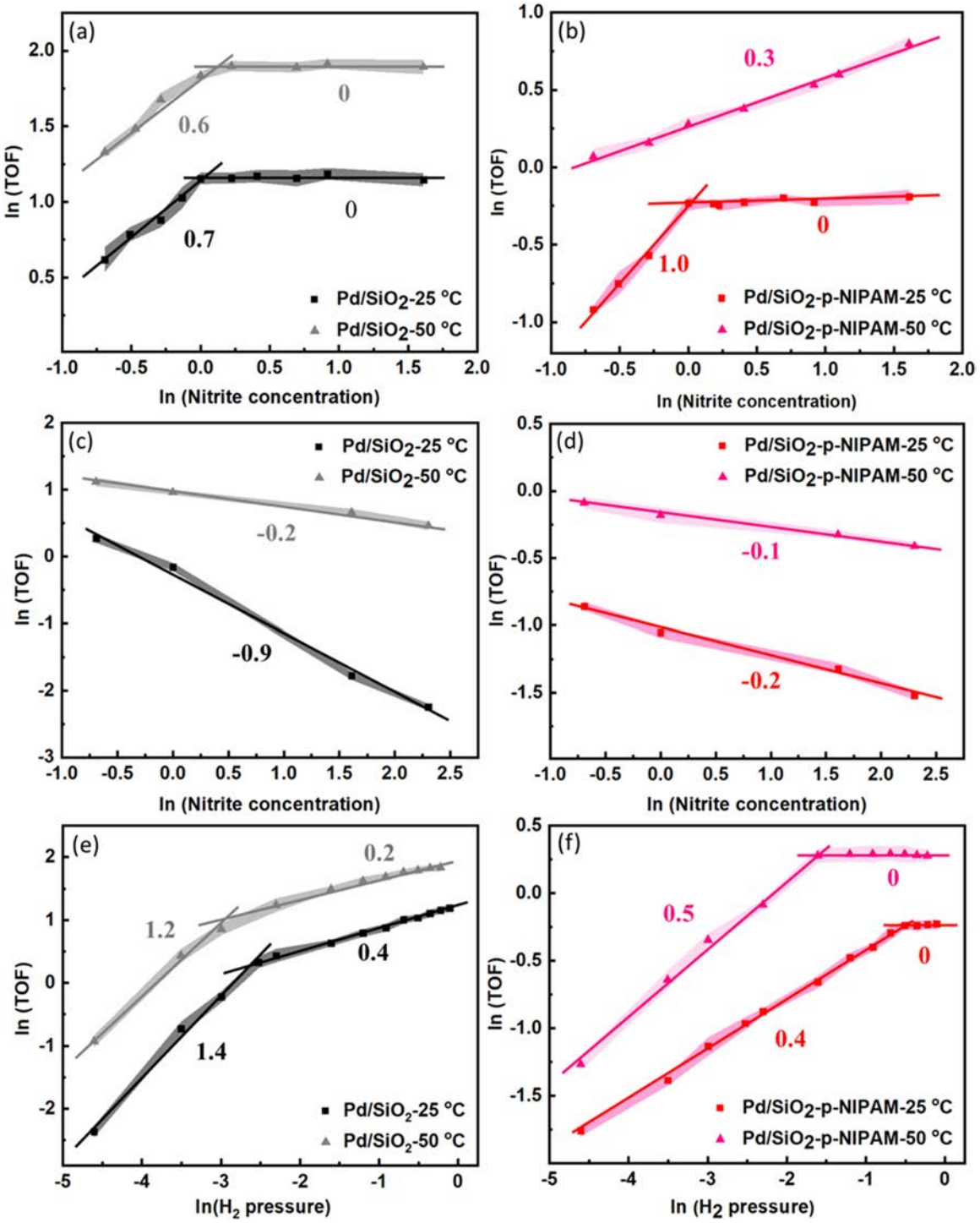

Figure 3. Effect of nitrite concentration on TOF at 0.8 bar H_2 (a-b) and 0.03 bar H_2 (c-d), and effect of hydrogen pressure on TOF at 1 mM nitrite concentration (e-f).

For the hydrogen order investigation, initially a positive reaction order of c.a. 1.4 and 1.2 was observed at low and high temperatures, respectively, when the H_2 pressure ranged from 0.01 to 0.1 bar on Pd/SiO_2. Increasing further the hydrogen partial pressure led to a reaction order of c.a. 0.5. These high H_2 orders on Pd/SiO_2 at low pressures are key. As explained in Chapter 2 these values suggest that there are two colimiting steps controlling the nitrite hydrogenation that include the sequential hydrogen insertion on NO* and HNO* surface species. The detailed derivations are shown in the section 6 of the supporting information. In sharp contrast, in the case of polymer-coated catalysts, the reaction rate showed a weaker dependence on the hydrogen surface coverage. In fact, at hydrogen pressures above 0.5 bar, the reaction order dropped from c.a. 0.5 to 0 at 25 °C. This data indicates that increasing the temperature above the LCST of p-NIPAM to 50 °C leads to an early onset of saturation kinetics, which suggests higher surface coverages of hydrogen. The summary of the reaction order investigation is shown in Table 2.

Table 2. Overview of the apparent reaction orders in hydrogen and nitrite in all ranges of the nitrite and hydrogen concentrations.

		Low H_2 pressure		High H_2 pressure		
		H_2 order	NB order	H_2 order	NB order (low con.)	NB order (high con.)
Pd/SiO_2	25 °C	1.4 ± 0.1	-0.9 ± 0.1	0.4 ± 0.1	0.7 ± 0.1	0 ± 0.1
	50 °C	1.2± 0.1	-0.2 ± 0.1	0.2 ± 0.1	0.6 ± 0.1	0 ± 0.1
Pd/SiO_2-p-NIPAM	25 °C	0.4 ± 0.1	-0.2 ± 0.1	0 ± 0.1	1.0 ± 0.1	0 ± 0.1
	50 °C	0.5± 0.1	-0.1 ± 0.1	0 ± 0.1	0.3 ± 0.1	0.3 ± 0.1

3.5. Apparent activation energy barriers

The activation energies of the reaction when using Pd/SiO_2 and Pd/SiO_2-p-NIPAM catalysts have been investigated at high and low concentrations of hydrogen in the range of 22 to 50 °C. For Pd/SiO_2 catalyst, a constant activation energy barrier was observed throughout the entire temperature range. As shown in Figure 4, when the reaction was conducted at low hydrogen pressure (0.03 bar) the apparent energy barrier was 36 ± 1 kJ mol^{-1}. This value is slightly higher than those reported in the literature (26,31 kJ mol^{-1}).[14][15] Here, one should consider that this energy barrier was obtained at low hydrogen pressure, while the values in the literature were obtained at a higher hydrogen partial pressures (e.g. 0.32 bar). In fact, we observed that when the reaction was conducted at 0.6 bar (Figure S4a) the activation energy barrier decreased to 29 ± 1 kJ mol^{-1}, highlighting the importance of surface coverage on the apparent barriers for this reaction.

Strikingly, the polymer-coated catalyst showed two distinct activation energies as temperature increased (Figure 4b). Essentially, when the reaction was conducted at temperatures below the LCST of p-NIPAM (swollen state) a low apparent activation barrier of 11 kJ mol^{-1} was observed. Increasing the temperature above the LCST (collapse state) led to a higher apparent barrier (c.a. 32 kJ mol^{-1}). The lower activation energy barriers obtained when the polymer was in the swollen state may be caused by changes in the mass transfer rates, particle size effects, and/or solvation effects. These effects will be discussed in more detailed in section 4.

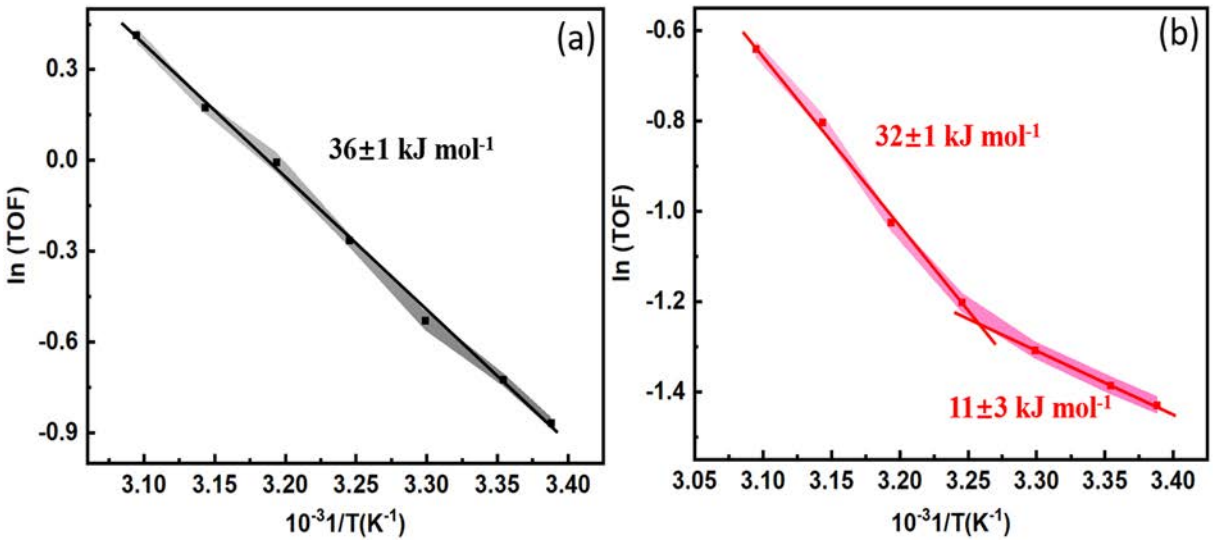

Figure 4. Arrhenius plots for the nitrite hydrogenation reaction using (a) Pd/SiO_2 (b) Pd/SiO_2-p-NIPAM at 0.03bar hydrogen pressure and 1 mM nitrite concentration.

4. Discussion

The detailed reaction kinetics indicated that the polymer coating on the Pd/SiO_2 catalyst increased fourfold the selectivity to NH_4^+. At the same time, higher reaction orders in nitrite suggest weaker binding and thus lower coverages, while the opposite trend was observed for hydrogen. These changes in apparent reaction orders were accompanied by a two distinct apparent barriers above and below the LCST of the p-NIPAM. Here, lower activation energies where observed a low temperature. To rationalize these observations we will discuss in the next section the potential interplay of (1) metal particle size, (2) mass transport, and (3) polymer induced micro-solvation effects with the catalyst activity and selectivity.

4.1. Metal particle size effects

During the synthesis of the Pd/SiO_2-p-NIPAM catalyst, the Pd loading decreased from 0.17% to 0.15%. This may be caused by the loss of large Pd particles (> 2nm) on the Pd/SiO_2 surface during the polymerization. The changes in Pd average particle size from 3 to 2 nm (Figure 1) could lead to changes in the NH_4^+ selectivity. The relationship between particle size and catalyst selectivity for this reaction is, however, in debate as contradictory results have been reported in the past. For instance, Yoshinaga et al.[16] and Zhao et al.[17] found that NH_4^+ formation is promoted when increasing the palladium particle within the range of 2 to 3 nm. In sharp contrast, D. Shuai et al.[18] found that the selectivity to NH_4^+ decreases by 8 fold when increasing Pd nanoparticle size from 1.4 to 9.6 nm. In this work, however, the polymer coated Pd/SiO_2-p-NIPAM catalyst shows fourfold enhancement of the NH_4^+ selectivity for a rather small change in the Pd particle from 3 to 2 nm. In this context, it is difficult to rationalize this drastic change in selectivity to such a small variation in the cluster size of Pd.

4.2. Mass transport effects

Nitrite hydrogenation is highly sensitive to the surface coverage of the reactant (e.g. H_2, NO_2^-, H^+).[19][20][21] For instance, a recent study from P. Xu et al. [22] indicates that when using a 20 % hydrophobic Al_2O_3 support, the transport of hydrogen can be enhanced, leading to a higher ammonia selectivity and higher catalytic activity. Similarly, J. K. Chinthaginjala et al. [23] reported that when using Pd supported on carbon nanofibers (Pd/CNF) the selectivity to ammonia increased significantly due to the improved mass transfer of H_2 in the catalyst support

as compared to nitrite diffusion inside the catalyst. While it is tempting to assign the higher selectivity to NH_4^+ on the polymer coated catalyst to faster H_2 mass transfer rates, the Weisz-Prater calculations and the fractional reaction orders of hydrogen suggest that mass transport limitations cannot be limiting the reaction rate or the selectivity.

In the same line, the low apparent barriers obtained using the Pd/SiO_2-p-NIPAM catalyst when the temperature is below the (Figure 4) are difficult to rationalize in terms of mass transport effects. Broadly speaking, when mass transport limitation start to control the reaction kinetics, the apparent barriers decrease by a factor of two as the diffusion processes have activation barriers that are substantially lower than those of the catalytic reactions.[24] In the results herein presented, however, we see the opposite trend (i.e. lower barriers and lower temperatures). Further confirmation of the absence of any mass transfer limitations can be extracted from the apparent reaction orders. If the concentration gradients were dominating the measured kinetics, then the observed reaction orders for hydrogen and nitrites should be equal to one as molecular diffusion is a first-order process. The reaction order investigation, however, presented in Figure 3 indicated that this is not case. Hence, the effect of mass transfer limitations on the observed trend can be neglected.

4.3 Solvation effects

The solvation effects were calculated based the transition state theory treatments as proposed by D. Flaherty et al.[25] In this case, we leverage the kinetic observations and the detailed reaction kinetics previously developed in Chapter 2 to derive the rate expression for this reaction. The detailed derivation is shown in the supporting information section 7.

$$\frac{r}{L} = \frac{k_b T}{h} \exp\left(\frac{\Delta S_{App}^{0,\ddagger} + \Delta S_{App}^{\varepsilon,\ddagger}}{R}\right) \exp\left(-\frac{\Delta H_{App}^{0,\ddagger} + \Delta H_{App}^{\varepsilon,\ddagger}}{RT}\right) [\mathrm{H_2}]^{2.5} [\mathrm{C_6H_5NO_2}]^{-1} \quad (2)$$

Here, L is the total number of active sites, r/L= TOF, k_b is the Boltzmann constant, h is the Planck constant, T is thermodynamic temperature, $\Delta S_{App}^{0,\ddagger}$ and $\Delta H_{App}^{0,\ddagger}$ are the enthalpy and entropy of the transition state in the reference state. To estimate the excess entropy and enthalpy of activation, the reference state was assumed to be that of the parent catalyst (Pd/SiO_2). Then, the excess quantities were estimated using the results obtained for the polymer coated catalyst (Figure S10a). The assumption of this equation is that polymer coating on the Pd/SiO_2-p-NIPAM catalyst provides excess $\Delta S_{App}^{\varepsilon,\ddagger}$ and $\Delta H_{App}^{\varepsilon,\ddagger}$ for the reaction. As a result, in the polymer

coated catalyst, the quantities $\Delta S^{\ddagger}_{app} = \Delta S^{0,\ddagger}_{App} + \Delta S^{\varepsilon,\ddagger}_{App}$ and $\Delta H^{\ddagger}_{app} = \Delta H^{0,\ddagger}_{App} + \Delta H^{\varepsilon,\ddagger}_{App}$ are calculated from the transition state theory reaction rate vs temperature plot (Figure S10b). The calculated entropy and enthalpy and excess free energy are shown in Table 3.

Table 3. Enthalpy and entropy of activation for the Pd/SiO_2 and Pd/SiO_2-p-NIPAM catalysts and excess enthalpy and entropy estimated for the polymer coated catalyst.

Temperature (°C)	Pd/SiO_2		Pd/SiO_2-p-NIPAM		Excess	
	$\Delta S^{0,\ddagger}_{App}$ (J/mol*K^{-1})	$\Delta H^{0,\ddagger}_{App}$ (kJ mol^{-1})	$\Delta S^{p-NIPAM,\ddagger}_{App}$ (J/mol*K^{-1})	$\Delta H^{P-NIPAM,\ddagger}_{App}$ (kJ mol^{-1})	$\Delta S^{\varepsilon,\ddagger}_{App}$ (J/mol*K^{-1})	$\Delta H^{\varepsilon,\ddagger}_{App}$ (kJ mol^{-1})
22-32	-34.8	36.4	-124.2	11.4	-89.4	-25.0
32-50			-58.4	31.6	-23.6	-4.8

This analysis reveals that when the reaction is conducted at low temperatures (22-32 °C), i.e. below the LCST of p-NIPAM, there is an enthalpic enhancement of the reaction rate. Essentially, the enthalpy of activation for the transition state decreases by c.a. 25 kJ mol^{-1} on the Pd/SiO_2-p-NIPAM .This stabilization, however, comes at the expense of losing degrees of freedom in the system that causes a drop in the entropy of activation (Table 3). Here, one could imagine that when the polymer is present, the arrangement and mobility of the water molecules surrounding the chemisorbed species is modified, leading to the observed weaker interaction of nitrites and stronger binding of hydrogen. Since, we know from Chapter 2 that water plays a key role in this reaction by facilitating the reduction via proton-electron transfer, it is possible that these small changes in the water structuring near the surface of the catalyst induce the decrease in the apparent barriers, with the concomitant reduction in the mobility due to the polymer-water interaction. We currently are conducting ab-initio molecular dynamics to unravel the exact nature of these changes in the apparent enthalpy and entropy of activation of the transition state.

5. Conclusion

We developed a temperature-sensitive polymer-coated catalyst that contains metallic palladium nanoparticles as active sites. We have shown that the polymer-induced micro-solvation environments can influence the Gibbs free energy of a reaction. In contrast to conventional Pd/SiO_2, the p-NIPAM coated catalyst displayed two distinct apparent activation barriers. At temperatures below the LCST, low activation energy barriers were obtained. Increasing the temperature, however, led to activation barriers similar to those observed on the conventional catalyst. These changes in the apparent barriers were followed by a weaker interaction of nitrite and stronger binding of hydrogen that led to higher ammonia selectivity. Transition state treatments of the reaction rate suggested that this enhancement was primarily driven by enthalpic stabilization induced by the polymer. This stabilization, however, led to a decrease in the entropic contribution to the transition state. This drop was attributed to the losses in the degrees of freedom of the chemisorbed species in the presence of the polymer. This interaction is believed to be related to the strong hydrogen bonding of the p-NIPAM at temperatures below the LCST. Upon collapsing at temperatures above the LCST the polymer-water interactions are disrupted and the structure of the water molecules near the active sites returns to its original configuration. We anticipate that these results will pave the way for developing more precise and scalable thermos-responsive polymers for the production of sustainable fuels and chemicals.

References

[1] J. Zhang, M. Zhang, K. Tang, F. Verpoort, T. Sun, Polymer-based stimuli-responsive recyclable catalytic systems for organic synthesis, Small. 10 (2014) 32–46. https://doi.org/10.1002/smll.201300287.

[2] P. Hervés, M. Pérez-Lorenzo, L.M. Liz-Marzán, J. Dzubiella, Y. Lub, M. Ballauff, Catalysis by metallic nanoparticles in aqueous solution: Model reactions, Chem. Soc. Rev. 41 (2012) 5577–5587. https://doi.org/10.1039/c2cs35029g.

[3] S. Angioletti-Uberti, Y. Lu, M. Ballauff, J. Dzubiella, Theory of Solvation-Controlled Reactions in Stimuli-Responsive Nanoreactors, J. Phys. Chem. C. 119 (2015) 15723–15730. https://doi.org/10.1021/acs.jpcc.5b03830.

[4] R. Roa, W.K. Kim, M. Kanduč, J. Dzubiella, S. Angioletti-Uberti, Catalyzed Bimolecular Reactions in Responsive Nanoreactors, ACS Catal. 7 (2017) 5604–5611. https://doi.org/10.1021/acscatal.7b01701.

[5] S. Wu, J. Dzubiella, J. Kaiser, M. Drechsler, X. Guo, M. Ballauff, Y. Lu, Thermosensitive Au-PNIPA yolk-shell nanoparticles with tunable selectivity for catalysis, Angew. Chemie - Int. Ed. 51 (2012) 2229–2233. https://doi.org/10.1002/anie.201106515.

[6] S. Carregal-Romero, N.J. Buurma, J. Pérez-Juste, L.M. Liz-Marzán, P. Hervés, Catalysis by Au@pNIPAM nanocomposites: Effect of the cross-linking density, Chem. Mater. 22 (2010) 3051–3059. https://doi.org/10.1021/cm903261b.

[7] M.J. Enes da Silva, A. Banerjee, L. Lefferts, J.A.F. Albanese, In-situ ATR-IR Spectroscopy Reveals Complex Absorption-Diffusion Dynamics in Model Polymer-Membrane-Catalyst Assemblies (PCMA), ChemCatChem. (2022). https://doi.org/10.1002/cctc.202101835.

[8] M.J.E. da Silva, L. Lefferts, J.A. Faria Albanese, N-isopropylacrylamide polymer brushes alter the micro-solvation environment during aqueous nitrite hydrogenation on Pd/Al2O3 catalyst, J. Catal. 402 (2021) 114–124. https://doi.org/10.1016/j.jcat.2021.08.003.

[9] P. Huang, Y. Yan, A. Banerjee, L. Lefferts, B. Wang, J.A.F. Albanese, Proton Shuttling Flattens the Energy Landscape of Nitrite Catalytic Reduction, J. Catal. (2022).

[10] W. Stöber, A. Fink, E. Bohn, Controlled growth of monodisperse silica spheres in the micron size range, J. Colloid Interface Sci. 26 (1968) 62–69.

[11] K. Matyjaszewski, D. Hongchen, W. Jakubowski, J. Pietrasik, A. Kusumo, Grafting from surfaces for "everyone": ARGET ATRP in the presence of air, Langmuir. 23 (2007) 4528–4531. https://doi.org/10.1021/la063402e.

[12] Y. Zhao, J.A. Baeza, N.K. Rao, L. Calvo, M.A. Gilarranz, Y.D. Li, L. Lefferts, Unsupported PVA-and PVP-stabilized Pd nanoparticles as catalyst for nitrite hydrogenation in aqueous phase, J. Catal. 318 (2014) 162–169.

[13] G. Bergeret, P. Gallezot, Particle size and dispersion measurements, Handb. Heterog. Catal. 2 (2008) 439.

[14] V. Höller, K. Rådevik, I. Yuranov, L. Kiwi-Minsker, A. Renken, Reduction of nitrite-ions in water over Pd-supported on structured fibrous materials, Appl. Catal. B Environ. 32 (2001) 143–150. https://doi.org/10.1016/S0926-3373(01)00139-4.

[15] A. Pintar, G. Berčič, J. Levec, Catalytic liquid-phase nitrite reduction: Kinetics and catalyst deactivation, AIChE J. 44 (1998) 2280–2292.

[16] Y. Yoshinaga, T. Akita, I. Mikami, T. Okuhara, Hydrogenation of nitrate in water to nitrogen over Pd–Cu supported on active carbon, J. Catal. 207 (2002) 37–45.

[17] Y. Takeuchi, Sagittal plane spinal mobility is associated with dynamic balance ability of community-dwelling elderly people, J. Phys. Ther. Sci. 29 (2017) 112–114. https://doi.org/10.1589/jpts.29.112.

[18] D. Shuai, J.K. Choe, J.R. Shapley, C.J. Werth, Enhanced activity and selectivity of carbon nanofiber supported Pd catalysts for nitrite reduction, Environ. Sci. Technol. 46 (2012) 2847–2855. https://doi.org/10.1021/es203200d.

[19] C.A. Clark, C.P. Reddy, H. Xu, K.N. Heck, G. Luo, T.P. Senftle, M.S. Wong, Mechanistic insights into pH-controlled nitrite reduction to ammonia and hydrazine over rhodium, ACS Catal. 10 (2019) 494–509.

[20] P. Xu, S. Agarwal, L. Lefferts, Mechanism of nitrite hydrogenation over Pd/γ-Al2O3 according a rigorous kinetic study, J. Catal. 383 (2020) 124–134.

[21] S.D. Ebbesen, B.L. Mojet, L. Lefferts, Effect of pH on the Nitrite Hydrogenation Mechanism over Pd/Al2O3 and Pt/Al2O3: Details Obtained with ATR-IR Spectroscopy, J. Phys. Chem. C. (2011) 1186–1194. https://doi.org/10.1021/jp106521t.

[22] P. Xu, S. Agarwal, J.F. Albanese, L. Lefferts, Enhanced transport in Gas-Liquid-Solid catalytic reaction by structured wetting properties: nitrite hydrogenation, Chem. Eng. Process. Intensif. 148 (2020) 107802.

[23] J.K. Chinthaginjala, L. Lefferts, Support effect on selectivity of nitrite reduction in water, Appl. Catal. B Environ. 101 (2010) 144–149.

https://doi.org/10.1016/j.apcatb.2010.09.023.

[24] U. Hanefeld, L. Lefferts, Catalysis: an integrated textbook for students, John Wiley & Sons, 2018.

[25] D.S. Potts, D.T. Bregante, J.S. Adams, C. Torres, D.W. Flaherty, Influence of solvent structure and hydrogen bonding on catalysis at solid–liquid interfaces, Chem. Soc. Rev. 50 (2021) 12308–12337. https://doi.org/10.1039/d1cs00539a.

Supporting information

1. Characterization

1.1 Zeta potential curves of synthesized SiO_2 particles

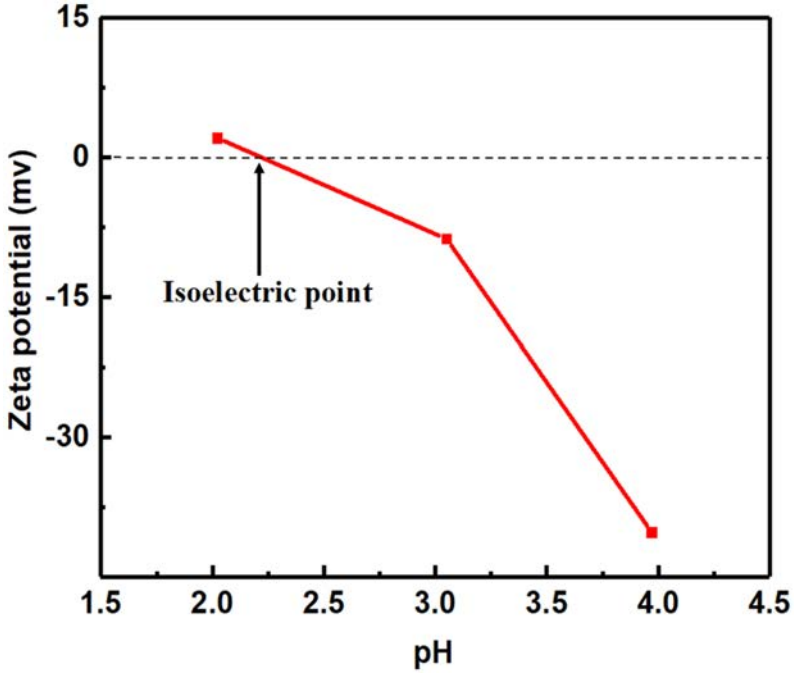

Figure S1. Zeta potential curves of synthesized SiO_2 particles.

1.2 TEM-EDX images of the synthesized Pd/SiO_2-p-NIPAM catalyst.

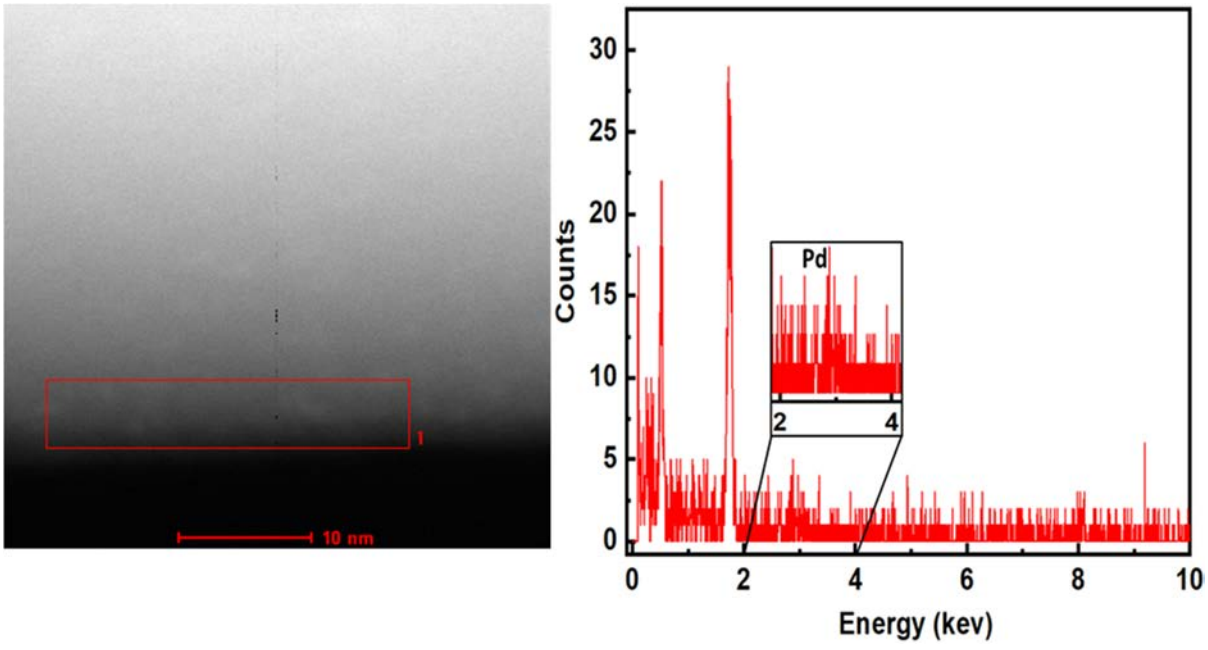

Figure S2. TEM-EDX image of Pd/SiO_2-p-NIPAM catalyst.

1.3 Dynamic light scattering measurement of the Pd/SiO_2-p-NIPAM catalyst

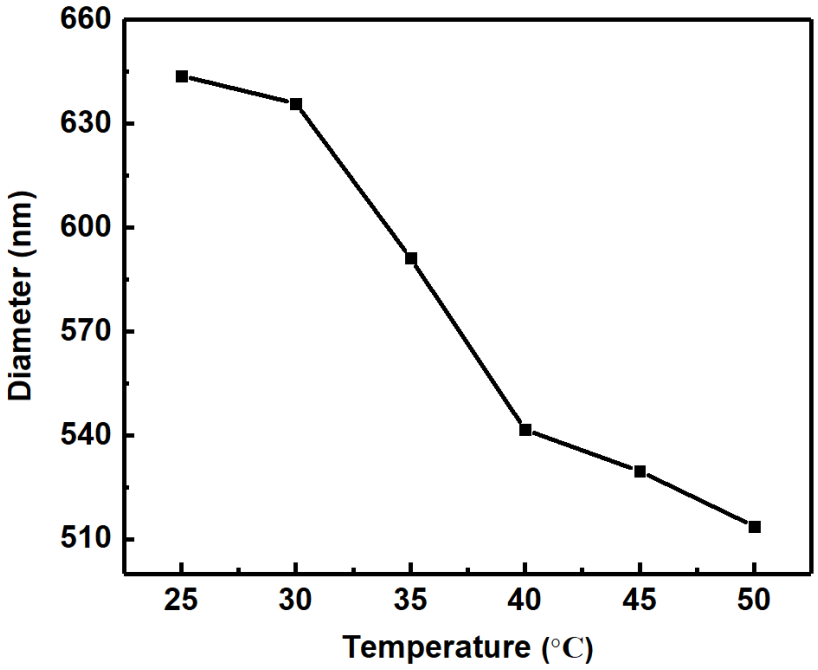

Figure S3. Dynamic light scattering measurement of the Pd/SiO_2-p-NIPAM catalyst.

2. Synthesis of Pd/SiO_2-p-NIPAM catalyst

2.1. Surface functionalization of Pd/SiO_2 catalyst

APTES was used to functionalize the surface of the Pd/SiO_2 catalyst with amino groups that can react with the initiator. The procedure to link these amino groups can be summarized as follows. Firstly, the pH of 200 mL water was adjusted to 10 by adding drops of NaOH 0.1 M and then, 5.0 g of Pd/SiO_2 catalyst were dispersed in this water via sonication during 30 min to deprotonate the hydroxyl groups of the surface. After that, the Pd/SiO_2 catalyst was rinsed with water twice followed by ethanol twice. Then the sample were dried in a vacuum oven at 40 °C overnight. Next, the Pd/SiO_2 powder were re-dispersed in 100 mL of ethanol via sonication during 20 min and the dispersion was put inside of a three-neck flask and submerged in a water bath at 40 °C and 2.0 g of APTES were added to the dispersion. After that, the flask was sealed with two Suba Seal and the reaction was allowed to proceed for 3 h at 40 °C under continuous stirring (200 rpm). Finally, the functionalized Pd/SiO_2 catalyst was rinsed with ethanol followed by anhydrous THF.

2.2 Initiation step

The APTES functionalized Pd/SiO_2 particles were re-dispersed in 20 mL of THF in a conical flask sealed with a Suba Seal. After that, 2.5 mL of BIBB (initiator of the polymerization) and 3.3 mL of Et_3N (catalyst of the reaction between BIBB and the amino groups) were added simultaneously through the Suba Seal septum with syringes. The reaction was allowed to proceed for 30 min at room temperature under vigorous stirring (900 rpm) due to the high viscosity of the mixture. After that, the Pd/SiO_2 particles were rinsed with THF, followed by ethanol twice, water twice and methanol twice. Finally, the particles were left dispersed in 50 mL of a methanol/water (4:1 v/v) solvent ready for the next step.

2.3 Polymerization step

Firstly, two dispersions were prepared in separated conical flasks. One of them (dispersion I) contained 0.016 g of $CuBr_2$ (catalyst of the polymerization) and 0.163 g of HMTETA (ligand of the catalyst) were dispersed in 50 mL of a methanol/water (4:1 v/v) solvent. The other (dispersion II) was prepared by adding 4.8 g of NIPAM to the Pd/SiO_2 dispersion obtained at the end of the initiation step. After that, the conical flasks were sealed with a Suba Seal and both dispersions were purged with N_2 during 15 min. Then, 0.083 g of ascorbic acid were added to the dispersion I to reduce the catalyst and both dispersions were purged with N_2 for a further 15 min. Next, the contents of the first flask (dispersion I) were quickly transferred to the second flask (dispersion II) with a syringe to start the polymerization.

The reaction was conducted at room temperature under continuous stirring (200 rpm). To obtain the samples, 10 mL of the reaction medium were removed and diluted with 24 mL of a chilled methanol/water (4:1 v/v) solvent to quench the reaction. The Pd/SiO_2-p-NIPAM samples were rinsed with water twice and dispersed in water for storage.

3. Nitrite hydrogenation reaction

3.1 Arrhenius plot of the two catalyst

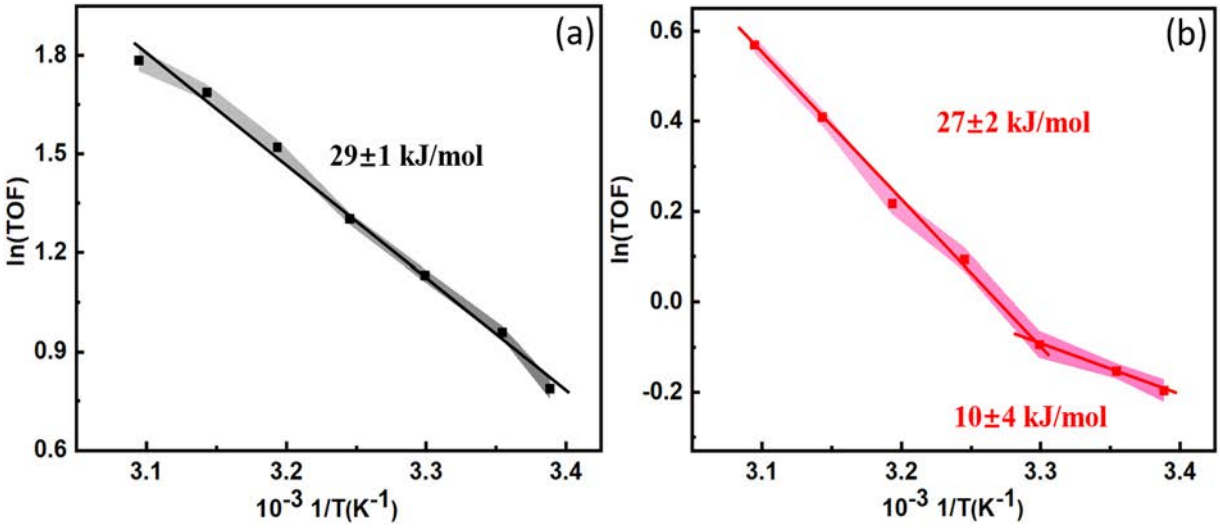

Figure S4. Arrhenius plot of the nitrite hydrogenation using (a) Pd/SiO_2 (b) Pd/SiO_2-p-NIPAM at 0.6 bar hydrogen pressure.

4. Calculation of the Pd dispersion from TEM

For the polymer coated Pd/SiO_2-p-NIPAM catalyst, CO chemisorption can't probe the accurate Pd dispersion as the polymer coating can cover the metal surface when the sample measured in a dry state. Hence, Pd dispersion is being calculated from TEM. The Pd dispersion was defined as:

$$D = \frac{N_S}{N_T} \qquad \text{(S1)}$$

N_S is the total number of metal atoms present on the surface and N_T is the total number of metal atoms (surface and bulk).

The specific surface area (S_{sp}) can be calculated using the following equation:

$$S_{sp} = \frac{\sum n_i A_i}{\rho \sum n_i V_i} \qquad \text{(S2)}$$

Since $A_i = \pi d_i^2$ and $V_i = \pi d_i^3/6$, S_{sp} is given by

$$S_{sp} = \frac{6\sum n_i d_i^2}{\rho \sum n_i d_i^3} \qquad \text{(S3)}$$

The mean particle size (d_{VA}) is defined as the volume-area mean diameter.

$$d_{VA} = \sum n_i d_i^3 / \sum n_i d_i^2 \qquad \text{(S4)}$$

According to the Pd particle size distribution show in Figure 1d-ii, the calculated $d_{VA} = 1.9\ nm$

$$S_{sp} = \frac{6}{\rho * d_{VA}} \quad \text{(S5)}$$

$$d_{VA} = \frac{6}{\rho * S_{sp}} = 6\frac{\sum n_i V_i}{\sum n_i A_i} = 6\frac{V_m N_T}{a_m N_S} \quad \text{(S6)}$$

Since $N_S/N_T = D$. Here, the Pd particle are on the catalyst surface, the assumption is half of the Pd on the surface are available for the reaction.

$$D = 6\frac{V_m/a_m}{d_{va}} \quad \text{(S7)}$$

Where v_m is the volume of a Pd atom in bulk palladium (14.70 $Å^3$) and a_m is the surface area occupied by an atom m on a polycrystalline surface (7.93 $Å^2$). These value can be obtained from the literature that when assume the proportions of low index planes: fcc (111) : (100) : (110) = 1 : 1 : 1.[1]

When substitute the value of v_m , a_m and d_{VA} to equation S7, the calculated Pd dispersion is 57.5%

For the Pd/SiO_2 catalyst, the mean particle size can be calculated according to equation S8, the mean particle size is 2.1 nm, which is very close the mean particle size of 2 nm from CO-chemisorption, and the calculated dispersion is 52.0%. which is close to the dispersion of 55.5% from CO chemisorption (Table 1). The 3% difference of the Pd dispersion between co chemisorption and TEM may be due to the insufficient resolution of the TEM measurement (e.g. undetectable particles in TEM).

5. Mass transfer

5.1 Internal mass transfer

5.1.1 Weisz-Prater criterion

Weisz-Prater criterion is normally used as the criteria to estimate whether pore diffusion resistance can significantly influence the reaction rate.[2]

$$C_{wp} = \frac{R_{obv} \times L^2 \times \rho_{Cat}}{C_s \times D_{eff}} \quad \text{(S8)}$$

Where R_{obv} is the reaction rate per mass of catalyst (mol*s^{-1}*kg^{-1}), L is characteristic length of a catalyst(m), ρ_{Cat} is the density of the catalyst particles (kg*m^{-3}), C_s is the reactant concentration at the particle surface (mol*m^{-3}), and D_{eff} is the effective diffusivity (m^2*s^{-1}).

$$L = d_p \quad \text{(S9)}$$

$$D_{eff} = \frac{D_{AB} \times \phi}{\tau} \quad \text{(S10)}$$

In which d_p is radius of the catalyst particles, D_{AB} is the molecular diffusivity of nitrite($1.91*10^{-5}$ cm^2/s) [3], ϕ is the particle porosity, normally between 0.2 and 0.7, and τ is the tortuosity, normally varies between 1 and 10.

If there is no obvious diffusion limitations: $C_{wp} < 1$

However, if there is severe diffusion limitations: $C_{wp} > 1$

According to the BET result and corresponding theoretical calculations, the silica support don't have any porous, so there is no need to consider the mass transfer limitation inside the SiO_2 support, only need to consider the internal mass transfer limitation caused by the external polymer coating.

(1) In order to prove that the calculated C_{wp} result is far less than 1, here we take the value to maximize the value. For ϕ,here we choose 0.2, for τ, here we choose 10 and the polymer density is 1.07 g/cm^3.[4]

$$D_{eff} = \frac{D_{AB}\times\phi}{\tau} = \frac{1.91*10^{-5}*10^{-4}\times 0.2}{10} = 3.82*10^{-11} \quad \text{(S11)}$$

$$C_{wp} = \frac{R_{obv}\times L^2\times \rho_{Cat}}{Cs\times Deff} = \frac{3.89*10^{-4}\times L^2\times 1.07*10^3}{1\times 3.82*10^{-11}} \quad \text{(S12)}$$

$$= 1.09*10^{10}\times L^2$$

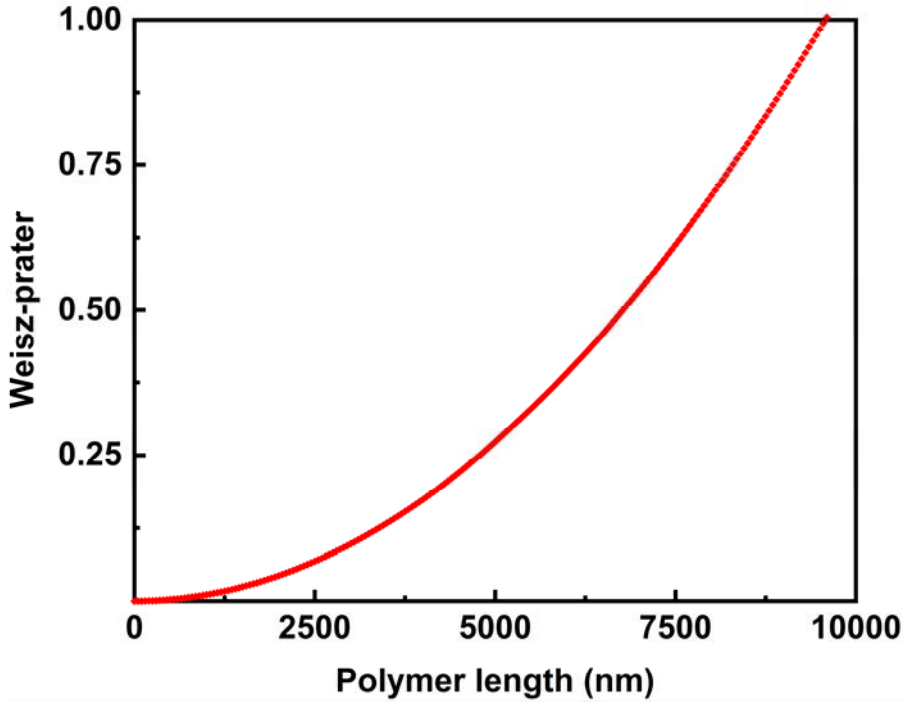

Figure S5. Weisz-Prater plot with different polymer length.

From the DLS result, the polymer length is from 6.9-71.9 nm. So the calculated C_{wp} is far away from 1.

(2) In order to investigate the relation between Weisz-Prater and tortuosity τ, here we take the value to maximize the value. For ϕ,here we choose 0.2, For polymer length, here we choose 71.9 nm.

$$D_{eff} = \frac{D_{AB}\times\phi}{\tau} = \frac{1.91 * 10^{-5} * 10^{-4} \times 0.2}{\tau} = \frac{3.82 * 10^{-10}}{\tau} \quad \text{(S13)}$$

$$C_{wp} = \frac{3.89*10^{-4} * (7.19*10^{-8})^{2} * 1.07 * 10^{3} \tau}{1*3.82*10^{-10}} = 5.63*10^{-6}\,\tau \quad \text{(S14)}$$

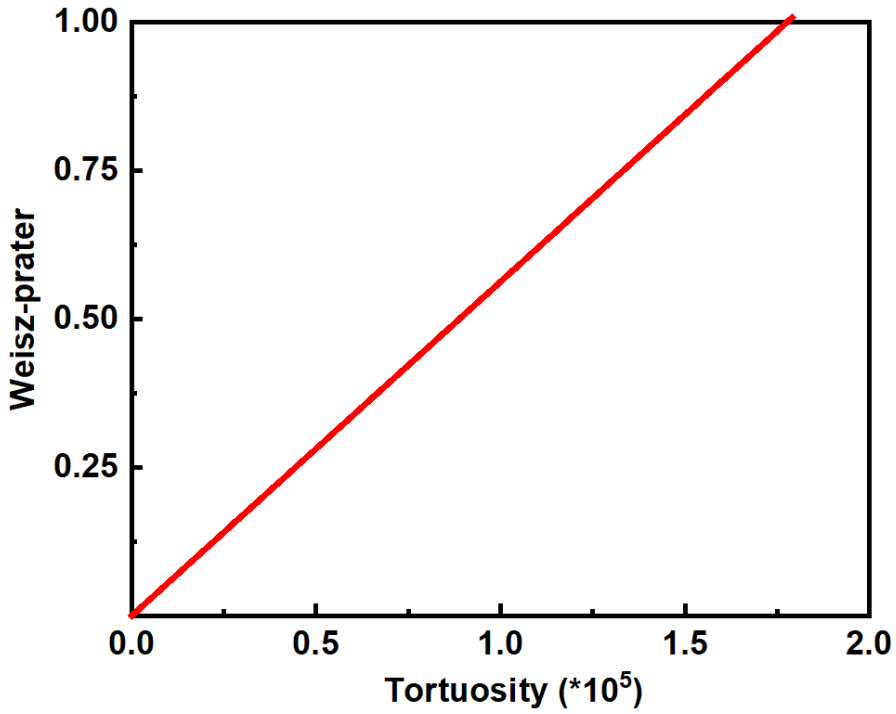

Figure S6. Weisz-Prater plot with different tortuosity τ.

Figure S6 shows the Weisz-Prater plot with different tortuosity τ. When the Weisz-Prater equal to 1.the τ equals to $1.78*10^5$, which is far away from the normal value that varies between 1 and 10.

(3) In order to investigate the relation between Weisz-Prater and diffusion coefficient D_{AB}, here we take the value to maximize the value. For ϕ, here we choose 0.2, for τ, here we choose 10.

$$D_{eff} = \frac{D_{AB} \times \phi}{\tau} = \frac{D_{AB} * 10^{-4} \times 0.2}{10} = 2 * 10^{-6} D_{AB} \quad \text{(S15)}$$

$$C_{wp} = \frac{3.89*10^{-4} * \left(7.19*10^{-8}\right)^2 * 1.07*10^3}{2*10^{-6} D_{AB}} = \frac{1.07*10^{-9}}{D_{AB}} = \quad \text{(S16)}$$

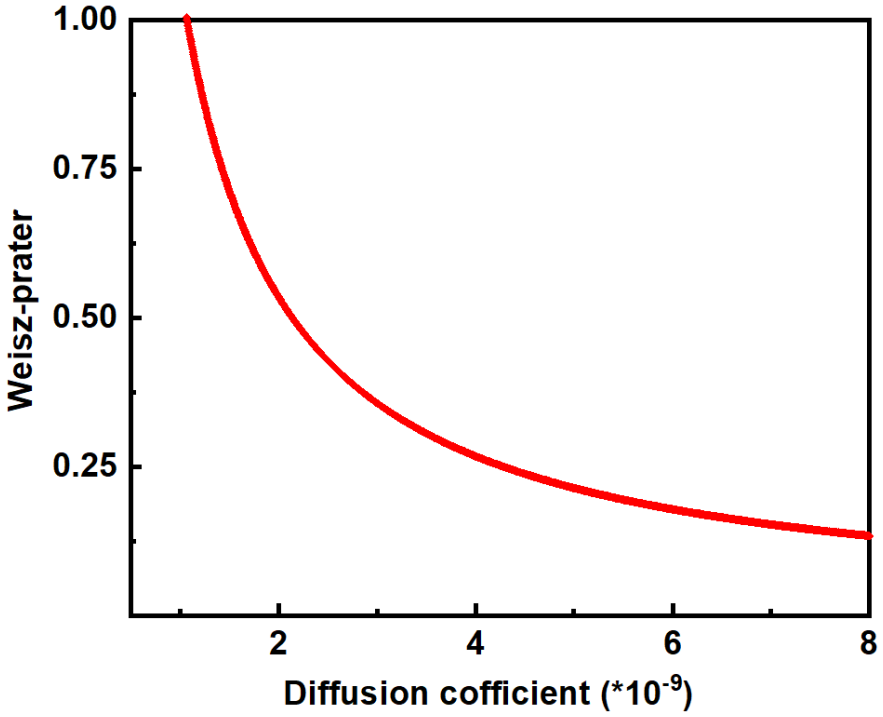

Figure S7. Weisz-Prater plot with diffusion coefficient D_{AB}.

Figure S7 shows the Weisz-Prater plot with diffusion coefficient D_{AB}. When the Weisz-Prater equals to 1, the D_{AB} equals to $1.07*10^{-9}$ cm^2/s, which is far away from diffusion coefficient in water $1.91*10^{-5}$ cm^2/s. also far away from the diffusion coefficient in p-NIPAM hydrogels $1.06*10^{-5}$ cm^2/s.[5]

(4) In order to investigate the relation between Weisz-Prater and particle porosity ϕ, here we take the value to maximize the value. For τ, here we choose 10.

$$D_{eff} = \frac{D_{AB}\times\phi}{\tau} = \frac{1.91*10^{-5}*10^{-4}\times\phi}{10} = 1.91 * 10^{-10} \times \phi \qquad \text{(S17)}$$

$$C_{wp} = \frac{3.89*10^{-4}*\left(7.19*10^{-8}\right)^2*1.07*10^3}{1.91*10^{-10}\times\phi} = \frac{1.13*10^{-5}}{\phi} \qquad \text{(S18)}$$

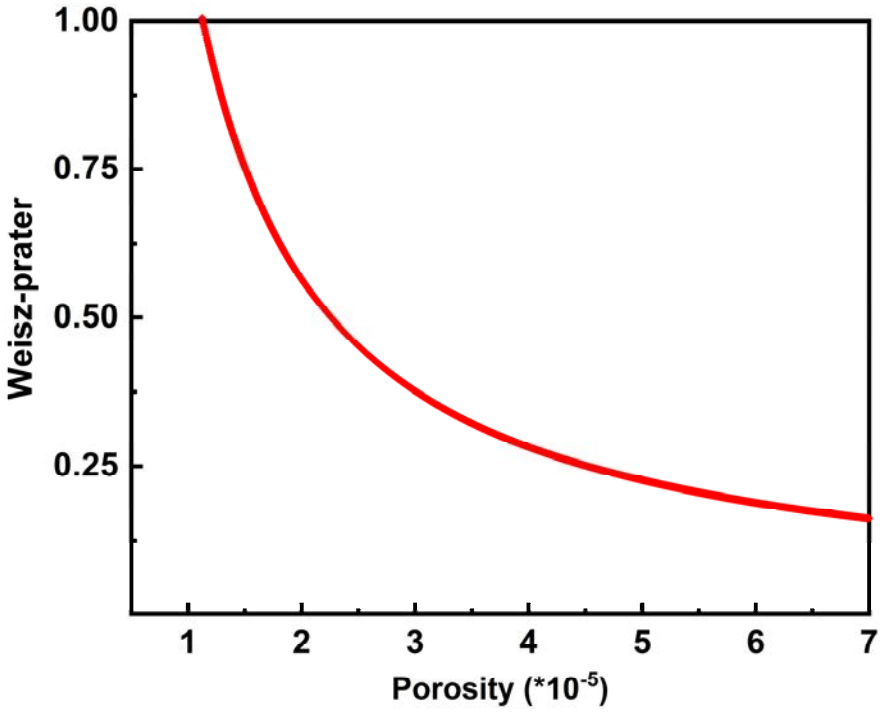

Figure S8. Weisz-Prater plot with particle porosity ϕ.

Figure S8 shows the Weisz-Prater plot with particle porosity ϕ. When the Weisz-Prater equals to 1, the ϕ equals to $1.13*10^{-5}$, which is far away from the normal value that varies between 0.2 and 0.7.

5.2 External mass transfer

5.2.1 Experiment check

Figure S9a shows the result when increasing the stirring speed from 0 to 750 rpm, no significant difference in activity were observed for agitation speed from 250-750 rpm. For 0 rpm, the activity is much lower than the activity with agitation, which is owing to the influence of gas mass transfer caused by the stagnant. Figure S9b shows the result when increasing the temperature to 50 °C. At lower stirring speed, the activity is much lower, which is because the molecular moves faster at high temperature, a gas mass transfer lamination were observed at low stirring speed. However, from 500 to 750 rpm, the reaction rate keep constant, the TOF for both catalyst didn't change along with the stirring speed, demonstrating experimentally that transport at the gas-liquid interface (G-L) is not limiting.

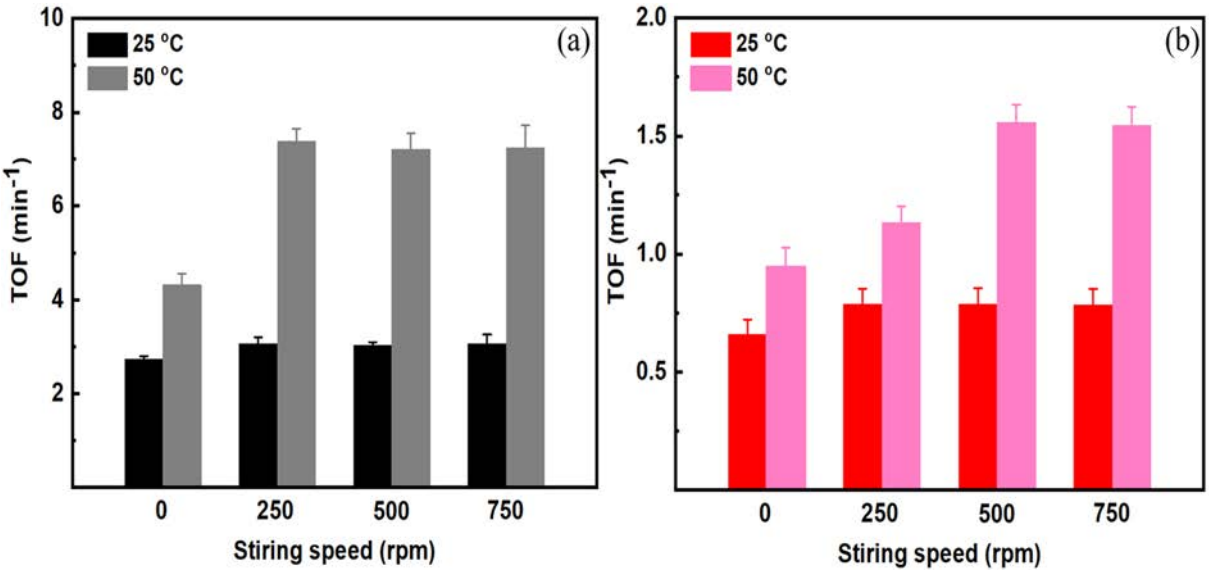

Figure S9. Influence of stirring speed on the activity of the catalyst. (a) Pd/SiO_2 and (b) Pd/SiO_2-p-NIPAM.

5.2.2 Liquid-Solid mass transfer

The external mass transfer, combined with G-L and L-S are calculated in chapter 2 (section 4.1.2 and section 4.1.3 of the supporting information)

6. Nitrite hydrogenation mechanism and derivation

6.1The mechanism consists of the following reaction steps:

1. $H_2 + 2* \rightleftharpoons 2H*$
2. $NO_2^- + * \rightleftharpoons NO_2^-*$
3. $NO_2^-* + H* + H^+ \rightleftharpoons NO* + * + H_2O$
4. $NO* + H* \rightleftharpoons HNO* + *$
5. $HNO* + H* \rightarrow HNOH* + *$

Where * represents an empty site on the Pd surface and H* represents an oxygen atom adsorbed on the Pd surface, as an example for all surface species.

$$\theta_H = K_1^{1/2}[H_2]^{1/2}\theta_v \quad \text{(S19)}$$

$$\theta_{NO_2^-} = K_2[NO_2^-]\theta_v \quad \text{(S20)}$$

$$\theta_{NO} = K_1^{1/2} K_2 K_3 [H_2]^{1/2} [NO_2^-][H^+][H_2O]^{-1}\theta_v \quad \text{(S21)}$$

$$\theta_{HNO} = K_1 K_2 K_3 K_4 [H_2][NO_2^-][H^+][H_2O]^{-1}\theta_v \quad \text{(S22)}$$

$$\theta_{HNOH} = K_1^{3/2} K_2 K_3 K_4 K_5 [H_2]^{3/2} [NO_2^-][H^+][H_2O]^{-1}\theta_v \quad \text{(S23)}$$

When consider the recent publication, the step 4 and step 5 are co-limiting. And the pseudo-steady state approximation is valid in this system, then one could capture the experimentally observed reaction rates as follows:

$$\frac{d(HNO)}{dt} = k_4\theta_{NO}\theta_H - k_{-4}\theta_{HNO}\theta_v - k_5\theta_{HNO}\theta_H = 0 \quad \text{(S24)}$$

$$k_4\theta_{NO}\theta_H = [k_{-4}\theta_v + k_5\theta_H]\theta_{HNO} \quad \text{(S25)}$$

$$\theta_{HNO} = \frac{k_4\theta_{NO}\theta_H}{k_{-4}\theta_v + k_5\theta_H} \quad \text{(S26)}$$

$$\theta_{HNO} = \frac{k_4 K_1 K_2 K_3 [H_2][NO_2^-][H^+]}{k_{-4} + k_5 K_1^{1/2}[H_2]^{1/2}} * \theta_v \quad \text{(S27)}$$

The rate expression for the consumption of NO_2^- per catalyst site can be written as a function of the rate determining step ($r_{overall} = \frac{r_i - r_{-i}}{\sigma_i}$, $_i$ is the stoichiometry of the ith elementary step), then (assuming that r_5 is irreversible) one can obtain the following:

$$r_{NO_2^-} = r_5 = k_5\theta_{HNO}\theta_H \quad \text{(S28)}$$

By substituting equation S27 and equation S19 to equation S28 one obtains the following rate expression:

$$r_{NO_2^-} = \left[k_5 \frac{\left[k_4 {K_1}^{3/2} K_2 K_3 [H_2]^{3/2}[NO_2^-][H^+]\right]}{k_{-4} + k_5 K_1^{\frac{1}{2}}[H_2]^{\frac{1}{2}}} \right] * {\theta_v}^2 \quad \text{(S29)}$$

Assuming that the Most Abundant Surface Reaction Intermediates (MASRI) on the surface are NO*, HNO*, H*, and NO_2^-* one could derive the equation S30:

$$\theta_v = \frac{1}{1 + K_1^{1/2} * [H_2]^{1/2} + K_2 * [NO_2^-] + K_1^{1/2} * K_2 * K_3 * [H_2]^{1/2} * [NO_2^-] * [H^+] + \cdots} \quad \text{(S30)}$$
$$K_1 * K_2 * K_3 * K_4 * [H_2] * [NO_2^-] * [H^+]$$

By substituting equation S30 on equation S29 one obtains the following rate expression:

$$r_{NO_2^-} = \frac{k_5 k_4 * {K_1}^{3/2} K_2 K_3 [H_2]^{3/2}[NO_2^-][H^+]}{\left[k_{-4} + k_5 K_1^{\frac{1}{2}}[H_2]^{\frac{1}{2}}\right] * \left[1 + K_1^{1/2}[H_2]^{\frac{1}{2}} + K_2[NO_2^-] + K_1^{1/2} K_2 K_3 [H_2]^{1/2}[NO_2^-][H^+] + \cdots\right]^2} \quad \text{(S31)}$$
$$K_1 K_2 K_3 K_4 [H_2][NO_2^-][H^+]$$

If one considers the system is maintained at constant pH ($[H^+]$ of 10^{-5} mol L^{-1}) thanks to the use of CO_2 as buffer, then the expression above can be simplified to:

$$r_{NO_2^-} = \frac{k_5 k_4 {K_1}^{3/2} K_2 K_3 [H_2]^{3/2} [NO_2{}^-]}{\left[k_{-4} + k_5 K_1^{1/2} [H_2]^{1/2}\right] * \left[1 + K_1^{1/2} [H_2]^{\frac{1}{2}} + K_2 [NO_2{}^-]\right]^2} \quad \text{(S32)}$$

6.2 Derivation to calculate the entropy and enthalpy

When considering the fact that only the initial rate are used, at the very beginning of the reaction, only the reactant are the most abundant species. Also, when the reaction conducted at low hydrogen pressure region. (e.g. 0.03 bar) The reaction order for H_2 is 1.5, while the reaction order for nitrite is -1 as show in Figure 2. This imply that nitrite are the dominate species on the catalyst surface and in this condition, we could assume $K_2[NO_2{}^-] \gg 1 + K_1^{1/2}[H_2]^{1/2}$.Then, the above equation can be simplifies to equation S33.

$$r_{4,5} = \frac{k_5 k_4 {k_{-4}}^{-1} {K_1}^{3/2} K_2 K_3 [H_2]^{3/2} [NO_2{}^-]}{\left[K_2 [NO_2{}^-]\right]^2} \quad \text{(S33)}$$

Reorganize the equation to get equation S34

$$r_{4,5} = k_5 k_4 {K_{-4}}^{-1} K_1^{\frac{3}{2}} {K_2}^{-1} K_3 [H_2]^{\frac{3}{2}} [NO_2{}^-]^{-1} \quad \text{(S34)}$$

Here, $k_5 k_4 {K_{-4}}^{-1} K_1^{\frac{3}{2}} {K_2}^{-1} K_3$ can be simplified to K_{app} as these are the equilibrium constant before the rate determine step. Then, equation S35 is observed.

$$r_{4,5} = k_{apparent}\, [H_2]^{3/2} [NO_2{}^-]^{-1} \quad \text{(S35)}$$

According to the transition state theory, the equation can be adjusted as below:

$$\frac{r}{L} = \frac{k_b T}{h} \exp\left(-\frac{\Delta G_{app}^{\ddagger}}{RT}\right) [\mathrm{H_2}]^{3/2} [\mathrm{NO_2}^-]^{-1} \quad \text{(S36)}$$

Considering that the collision frequency term is nearly constant for the reaction conditions herein employed one can substitute the term $\frac{k_b T}{h}$ by the average value of (6.73±0.23)*10^{11}. Here, L is the total active sites, $\Delta G_{app}^{\ddagger}$ is the apparent activation energy and A is $\frac{k_b T}{h}$. As $\Delta G_{app}^{\ddagger} = \Delta H_{app}^{\ddagger} - \mathrm{T}\Delta S_{app}^{\ddagger}$, the rate can be further organized as equation S37.

$$\ln(\frac{\frac{r}{L}}{\mathrm{A}}) - \ln([\mathrm{H_2}]^{\frac{3}{2}}[\mathrm{NO_2}^-]^{-1}) = \frac{\Delta S^{\ddagger}_{app}}{\mathrm{R}} - \frac{\Delta H^{\ddagger}_{app}}{\mathrm{RT}} \quad \text{(S37)}$$

Based on the reaction rate observed at different temperature with a low hydrogen pressure of 0.03 bar (Figure 4), the $\Delta H^{\ddagger}_{app}$ and $\Delta S^{\ddagger}_{app}$ are being calculated for the Pd/SiO_2 and Pd/SiO_2-p-NIPAM catalyst from the slope and intercept as show in Figure S10 respectively.

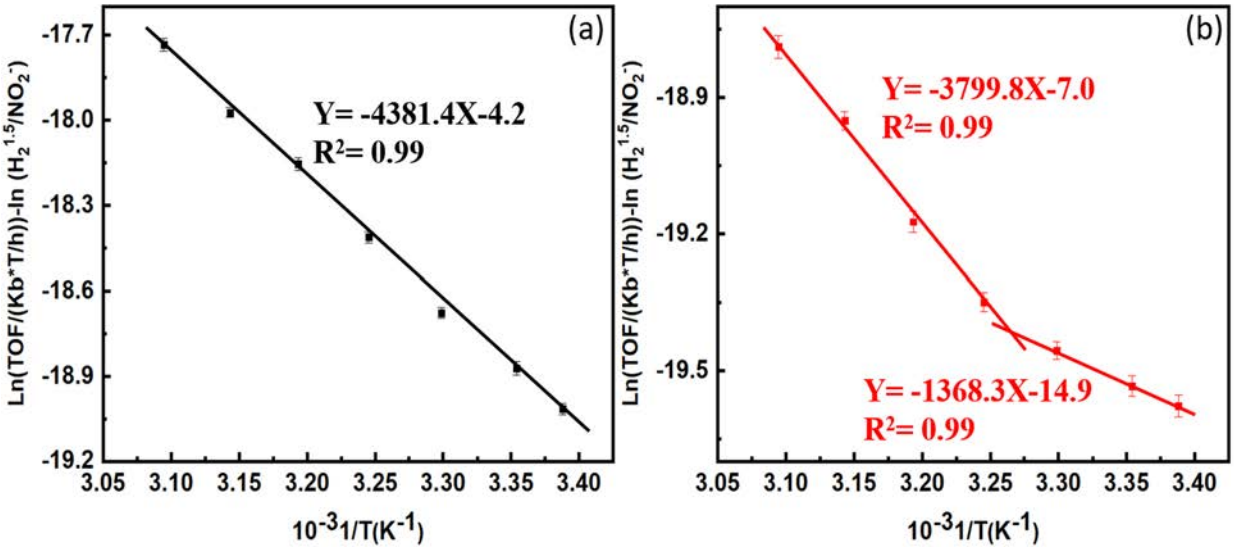

Figure S10. Transition state theory reaction rate vs temperature for the catalyst (a) Pd/SiO_2, (b)Pd/SiO_2-p-NIPAM.

7. Solvation effect calculation

The transition state theory is used to express the rate of reaction, according to the review paper from David W. Flaherty et al.[6] The rate equation for nitrite hydrogenation reaction can be defined as equation S38.

$$\frac{r}{L} = \frac{k_b T}{h} \exp\left(-\frac{\Delta G^{\ddagger}_{app}}{RT}\right)[\mathrm{H_2}]^{3/2}[\mathrm{NO_2}^-]^{-1} \quad \text{(S38)}$$

Here, $\Delta G^{\ddagger}_{app}$ is the apparent free energy barrier for the transition state, which is equal to the difference between the free energies of the transition state and the molecules in the liquid. On one hand, the Gibbs free energy of the transition state includes the free energy of the activated complex in the reference state ($G^{0,\ddagger}$) and the corresponding excess of Gibbs free energy $G^{\varepsilon,\ddagger}$ induced by its solvation layer. On the other hand, the Gibbs free energy of the reactive species

in the liquid includes the free energy of the molecule in the reference state (G_i^0) and its excess free energy in the solvent (G_i^ε)

$$\Delta G_{app}^{\ddagger} = (G^{0,\ddagger} + G^{\varepsilon,\ddagger}) - (G_i^0 + G_i^\varepsilon) \quad \text{(S39)}$$

The excess free energy (G^ε) quantifies the impact of solvent interactions on the free energy of each component. The activity coefficients of reactive species can be related to excess Gibbs free-energy contributions as follows:

$$\gamma_i = \exp\left(\frac{G_i^\varepsilon}{RT}\right) \quad \text{(S40)}$$

Substituting equation S40 and equation S39 into equation S38 gives a rate expression restated in a manner that includes activity coefficients:

$$\frac{r}{L} = \frac{k_b T}{h} \exp\left(-\frac{G^{0,\ddagger} - G_{H_2}^0 - G_{NO_2^-}^0}{RT}\right) * \frac{\gamma_{H_2} * \gamma_{NO_2^-}}{\gamma_\ddagger} [H_2]^{\frac{3}{2}} [NO_2^-]^{-1} \quad \text{(S41)}$$

This leads to a new apparent rate expression that contains the excess Gibbs free energy and standard Gibbs free energy.

$$\frac{r}{L} = \frac{k_b T}{h} \exp\left(-\frac{\Delta G_{app}^{0,\ddagger} + \Delta G_{app}^{\varepsilon,\ddagger}}{RT}\right) [H_2]^{3/2} [NO_2^-]^{-1} \quad \text{(S42)}$$

As $\Delta G_{app} = \Delta H - T\Delta S$, the rate can be further organized as equation S43

$$\frac{r}{L} = \frac{k_b T}{h} \exp\left(\frac{\Delta S_{App}^{0,\ddagger} + \Delta S_{App}^{\varepsilon,\ddagger}}{R}\right) \exp\left(-\frac{\Delta H_{App}^{0,\ddagger} + \Delta H_{App}^{\varepsilon,\ddagger}}{RT}\right) [H_2]^{3/2} [NO_2^-]^{-1} \quad \text{(S43)}$$

Reference

[1] G. Bergeret, P. Gallezot, Particle size and dispersion measurements, Handb. Heterog. Catal. 2 (2008) 439.

[2] D. Shuai, J.K. Choe, J.R. Shapley, C.J. Werth, Enhanced activity and selectivity of carbon nanofiber supported Pd catalysts for nitrite reduction, Environ. Sci. Technol. 46 (2012) 2847–2855. https://doi.org/10.1021/es203200d.

[3] R. Brunet Espinosa, D. Rafieian, R.G.H. Lammertink, L. Lefferts, Carbon nano-fiber based membrane reactor for selective nitrite hydrogenation, Catal. Today. 273 (2016) 50–61. https://doi.org/http://dx.doi.org/10.1016/j.cattod.2016.02.057.

[4] L. Zhang, E.S. Daniels, V.L. Dimonie, A. Klein, Synthesis and characterization of PNIPAM/PS Core/Shell particles, J. Appl. Polym. Sci. 118 (2010) 2502–2511.

[5] M. Kalagasidis Krušić, M. Ilić, J. Filipović, Swelling behaviour and paracetamol release from poly(N-isopropylacrylamide- itaconic acid) hydrogels, Polym. Bull. 63 (2009) 197–211. https://doi.org/10.1007/s00289-009-0086-3.

[6] D.S. Potts, D.T. Bregante, J.S. Adams, C. Torres, D.W. Flaherty, Influence of solvent structure and hydrogen bonding on catalysis at solid–liquid interfaces, Chem. Soc. Rev. 50 (2021) 12308–12337. https://doi.org/10.1039/d1cs00539a.

Chapter 4

Modulating the Transition States of Nitrobenzene Hydrogenation on Nanohybrid Stimulus-Responsive Polymer-Metal Catalysts

Abstract

In designing effective catalysts, one must consider how to control the accessibility and activity of the active sites. Inspired by nature, we have leveraged the chemistry of thermo-responsive poly(N-isopropylacrylamide) (p-NIPAM) to tailor the extent of solvation of the transition state key surface reaction intermediates during the hydrogenation of nitrobenzene to anillin on Pd/SiO_2. Detailed reaction kinetics, catalyst characterization, and NMR DOSY/NOESY experiments indicate that nitrobenzene reduction is co-limited by both the formation and the hydrodeoxygenation of phenylhydroxylamine (PHA) to aniline precursor. Transition state treatment of the kinetic data revealed that when the temperature is below the Lower Critical Solution Temperature (LCST) of p-NIPAM (32 °C), the apparent enthalpy of activation decreases three-fold. This enthalpic stabilization is attributed to the strong interactions of the polymer with the reactants in the swollen state. A concomitant reduction in the apparent entropy of activation was obtained at these conditions, indicative of losses in the degree of freedom of the kinetically controlled surface species. At temperatures above the LCST, it was possible to reverse these effects leading to similar apparent Gibbs free energy of activation as that observed in the Pd/SiO_2 catalyst. These results establish the foundational work on the development of materials capable of taming the intrinsic activity of the active site in a fast, reversible manner. We envision that these results will facilitate the development of catalysts that can mimic the homeostatic behavior of enzymes, allowing more stable operation even when complex feedstocks are employed (e.g. biomass conversion and pollution control).

1. Introduction

Precise control of molecular transfer of reactants and products in and out the catalyst and the extent of stabilization of the transition state of key surface reactions is essential in the designing of efficient heterogeneous catalysts. In nature, enzymes have achieved exquisite substrate specificity, product selectivity, and activity thanks to thousands of years of evolution. While these materials can respond to changes in the chemical environment (e.g. temperature, pH, solvent) their stability is often compromised, leading to denaturalized catalysts. An interesting alternative to overcome these limitations is to employ polymer coatings that can sustain the operating conditions employed in conventional reactors while preserving the desired responsiveness, selectivity, and activity of the enzymatic counterparts.

Stimuli-responsive polymers are a class of materials that recently have been shown to induce mass transfer effects on heterogeneous catalysts in a fully reversible fashion mimicking the operation of enzymes.[1][2][3] Here, metal nanoclusters are embedded in a polymer layer that can respond to an external stimulus. Essentially, when the polymer is swollen the catalyst is readily accessible, allowing fast reaction kinetics. Upon reaching a critical solubility threshold the polymer collapses, leading to mass transport limitations due to the formation of a highly dense polymer layer around the catalyst particles with a hydrophobic character that hinders diffusion of polar species. These conformational transitions in the polymer can be triggered by pH, magnetic field, and/or temperature, making it a highly flexible platform for creating bio-inspired catalysts.[4][5][6] The archetypal example of such active carriers are the colloidal gels made from cross-linked p-NIPAM that undergo a volume phase transition at the Lower Critical Solution Temperature (LCST) of 32 °C.[7] Currently, all the reported literature on stimulus-responsive nano-reactors, however, is focused on the utilization of reversible changes in mass transfer to induce a decrease in the reaction rate.[8] In that description, the observed reaction rates measured below the LCST are believed to be equal to those observed on the uncoated catalyst. That is that the presence of the polymer in the swollen state does not change the binding of the molecules to the active sites nor the energetics of the activated complex.[9][10][11][12]

In this contribution, we challenge this construct using nonporous catalysts consisting of Pd clusters supported on dense SiO_2 spheres that are decorated with thermo-responsive p-NIPAM brushes that allow fast and reversible transitions from swollen to collapsed states with negligible impact on the mass transfer rates. Since the diffusion of reactants was unrestricted, even when the polymer is collapsed, it was possible to interrogate the thermal responsive solvation effect and reaction mechanisms using rigorous reaction kinetics and NMR studies.

Nitrobenzene (NB) hydrogenation in the aqueous phase was used as a probe reaction to study the influence of p-NIPAM induced solvation effects. Industrially, this reaction is key for the production of plastics and insulation materials.[13,14] The reaction was initially described in 1898 by F. Harber [15] using Pd-based electro-catalysts. The mechanism was believed to involve a three-step process in which nitrosobenzene (NSB) and phenylhydroxylamine (PHA) were proposed as the key reaction intermediates (see Figure 1). However, more recent studies by E. A. Gelder et al.[16] using palladium supported on carbon as a thermo-catalyst claimed that NSB is a spectator in the process (i.e. NSB is not participating in the rate-determining step). Instead, the authors suggested that $(C_6H_5)NOH_{ads}$ is the key surface reaction intermediate in the mechanism. In this system, it has been also postulated that at elevated NB concentrations, the coupling pathway to AN controls the chemistry, particularly when alkaline media is employed. At the same time, subsequent density functional theory (DFT) studies have shown that at low and moderate concentrations of NB the sequential mechanism is indeed less energetic than the NSB pathway proposed by F. Haber.[17][18][19] Besides aniline formation as the main product, para-aminophenol (PAP) can be observed as a byproduct. The formation of PAP from PHA is acid catalyzed, thus low pH and low hydrogen partial pressures favor the formation of PAP from PHA [20] (Figure 1). While there is substantial spectroscopic and theoretical evidence that supports the mechanism involving $(C_6H_5)NOH_{ads}$ as key surface reaction intermediate the experimentally measured reaction orders reported in the literature for hydrogen typically vary between zero and one, which is surprising as the theoretical values could be as high as two and a half (2.5) when the rate-determining step is the formation of phenylhydroxylamine (PHA).
Our results suggest that it is possible to manipulate the catalyst activity by leveraging the extent of solvation of the transition state that the thermo-responsive polymer can induce during reaction. The differences in the solvation at temperatures below and above the P-NIPAM LCST allowed us to precisely control the apparent barriers of activation of the nitrobenzene hydrogenation in a fully reversible fashion. Furthermore, we showed that contrary to previous results, the NB hydrogenation is determined by two elementary surface reactions that include the formation and subsequent hydrodeoxygenation of phenylhydroxylamine (PHA) surface intermediate on both bare and p-NIPAM coated Pd/SiO_2 catalysts, suggesting a complex interplay between the surface coverage and true activation barriers.

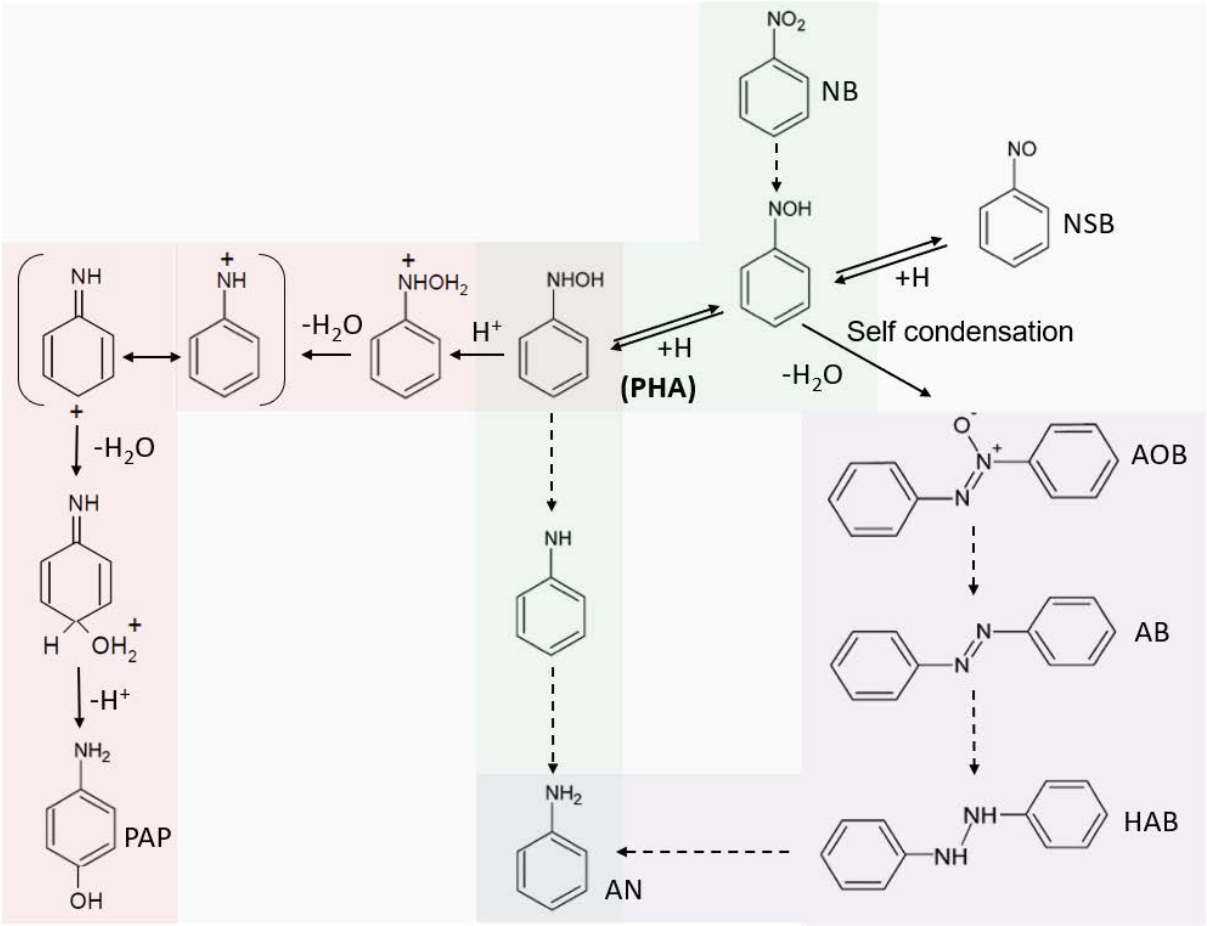

Figure 1. Reaction pathway for the formation of aniline and pathway for Bamberger rearrangement of phenylhydroxylamine to p-aminophenol.

2. Experimental section

2.1 Materials

Nitrobenzene (NB, ≥99.0%), tetraethyl orthosilicate (TEOS, 98 %), ammonium hydroxide solution (NH_4OH, 25% NH_3 basis), sodium hydroxide (NaOH, 99 %), tetraamminepalladium(II) nitrate solution ($Pd(NH_3)_4(NO_3)_2$, 10 wt. % in H_2O, 99.99%), N-isopropylacrylamide (NIPAM, 97%), trimethylamine (Eth_3N, 99%),3-aminopropyltriethoxysilane (APTES, 99%), copper (II) bromide ($CuBr_2$, 99%), α-bromoisobutyryl bromide (BIBB, 98%), L-ascorbic acid (99%), 1,1,4,7,10,10-hexamethyltriethylenetetramine (HMTETA, 97%), n-hexane (99.4%), tetrahydrofuran (THF, anhydrous, ≥99.9%) were purchased from Sigma-Aldrich. The molecular sieves (4Å, 4-8 mesh) used to dry THF were procured from Honeywell. The glass reactor (Duran baffled, wide mouth bottle GLS 80) with a diameter of 10.1 cm and a height of 22.2 cm. The syringe filter (PTFE

0.2 μm, Whatman) and sampling syringe (BD Plastipak) were employed to take liquid aliquots during the reaction to determine the reaction rates.

2.2 Catalyst preparation

2.2.1 Synthesis of SiO_2 spheres and Pd/SiO_2 catalyst

The SiO_2 spheres and Pd/SiO_2 were synthesized following a previously published method.[21] In short, The SiO_2 spheres were prepared using the method reported by Stöber et al.[22] to get a dense Silica spheres.. After that, the Pd/SiO_2 catalyst was prepared using the strong electrostatic adsorption (SEA) method to load Pd on the surface of obtained SiO_2 spheres.

2.2.2 Synthesis of Pd/SiO_2-p-NIPAM catalyst

The p-NIPAM brush modified Pd/SiO_2 particles were synthesized via the 'grafted from' technique so-called surface-initiated atom transfer radical polymerization (ATRP). The synthesis was performed on bromine functionalized silica particles and carried out in a methanol/water solvent mixture (4:1 v/v) and reagents NIPAM/$CuBr_2$/HMTETA/ascorbic acid was used in the molar ratios 900/1.5/15/10, with a monomer to solvent mass ratio of 0.058/1. The comprehensive particle preparation and brush synthesis protocol are available in chapter 3 (section 2 in SI).

2.3 Catalyst characterization

The transmission electron microscopy (TEM) analysis results were obtained by using a Tecnai F30 field emission TEM with an accelerating voltage of 300KV. The Scanning Electron Microscopy (SEM) was conducted by using a JEOL, LA6010 with a resolution of 4 nm at 20 kV. Brunauer–Emmett–Teller (BET) surface area analysis was conducted by using a Micromeritics Model ASAP 2400 instrument based on nitrogen adsorption isotherm measurements. For each analysis, 0.2–0.3 g of sample were degassed at 120 °C for 24 h before measurement. The metal loading of the Pd/SiO_2 samples was determined by X-ray fluorescence (XRF) (Bruker, S8 TIGER). The metal dispersion of the Pd on the samples was determined by CO chemisorption at room temperature (Micromeritics, Chemisorb 2750) and TEM measurement. The samples were reduced in H_2 at room temperature for 1 h and then flushed in He for 30 min. After that, CO was introduced in pulses and the response was recorded using a thermal conductivity detector (TCD) detector. The thermal gravimetric analysis (TGA)

(Mettler-Toledo, TGA/SDTA 851) was performed from 25 to 1000 °C at a ramp rate of 10 °C/min under a constant flow of argon at 30 mL/min. Dynamic light scattering (DLS) was conducted by using a Malvern Mastersizer 2000 (0.3-300 μm) to determine the particle size of the supported catalysts.

^{1}H Nuclear Magnetic Resonance (NMR) analysis was conducted on a Bruker 14.1 T (operating at 600.16 MHz for ^{1}H) Avance NEO spectrometer equipped with a 5 mm BBO solution state probe, equipped with a 50 G/cm gradient unit on the z-axis. Samples were prepared with 1.67 g/L of Pd/SiO_2-p-NIPAM catalyst suspended in either D_2O, or 90% H_2O and 10% D_2O as a solvent. Furthermore, a sample using the same composition in D_2O with 5 mM nitrobenzene was used, alongside a 10 g/L commercial p-NIPAM (Sigma Aldrich, M_n = 40 kDa) in 90% H_2O and 10% D_2O, was used for comparative studies. The samples were analyzed at 25 and 40 °C, and the temperature was regulated under a 400 L/h gas flow. All experiments were measured with a spectral width of 12 ppm or 16 ppm, centered at the water peak, with 8192, 16384, or 32768 complex points, employing a 90° pulse of ~12.8 μs, and a relaxation delay of 5 s. All spectra were referenced by the residual methanol methyl peak. Water suppression experiments were acquired with an excitation sculpting sequence [23] using 2.24 ms sinc 180° selective pulses set on water, with 4096 averages. ^{1}H-^{1}H Nuclear Overhauser Effect Spectroscopy (NOESY) was acquired coupled to the aforementioned excitation sculpting water suppression acquisition, with 128 points in the indirect dimension, and with a mixing time of 350 ms, with 16 averages. Diffusion Ordered Spectroscopy (DOSY) was measured with a stimulated echo and LED sequence, using bipolar gradient pulse pairs, with and without coupling to excitation sculpting.[24,25] DOSY spectra were measured with 1 ms gradient length (δ), and with a diffusion time (Δ) of 100 or 650 ms, with 64 or 128 linearly varying gradient intensities, employing 32 averages. All the processing was performed in Bruker Topspin, with the 1D and pseudo-2D methods being zero-filled twice, phased, and apodised with an exponential multiplication, while a sine-bell-shaped window function was applied to NOESY datasets. DOSY plots were generated with adaptive exponential fitting using MestreNova.

2.4 Catalytic tests

The nitrobenzene hydrogenation reaction was conducted in a 1 L batch reactor operating in a temperature range of 22-50 °C, with a pH value of 5.5 achieved by buffering continuously CO_2 gas (0.1 bar). The reactor used for the reaction had four connections on the reactor lid for gas-

in, gas-out, sampling, and stirring shaft equipped with 4 stirring blades. The reaction was conducted by adding 0.02g catalyst to 0.3 L deionized water and stirring at 500 rpm under continuous hydrogen flow for at least 1 h, removing dissolved oxygen and reducing the catalyst. After that, the reaction is started by adding 20 mL of an aqueous solution of nitrobenzene (15 mM) to the glass reactor. The hydrogen pressure varied between 0.01 and 0.8 bar, while the nitrobenzene concentration varied between 0.1 and 3 mM. During the catalytic test, samples were collected using a 2.5 mL syringe and filtered using a syringe filter with a pore size of 0.2 μm to remove catalyst particles.

The reactant and product were measured using high-performance liquid chromatography (Shimadzu HPLC10AVP) equipped with an autosampler. Figure S5 shows a typical experiment plot for nitrobenzene concentration, aniline (AN), and p-aminophenol (PAP) concentration changes over time. From these plots, the reaction rate was determined based on the initial activity at low nitrobenzene conversion (<10%) to regress the instantaneous reaction rate at time zero. The Turnover Frequency (TOF) was calculated as the reaction rate per surface atom of palladium as determined with XRF, CO chemisorption, and TEM measurements.

The nitrobenzene conversion and the integral aniline and p-aminophenol selectivity was calculated with equation 1-3.

$$Nitrobenzene\ \text{conversion}_{t1} = \frac{[\mathrm{NB}]_{t0} - [\mathrm{NB}]_{t1}}{[\mathrm{NB}]_{t0}} * 100 \qquad (1)$$

$$Aniline\ \text{selectivity}_{t1} = \frac{[\mathrm{AN}]_{t1}}{[\mathrm{NB}]_{t0} - [\mathrm{NB}]_{t1}} * 100 \qquad (2)$$

$$p-aminophenol\ \ \text{selectivity}_{t1} = \frac{[\mathrm{PAP}]_{t1}}{[\mathrm{NB}]_{t0} - [\mathrm{NB}]_{t1}} * 100 \qquad (3)$$

Where $[\mathrm{NB}]_{t0}$ is the initial concentration of nitrobenzene, $[\mathrm{NB}]_{t1}$ is the concentration of nitrobenzene at t_1,$[AN]_{t1}$is the concentration of aniline at t_1, $[\mathrm{PAP}]_{t1}$ is the concentration of p-aminophenol at t_1.

3. Results and discussion

3.1 Catalyst Characterization

The same catalyst in chapter 3 are used for the nitrobenzene hydrogenation reaction. The characterization results of the prepared catalysts are shown in Table 1 in chapter 3. And the

Dynamic light scattering measurements (DLS) of the Pd/SiO_2-p-NIPAM are show in chapter 3 (Figure S3).

3.2 NMR catalyst characterization

Pd/SiO_2-p-NIPAM catalyst was suspended in either fully or partially (10 %) deuterated water and analyzed by NMR at room temperature and above the LCST (specifically at 40 °C). Characterization of suspended 20-120 nm silica nanoparticles with ^{1}H NMR was recently demonstrated, revealing information on the composition of their surfaces. [26,27] The result of the analysis of the catalyst by ^{1}H and ^{1}H-^{1}H NOESY NMR can be found in Figure 2. The assignment of the resonances belonging to p-NIPAM itself was performed in accordance with F. Zeng et al. [28] The change of the temperature above the LCST leads to a drop in intensity of ~2.5 times for all peaks (Figure 2a,b). This is most clear for the amide resonances (between 7 and 8 ppm), which also present an alteration of their chemical shift (upfield), due to their labile nature. The phenomenon of a loss in signal intensity had already been observed for p-NIPAM and related polymers, it was found to be associated to phase separation and formation of large aggregates.[28,29] However, this effect is rather subtle in the catalyst than in the p-NIPAM in the solution. As can be confirmed in Figure S1a,b the free p-NIPAM registers a drop in intensity of ~45 times at 40 °C, indicating the aforementioned phase separation. The spatial interactions within p-NIPAM were also studied for the catalyst (Figure 2c,d) and for the free polymer itself (Figure S1c,d) by NOESY NMR. These evidenced a similar trend when going from room temperature to 40 °C, the cross-peaks within the polymer is far lowered above the LCST, indicating fewer preferential interactions. These results suggest that there is a less ordered environment at temperatures above the LCST.

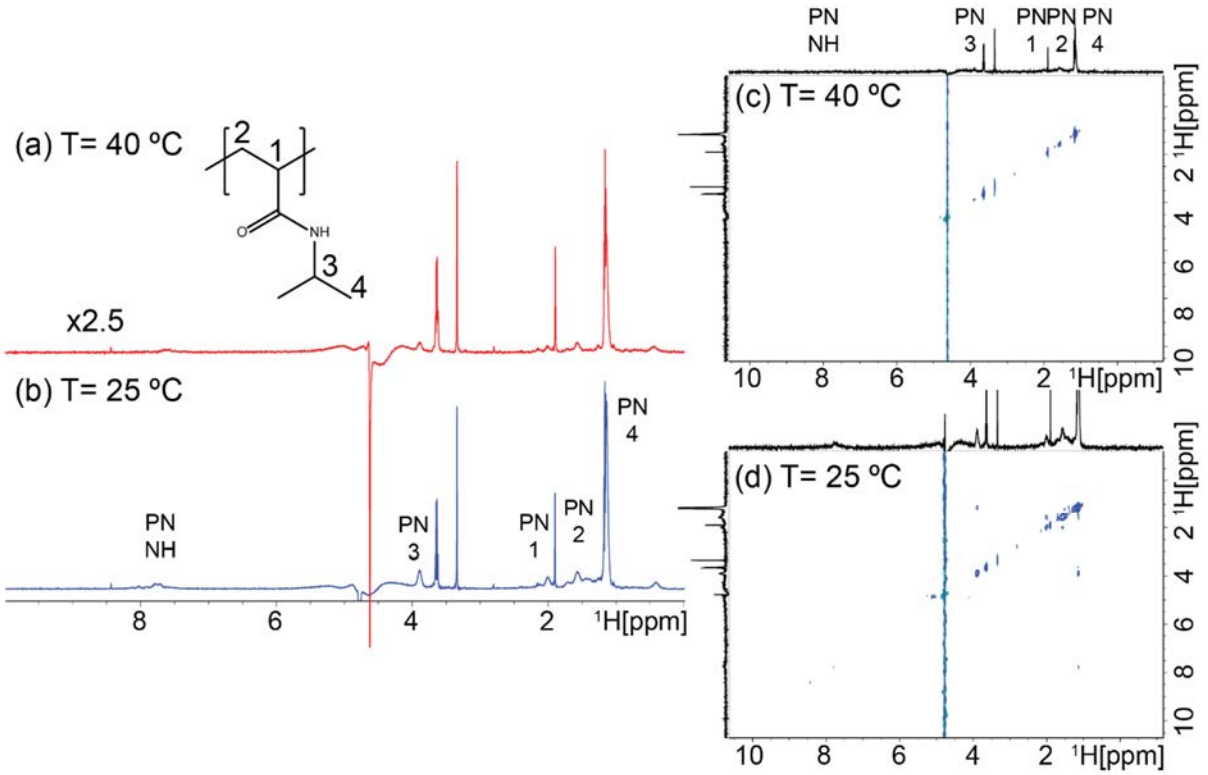

Figure 2. NMR characterization of Pd/SiO_2-p-NIPAM suspended in 90% D_2O:10% H_2O. (a) and (b) correspond to water suppression spectra performed above (40 °C) and below LCST (25 °C), respectively. The intensities of spectrum a is 2.5 times multiplied in order to match the peak size of spectrum b. (c) and (d) are water suppressed-NOESY spectra of the same sample, at 40 and 25 °C, respectively.

3.3 Nitrobenzene hydrogenation activity and selectivity

Prior to the study of reaction kinetics, the internal and external mass transfer limitations were evaluated (see supporting information section 5). This analysis indicated that mass transfer limitations are negligible reaction conditions herein explored. Figure 3 indicates that comparable TOFs are obtained for coated and uncoated catalysts when the reaction is conducted below the LCST regardless of the hydrogen pressure. Increasing the temperature above 32 °C drastically increased the rate of reaction on the parent Pd/SiO_2, but much less increase on Pd/SiO_2-p-NIPAM. This may be attributed to the polymer collapse that covers partly the Pd surface at high temperatures.

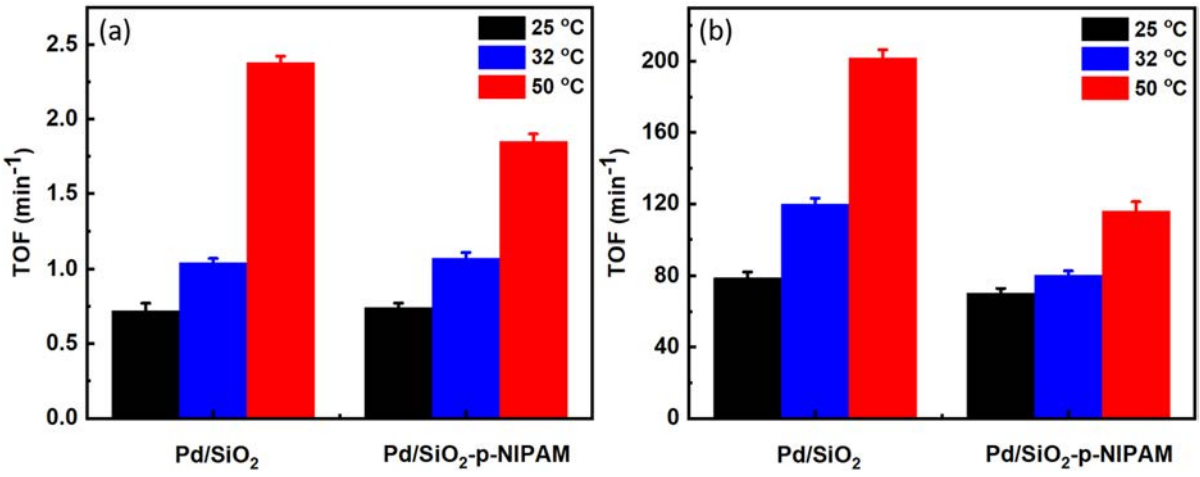

Figure 3. TOF of Pd/SiO_2 and Pd/SiO_2-p-NIPAM catalyst at different hydrogen pressure (a) 0.03 bar H_2 (b) 0.8 bar H_2.

The results obtained at 10 % conversion (Figure 4) indicate that regardless of the catalyst and reaction conditions employed, the main product observed in the hydrogenation of nitrobenzene was aniline (88-97 %) followed by p-aminophenol (0.25-0.52 %). The dimerization products of nitrobenzene were detected in trace amounts only. This is not surprising as the reaction conditions employed here are weakly acidic, not favoring the condensation pathway.[30] The selectivity to p-aminophenol increased with temperature on the parent Pd/SiO_2 catalyst at the expense of anillin formation. Similar results have been reported on Pt-based catalysts while exploring nitrobenzene to p-aminophenol via the Bamberger rearrangement.[31] The most notable feature is that the addition of the polymer led to higher selectivity towards aniline (c.a. 93-96 %) even at high temperatures. This may be due to the presence of the N-rich polymer brushes that favors the aniline formation as described by Z. Zhang et al. who reported that N-rich poly(ionic liquids) supported Pd catalyst favors aniline formation.[32]

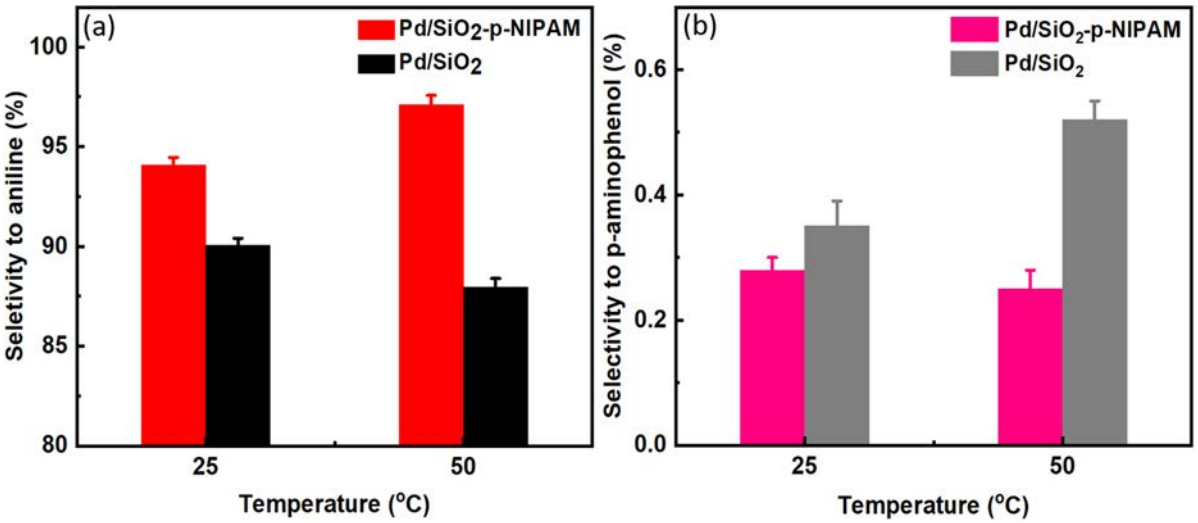

Figure 4. Selectivity to aniline (a) and p-aminophenol (b) for Pd/SiO_2 and Pd/SiO_2-p-NIPAM catalysts at 10 % conversion of nitrobenzene.

3.4 Apparent reaction orders of nitrobenzene hydrogenation

Rigorous reaction kinetics were employed to interrogate the underlying reaction mechanism for the nitrobenzene hydrogenation on both catalysts. For this purpose, the apparent reaction orders of nitrobenzene were investigated at low and high partial pressures of hydrogen for the parent Pd/SiO_2 and p-NIPAM coated catalysts (Figure 5a-5d).

In the case of the Pd/SiO_2 catalyst, the reaction order of nitrobenzene at high hydrogen pressure (0.8 bar) varied between 1 and -0.6 for nitrobenzene concentrations ranging from 0.1 and to 3 mM, respectively. In contrast, when the reaction was conducted at low hydrogen partial pressure (0.03 bar), exclusively negative reaction orders in nitrobenzene were observed (Figure 5c). This suggests that nitrobenzene and hydrogen compete for the same active sites, which is in line with previous work from L.B. Belykh et al. on Pd-based catalysts.[33] The apparent reaction order in hydrogen at low partial pressures was c.a. 2.5 on the bare Pd/SiO_2 catalyst (Figure 5e) while Increasing the hydrogen pressure led to first-order kinetics. The first-order kinetics have been observed in several studies on Pt and Pd catalysts. [34][35][36][37] The high apparent orders herein obtained would suggest that several pre-equilibrated steps involving hydrogen insertion in the nitrobenzene molecule are required before reaching the rate-determining step. Surprisingly, increasing temperature led to lower reaction orders (Figure 5e). This is a counterintuitive result, as one would expect the surface coverage to decrease with increasing temperature, which in turn should lead to higher reaction orders. Table S2 shows a summary of the reaction orders. The exact nature of these changes is addressed in Section 4.

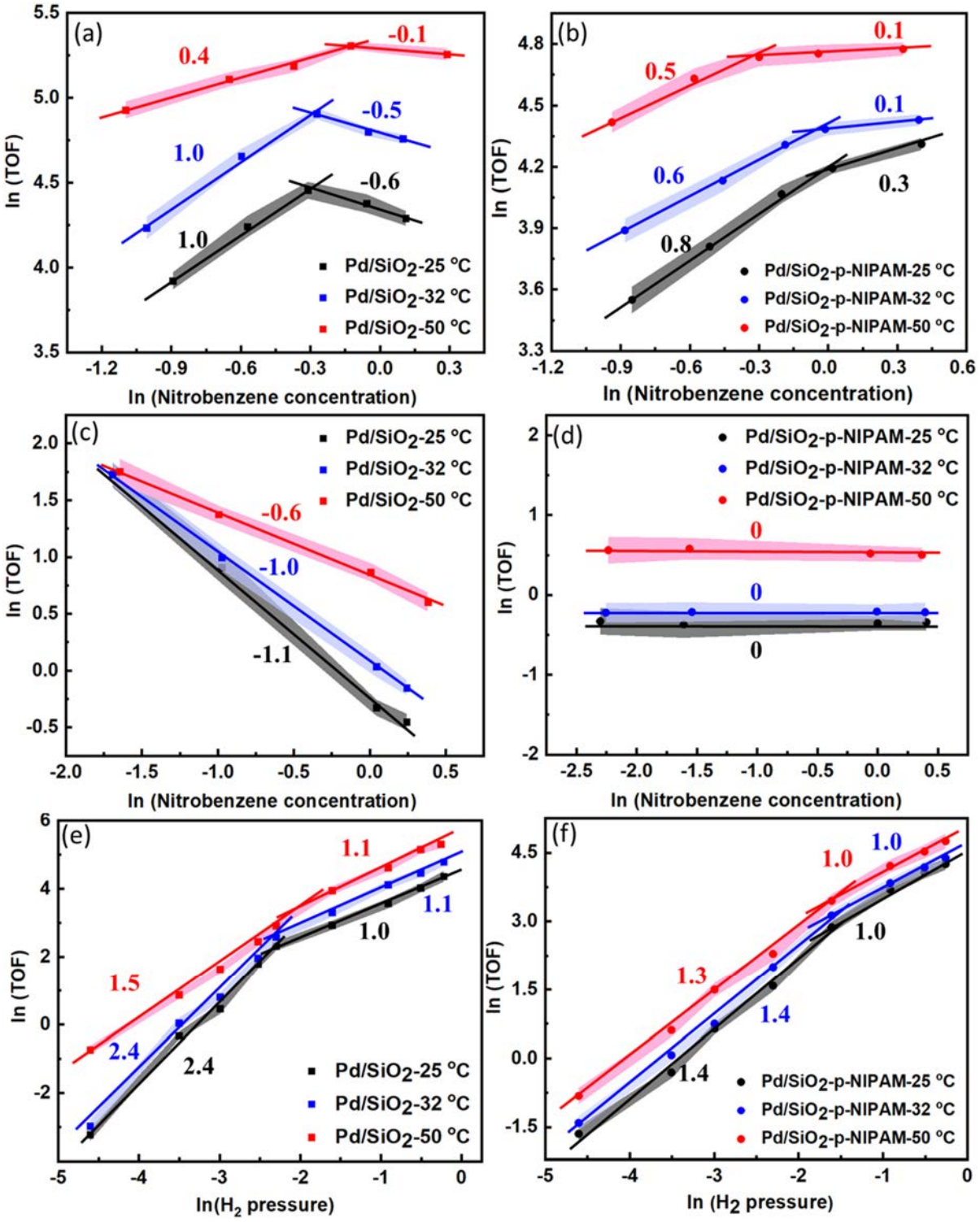

Figure 5. Effect of nitrobenzene concentration on reaction rate using (a) Pd/SiO_2 and (b) Pd/SiO_2-p-NIPAM catalyst with 0.8 bar H_2 pressure. and (c) Pd/SiO_2 and (d) Pd/SiO_2-p-NIPAM catalyst with 0.03 bar H_2 pressure. Effect of hydrogen pressure on reaction rate with 1mM nitrobenzene using (e) Pd/SiO_2 and (f) Pd/SiO_2-p-NIPAM catalyst. The shades indicate experimental error based on repeated experiments.

When the polymer-coated Pd/SiO_2-p-NIPAM catalyst was employed, the apparent reaction orders in nitrobenzene vary between 0.8 and 0.1 at high hydrogen partial pressure (0.8 bar, Figure 5b). Notably, at low hydrogen partial pressure (0.03 bar), zero-order or "saturation" kinetics were observed (Figure 5d). Similarly, the apparent hydrogen reaction orders for Pd/SiO_2-p-NIPAM (Figure 5f) are lower (1.4) compared to Pd/SiO_2 at temperatures below LCST (Figure 5e). These results would suggest that p-NIPAM facilitates hydrogen adsorption over nitrobenzene. Alternatively, these changes in the apparent reaction orders could be associated with shifts in the rate determining step to an earlier one.

3.5 Apparent activation energies

The activation energy barrier was 41±1 and 39±1 kJ mol^{-1} for the Pd/SiO_2 catalyst at 0.03 and 0.6 bar of hydrogen, respectively (see Figure 6a and Figure S6a). These values are in line with previously reported apparent barriers on Pd-based catalysts (c.a. 35 kJ mol^{-1} at 2 Mpa H_2 pressure).[36] Strikingly, when the polymer coated catalyst (Pd/SiO_2-p-NIPAM) was employed the apparent activation energy varied with the temperature (Figure 6b and Figure S6b) at low and high hydrogen partial pressures. That is that at temperatures below the LCST (T<32 °C) a low apparent activation barrier was observed (14±3 and 12±4 kJ mol^{-1} at 0.03 and 0.6 bar, respectively), while above the LCST higher apparent barriers were observed (37±2 and 30±2 kJ mol^{-1} at 0.03 and 0.6 bar, respectively).

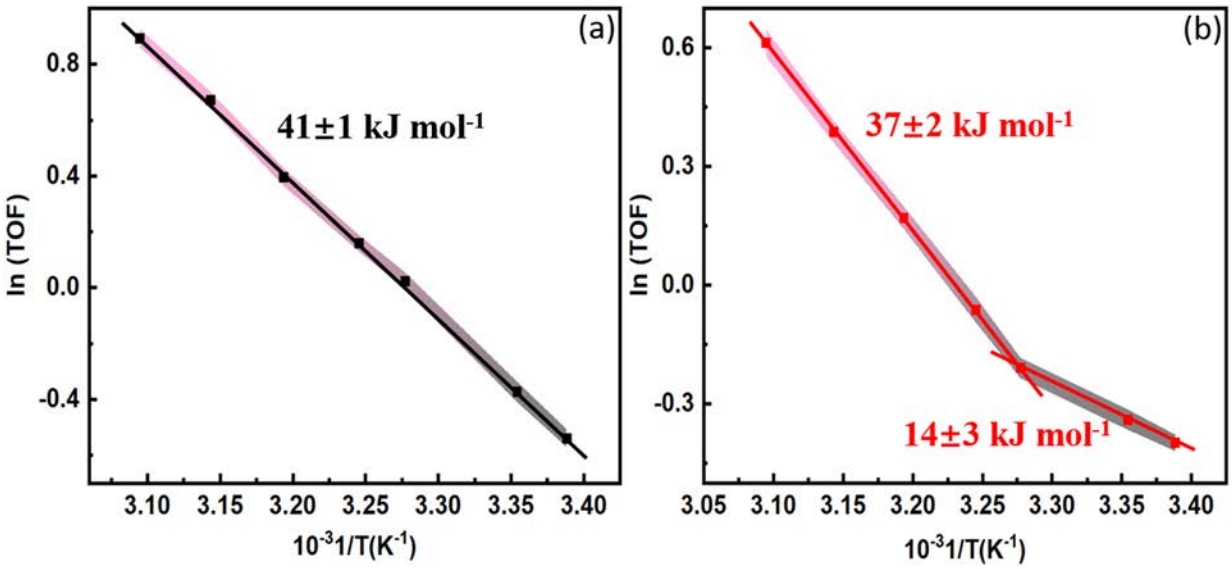

Figure 6. Temperature dependence of TOF at 0.03 bar H_2 pressure and 1mM nitrobenzene concentration. (a) Pd/SiO_2 catalyst; (b) Pd/SiO_2-p-NIPAM catalyst. The shades indicate the experimental error.

3.6 Nitrobenzene-polymer interactions and mobility

The dynamics of different components in the catalyst mixture has been studied in detail by NMR, both approaching intermolecular interactions and translational motion. While the NOESY data from Figure 2 indicated a collapse of the polymer brush structures at a temperature above the LCST by the loss of preferential interactions, the NOESY results (Figure S2, 1.67 g/L catalysts mixed with 5 mM NB in D_2O) indicated that there are no observable preferential interactions between catalyst and substrate. Since only protons were observed and the labile amides are complicated to interrogate, this data can only reveal partial information on intermolecular interactions.

Therefore, we performed diffusion ordered spectroscopy (DOSY) experiments, which can provide information for the different components of mixtures related to binding and interactions, influencing the hydrodynamic radius and consequently diffusivity.[38] These were performed in samples of 1.67 g/L of the p-NIPAM coated catalyst (Pd/SiO_2-p-NIPAM) with and without nitrobenzene (5 mM), and in 10 g/L free p-NIPAM, all dissolved in D_2O, for comparison (see Figure 7 and Table S1). Here, it was observed that the free diffusion coefficients of the solvent (water) in the presence of polymer-coated catalyst were similar to that of what is reported for free water,[39] at the same time, the diffusion coefficients of nitrobenzene are also consistent with the value when NB in pure water (Table S1).[40] We can thus remark these were not significantly altered by the presence of the polymer-coated catalyst.

For the p-NIPAM polymer in solution, it was observed that increasing the temperature led to slightly higher self-diffusion coefficients. Essentially, when the temperature was above the LCST, the polymer (free p-NIPAM) in the solution collapses and coagulates (Figure S4). Here, one would expect the mobility of the coagulated polymer to be lower than that of the dissolved polymer in solution. However, the higher temperature employed to conduct the measurement increases the Brownian motion of the agglomerated polymer leading to moderately higher self-diffusion coefficients (Figure S4).

The behavior of the p-NIPAM coated on Pd/SiO_2 catalyst, however, differed substantially from that of the polymer is solution. Here, it was observed that at low temperature the self-diffusion coefficient of p-NIPAM was c.a. seven time lower than that of the free p-NIPAM in solution. This can be attributed to the larger particle size and mass of the Pd-SiO_2-p-NIPAM (c.a. 570 nm) when compared to the free p-NIPAM dissolved in water. Strikingly, at temperatures above the LCST, diffusivity of the p-NIPAM coated on Pd/SiO_2 increased by c.a. one order of

magnitude. To rationalize this one could argue that at low temperatures, when the polymer is swollen, the strong interactions between the polymer brushes with the surrounding water molecules increases substantially the molecular friction of the colloidal particles in the media, which explains the low initial self-diffusion coefficient below the LCST. At high temperatures the polymer wettability in water decreases, i.e. p-NIPAM becomes hydrophobic, resulting in the collapse of the polymer brushes on the catalyst surface. The hydrophobicity of resulting surface effectively decreases the friction of the particles in the aqueous environment, resembling a slippery boundary. This explains the drastic enhancement in the self-diffusion coefficients of the p-NIPAM coated on Pd-SiO_2 above the LCST.

Notably, the presence of NB decreased the self-diffusion coefficient of p-NIPAM on the coated catalyst at high temperatures. This could be attributed to the increase in NB-polymer interactions at temperatures above the LCST in which the hydrophobic p-NIPAM can preferentially bind with NB over water, reducing its self-diffusion coefficient. This would be in line with previous data showing that the hydrophobic nitrobenzene molecules react at a much higher rate at elevated when using thermosensitive Au-PNIPAM yolk-shell systems.[4]

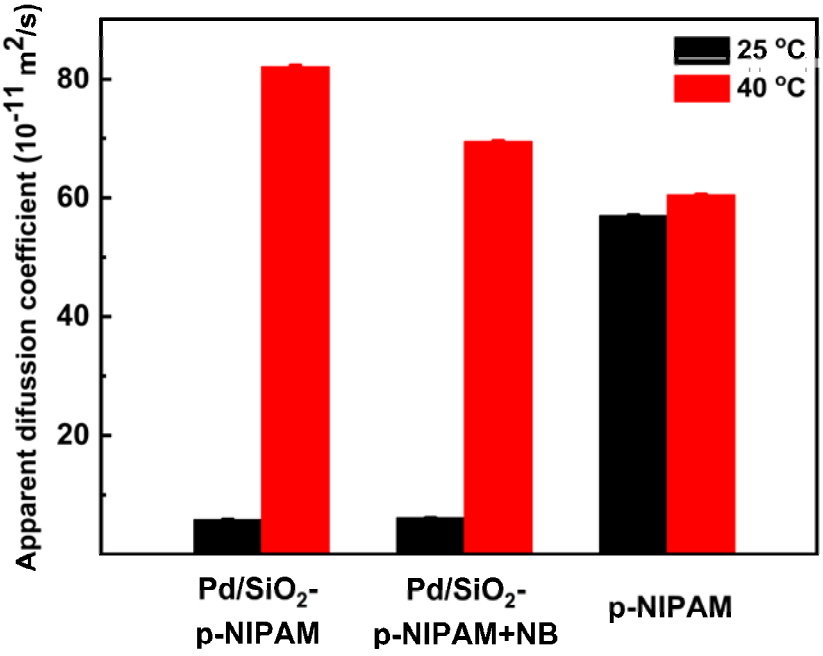

Figure 7. Apparent diffusion coefficients of p-NIPAM from the DOSY NMR experiments at 25 and 40 ºC for the three different samples studied. The methyl groups in p-NIPAM (labeled as 4 in Figure 2) were used as reporters for the diffusivity given their higher sensitivity.

4. Discussion

First, let us start with the summary of the observed trends in the reaction kinetic studies: (1) hydrogen and nitrobenzene compete for the same active sites as evidenced by the negative reaction orders on nitrobenzene at low hydrogen partial pressures on the Pd/SiO_2 (Figure 5), (2) the high hydrogen reaction order suggests that several pre-equilibration steps involving H-insertion are required prior the rate-determining step (Figure 5), (3) increasing temperature lowers the reaction orders of hydrogen and nitrobenzene (Figure 5), (4) addition of p-NIPAM coatings leads to lower reaction orders and TOFs (Figure 5 and Figure S11), (5) lower selectivity to PAP is observed on the Pd/SiO_2-p-NIPAM catalyst (Figure 4), and (6) a three-fold reduction of the apparent activation barrier at temperatures below the LCST was observed on the thermo-responsive catalyst, while above the LCST the apparent barriers resembled those measured on the parent catalyst (Figure 6).

4.1 NB hydrogenation mechanism

The high reaction orders obtained on the Pd/SiO_2 catalyst at low partial pressures as well as the competitive adsorption between nitrobenzene and hydrogen are both in agreement with the mechanism proposed by E. A. Gelder et al.[16] In this case, hydrogen insertion on nitrobenzene occurs on the metal surface in a sequential manner before the removal of the oxygen atom to form aniline, as shown in Figure 1 (green path).[17][18][19] This is in line with recent density functional theory (DFT) studies that show that the sequential mechanism offers the lowest barriers.[17][18] In these studies, the reduction of phenylhydroxylamine (PHA) to $C_6H_5NH^*$ is considered as the rate-limiting step. Furthermore, studies using *in-situ* infrared spectroscopy of nitrobenzene on Pd [41] have shown no evidence of dimer species via self-condensation. While it is possible that the condensation pathway to AN could play a role in this reaction the weakly acidic conditions used in this work do not favor this pathway.[42][43] Hence, it is very likely that the mechanism operating in our study follows the sequential hydrogenation pathway.

Next, one could use the observed apparent reaction orders to identify qualitatively the rate-determining step. For instance, if one assumes that the reaction involves dissociative chemisorption of hydrogen and molecular adsorption of nitrobenzene on the same active site, in which the adsorbed nitrobenzene would undergo sequential hydrogenation-dehydration reactions until the final product aniline is formed, then one could derive a Langmuir-Hinshelwood mechanism that could accommodate the observations herein observed. To

illustrate this a LH reaction expression has been developed in detailed in the supporting information section 4.1. Since our data suggests that the rate determining step must be after the addition of at least 5 hydrogen atoms, as indicated by the reaction order of hydrogen of 2.5, then one could propose two potentially assume a single rate determining step. As shown in equation 4, when the rate determining step is assumed to be the hydrodehydration of C_6H_5NHOH* surface intermediate the theoretical reaction orders in the low and high hydrogen pressure regime are between 2.5 and 1.5.

Single RDS (Step 7)

$$\mathbf{C_6H_5NHOH*} + \mathbf{H*} \rightarrow \mathbf{C_6H_5NH*} + \mathbf{H_2O*} \quad (4)$$

Experimentally, however, the lowest reaction order in hydrogen that we have observed is c.a. one. Furthermore, in this scenario, increasing temperature will lower the surface coverages leading to higher reaction orders for hydrogen and nitrobenzene, the results shown in Figure 5 indicate that increasing temperature lowers the reaction orders. Alternatively, the change in reaction order with temperature could be due to a change in the rate determining step.[21] In this scenario, the degree of rate control could shift from the late rate-determining step (i.e. high reaction orders) to the preceding reaction step (i.e. lower reaction orders) with increasing temperature. To account for this we consider a dual rate-determining step involving the reduction of the partly hydrogenated nitrosobenzene specie to phenylhydroxylamine (step 6 in the mechanism) and its subsequent hydrodeoxygenation reaction (step 7) (Equations 5 and 6 and complete derivation in the supporting information section 4.1.1).

Dual RDS (Steps 6 and 7)

$$\mathbf{C_6H_5NOH*} + \mathbf{H*} \rightleftharpoons \mathbf{C_6H_5NHOH*} + * \quad (5)$$

$$\mathbf{C_6H_5NHOH*} + \mathbf{H*} \rightarrow \mathbf{C_6H_5NH*} + \mathbf{H_2O*} \quad (6)$$

This equation can be simplified considering that recent *in-situ* FTIR spectroscopic data reports exclusively the presence of adsorbed nitrobenzene and partly hydrogenated nitroso-benzene species.[41] This would suggest that the catalyst surface is populated primarily by the reactants under these conditions, thus simplifying the reaction rate expression to equation 7.

$$r_{C_6H_5NO_2} = \frac{k_7 k_6 {K_1}^{2.5} \prod_{i=2}^{5} K_i [H_2]^{2.5} [C_6H_5NO_2]}{\left[k_{-6} + k_7 {K_1}^{0.5} [H_2]^{0.5}\right] * \left[1 + {K_1}^{0.5} [H_2]^{0.5} + K_2 [C_6H_5NO_2]\right]^2} \quad (7)$$

The reaction order in hydrogen in this case would fluctuate from 2.5 to 1 when the hydrogenation pressure is low and high, respectively, while nitrobenzene reaction orders would

vary between 1 to -1. Furthermore, increasing temperature shifts the degree of rate control to the early step explaining the lower reaction orders as previously shown for the hydrogenation of nitrate on Pd.[21]

4.2 Catalyst-polymer interplay

Compared to Pd/SiO_2 catalyst, the p-NIPAM brushes attached to the surface of the dense silica containing palladium nanoparticles (Pd/SiO_2) lowered the TOF (Figure 3), increased the selectivity to aniline from 88% to 97%, at the expense of halving the p-aminophenol selectivity (Figure 4). Also, the polymer-coated catalyst showed a significantly lower activation energy barrier when the temperature was below the LCST (Figure 6). The underlaying cause for these differences could be related to (1) mass transport limitations, (2) metal particle size effects, or (3) changes in the reaction energy landscape induced by the micro-solvation environment. In the next section we address each of these issues.

4.2.1 Mass transport effects

Internal mass transfer limitations are not possible as the catalyst support is dense and only the external surface contributes to catalytic activity. The diffusion of the reactants in the polymer layer is discussed in the supporting information section 3.1. Here, it was demonstrated that the polymer even in the collapsed state does not limit the mass transfer. The external mass transfer limitations have been also rigorously assessed via experiments and calculations as shown in supporting information section 3. The results show that external mass transfer limitations can be excluded. Further evidence of the kinetic control on the polymer-coated catalyst comes from the analysis of the apparent reaction orders (Figure 5). Here, we observed orders that fluctuate between 1 to 2.5 and -1 to 0 for hydrogen and nitrobenzene, respectively. Since mass transfer is a first order process[44] one can neglect the presence of diffusional limitations. In addition, Figure 6b shows that on the p-NIPAM coated catalyst the low apparent barriers are observed at temperatures below the LCST of 32°C. This is rather unexpected result as mass transfer limitations often become more dominant at high temperatures as the rate of diffusion, characterized by low activation barriers, cannot keep-up with the surface reaction kinetics.

Finally, the NMR-derived diffusivity measurements suggest that the polymer does not reduce the molecular mobility of the reactants. Here, it was observed that in the presence of $Pd\text{-}SiO_2$-p-NIPAM, both water and nitrobenzene have diffusion coefficients that are similar to those of free water [39] and nitrobenzene in pure water[40] respectively (Table S1). Therefore, one can

neglect the changes in the self-diffusion coefficient of the reactants in the presence of polymer brushes in the catalyst.

4.2.2 Metal particle size effects

The growth of p-NIPAM brushes on the Pd/SiO_2 surface decreased the Pd loading, possibly due to the loss of the largest palladium nanoparticles (> 2 nm) during the ATRP polymerization (Table 1 in chapter 3). This metal detachment shifted slightly the particle size distribution to smaller values. Here, one might argue that this could lead to a change in p-aminophenol selectivity without affecting the nitrobenzene conversion. For instance, Arai et al. reported that both the total conversion and aniline selectivity decreased with the Pt particle size, while the azobenzene selectivity slightly increased.[45] Similarly, J. Lyu et al. [46] observed that when the average Pd particle size increased from 2.1 to 28.4 nm, the selectivity of aniline decreased significantly from 22.3 % to 0.1 %. In the work herein presented, however, the Pd particle size only changed from c.a. 2.1 nm (Pd/SiO_2) to 1.9 nm (Pd/SiO_2-p-NIPAM), which cannot explain the large differences in aniline and p-aminophenol selectivity observed (Figure 4).

The lower reaction rate observed on the p-NIPAM coated catalyst is likely due to the partial blockage of active sites. Similar observations were reported by M. J. E. da Silva et al.[44] during the hydrogenation of nitrites on Pd/Al_2O_3-p-NIPAM. Furthermore, the changes in the particle size cannot explain the differences in activation energy barriers with temperature observed on the polymer-coated catalyst.

4.2.3 Solvation effects

Using the rate expression shown in equation 4 one can estimate the extent of solvation effects using the transition state treatments developed by J. A. Dumesic[47] and latter refined by D. Flaherty.[48] This analysis results in the rate expression shown in equation 8 (see supporting information section 5 for the detailed derivation).

$$\frac{r}{L} = \frac{k_b T}{h} \exp\left(\frac{\Delta S_{App}^{0,\ddagger} + \Delta S_{App}^{\varepsilon,\ddagger}}{R}\right) \exp\left(-\frac{\Delta H_{App}^{0,\ddagger} + \Delta H_{App}^{\varepsilon,\ddagger}}{RT}\right) [\mathrm{H_2}]^{2.5} [\mathrm{C_6H_5NO_2}]^{-1} \quad (8)$$

In this equation, L is the total number of active sites, r/L is the turnover frequency, k_b is the Boltzmann constant, h is the Planck constant, T is thermodynamic temperature, $\Delta S_{App}^{0,\ddagger}$ and $\Delta H_{App}^{0,\ddagger}$ are the apparent entropy and enthalpy of activation. Next, one could estimate the standard apparent enthalpy and entropy of activation by defining the Pd/SiO_2 catalyst as the

reference state for the standard conditions (see supporting information section 4.2). The $\Delta S_{App}^{0,\ddagger}$ and $\Delta H_{App}^{0,\ddagger}$ are obtained from Figure S12a. In this setting, any changes in the reaction rate upon addition of the p-NIPAM will be captured by the excess of enthalpy ($\Delta H_{App}^{\varepsilon,\ddagger}$) and entropy ($\Delta S_{App}^{\varepsilon,\ddagger}$) of activation. As a result, $\Delta S_{app}^{\ddagger} = \Delta S_{App}^{0,\ddagger} + \Delta S_{App}^{\varepsilon,\ddagger}$ and $\Delta H_{app}^{\ddagger} = \Delta H_{App}^{0,\ddagger} + \Delta H_{App}^{\varepsilon,\ddagger}$ can be calculated from Figure S12b for the Pd/SiO_2-p-NIPAM catalyst. Using the kinetic data gathered in Figure 5 to study the reaction mechanism and based on the derivation in sections 4.2 and section 5 of the supporting information, the excess enthalpies and entropies of activation were calculated (see Table 1).

Table 1. Enthalpy and entropy of activation for the Pd/SiO_2 and Pd/SiO_2-p-NIPAM catalysts and excess enthalpy and entropy estimated for the polymer coated catalyst.

Temperature (°C)	Pd/SiO_2		Pd/SiO_2-p-NIPAM		Excess	
	$\Delta S_{App}^{0,\ddagger}$ (J/mol*K^{-1})	$\Delta H_{App}^{0,\ddagger}$ (kJ/mol)	$\Delta S_{App}^{p-NIPAM,\ddagger}$ (J/mol*K^{-1})	$\Delta H_{App}^{P-NIPAM,\ddagger}$ (kJ/mol)	$\Delta S_{App}^{\varepsilon,\ddagger}$ (J/mol*K^{-1})	$\Delta H_{App}^{\varepsilon,\ddagger}$ (kJ/mol)
22-32	70.8	40.6	-17.6	14.2	-88.4	-26.4
32-50			58.2	37.3	-12.6	-3.3

At low temperatures (22-32 °C), i.e. when the polymer is swollen, a large negative excess of apparent entropy and enthalpy of activation is observed. This suggests that the lower apparent barriers are enthalpically driven by the stabilization of the transition state of the reaction via the polymer. This stabilization, however, comes at the expense of a drastic drop in the entropy change of activation. At temperatures above the LCST of p-NIPAM (32-50 °C), i.e. when the polymer is collapsed, the stabilization significantly diminishes as evidenced by a small drop in the excess of apparent entropy and enthalpy of activation. These results are in line with the observed loss of preferential interactions at elevated temperatures in the NOESY NMR in Figure 2c,d, and these results unambiguously show that thermo-responsive polymers can modify the catalyst in a completely reversible manner, the energy landscape of a catalytic reaction by changing the extent of enthalpic stabilization of the transition state is shown in Figure 8.

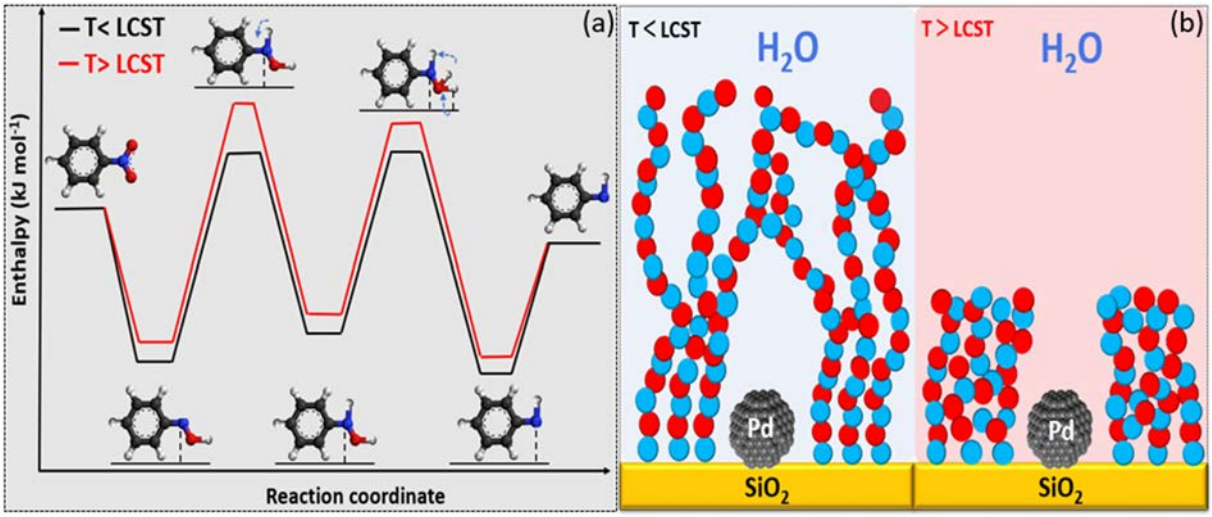

Figure 8. (a) Illustrative representation of the change in the reaction energy diagram of the nitrobenzene hydrogenation as a function of the extent of solvation effects induced by stimulus-responsive polymer p-NIPAM.

5. Conclusions

This work provides for the first time a mechanistic description of solvation effects, induced in an ON-/OFF- fashion by stimulus-responsive polymers during the reduction of nitrobenzene on Pd/SiO_2 catalysts. Detailed reaction kinetics, transition state treatments, and NMR studies demonstrate that the lower apparent activation barriers observed on p-NIPAM coated catalysts at low temperatures are driven by the enthalpic stabilization of the transition state. This reduction in the apparent enthalpy of activation came at the expense of reducing the apparent entropy of activation. We envision that this concept of stimulus-responsive solvation effects can be extrapolated to other catalysts and reaction processes occurring in the liquid phases such as biomass valorization, organic-synthesis, and pollution control.

References

[1] Y. Wang, A. Feng, J. Yuan, Application of stimuli-responsive polymer in catalyst systems of gold nanoparticles, Prog. Chem. 28 (2016) 1054.

[2] J. Zhang, M. Zhang, K. Tang, F. Verpoort, T. Sun, Polymer-based stimuli-responsive recyclable catalytic systems for organic synthesis, Small. 10 (2014) 32–46. https://doi.org/10.1002/smll.201300287.

[3] W. Lee, D. Kim, S. Lee, J. Park, S. Oh, G. Kim, J. Lim, J. Kim, Stimuli-responsive switchable organic-inorganic nanocomposite materials, Nano Today. 23 (2018) 97–123.

[4] S. Wu, J. Dzubiella, J. Kaiser, M. Drechsler, X. Guo, M. Ballauff, Y. Lu, Thermosensitive Au-PNIPA yolk-shell nanoparticles with tunable selectivity for catalysis, Angew. Chemie - Int. Ed. 51 (2012) 2229–2233. https://doi.org/10.1002/anie.201106515.

[5] Y. Lu, Y. Mei, M. Drechsler, M. Ballauff, Thermosensitive core-shell particles as carriers for Ag nanoparticles: Modulating the catalytic activity by a phase transition in networks, Angew. Chemie - Int. Ed. 45 (2006) 813–816. https://doi.org/10.1002/anie.200502731.

[6] M.J. Enes da Silva, A. Banerjee, L. Lefferts, J.A.F. Albanese, In-situ ATR-IR Spectroscopy Reveals Complex Absorption-Diffusion Dynamics in Model Polymer-Membrane-Catalyst Assemblies (PCMA), ChemCatChem. (2022). https://doi.org/10.1002/cctc.202101835.

[7] G. Wang, K. Kuroda, T. Enoki, A. Grosberg, S. Masamune, T. Oya, Y. Takeoka, T. Tanaka, Gel catalysts that switch on and off, Proc. Natl. Acad. Sci. 97 (2000) 9861–9864.

[8] S. Angioletti-Uberti, Y. Lu, M. Ballauff, J. Dzubiella, Theory of Solvation-Controlled Reactions in Stimuli-Responsive Nanoreactors, J. Phys. Chem. C. 119 (2015) 15723–15730. https://doi.org/10.1021/acs.jpcc.5b03830.

[9] M.A. Cole, N.H. Voelcker, H. Thissen, H.J. Griesser, Stimuli-responsive interfaces and systems for the control of protein–surface and cell–surface interactions, Biomaterials. 30 (2009) 1827–1850.

[10] S. Balamurugan, S. Mendez, S.S. Balamurugan, M.J. O'Brien, G.P. Lopez, Thermal response of poly (N-isopropylacrylamide) brushes probed by surface plasmon resonance, Langmuir. 19 (2003) 2545–2549.

[11] G. Liu, G. Zhang, Collapse and swelling of thermally sensitive poly (N-isopropylacrylamide) brushes monitored with a quartz crystal microbalance, J. Phys. Chem. B. 109 (2005) 743–747.

[12] G. Zhang, Study on conformation change of thermally sensitive linear grafted poly (N-isopropylacrylamide) chains by quartz crystal microbalance, Macromolecules. 37 (2004) 6553–6557.

[13] A.M. Tafesh, J. Weiguny, A review of the selective catalytic reduction of aromatic nitro compounds into aromatic amines, isocyanates, carbamates, and ureas using CO, Chem. Rev. 96 (1996) 2035–2052. https://doi.org/10.1021/cr950083f.

[14] S. Yalçınkaya, N. Çolak, Synthesis and Characterization of Poly(Aniline-co-o-Aminoaniline), Des. Monomers Polym. 15 (2012) 147–157. https://doi.org/10.1163/156855511X615038.

[15] F. Haber, Über stufenweise Reduktion des Nitrobenzols mit begrenztem Kathodenpotential, Z. Elektrochem. 4 (1898) 506–514.

[16] E.A. Gelder, S.D. Jackson, C.M. Lok, The hydrogenation of nitrobenzene to aniline: a new mechanism, Chem. Commun. (2005) 522–524.

[17] L. Zhang, J. Jiang, W. Shi, S. Xia, Z. Ni, X. Xiao, Insights into the hydrogenation mechanism of nitrobenzene to aniline on Pd 3/Pt (111): a density functional theory study, RSC Adv. 5 (2015) 34319–34326.

[18] L. Zhang, Z.-J. Shao, X.-M. Cao, P. Hu, Interface-tuned selective reductive coupling of nitroarenes to aromatic azo and azoxy: a first-principles-based microkinetics study, Phys. Chem. Chem. Phys. 21 (2019) 12555–12565.

[19] L. Zhang, Z.-J. Shao, X.-M. Cao, P. Hu, Insights into different products of nitrosobenzene and nitrobenzene hydrogenation on Pd (111) under realistic reaction conditions, J. Phys. Chem. C. 122 (2018) 20337–20350.

[20] M.J. Vaidya, Catalysis and Kinetics of Hydrogenation of Nitrobenzene to p-Aminophenol, (2002).

[21] P. Huang, Y. Yan, A. Banerjee, L. Lefferts, B. Wang, J.A.F. Albanese, Proton Shuttling Flattens the Energy Landscape of Nitrite Catalytic Reduction, J. Catal. (2022).

[22] W. Stöber, A. Fink, E. Bohn, Controlled growth of monodisperse silica spheres in the micron size range, J. Colloid Interface Sci. 26 (1968) 62–69.

[23] T.L. Hwang, A.J. Shaka, Water Suppression That Works. Excitation Sculpting Using Arbitrary Wave-Forms and Pulsed-Field Gradients, J. Magn. Reson. Ser. A. 112 (1995)

275–279. https://doi.org/10.1006/jmra.1995.1047.

[24] D.H. Wu, A.D. Chen, C.S. Johnson, An Improved Diffusion-Ordered Spectroscopy Experiment Incorporating Bipolar-Gradient Pulses, J. Magn. Reson. Ser. A. 115 (1995) 260–264. https://doi.org/10.1006/jmra.1995.1176.

[25] S. Balayssac, M.A. Delsuc, V. Gilard, Y. Prigent, M. Malet-Martino, Two-dimensional DOSY experiment with Excitation Sculpting water suppression for the analysis of natural and biological media, J. Magn. Reson. 196 (2009) 78–83. https://doi.org/10.1016/j.jmr.2008.09.022.

[26] F. Kunc, V. Balhara, A. Brinkmann, Y. Sun, D.M. Leek, L.J. Johnston, Quantification and Stability Determination of Surface Amine Groups on Silica Nanoparticles Using Solution NMR, Anal. Chem. 90 (2018) 13322–13330. https://doi.org/10.1021/acs.analchem.8b02803.

[27] F. Kunc, V. Balhara, Y. Sun, M. Daroszewska, Z.J. Jakubek, M. Hill, A. Brinkmann, L.J. Johnston, Quantification of surface functional groups on silica nanoparticles: Comparison of thermogravimetric analysis and quantitative NMR, Analyst. 144 (2019) 5589–5599. https://doi.org/10.1039/c9an01080g.

[28] F. Zeng, Z. Tong, H. Feng, NMR investigation of phase separation in poly(N-isopropyl acrylamide)/water solutions, Polymer (Guildf). 38 (1997) 5539–5544. https://doi.org/10.1016/S0032-3861(97)00118-3.

[29] M.V. Deshmukh, A.A. Vaidya, M.G. Kulkarni, P.R. Rajamohanan, S. Ganapathy, LCST in poly(N-isopropylacrylamide) copolymers: high resolution proton NMR investigations, Polymer (Guildf). 41 (2000) 7951–7960. https://doi.org/10.1016/S0032-3861(00)00174-9.

[30] L. Pei, H. Tan, M. Liu, R. Wang, X. Gu, X. Ke, J. Jia, Z. Zheng, Hydroxyl-group-modified polymeric carbon nitride with the highly selective hydrogenation of nitrobenzene to N-phenylhydroxylamine under visible light, Green Chem. 23 (2021) 3612–3622.

[31] Y. Liu, Y. Fang, X. Lu, Z. Wei, X. Li, Hydrogenation of nitrobenzene to p-aminophenol using Pt/C catalyst and carbon-based solid acid, Chem. Eng. J. 229 (2013) 105–110.

[32] Z. Zhang, H. Gai, Q. Li, B. Feng, M. Xiao, T. Huang, H. Song, Effect anions on the hydrogenation of nitrobenzene over N-rich Poly (ionic liquid) supported Pd catalyst, Chem. Eng. J. 429 (2022) 132224.

[33] L.B. Belykh, N.I. Skripov, T.P. Stepanova, F.K. Shmidt, Liquid-phase hydrogenation

of nitrobenzene and o-nitrochlorobenzene in the presence of phosphorus-containing palladium nanoparticles, Kinet. Catal. 56 (2015) 181–189.

[34] I.I. Obraztsova, N.K. Eremenko, Y.N. Velyakina, Reaction kinetics of nitrobenzene hydrogenation on a palladium catalyst supported on nanodiamonds, Kinet. Catal. 49 (2008) 401–406.

[35] C. V Rode, M.J. Vaidya, R. Jaganathan, R. V Chaudhari, Hydrogenation of nitrobenzene to p-aminophenol in a four-phase reactor: reaction kinetics and mass transfer effects, Chem. Eng. Sci. 56 (2001) 1299–1304.

[36] M. Turáková, T. Salmi, K. Eränen, J. Wärnå, D.Y. Murzin, M. Králik, Liquid phase hydrogenation of nitrobenzene, Appl. Catal. A Gen. 499 (2015) 66–76.

[37] E.H. Boymans, Pd and Pt nanoparticles as selective hydrogenation catalysts, Eindhoven Univ. Technol. Libr. (2015).

[38] T. Brand, E. Cabrita, S. Berger, Intermolecular interaction as investigated by NOE and diffusion studies Related papers, Prog. Nucl. Magn. Reson. Spectrosc. 46 (2005) 159–196. https://doi.org/10.1016/j.pnmrs.2005.04.003.

[39] M.H.S.H.A. Sacco, Temperature-dependent self-diausion coefficients of water and six selected molecular liquids for calibration in accurate 1h nmr pfg measurements, Phys. Chem. Chem. Phys. 2 (2000) 4740–4742.

[40] J. Feng, S.N.V.K. Aki, J.E. Chateauneuf, J.F. Brennecke, Hydroxyl radical reactivity with nitrobenzene in subcritical and supercritical water, J. Am. Chem. Soc. 124 (2002) 6304–6311.

[41] G. Richner, J.A. van Bokhoven, Y.-M. Neuhold, M. Makosch, K. Hungerbühler, In situ infrared monitoring of the solid/liquid catalyst interface during the three-phase hydrogenation of nitrobenzene over nanosized Au on TiO2, Phys. Chem. Chem. Phys. 13 (2011) 12463–12471.

[42] B. Wang, Z. Deng, Z. Li, Efficient chemoselective hydrogenation of nitrobenzene to aniline, azoxybenzene and azobenzene over CQDs/ZnIn2S4 nanocomposites under visible light, J. Catal. 389 (2020) 241–246.

[43] R. Zhao, C. Tan, Y. Xie, C. Gao, H. Liu, Y. Jiang, One step synthesis of azo compounds from nitroaromatics and anilines, Tetrahedron Lett. 52 (2011) 3805–3809.

[44] M.J.E. da Silva, L. Lefferts, J.A. Faria Albanese, N-isopropylacrylamide polymer brushes alter the micro-solvation environment during aqueous nitrite hydrogenation on Pd/Al2O3 catalyst, J. Catal. 402 (2021) 114–124. https://doi.org/10.1016/j.jcat.2021.08.003.

[45] F. Zhao, Y. Ikushima, M. Arai, Hydrogenation of nitrobenzene with supported platinum catalysts in supercritical carbon dioxide: effects of pressure, solvent, and metal particle size, J. Catal. 224 (2004) 479–483.

[46] J. Lyu, J. Wang, C. Lu, L. Ma, Q. Zhang, X. He, X. Li, Size-dependent halogenated nitrobenzene hydrogenation selectivity of Pd nanoparticles, J. Phys. Chem. C. 118 (2014) 2594–2601.

[47] M.A. Mellmer, C. Sanpitakseree, B. Demir, P. Bai, K. Ma, M. Neurock, J.A. Dumesic, Solvent-enabled control of reactivity for liquid-phase reactions of biomass-derived compounds, Nat. Catal. 1 (2018) 199–207. https://doi.org/10.1038/s41929-018-0027-3.

[48] D.S. Potts, D.T. Bregante, J.S. Adams, C. Torres, D.W. Flaherty, Influence of solvent structure and hydrogen bonding on catalysis at solid–liquid interfaces, Chem. Soc. Rev. 50 (2021) 12308–12337. https://doi.org/10.1039/d1cs00539a.

Supporting information

1. Characterization

1.1 NMR spectroscopy characterization

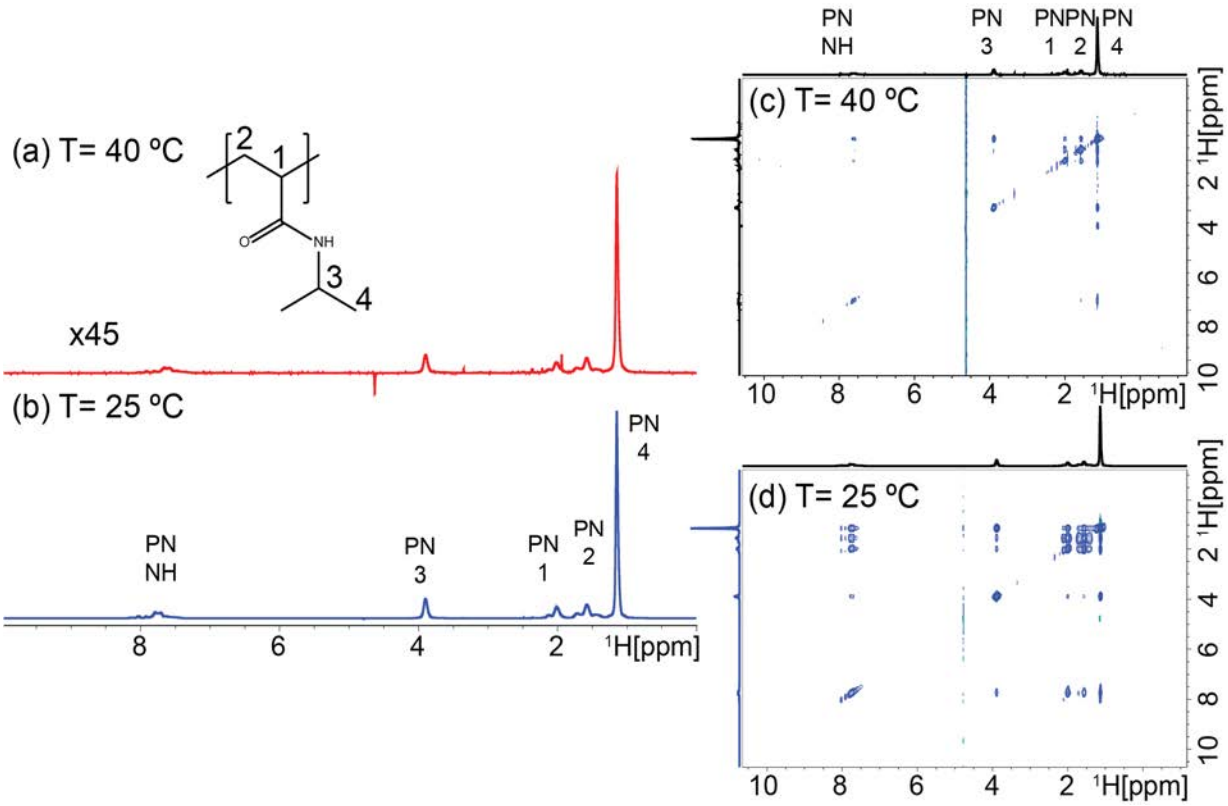

Figure S1. NMR characterization of p-NIPAM in 90% D_2O:10% H_2O. (a) and (b) correspond to water suppression spectra performed above (40 °C) and below LCST (25 °C), respectively. The intensities of spectrum (a) had to be scaled up by 45 times to match those of (b). (c) and (d) are water suppressed-NOESY spectra of the same sample, at 40 and 25°C, respectively.

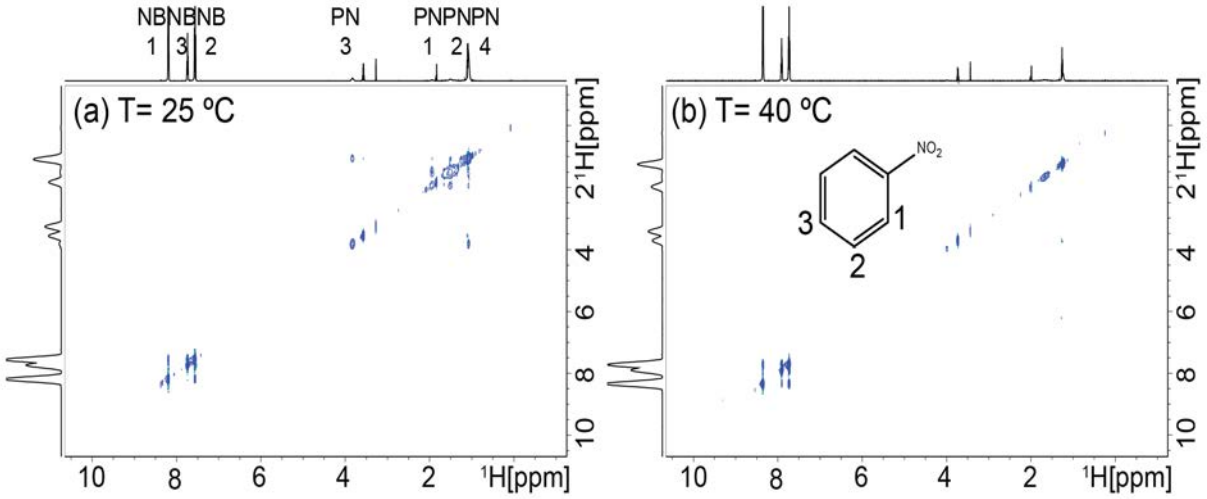

Figure S2. NOESY NMR spectra of Pd/SiO_2-p-NIPAM with NB in D_2O. (a) is the NOESY spectrum at below LCST (25 °C), and (b) is performed above LCST at 40 °C.

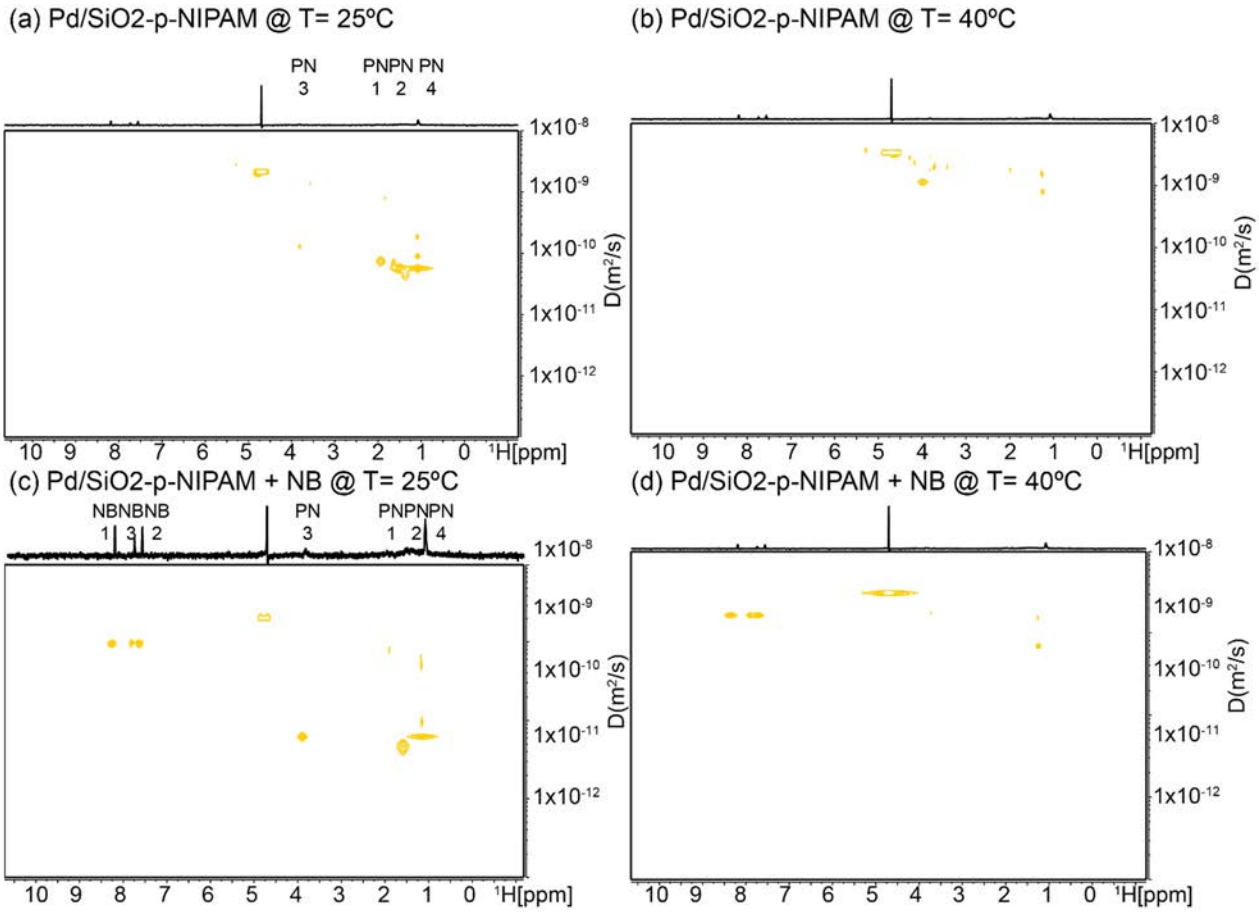

Figure S3. DOSY spectra of Pd/SiO_2-p-NIPAM in D_2O (a) below LCST (25 °C), and (b) above LCST. DOSY spectra of Pd/SiO_2-p-NIPAM with NB in D_2O (c) below LCST (25 °C), and (d) above LCST at 40 °C.

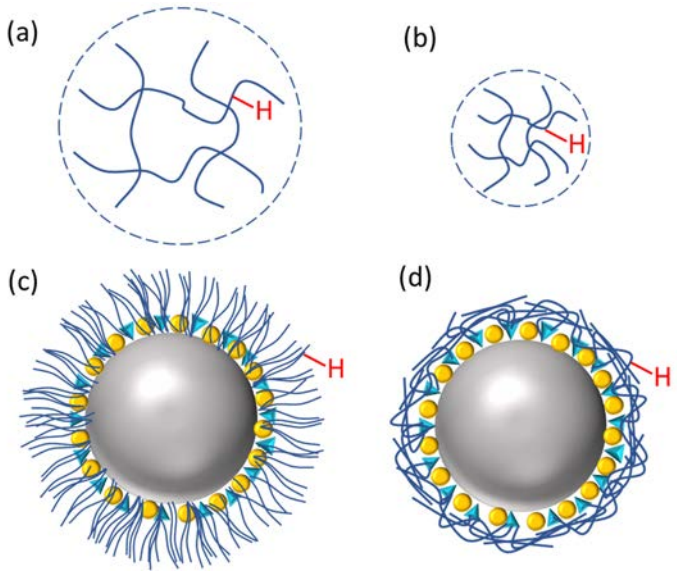

Figure S4. Polymer behavior with temperature, (a) Free p-NIPAM at a temperature below the LCST, (b) Free p-NIPAM at a temperature above the LCST. (c) Pd/SiO_2-p-NIPAM at a temperature below the LCST, (b) Pd/SiO_2-p-NIPAM at a temperature above the LCST.

Table S1. Quantitative results of the DOSY NMR measurements. Apparent diffusion coefficients taken for the different samples studied are shown in m^2/s; the methyl groups in p-NIPAM (labeled as 4 in Figure 2) were used as reporters for the diffusivity given their higher sensitivity. NP – Not Present; NM – Not measured (water suppressed experiments were performed).

Sample	T (°C)	D(p-NIPAM)	D(NB)	D(H_2O)
Pd/SiO_2-p-NIPAM in D_2O	25	$5.87\pm0.01\times10^{-11}$	NP	$2.00\pm0.01\times10^{-9}$
	40	$8.22\pm0.01\times10^{-10}$	NP	$3.18\pm0.01\times10^{-9}$
Pd/SiO_2-p-NIPAM w/ NB in D_2O	25	$6.16\pm0.01\times10^{-11}$	$9.30\pm0.01\times10^{-10}$	$2.04\pm0.01\times10^{-9}$
	40	$6.95\pm0.01\times10^{-10}$	$1.65\pm0.01\times10^{-9}$	$3.16\pm0.01\times10^{-9}$
p-NIPAM in 10 % D_2O	25	$5.70\pm0.01\times10^{-10}$	NP	NM
	40	$6.05\pm0.01\times10^{-10}$	NP	NM
Pure water	25	NP	9.2×10^{-10} [1]	2.3×10^{-9} [2]

2. Nitrobenzene hydrogenation reaction

2.1 Nitrobenzene and aniline concentration profile

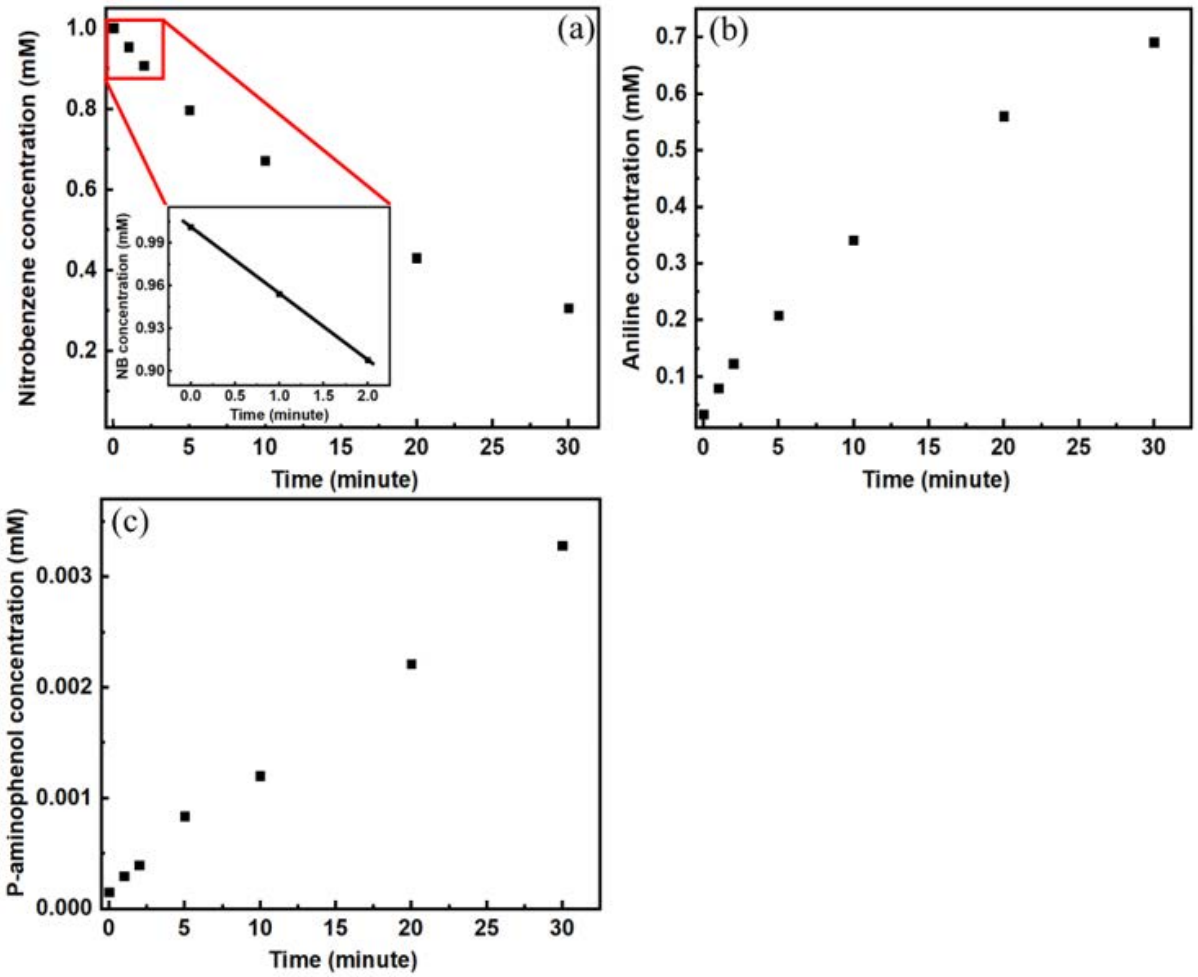

Figure S5. (a) nitrobenzene concentration as a function of time with 1mM initial nitrobenzene concentration and 0.8 bar hydrogen pressure, with a zoomed-in initial points that are used to obtain initial rate, (b) aniline concentration as a function of time, (c) p-aminophenol concentration as a function of time.

2.2 Summary of the reaction order

Table S2. Overview of the apparent reaction orders in nitrobenzene and hydrogen information in all ranges of the nitrobenzene and hydrogen concentrations.

		Low H_2 pressure		High H_2 pressure		
		H_2 order	NB order	H_2 order	NB order (Low con.)	NB order (High con.)
Pd/SiO_2	25 °C	2.4 ± 0.1	-1.1 ± 0.1	1.0 ± 0.1	1.0 ± 0.1	-0.6 ± 0.3
	32 °C	2.4 ± 0.1	-1.0 ± 0.1	1.1 ± 0.1	1.0 ± 0.1	-0.5 ± 0.2
	50 °C	1.5± 0.1	-0.6 ± 0.1	1.1 ± 0.1	0.4 ± 0.1	-0.1 ± 0.1
Pd/SiO_2-p-NIPAM	25 °C	1.4 ± 0.1	0 ± 0.1	1.0 ± 0.1	0.8 ± 0.1	0.3 ± 0.2
	32 °C	1.4 ± 0.1	0 ± 0.1	1.0 ± 0.1	0.6 ± 0.1	0.1 ± 0.2
	50 °C	1.3± 0.1	0 ± 0.1	1.0 ± 0.1	0.5 ± 0.1	0.1 ± 0.1

2.3 Arrhenius plot of the two catalyst

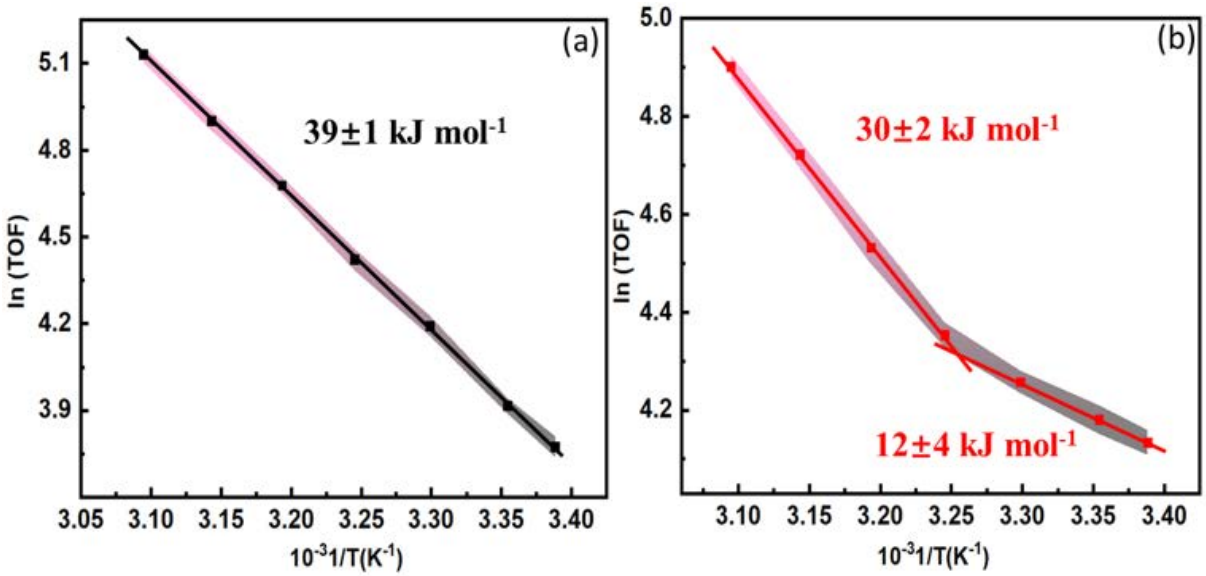

Figure S6. Arrhenius plot of the nitrobenzene hydrogenation reaction using (a) Pd/SiO_2 (b) Pd/SiO2-p-NIPAM at 0.6bar H_2.

3. Mass transfer

3.1 Internal mass transfer

3.1.1 Weisz-Prater criterion

Weisz-Prater criterion is normally used as the criteria to estimate whether pore diffusion resistance can significantly influence the reaction rate.[3]

$$C_{wp} = \frac{R_{obv} \times L^2 \times \rho_{Cat}}{C_s \times D_{eff}} \quad \text{(S1)}$$

Where R_{obv} is the reaction rate per mass of catalyst (mol*s^{-1}*kg^{-1}), L is characteristic length of a catalyst(m), ρ_{Cat} is the density of the catalyst particles (kg*m^{-3}), C_s is the reactant concentration at the particle surface (mol*m^{-3}), and D_{eff} is the effective diffusivity (m^2*s^{-1}).

$$L = d_p \quad \text{(S2)}$$

$$D_{eff} = \frac{D_{AB} \times \phi}{\tau} \quad \text{(S3)}$$

In which d_p is radius of the catalyst particles, D_{AB} is the bulk diffusion coefficient of nitrobenzene at 25 °C (0.92*10^{-5}cm^2/s),[1] ϕ is the particle porosity, normally between 0.2 and 0.7, and τ is the tortuosity, normally varies between 1 and 10.

If there is no obvious diffusion limitations: $C_{wp} < 1$

However, if there is severe diffusion limitations: $C_{wp} > 1$

According to the BET result and corresponding theoretical calculations, the silica support don't have any porous, so there is no need to consider the mass transfer limitation inside the SiO_2 support, only need to consider the internal mass transfer limitation caused by the external polymer coating.

1) Polymer length.

Here, we have considered a porosity (ϕ) of 0.2, tortuosity of (τ) 10, a self-diffusion coefficient of 0.92 *10^{-5} cm^2/s, and a polymer density of 1.07 g/cm^3.[4] Then, the Weisz-Prater value was estimated with increasing polymer length (see Figure S7). Here, one can recognize that for the polymer layers herein considered, with values from 7 to 71.9 nm in the dry and wet states, respectively, the C_{wp} is substantially below one.

$$D_{eff} = \frac{D_{AB}\times\phi}{\tau} = \frac{0.92*10^{-5}*10^{-4}\times0.2}{10} = 1.84*10^{-11} \quad \text{(S4)}$$

$$C_{wp} = \frac{R_{obv}\times L^2\times\rho_{Cat}}{Cs\times Deff} = \frac{5.82*10^{-3}\times L^2\times1.07*10^{3}}{1\times1.84*10^{-11}} \quad \text{(S5)}$$

$$= 3.38*10^{11}\times L^2$$

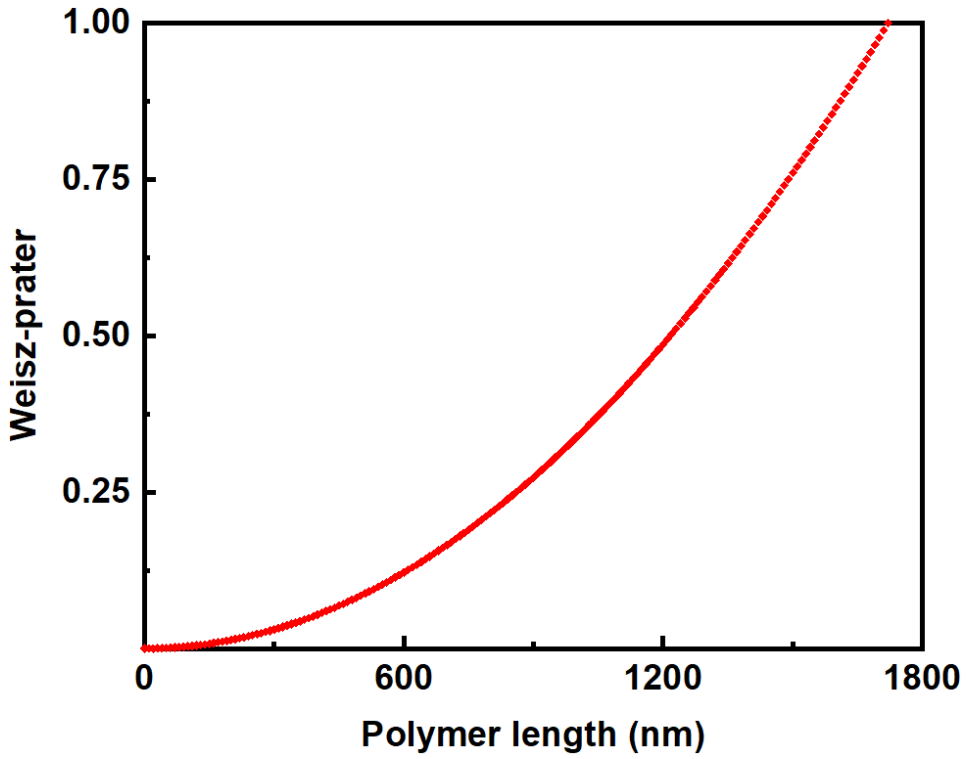

Figure S7. Weisz-Prater plot with different polymer length.

2) Tortuosity of the polymer layer.

To estimate the impact of the tortuosity τ on the Weisz-Prater we used a porosity of 0.2, self-diffusion coefficient of 0.92 $*10^{-5}$ cm^2/s, and a polymer length of 71.9 nm.

$$D_{eff} = \frac{D_{AB}\times\phi}{\tau} = \frac{0.92*10^{-5}*10^{-4}\times0.2}{\tau} = \frac{1.84*10^{-10}}{\tau} \quad \text{(S6)}$$

$$C_{wp} = \frac{5.82*10^{-3}*(7.19*10^{-8})^2*1.07*10^{3}\tau}{1*1.84*10^{-10}} = 1.75*10^{-4}\tau \quad \text{(S7)}$$

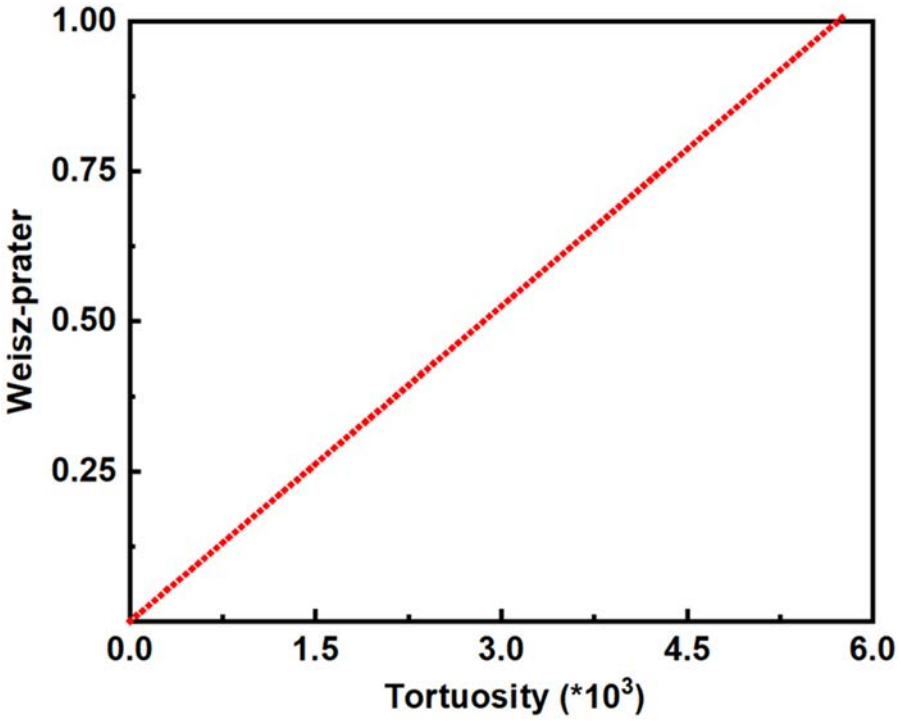

Figure S8. Weisz-Prater plot with different tortuosity τ.

Figure S8 shows that the Weisz-Prater number stays below one for the typical tortuosity values (3-10) encountered on porous catalysts. In this system with ultra-thin (nm) diffusional pathways, the τ must reach values that are at least three orders of magnitude higher than in a conventional porous catalyst, when the Weisz-Prater is equal to one, the tortuosity is $5.75*10^3$.

3) Self-diffusion coefficient of nitrobenzene in water (D_{AB}).

Here, porosity (ϕ) was fixed at 0.2, and tortuosity (τ) was equal to 10.

$$D_{eff} = \frac{D_{AB} \times \phi}{\tau} = \frac{D_{AB} * 10^{-4} \times 0.2}{10} = 2 * 10^{-6} D_{AB} \quad \text{(S8)}$$

$$C_{wp} = \frac{5.82*10^{-3} * (7.19*10^{-8})^2 * 1.07*10^3}{2*10^{-6} D_{AB}} = \frac{1.61*10^{-8}}{D_{AB}} \quad \text{(S9)}$$

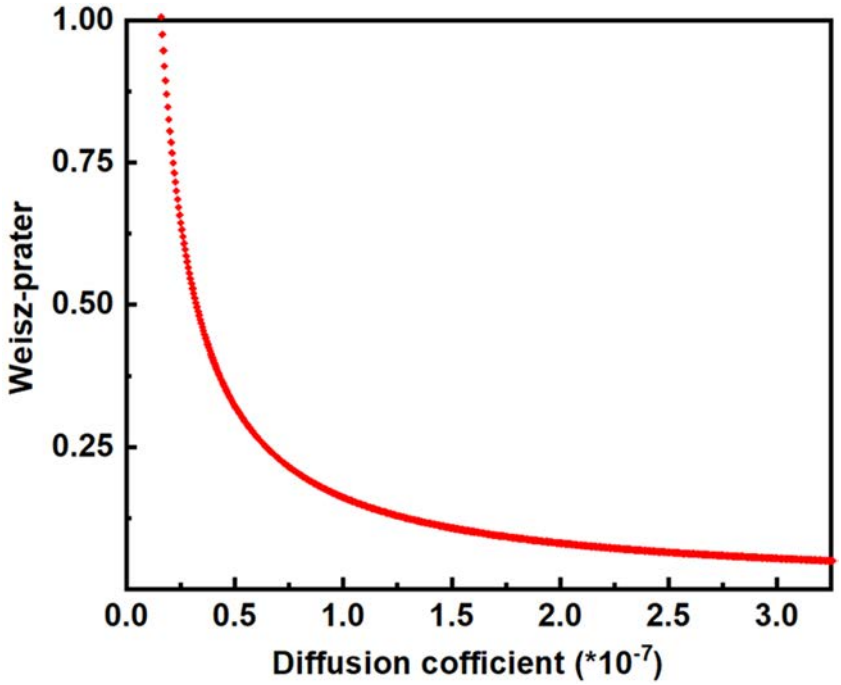

Figure S9. Weisz-Prater plot with diffusion coefficient D_{AB}.

Figure S9 shows the Weisz-Prater plot with diffusion coefficient DAB. When the Weisz-Prater equal to unity the DAB equals to $1.6*10^{-8}$, which is three orders of magnitude lower than that of nitrobenzene in water ($1.91*10^{-5}$ cm^2/s). also far away from the diffusion coefficient in p-NIPAM hydrogels $1.06*10^{-5}$ cm^2/s.[5]

4) Porosity of the polymer layer.

Here, the tortuosity (τ) was assumed to be equal to 10, the diffusion coefficient was $0.92*10^{-5}$ cm^2/s, and the polymer length was 71.9 nm.

$$D_{eff} = \frac{D_{AB}\times\phi}{\tau} = \frac{0.92*10^{-5}*10^{-4}\times\phi}{10} = 9.2 * 10^{-11} \times \phi \qquad \text{(S10)}$$

$$C_{wp} = \frac{5.82*10^{-3}*(7.19*10^{-8})^2*1.07*10^{3}}{9.2*10^{-11}\times\phi} = \frac{3.5*10^{-4}}{\phi} \qquad \text{(S11)}$$

As presented in Figure S10, the Weisz-Prater reaches a value close to one for porosities of c.a. $3.5*10^{-4}$, which are extremely small for a particle porosity (normally value between 0.2 and 0.7).

From these analyses, it shows conclusively that the polymer layer on these catalysts cannot exert sufficiently large mass transfer limitations to induce changes in the observed reaction kinetics.

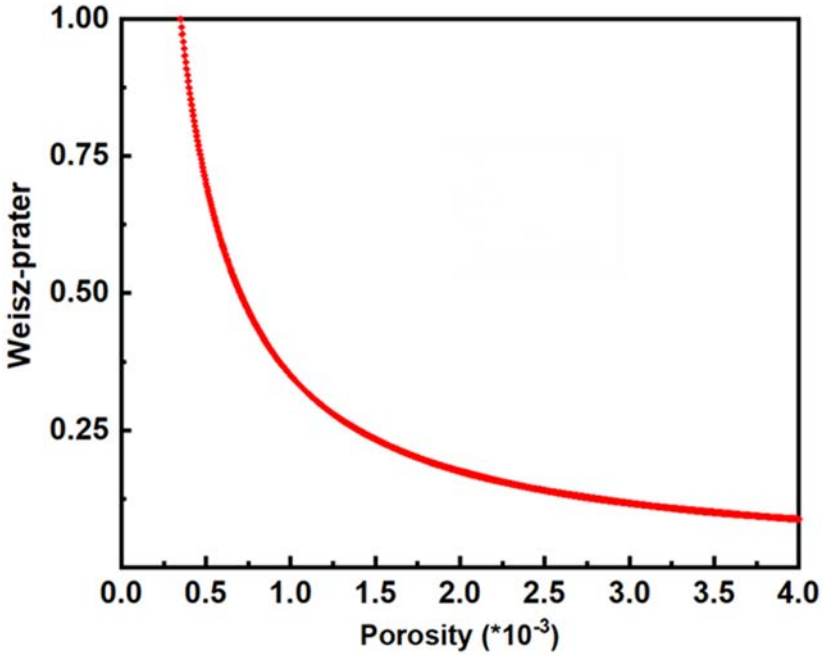

Figure S10. Weisz-Prater plot with particle porosity ϕ.

3.2 External mass transfer

3.2.1 Experiment check

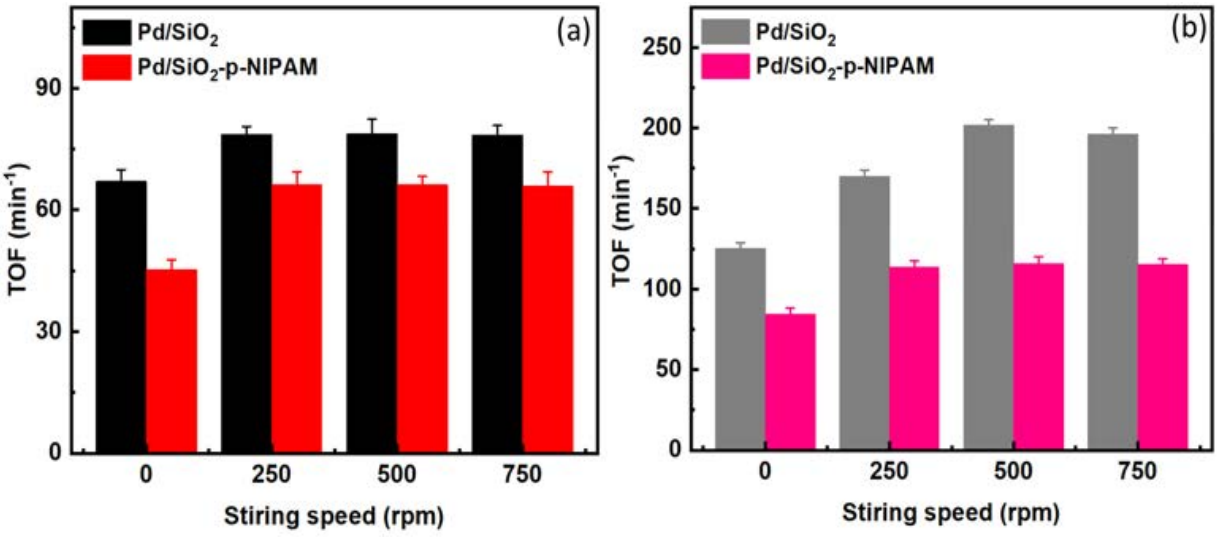

Figure S11. Influence of stirring speed on activity of the catalyst under 0.8bar H_2 pressure and 1mM nitrobenzene concentration. (a) Pd/SiO_2 and Pd/SiO_2-p-NIPAM at 25 °C. (b) Pd/SiO_2 and Pd/SiO_2-p-NIPAM at 50 °C.

3.2.2 Liquid-Solid mass transfer

The liquid-solid (L-S) mass transfer rate constant for nitrobenzene was calculated based on the literature.[6] Slip velocity of the catalyst particles is first calculated and used to conservatively estimate the mass transfer rate between aqueous solution and the solid. Stokes' law was assumed to apply and the particle's slip velocity was calculated by:

$$\mathcal{U}_t = \frac{g * d_p^2 * (\rho_p - \rho)}{18\mu} = \frac{9.81 * (5.57 * 10^{-7})^2 * (1890 - 1)}{18 * 1.002 * 10^{-3}} = 3.19 * 10^{-7}\ m * s^{-1} \quad \text{(S12)}$$

Where g is the standard gravity (9.81 m*s^{-2}), ρ_p is average density of the catalysts (1890 kg*m^{-3}), ρ is water density (1 kg*m^{-3} at 20 °C and d_p is the hydrodynamic size of the catalysts 5.57*10^{-7} m.[7] μ is absolute viscosity of water (1.002 g m^{-1} s^{-1} at 20 °C). Hence, the slip velocity is 4.26 * 10^{-7} m*s^{-1}. The corresponding Reynolds number was calculated by the following expression:

$$R_e = \frac{d_p * \mathcal{U}_t}{\upsilon} = \frac{5.57 * 10^{-7} * 3.19 * 10^{-7}}{1.003 * 10^{-6}} = 1.77 * 10^{-7} \quad \text{(S13)}$$

In which υ is kinematic viscosity of water (1.003 * 10^{-6} m^2*s^{-1} at 20 °C). The Reynolds number Re is $1.77 * 10^{-7} < 1$. This is indicative of laminar flow and Stokes law is applicable.

The Peclet number (Pe) and Sherwood number (Sh) were calculated based on the following equations:

$$Pe = \frac{d_p * \mathcal{U}_t}{D} = \frac{5.57 * 10^{-7} * 3.19 * 10^{-7}}{9.2 * 10^{-10}} = 1.93 * 10^{-4} \quad \text{(S14)}$$

$$Sh = \frac{4}{Pe} * ln\left(\frac{1}{1 - \frac{Pe}{2}}\right) = \frac{4}{1.93 * 10^{-4}} * \ln\left(\frac{1}{1 - \frac{1}{2} * 1.93 * 10^{-4}}\right) = 2.0 \quad \text{(S15)}$$

Where D is the nitrobenzene diffusion coefficient in pure water (9.2×10^{-10} m^2*s^{-1}).[1] The value of Sh is rather similar to the value for a particle in stagnant liquid (Sh=2), which is typical for a slurry reactor as the small particles essentially move with the liquid, with limited shear at the surface of the particles. The L-S mass transfer coefficient for nitrobenzene is calculated according to the following expression:

$$k_{ls} = \frac{D * Sh}{d_p} = \frac{9.2 * 10^{-10} * 2.00}{5.57 * 10^{-7}}\ m * s^{-1} = 3.3 * 10^{-3}\ m * s^{-1} \quad \text{(S16)}$$

The geometric surface area of the catalyst per volume of solution is:

$$a_s = \frac{A_p * m}{\rho_c * V_p * V_R} \quad \text{(S17)}$$

Where A_p is the geometric surface area of one catalyst particle (m^2), m is the mass of the catalyst in the experiments (kg), V_p is the volume of one catalyst particle (m^3), and V_R is the volume of reaction solution (m^{-3}).

$$a_s = \frac{4\pi * (2.5 * 10^{-7}\ m)^2 * 2 * 10^{-5}\ kg}{1890\ kg * m^{-3} * \frac{4\pi}{3} * (2.5 * 10^{-7}\ m)^3 * 3 * 10^{-4}\ m^3} = 423.3\ m^{-1} \quad \text{(S18)}$$

The mass transfer rate constant was calculated by multiplying the mass transfer coefficient by the geometric surface area of the catalyst per volume of solution:

$k_{ls} * a_s = 3.3 * 10^{-3} * 423.3 = 1.397\ s^{-1}$ = 83.81 min^{-1} (S19)

The mass transfer is first order. So the maximum mass transfer rate at concentration C_s in the bulk of the liquid, can be calculated by the following equation:

$$Max\ mass\ transfer\ rate = k_{ls} * a_s * C_s \quad \text{(S20)}$$

For example, at nitrobenzene concentration is 1 mM, the mass transfer rate is 83.81mM*min^{-1}, which is significantly larger than even the highest reaction rate (0.065 mM*min^{-1}) at the same nitrobenzene concentration. Therefore, L-S mass transfer is not limiting.

3.2.3 External mass transfer; combined G-L and L-S

Mears criterion allows to estimate any limitation at the G-L and/or L-S interface.[8,9] External mass transfer limitations can be neglected if the Mears' criterion listed below is satisfied:

$$\frac{-r_{obs}\rho_b d_p n}{K_c C_s} < 0.15 \quad \text{(S21)}$$

Where $-r_{obs}$ is the observed rate per unit mass of catalyst (mol*kg^{-1}*s^{-1}), n is the reaction order, d_p is the catalyst particle radius (m), ρ_b is bulk density of the catalyst (kg*m^{-3}), C_s is bulk concentration (mol*m^{-3}), and K_c is the mass transfer coefficient (m/s).

According to the previous section 3.2.2. calculation, the Re number is $1.77 * 10^{-7}$ much smaller than 1, which indicates the mass transfer coefficient can be estimated based on following equation. [8]

$$Sh = \frac{K_c * 2 * d_p}{D_{AB}} = 2 \quad \text{(S22)}$$

Where Sh is the Sherwood number, d_p is the catalyst particle radius (m), D_{AB} is H_2 gas phase diffusivity (m^2*s^{-1}). Here, the diffusivity D_{AB} for H_2 is $6.3*10^{-5}$ m^2*s^{-1}.[8]

$$K_c = \frac{D_{AB}}{d_p} = \frac{6.3 * 10^{-5}\ m^2 * s^{-1}}{2.5 * 10^{-7}\ m} = 252\ m * s^{-1} \quad \text{(S23)}$$

Table S3. Value of the different parameters and the results of Mears criteria

$-r_{obs}(H_2)$	$mol*s^{-1}*kg^{-1}$	$1.625*10^{-2}$
ρ_b	$kg*m^{-3}$	1890
n	N/A	1
d_p	m	$2.5*10^{-7}$
C_s (H_2)	$mol*m^{-3}$	0.624
K_c (H_2)	$m*s^{-1}$	252
Mears criteria (H_2)	N/A	$4.88*10^{-8}$

Based on the calculation, it shows that the gas-liquid and liquid-solid mass transfer limitation can be ignored.

4. Nitrobenzene hydrogenation mechanism and derivation

4.1 Jackson mechanism direct pathway

The nitrobenzene hydrogenation mechanism proposed by Jackson et al.[10] has been supported by previous work using density functional theory (DFT).[11][12][13] In addition, experimental work has shown that the condensation pathway is less favorable on palladium than the direct pathway.[14] These observations were in line with in-situ infrared spectroscopy data in which no evidence was found for the presence of intermediate species (e.g. azoxy- or azobenzene) for the condensation route.[15] Having said that, the overall rate equation is derived based on the elementary steps shown below in which the step 7 is selected as rate determine steps (RDS) in the direct hydrogenation mechanism.

$H_2 + 2 * \rightleftharpoons 2H *$ (equilibrium reaction 1; K_1)

$C_6H_5NO_2 + * \rightleftharpoons C_6H_5NO_2 *$ (equilibrium reaction 2; K_2)

$C_6H_5NO_2 * + H * \rightleftharpoons C_6H_5NO_2H * + *$ (equilibrium reaction 3; K_3)

$C_6H_5NO_2H * + H * \rightleftharpoons C_6H_5NO_2H_2 * + *$ (equilibrium reaction 4; K_4)

$C_6H_5NO_2H_2 * + H * \rightleftharpoons C_6H_5NOH * + H_2O *$ (equilibrium reaction 5; K_5)

$C_6H_5NOH * + H * \rightleftharpoons C_6H_5NHOH * + *$ (equilibrium reaction 6; K_6)

$C_6H_5NHOH * + H * \rightarrow C_6H_5NH * + H_2O *$ (reaction 7; k_7) RDS

Where * represents an empty site on the Pd surface and H* represents an oxygen atom adsorbed on the Pd surface, as an example for all surface species.

$$\theta_H = K_1{}^{0.5}[H_2]^{0.5}\theta_v \quad \text{(S24)}$$

$$\theta_{C_6H_5NO_2} = K_2[C_6H_5NO_2]\theta_v \quad \text{(S25)}$$

$$\theta_{C_6H_5NO_2H} = K_1{}^{0.5}K_2K_3[H_2]^{0.5}[C_6H_5NO_2]\theta_v \quad \text{(S26)}$$

$$\theta_{C_6H_5NO_2H_2} = K_1K_2K_3K_4[H_2][C_6H_5NO_2]\theta_v \quad \text{(S27)}$$

$$\theta_{C_6H_5NOH} = K_1{}^{1.5}K_2K_3K_4K_5[H_2]^{1.5}[C_6H_5NO_2]\theta_v \quad \text{(S28)}$$

$$\theta_{C_6H_5NHOH} = K_1{}^{2}K_2K_3K_4K_5K_6[H_2]^{2}[C_6H_5NO_2]\theta_v \quad \text{(S29)}$$

$$\theta_{C_6H_5NH} = K_1{}^{2.5}K_2K_3K_4K_5K_6K_7[H_2]^{2.5}[C_6H_5NO_2]\theta_v \quad \text{(S30)}$$

$$1 = \theta_H + \theta_{C_6H_5NO_2} + \theta_{C_6H_5NO_2H} + \theta_{C_6H_5NO_2H_2} + \theta_{C_6H_5NOH} + \theta_{C_6H_5NHOH} + \theta_v \quad \text{(S31)}$$

By substituting the above intermediate species to equation S31, the surface coverage for empty sites and overall rate equation are as follows.

$$\theta_v = \frac{1}{1+K_1{}^{0.5}[H_2]^{0.5}+K_2[C_6H_5NO_2]+K_1{}^{0.5}K_2K_3[H_2]^{0.5}[C_6H_5NO_2]+K_1K_2K_3K_4[H_2][C_6H_5NO_2]+ K_1{}^{1.5}K_2K_3K_4K_5[H_2]^{1.5}[C_6H_5NO_2]+K_1{}^{2}K_2K_3K_4K_5K_6[H_2]^{2}[C_6H_5NO_2]} \quad \text{(S32)}$$

$$r_7 = k_7\theta_{C_6H_5NHOH}\theta_H$$

$$= \frac{k_7K_1{}^{2.5}K_2K_3K_4K_5K_6[H_2]^{2.5}[C_6H_5NO_2]}{\left(1+K_1{}^{0.5}[H_2]^{0.5}+K_2[C_6H_5NO_2]+K_1{}^{0.5}K_2K_3[H_2]^{0.5}[C_6H_5NO_2]+K_1K_2K_3K_4[H_2][C_6H_5NO_2]+ K_1{}^{1.5}K_2K_3K_4K_5[H_2]^{1.5}[C_6H_5NO_2]+K_1{}^{2}K_2K_3K_4K_5K_6[H_2]^{2}[C_6H_5NO_2]\right)^2} \quad \text{(S33)}$$

4.1.1 Step 6,7 as RDS

If one assumes that (1) two steps contribute to the rate (e.g. step 6 and step 7) and (2) the pseudo-steady state approximation is valid in this system, then one could capture the experimentally observed reaction rates as follows:

$\mathbf{C_6H_5NOH} * + \mathbf{H} * \rightleftharpoons \mathbf{C_6H_5NHOH} * + *$ **(reaction 6; k_6) RDS**

$\mathbf{C_6H_5NHOH} * + \mathbf{H} * \rightarrow \mathbf{C_6H_5NH} * + \mathbf{H_2O} *$ **(reaction 7; k_7) RDS**

This leads to the following derivations:

$$\frac{d(\mathrm{C_6H_5NOH})}{dt} = k_6\theta_{\mathrm{C_6H_5NOH}}\theta_H - k_{-6}\theta_{\mathrm{C_6H_5NHOH}}\theta_v - k_7\theta_{\mathrm{C_6H_5NHOH}}\theta_H = 0 \quad \text{(S34)}$$

$$k_6\theta_{\mathrm{C_6H_5NOH}}\theta_H = [k_{-6}\theta_v + k_7\theta_H]\theta_{\mathrm{C_6H_5NHOH}} \quad \text{(S35)}$$

$$\theta_{\mathrm{C_6H_5NHOH}} = \frac{k_6\theta_{\mathrm{C_6H_5NOH}}\theta_H}{k_{-6}\theta_v + k_7\theta_H} \quad \text{(S36)}$$

$$\theta_{\mathrm{C_6H_5NHOH}} = \frac{k_6 {K_1}^2 K_2K_3K_4K_5[H_2]^2[\mathrm{C_6H_5NO_2}]\theta_v}{k_{-6} + k_7 {K_1}^{0.5}[H_2]^{0.5}} \quad \text{(S37)}$$

The rate expression for the consumption of nitrobenzene per catalyst site can be written as a function of the rate determining step ($r_{overall} = \frac{r_i - r_{-i}}{\sigma_i}$, i is the stoichiometry of the ith elementary step), then (assuming that r_7 is irreversible) one can obtain the following:

$$r_{\mathrm{C_6H_5NO_2}} = k_7\theta_{\mathrm{C_6H_5NHOH}}\theta_H \quad \text{(S38)}$$

By substituting equation S37 and equation S27 to equation S38, one obtains the following rate expression:

$$r_{\mathrm{C_6H_5NO_2}} = \left[k_7 \frac{k_6 {K_1}^{2.5} K_2K_3K_4K_5k_6[H_2]^{2.5}[\mathrm{C_6H_5NO_2}]}{k_{-6} + k_7 {K_1}^{0.5}[H_2]^{0.5}}\right] * {\theta_v}^2 \quad \text{(S39)}$$

By substituting equation S32 to equation S39, the following expression is obtained:

$$r_{\mathrm{C_6H_5NO_2}} =$$

$$\frac{k_7k_6{K_1}^{2.5}K_2K_3K_4K_5[H_2]^{2.5}[\mathrm{C_6H_5NO_2}]}{[k_{-6}+k_7{K_1}^{0.5}[H_2]^{0.5}]*\left[\begin{matrix}1+{K_1}^{0.5}[H_2]^{0.5}+K_2[\mathrm{C_6H_5NO_2}]+{K_1}^{0.5}K_2K_3[H_2]^{0.5}[\mathrm{C_6H_5NO_2}]+K_1K_2K_3K_4[H_2][\mathrm{C_6H_5NO_2}]+\\ {K_1}^{1.5}K_2K_3K_4K_5[H_2]^{1.5}[\mathrm{C_6H_5NO_2}]+{K_1}^2K_2K_3K_4K_5K_6[H_2]^2[\mathrm{C_6H_5NO_2}]\end{matrix}\right]^2}$$

(S40)

4.2 Derivation to calculate the entropy and enthalpy

To obtain the apparent kinetic constants for the two catalysts at temperatures above and below the LCST, one can simplify the reaction expression by considering that at the very beginning of the reaction, when we acquired the kinetic data (c.a. < 10 % Conversion), the surface is covered primarily by the reactants. Here, the use of high concentrations of nitrobenzene and low concentrations of hydrogen (e.g. 0.03 bar) led to reaction orders for H_2 and nitrobenzene of 2.5 and -1, respectively (Figure 4). This implies that nitrobenzene is the dominating specie on the catalyst surface. As a result, the above equation can be simplified to equation S41.

$$Rate = k_7\theta_{C_6H_5NHOH}\theta_H = \frac{k_7k_6{K_1}^{2.5}K_2K_3K_4K_5{k_{-6}}^{-1}[H_2]^{2.5}[C_6H_5NO_2]}{(K_2[C_6H_5NO_2])^2} \quad (S41)$$

Here, one can reorganize the equation S41 to get equation S42.

$$Rate = k_7\theta_{C_6H_5NHOH}\theta_H = k_7k_6{K_1}^{2.5}{K_2}^{-1}K_3K_4K_5{k_{-6}}^{-1}[H_2]^{2.5}[C_6H_5NO_2]^{-1} \quad (S42)$$

Here, $k_7{K_1}^{2.5}K_2K_3K_4K_5K_6$ can be simplified to K_{app} as these are the equilibrium constant before the rate determine step. Then, equation S43 is obtained.

$$Rate = k_7\theta_{C_6H_5NHOH}\theta_H = k_{apparent}[H_2]^{2.5}[C_6H_5NO_2]^{-1} \quad (S43)$$

Leveraging transition state theory treatments one can express the rate of reaction as a function of the apparent Gibbs free energy of activation.[16] The above rate equation for NB hydrogenation reaction can be converted to the equation below.

$$\frac{r}{L} = \frac{k_bT}{h}\exp\left(-\frac{\Delta G^{\ddagger}_{app}}{RT}\right)[H_2]^{2.5}[C_6H_5NO_2]^{-1} \quad (S44)$$

Considering that the frequency term is nearly constant for the reaction conditions herein employed one can substitute the term $\frac{k_bT}{h}$ by the average value of (6.74±0.22)*10^{11}. Here, L is the total active sites, $\Delta G^{\ddagger}_{app}$ is the apparent activation energy and A is $\frac{k_bT}{h}$. As $\Delta G^{\ddagger}_{app} = \Delta H^{\ddagger}_{app} - T\Delta S^{\ddagger}_{app}$, the rate can be further organized as equation S45.

$$\ln(\frac{\frac{r}{L}}{A}) - \ln([H_2]^{2.5}[C_6H_5NO_2]^{-1}) = \frac{\Delta S^{\ddagger}_{app}}{R} - \frac{\Delta H^{\ddagger}_{app}}{RT} \quad (S45)$$

Based on the reaction rate observed at different temperature with a low hydrogen pressure of 0.03bar (Figure 6), the $\Delta H_{app}^{\ddagger}$and $\Delta S_{app}^{\ddagger}$ are being calculated for the Pd/SiO_2 and Pd/SiO_2-p-NIPAM catalyst from the slope and intercept as show in Figure S12 respectively.

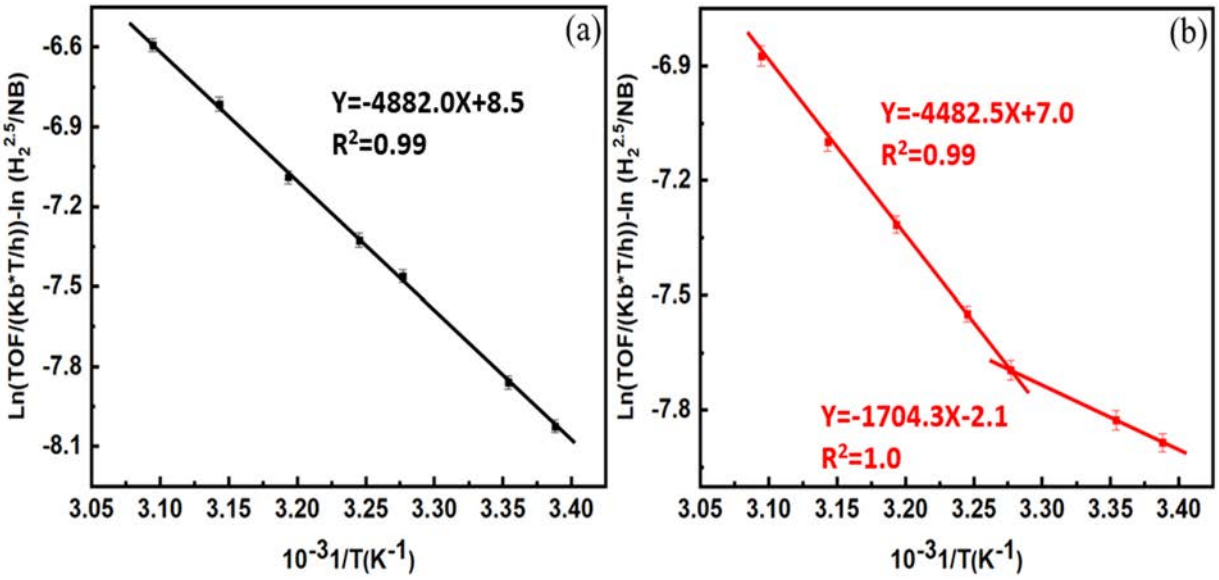

Figure S12. Transition state theory reaction rate vs temperature when using (a) Pd/SiO_2 and (b)Pd/SiO_2-p-NIPAM catalyst.

5. Solvation effect calculation

From the above section, the rate equation for NB hydrogenation reaction is

$$\frac{r}{L} = \frac{k_b T}{h} \exp\left(-\frac{\Delta G_{app}^{\ddagger}}{RT}\right) [\mathrm{H_2}]^{2.5} [\mathrm{C_6H_5NO_2}]^{-1} \quad \text{(S46)}$$

Here, $\Delta G_{app}^{\ddagger}$ is the apparent free energy barrier for the transition state, which is equal to the difference between the free energies of the transition state and the molecules in the liquid. On one hand, the Gibbs free energy of the transition state includes the free energy of the activated complex in the reference state ($G^{0,\ddagger}$) and the corresponding excess of Gibbs free energy $G^{\varepsilon,\ddagger}$ induced by its solvation layer. On the other hand, the Gibbs free energy of the reactive species in the liquid include the free energy of the molecule in the reference state (G_i^0) and its excess free energy in the solvent ($\mathrm{G}_i^{\varepsilon}$)

$$\Delta G_{app}^{\ddagger} = (G^{0,\ddagger} + G^{\varepsilon,\ddagger}) - (\mathrm{G}_i^0 + \mathrm{G}_i^{\varepsilon}) \quad \text{(S47)}$$

The excess free energy (G^{ε}) quantifies the impact of solvent interactions on the free energy of each component. The activity coefficients of reactive species can be related to excess Gibbs free-energy contributions as follows:

$$\gamma_i = \exp\left(\frac{G_i^{\varepsilon}}{RT}\right) \tag{S48}$$

Substituting equation S48 and equation S47 into equation S46 gives a rate expression restated in a manner that includes activity coefficients:

$$\frac{r}{L} = \frac{k_b T}{h} \exp\left(-\frac{G^{0,\ddagger} - \mathrm{G}^0_{H_2} - \mathrm{G}^0_{\mathrm{C_6H_5NO_2}}}{RT}\right) * \frac{\gamma_{\mathrm{H_2}} * \gamma_{\mathrm{C_6H_5NO_2}}}{\gamma_{\ddagger}} [\mathrm{H_2}]^{2.5} [\mathrm{C_6H_5NO_2}]^{-1} \tag{S49}$$

This leads to a new apparent rate expression that contains the excess Gibbs free energy and standard Gibbs free energy.

$$\frac{r}{L} = \frac{k_b T}{h} \exp\left(-\frac{\Delta G^{0,\ddagger}_{app} + \Delta G^{\varepsilon,\ddagger}_{app}}{RT}\right) [\mathrm{H_2}]^{2.5} [\mathrm{C_6H_5NO_2}]^{-1} \tag{S50}$$

As $\Delta G_{app} = \Delta \mathrm{H} - \mathrm{T}\Delta \mathrm{S}$, the rate can be further organized as equation S51.

$$\frac{r}{L} = \frac{k_b T}{h} \exp\left(\frac{\Delta S^{0,\ddagger}_{App} + \Delta S^{\varepsilon,\ddagger}_{App}}{R}\right) \exp\left(-\frac{\Delta H^{0,\ddagger}_{App} + \Delta H^{\varepsilon,\ddagger}_{App}}{RT}\right) [\mathrm{H_2}]^{2.5} [\mathrm{C_6H_5NO_2}]^{-1} \tag{S51}$$

References

[1] J. Feng, S.N.V.K. Aki, J.E. Chateauneuf, J.F. Brennecke, Hydroxyl radical reactivity with nitrobenzene in subcritical and supercritical water, J. Am. Chem. Soc. 124 (2002) 6304–6311.

[2] M.H.S.H.A. Sacco, Temperature-dependent self-diausion coefficients of water and six selected molecular liquids for calibration in accurate 1h nmr pfg measurements, Phys. Chem. Chem. Phys. 2 (2000) 4740–4742.

[3] D.M. Shuai, J.K. Choe, J.R. Shapley, C.J. Werth, J. Charles, C.J. Werth, Enhanced Activity and Selectivity of Carbon Nanofiber Supported Pd Catalysts for Nitrite Reduction, Environ. Sci. Technol. 46 (2012) 2847–2855. https://doi.org/10.1021/es203200d.

[4] L. Zhang, E.S. Daniels, V.L. Dimonie, A. Klein, Synthesis and characterization of PNIPAM/PS Core/Shell particles, J. Appl. Polym. Sci. 118 (2010) 2502–2511.

[5] M.K. Krušić, M. Ilić, J. Filipović, Swelling behaviour and paracetamol release from poly (N-isopropylacrylamide-itaconic acid) hydrogels, Polym. Bull. 2 (2009) 197–211.

[6] D.C. Hoekstra, K. Nickmans, J. Lub, M.G. Debije, A.P.H.J. Schenning, Air-curable, high-resolution patternable oxetane-based liquid crystalline photonic films via flexographic printing, ACS Appl. Mater. Interfaces. 11 (2019) 7423–7430.

[7] S.L. Greasley, S.J. Page, S. Sirovica, S. Chen, R.A. Martin, A. Riveiro, J. V. Hanna, A.E. Porter, J.R. Jones, Controlling particle size in the Stöber process and incorporation of calcium, J. Colloid Interface Sci. 469 (2016) 213–223. https://doi.org/10.1016/j.jcis.2016.01.065.

[8] W.S. Lee, Z. Wang, W. Zheng, D.G. Vlachos, A. Bhan, Vapor phase hydrodeoxygenation of furfural to 2-methylfuran on molybdenum carbide catalysts, Catal. Sci. Technol. 4 (2014) 2340–2352. https://doi.org/10.1039/c4cy00286e.

[9] D.E. Mears, Tests for Transport Limitations in Experimental Catalytic Reactors, Ind. Eng. Chem. Process Des. Dev. 10 (1971) 541–547. https://doi.org/10.1021/i260040a020.

[10] E.A. Gelder, S.D. Jackson, C.M. Lok, The hydrogenation of nitrobenzene to aniline: a new mechanism, Chem. Commun. (2005) 522–524.

[11] L. Zhang, J. Jiang, W. Shi, S. Xia, Z. Ni, X. Xiao, Insights into the hydrogenation mechanism of nitrobenzene to aniline on Pd 3/Pt (111): a density functional theory study, RSC Adv. 5 (2015) 34319–34326.

[12] L. Zhang, Z.-J. Shao, X.-M. Cao, P. Hu, Interface-tuned selective reductive coupling of nitroarenes to aromatic azo and azoxy: a first-principles-based microkinetics study, Phys. Chem. Chem. Phys. 21 (2019) 12555–12565.

[13] L. Zhang, Z.-J. Shao, X.-M. Cao, P. Hu, Insights into different products of nitrosobenzene and nitrobenzene hydrogenation on Pd (111) under realistic reaction conditions, J. Phys. Chem. C. 122 (2018) 20337–20350.

[14] M. Turáková, T. Salmi, K. Eränen, J. Wärnå, D.Y. Murzin, M. Králik, Liquid phase hydrogenation of nitrobenzene, Appl. Catal. A Gen. 499 (2015) 66–76.

[15] G. Richner, J.A. van Bokhoven, Y.-M. Neuhold, M. Makosch, K. Hungerbühler, In situ infrared monitoring of the solid/liquid catalyst interface during the three-phase hydrogenation of nitrobenzene over nanosized Au on TiO2, Phys. Chem. Chem. Phys. 13 (2011) 12463–12471.

[16] D.S. Potts, D.T. Bregante, J.S. Adams, C. Torres, D.W. Flaherty, Influence of solvent structure and hydrogen bonding on catalysis at solid–liquid interfaces, Chem. Soc. Rev. 50 (2021) 12308–12337. https://doi.org/10.1039/d1cs00539a.

Chapter 5

Modifying Reaction Rates and Stimulus-Responsive Behavior of Polymer-Coated Catalysts Using Aprotic Solvents

Abstract

The impact of solvent composition on the reaction rates and apparent activation barriers has been investigated by changing the solvent from pure water to mixtures with increasing concentrations of 1-methyl-2-pyrrolidone (NMP). When using pure NMP as the solvent, the activity was negligible and high activation energy barrier were observed. Switching to water led to faster reaction rates and lower apparent barriers. Considering that previous research has demonstrated that water molecules near the catalyst surface facilitate the hydrogen insertion on R-NO* and R-HNO* surface species via proton-electron transfer, it is possible to link the herein observed trends in activity for the nitrobenzene hydrogenation to the ability of the reaction media to shuttle protons during reaction. Furthermore, the polymer-induced solvation effect was investigated using thermo-responsive Pd/SiO_2-p-NIPAM catalyst. Here, we observed that the utilization of NMP shortcuts the thermo-responsive behaviour of p-NIPAM. This explains the constant particle size measured at different temperatures dynamic light scatting characterization (DLS). We speculate that this non-responsive behaviour of the poly(N-isopropylacrylamide) or p-NIPAM in the presence of NMP is the cause of the constant activation energy barrier at temperatures above and below the lower critical solution temperature (LCST) of the polymer (32 °C). When the reaction was conducted in pure water, the polymer-coated catalyst showed significant changes in both the apparent enthalpy and entropy of activation for temperatures below and above the LCST. This suggests that the microenvironment of surface species induced by the polymer can significantly influence the reaction rate.

1. Introduction

Solvents play a germane role in many chemical conversion processes as they can greatly alter the reactivity, selectivity, and stability of catalytic materials.[1][2][3] These high functional requirements greatly limit the potential candidates that can be employed as solvents. As a result, traditional solvents often comprise of aprotic organic molecules that can solvate simultaneously reactants, products, and catalysts. The high toxicity of these molecules, however, has become a major issue in the specialty chemical industry. This has triggered substantial research in developing more sustainable and environmentally friendly solvents. In this context, water is a non-toxic and sustainable solvent that is ubiquitous in naturally occurring biological processes. Because of the high polarity of water molecules, it is possible to conduct catalytic reactions involving oxygen-containing molecules, such as those found in biomass. For this reason, aqueous reaction environments have gained increasing attention to produce fuels and chemicals from bio-derived feedstocks. While water molecules can act as ideal solvents for polar species, their polarity, proton-conductive character, and strong hydrogen bonding ability can interfere with key processes occurring on heterogeneous catalysts. These so-called “solvation effects” are induced by the structure and chemical interaction of water molecules with chemisorbed species and catalysts, which can greatly modify apparent activation barriers, selectivity, and reaction rates. Previous research has found that the presence of water can enhance the reaction rate through (1) water-assisted remote bond polarization in the liquid phase, (2) H-shuttling for H-assisted C−O and N-O dissociation reactions on metals, (3) charge separation and water promotion in H transfer in carbonyl hydrogenation reactions, and (4) co-catalyst as dissociated water.[4]

The utilization of water as solvent, however, is greatly hindered in many cases by the low solubility of the hydrophobic compounds in the aqueous environment. An interesting proposition is to overcome this limitation by creating miscible liquid mixtures of H_2O and dipolar aprotic solvents. By increasing the concentrations of water in the liquid phase thanks to the dipolar aprotic solvent, the reaction rate, selectivity, and mass transfer can be strongly accelerated. For instance, P. Lozano et al. reported that water-miscible aprotic solvents enhanced greatly the synthetic activity proportionally to their hydrophilicity properties.[5] J. He et al.[6] studied the conversion of cellulose to levoglucosenone and 5-hydroxymethylfurfural using polar aprotic solvent–water mixtures, reporting that increasing the water content (up to 5 wt.%) results in high yields towards 5-hydroxymethyl furfural (5-HMF). M. Mohan et al.[7] reported that the protic or aprotic solvents can be added as cosolvent to

reduce the viscosity of IL's. The lower viscosity helped to accelerate the reaction as higher mass transfer rates can be achieved.

In this context, the impact of solvents on nitrobenzene hydrogenation has been widely studied in the past as this an archetypical chemistry in the synthesis of aromatic amines. This is an industrially relevant reaction for the manufacturing of aniline (AN), which is used in the production of dyes, pharmaceuticals, resins, varnishes, perfumes, and vulcanizing rubber.[8] Another important product is p-aminophenol (PAP), which is an intermediate for the manufacture of phenacetin, acetanilide, and paracetamol.[9] F. Leng et al. [10] reported that the nitrobenzene hydrogenation reaction is solvent sensitive and proceeds more quickly in methanol than in ethanol, and isopropyl alcohol. The authors ascribed the observed trend to the differences in relative permittivity (ε_r), which follows the order MeOH (ε_r = 32.7) > EtOH (ε_r = 24.5) > iPrOH (ε_r = 17.9). It has been proposed that the interaction between the reactant and solvent is the dominant factor that influences the overall effect of solvent on hydrogenation rate. G. Quartarone et al. reported that the reaction is practically inhibited when using dimethyl sulfoxide as the solvent for nitrobenzene hydrogenation,[11] while high activity is observed in protic solvent (e. g. H_2O and alcohols).[10][12] Despite the efforts in identifying these solvent-catalytic performance relationships, there are no reports on the impact of aprotic solvents on the performance of so-called stimulus-responsive catalysts.

The hydrogenation of nitrobenzene (NB) was used as a probe reaction to study the interplay between the solvent chemistry and the catalytic performance of thermo-responsive catalysts consisting of Pd clusters supported on non-porous silica spheres coated with poly(N-isopropylacrylamide) of p-NIPAM. To interrogate these stimulus-responsive catalysts we conducted detailed nitrobenzene hydrogenation kinetics in NMP/H_2O mixtures with varying compositions on conventional and polymer coated catalysts. Here, we assessed two potential working hypotheses: (1) if proton shuttling is not relevant for the RDS, then changing the solvent to a non-protonic molecular should not affect the reaction rate, and (2) if p-NIPAM is used in an aprotic solvent, then the activation energy barrier should change with temperature variation below and above the LCST when the polymer becomes hydrophilic and hydrophobic, respectively. Surprisingly, our results suggest that the ability to shuttle protons in the reaction media is key to achieve measurable reaction rates, and that aprotic solvents perturbed the stimulus-responsive behaviour of the p-NIPAM and thus its ability to modify the reaction kinetics at temperatures above and below the LCST.

2. Experimental section

2.1 Materials

1-methyl-2-pyrrolidinone (NMP, 99%) Tetraethyl orthosilicate (TEOS, 98 %), Nitrobenzene (NB, ≥99.0%), ammonium hydroxide solution (NH_4OH, 25 % (NH_3 basis)), sodium hydroxide (NaOH, 99 %), Tetraamminepalladium(II) nitrate solution ($Pd(NH_3)_4(NO_3)_2$, 10 wt. % in H_2O, 99.99%), sodium hydroxide (NaOH, 99 %), (3-aminopropyl) triethoxysilane (APTES, 99%), triethylamine (Eth_3N, 99.5%), Bromoisobutyryl bromide (BIBB, 98%), copper(II) bromide ($CuBr_2$, 99%), 1,1,4,7,10,10-hexamethyltriethylenetetramine (HMTETA,97%), L-ascorbic acid (99%), methanol (99.9%), ethanol (99.8%) and 1-Methyl-2-pyrrolidinone (99 %) were purchased from Sigma-Aldrich and used as received. N-isopropylacrylamide (NIPAM, Sigma-Aldrich, 97%) was purified by recrystallization in n-hexane (Sigma-Aldrich, 99.1 %) and stored below 4 °C prior to use. Tetrahydrofuran (THF, Sigma-Aldrich, 99.8%) was dried for at least one day over 4 Å molecular sieves (Honeywell) before use. All the aqueous solutions were prepared using ultra-purified water obtained from a water purification system (Millipore, Synergy).The glass reactor (Duran baffled, wide mouth bottle gls 80) with a diameter of 10.1 cm and a height of 22.2 cm. Syringe filter (PTFE 0.2 μm, Whatman), Syringe (BD Plastipak).

2.2 Catalyst preparation

2.2.1 Synthesis of SiO_2 spheres and Pd/SiO_2 catalyst

The SiO_2 spheres and Pd/SiO_2 were synthesized following our previous method.[13] In short, The SiO_2 spheres were prepared using the method reported by Stöber et al.[14] to get dense Silica spheres. After that, the Pd/SiO_2 catalyst was prepared using the strong electrostatic adsorption (SEA) method to load Pd on the surface of obtained SiO_2 spheres.

2.2.3 Synthesis of Pd/SiO_2-p-NIPAM catalyst

The p-NIPAM brush modified Pd/SiO_2 particles were synthesized via the 'grafted from' technique so-called surface-initiated atom transfer radical polymerization (ATRP). The synthesis was performed on bromine functionalized silica particles and carried out in a methanol/water solvent mixture (4:1 v/v) and reagents NIPAM/$CuBr_2$/HMTETA/ascorbic acid was used in the molar ratios 900/1.5/15/10, with a monomer to solvent mass ratio of 0.058/1. The comprehensive particle preparation and brush synthesis protocol are available in the chapter 3 (section 2 in SI).

2.3 Catalyst characterization

Brunauer–Emmett–Teller (BET) surface area analysis was conducted by using a Micromeritics Model ASAP 2400 instrument. For each analysis, 0.2–0.3 g of sample was degassed at 120 °C for 24 h before measurement. The transmission electron microscopy (TEM) analysis results were obtained by using a Tecnai F30 field emission TEM. The Scanning Electron Microscopy (SEM) was conducted by using a JEOL, LA6010 with a resolution of 4 nm @ 20 kV. The metal loading of the Pd/SiO_2 samples was determined by X-ray fluorescence (XRF) (Bruker, S8 TIGER). The metal dispersion of the Pd/SiO_2 samples was determined by CO chemisorption at room temperature (Micromeritics, Chemisorb 2750). The samples were reduced in H_2 at room temperature for 1 h and then flushed in He for 30 min. After that, CO was introduced as pulses and the response was recorded using a TCD detector. Dynamic light scattering (DLS) was conducted by using a Malvern Mastersizer 2000 (0.3-300 μm).

2.4. Catalytic tests

The nitrobenzene hydrogenation reaction was conducted in a 1L batch reactor with a temperature range from 22-50 °C. The solution is buffered by maintaining a constant CO_2 gas pressure (0.1 bar). The reactor used for the reaction has four connections on the reactor lid for gas-in, gas-out, sampling, and stirring shaft equipped with 4 stirring blades. The reaction was conducted by adding different ratios of NMP/H_2O as the solvent to get a volume of 150 ml and stirred at 500 rpm under continuous hydrogen flow for at least 1 h, removing dissolved oxygen and reducing the catalyst. After that, the reaction is started by adding 1mL nitrobenzene (150 mM in NMP) to the glass reactor. During the catalytic test, samples were collected using a 2.5 mL syringe and filtered using a syringe filter to remove catalyst particles. The reactant and product were measured using high-performance liquid chromatography (Shimadzu HPLC10AVP) equipped with an autosampler.

The typical experiment plot for nitrobenzene concentration, aniline (AN), and p-aminophenol (PAP) concentration changes over time and Turnover Frequency (TOF) show in chapter 4 (Figure S5)

3. Results and discussion

3.1 Catalyst Characterization

Dynamic light scatting (DLS) measurements were conducted to assess the changes in the particle size of the catalysts as a function of temperature (Figure 1). Here, D_o is the average diameter of the particle at 25 °C, while D_i is the diameter measured at different temperatures. The results show that the particle size of the Pd/SiO_2 catalyst is almost constant with the temperature, while the particle size of the polymer coated catalyst decreases with increasing temperature when using pure water as solvent. Notably, the presence of NMP attenuated the polymer phase transition from swollen to collapse as the temperature increased. Previous research has shown that p-NIPAM swells strongly in NMP at a temperature below the LCST.[15][16] When the temperature increases, the polymer becomes hydrophobic, favoring the absorption of NMP molecules over water. As a result, the effective polymer thickness stays constant with increasing temperature.

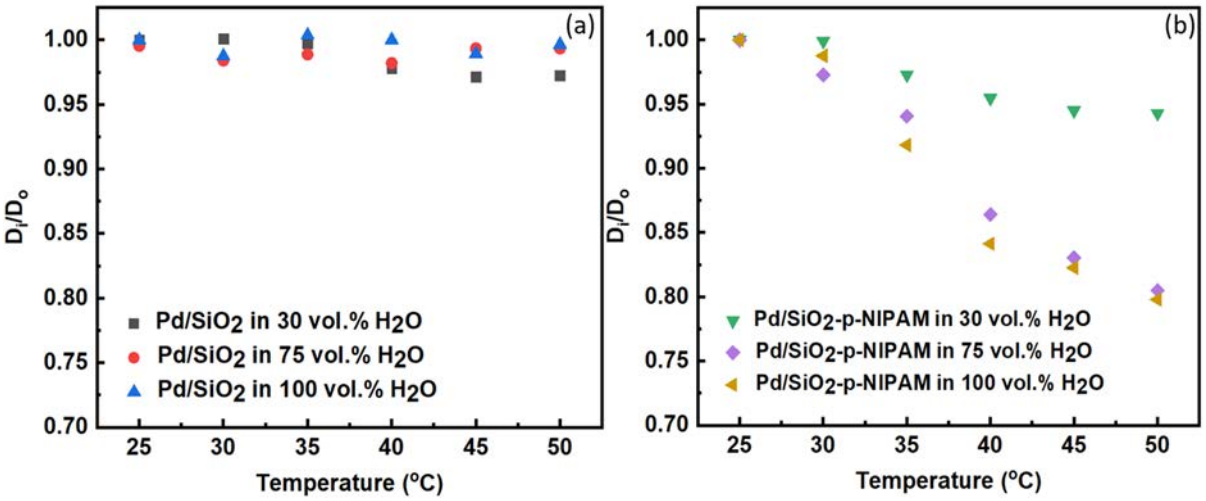

Figure 1. Dynamic light scatting measurement of the catalyst in different ratio of H_2O/NMP using (a) Pd/SiO_2 and (b) Pd/SiO_2-p-NIPAM catalysts.

3.2 Catalytic performance using H_2O/NMP as solvent

The interplay between the observed catalytic activity and the solvent-polymer interaction was interrogated using the intrinsic kinetics measured on both the parent and polymer-coated catalysts. For this purpose, increasing concentrations of water in the liquid phase were employed to trigger the changes in the solvation layer around the active site. Here, one can notice that the polymer-coated catalyst has a slightly lower Turn Over Frequency (TOF) than the parent Pd/SiO_2 (Figure 2). A recent study by M. J. E. da Silva et al.[17] showed that p-NIPAM polymers can interact with the Pd surface, leading to lower reaction rates. Similar results were reported by Y. Zhao et al.[18] where polymer segments block partly the active

sites, suggesting that polymers can occupy sites on the catalyst surface leading to slightly lower TOFs.

Next, it was observed that the activity decreased for both catalysts when NMP was present in the solvent, reaching negligible activities for pure NMP. Low activities in the presence of NMP have been reported in earlier work. Unfortunately, there is no clear consensus on how the solvent molecules of NMP modify the activity of supported metal catalysts. For instance, J. Panpranot et al.[19] conducted hydrogenation of cyclohexene in different organic solvents using a Pd/SiO_2 catalyst. Here, it was found that the use of NMP as solvent leads to lower conversions, which is in line with the observations herein presented. They also concluded that the use of highly polar organic solvents can result in low hydrogenation activities. In another study it was reported that low activities are obtained when using dipole aprotic solvents. In that case, the poor performance was attributed to metal sintering and leaching during the reaction.[20] While it is true that operating in liquid phase can lead to catalyst stability issues, the mild temperatures and pH values employed in our experiments would not enable facile sintering and/or lixiviation of the metal. Clearly, these studies fail in providing convincing arguments for the low activity of Pd in the presence of NMP.

Recently, it is has become clear that water can enhance reaction rates via H-shuttling processes occurring in H-insertion reactions, such as hydrogenation of phenol,[21] and Fischer−Tropsch synthesis.[22] [23] Thus, one could argue that reducing the concentration of water unavoidably limits the proton-electron transfer process associated with the H-shuttling mechanism, leading to lower rates. At the same time, one could attribute the lower rates in NMP to either competitive adsorption of NMP and reactants (NB and H_2) on Pd or the alterations in the intrinsic activity of the catalyst due to changes in the interactions between the solvent molecules near the active site and the kinetically relevant surface chemisorbed species.

The selectivity of the reaction obtained at 10% conversion for the two catalysts was investigated using 30 vol.% H_2O/NMP as solvent (Figure S1). These results indicate that the main product observed in the hydrogenation of nitrobenzene was aniline (>85%) with p-aminophenol as the dominant byproduct. The selectivity to aniline slightly decreases with temperature on the parent Pd/SiO_2 catalyst. A similar trend has been reported on Pt-based catalysts.[24] The most notable feature is that the addition of the polymer led to the opposite trend, i.e. the selectivity towards aniline increased with temperature.

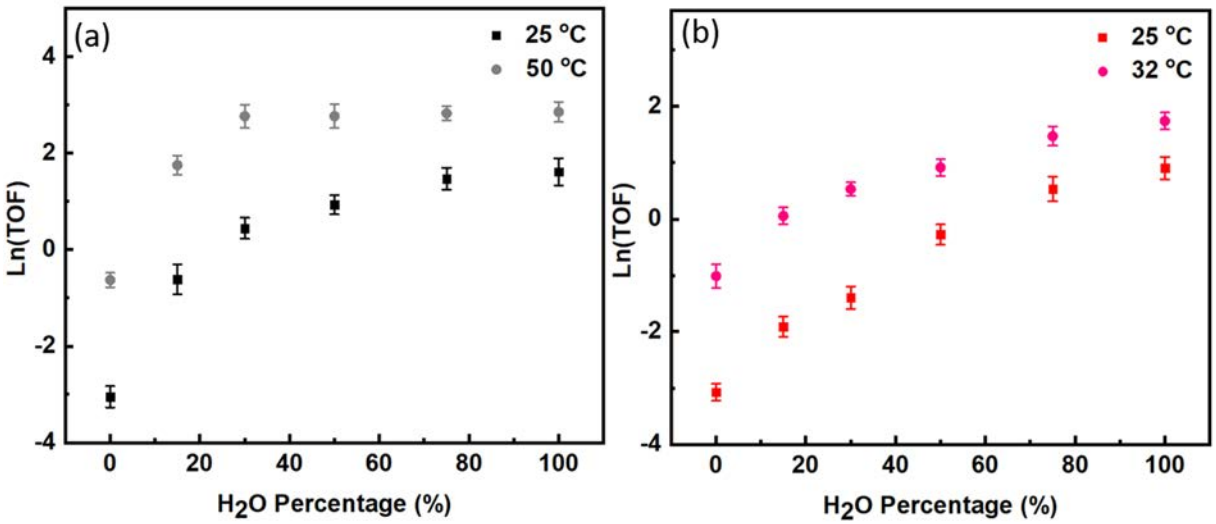

Figure 2. Catalytic performance of the two catalysts using different concentrations of H_2O and NMP in the solution at 0.05 bar H_2, 1mM NB concentration and different temperature for (a) Pd/SiO_2, and (b) Pd/SiO_2-p-NIPAM.

3.3 Apparent activation energy

The activation energy barriers are essentially constant throughout the entire temperature range for the Pd/SiO_2 catalyst with an activation energy of 75 kJ mol^{-1} when using 30 vol.% H_2O/NMP as solvent (Figure 3). This result is significantly higher than the value of 41 kJ mol^{-1} observed when using pure water as solvent (Figure S3).

For the polymer coated catalyst, using 30 vol.% H_2O/NMP as a solvent (Figure 3) shows an activation energy barrier of ~ 60 kJ mol^{-1} throughout the entire temperature range. In contrast, different activation energies were observed when pure H_2O was employed as the solvent (Figure S3). At temperatures below the Lower Critical Solubility Temperature (LCST, c.a. 32 °C for p-NIPAM), when the polymer in the swollen state, low apparent activation barriers (c.a. 14 kJ mol^{-1}) were observed. A higher activation energy barrier of 37 kJ mol^{-1} was observed at reaction temperatures above the LCST.

To understand this phenomenon, Dynamic Light Scattering (DLS) experiments have been conducted as shown in Figure 1. For Pd/SiO_2 catalyst, the particle size is almost constant when varying the temperature, independent of the solvent. For Pd/SiO_2-p-NIPAM catalyst, the particle size changes with temperature and the extent of particle size change varied with the solvent composition. When using pure H_2O as the solvent, the particle size decreased significantly with increasing the temperature. In stark contrast, when the particles were dispersed in a solution containing 30 vol.% H_2O/NMP it was observed a negligible change in

the particle size above the LCST of p-NIPAM. That is that when NMP dominates the solvent, the polymer on Pd/SiO_2-p-NIPAM catalyst does not collapse. Hence, there are no changes in the activation energy when varying the temperature. Finally, the presence of polymer leads to a small decrease in the apparent activation energy barrier when compared with the Pd/SiO_2 catalyst even in the presence of the NPM.

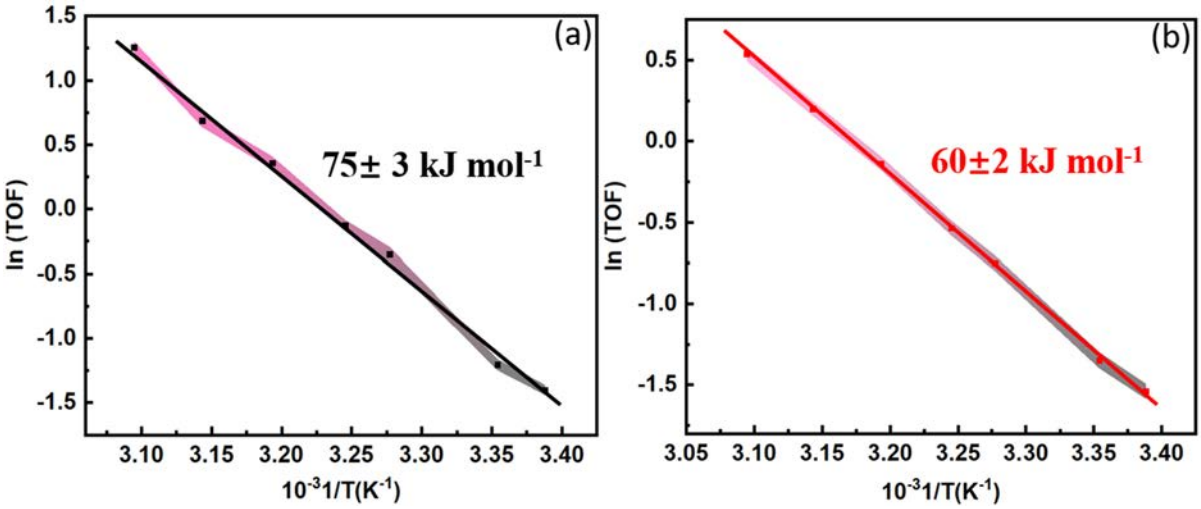

Figure 3. Temperature dependence of turn over frequency (TOF) at 0.05 bar H_2 pressure using 30 vol.% H_2O in NPM as solvent. (a) Pd/SiO_2 catalyst, (b) Pd/SiO_2-p-NIPAM catalyst

4. Discussion

4.1 Competitive adsorption effects

When increasing the water concentration, the reaction rate increased significantly (Figure 2), while the activation energy barrier decreased on the parent Pd/SiO_2 (Figure 3 and Figure S3). Notably, in pure NMP, the activity was negligible. Here, it would be tempting to assign the lower activities and higher apparent barriers with increasing NMP concentrations to competitive adsorption of NMP and nitrobenzene. However, the experimental data shows that even with NMP concentrations as high as 25 vol.%, the reaction rate for nitrobenzene reduction remains essentially unaltered (Figure 2a), suggesting that competitive adsorption cannot explain the observed trends. This becomes more evident when comparing the concentration of nitrobenzene (1 mM) to NMP as the former is about three orders of magnitude lower than that of 25 vol.% NMP (2.6 Mol/L). Since in this scenario NMP would compete with both hydrogen as well as NB, one would expect such competitive adsorption to substantially decrease the reaction rate. This, however, is not observed in the presence of 25 vol.% NMP. A mathematical explanation is provided in section 2 in the supporting information. Also, previous DFT

calculations have shown that nitrobenzene adsorbs strongly on Pd (111) with heats of adsorption ranging from -217.1 kJ mol^{-1} to -85.9 kJ mol^{-1},[25] indicating that competitive adsorption of nitrobenzene and NMP is not likely the main cause for the observed changes in catalytic activity and apparent activation energies.

For the polymer-coated Pd/SiO_2-p-NIPAM catalyst, a lower energy barrier was obtained compared with the catalyst without polymer coating. This may be caused by a solvation effect induced by the polymer coating, as will be further discussed in Section 5.3.

4.2 Proton shuttling effect

An alternative proposition is that the enhanced activity and concomitant decrease in the apparent activation energies with the water concentration is related the proton shuttling ability of water molecules during hydrogenation of nitrobenzene (Figure 4a). As described by Z. Zhao et al.[26], in this concept, H* atoms on the Pd surface split into an electron, which can be transfer to the Pd metal particle, and a H^+ that can combine with H_2O molecules adjacent to the active site to form H_3O^+. These protons can be transported rapidly in water to adsorbed surface species via the Grotthuss mechanism,[27] while electrons transfer rapidly in the Pd metal particles. The proton and the electron recombine on the surface intermediate species resulting in hydrogenation product.

Similar enhancements on activity have been observed when increasing the water concentration during hydrogenation of other aromatic species. For instance, Z. Zhao et al.[26] observed that when conducting the hydrogenation of furfural on Pd/α-Al_2O_3 catalysts the addition of water influenced the hydrogenation rate by taking part in the kinetically relevant step of furfural activation. As a result, the authors reported higher conversions when the reaction was conducted in water as compared to organic solvents like cyclohexane. Likewise, J. Hájek et al.[28] reported significantly higher activity for the selective hydrogenation of cinnamaldehyde in a protic solvent compared to a dipolar aprotic solvent like NMP.

The lower apparent activation energy when using water as the solvent instead of 30 vol.% water in NMP (Figure 3 and Figure S3) could be related to the proton shuttling in water.[13] As we showed in Chapter 2, the proton shuttling lowers the energy barrier of nitrite hydrogenation reaction. Essentially, the water-induced proton shuttling flattened the energy landscape of the reaction. Similar work conducted by Z. Zhao et al.[26] concluded that proton hopping within the first solvation shell and shuttling through the hydrogen-bonded water network reduces the

activation barrier for hydrogenation of the carbonyl group. Also, G. Li et al.[4] found that the rate of Fischer-Tropsch synthesis on metal catalysts increases with increasing H_2O vapor pressure. These results suggest that water acts as an H-shuttling mediator that helps the transfer of H from the surface to the chemisorbed reactants, reducing the energy barrier of the rate-limiting H-assisted reaction step even when the reaction is conducted in the gas phase.

From the herein reported observations, we may conclude that the proton shuttling effect can explain the changes in activity and activation energy when aprotic solvents are employed in combination with stimulus-responsive polymers. As a result, one could argue that the presence of the aprotic NMP solvent hinders the proton shuttling, and thus the reaction rate and apparent activation energy barriers (Figure 4b).

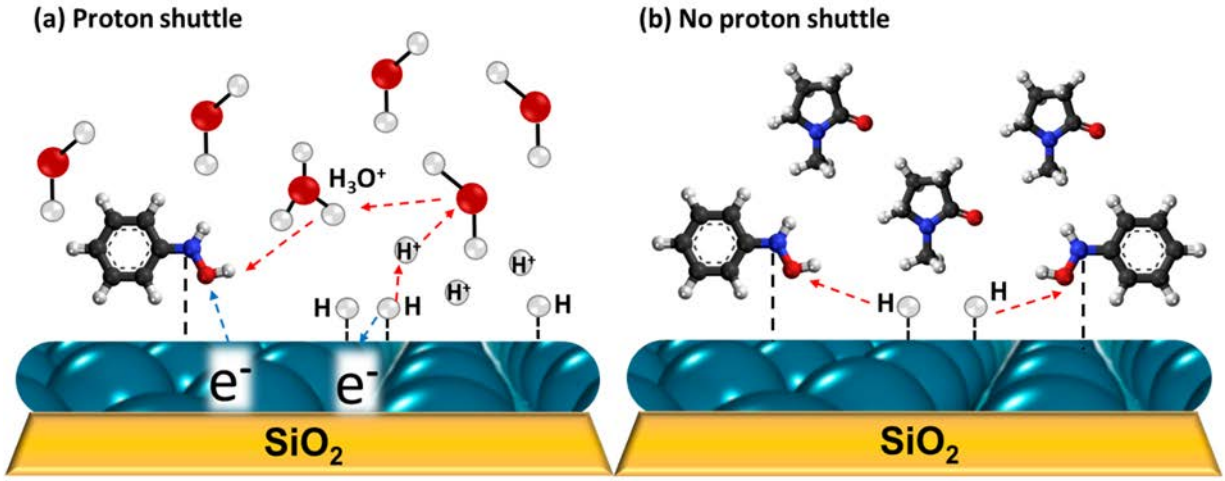

Figure 4. Reaction diagram of the nitrobenzene hydrogenation reaction, (a) proton shuttling mechanism using water as solvent, (b) NMP as solvent hinders the proton shuttling effect.

4.3 Solvation effect

In the previous chapter (Chapter 4), the difference in activation energy barrier when using Pd/SiO_2 and Pd/SiO_2-p-NIPAM catalyst was explained in terms of changes in the extent of solvation induced by the polymer coating, meaning that the polymer influences the energy of adsorbed species including activated complexes of surface reactions. Here, the activation energy plot (Figure 3) shows different activation energy barriers when the reaction is conducted in 30 vol.% H_2O/NMP using Pd/SiO_2 and Pd/SiO_2-p-NIPAM catalyst.

The solvation effect on reactive species induced by the polymer coating was calculated using the theoretical framework initially proposed by J.A. Dumesic [29] and later revised by David

W. Flaherty.[30] The rate expression in equation 10 was used, as described in detail in chapter 4 (section 5 of the supporting information)

$$\frac{r}{L} = \frac{k_b T}{h} \exp\left(\frac{\Delta S_{App}^{0,\ddagger} + \Delta S_{App}^{\varepsilon,\ddagger}}{R}\right) \exp\left(-\frac{\Delta H_{App}^{0,\ddagger} + \Delta H_{App}^{\varepsilon,\ddagger}}{RT}\right) [\mathrm{H_2}]^{2.5} [\mathrm{C_6H_5NO_2}]^{-1} \quad (10)$$

In this equation, L is the total number of active sites, r/L is the turnover frequency, k_b is the Boltzmann constant, h is the Planck constant, T is temperature, $\Delta S_{App}^{0,\ddagger}$ and $\Delta H_{App}^{0,\ddagger}$ are the standard apparent entropy and enthalpy of activation by defining the Pd/SiO_2 as the catalyst as the reference state for the standard conditions. This is calculated from the transition state theory reaction rate vs temperature plot for Pd/SiO_2 (Figure S3a). The difference between activation entropy and activation enthalpy between Pd/SiO_2 and Pd/SiO_2-p-NIPAM (according to the transition state theory reaction rate vs temperature plot in Figure S3b) is defined as the excess enthalpy and free energy: $\Delta S_{app}^{\ddagger} = \Delta S_{App}^{0,\ddagger} + \Delta S_{App}^{\varepsilon,\ddagger}$ and $\Delta H_{app}^{\ddagger} = \Delta H_{App}^{0,\ddagger} + \Delta H_{App}^{\varepsilon,\ddagger}$.

One of the key assumptions in this analysis is that the rate determining step is the same for the parent and polymer coated catalysts when using the pure water and 30 vol.% H_2O/NPM solvents. To address this issue, we conducted a reaction order investigation using 30 vol.% H_2O/NMP as solvent (Figure S2). Here, one can note that hydrogen orders of c.a. 2.5 and 1.2, and nitrobenzene order of c.a. -1 and 0 were observed when using Pd/SiO_2 and Pd/SiO_2-p-NIPAM catalysts, respectively. These results show that indeed the reaction orders in water and 30 vol.% H_2O/NMP are essentially the same (Chapter 4). Hence, it is possible to assume that the rate determining step is the same for both systems. The excess enthalpies and entropies induced by the polymer coating are presented in Table 1.

Clearly, the activation barrier for the polymer-coated catalyst in water depends on the temperature window explored, whereas in the 30 vol.% H_2O/NMP, there is no temperature-responsiveness of the catalyst. This is evident from Table 1 as well as Figures 3b and S3b. At the same time, the DLS measurements (Figure 1) revealed that as the NMP concentration increases the transition of the polymer from swollen to collapse states at temperatures above the lower critical solution temperature (LCST) is substantially inhibited. This suggests that as the polymer changes from hydrophilic state at low temperatures to hydrophobic at high temperatures, the concentration of NMP inside the polymer layer increases, sustaining the layer thickness invariable at temperatures above and below the LCST. These results indicate that the critical role of water molecules in the reaction and in the stimulus-responsiveness of the p-NIPAM drastically changes the energy landscape of the nitrobenzene hydrogenation.

Table 1. The calculated enthalpy and entropy of activation and excess free energy form Pd/SiO_2-p-NIPAM catalyst using pure water and 30 vol.% H_2O/NMP as solvent.

Solvent	Temperature (°C)	Pd/SiO_2		Pd/SiO_2-p-NIPAM		Excess	
		$\Delta S_{App}^{0,\ddagger}$ (J/mol*K^{-1})	$\Delta H_{App}^{0,\ddagger}$ (kJ mol^{-1})	$\Delta S_{App}^{p-NIPAM,\ddagger}$ (J/mol*K^{-1})	$\Delta H_{App}^{p-NIPAM,\ddagger}$ (kJ mol^{-1})	$\Delta S_{App}^{\varepsilon,\ddagger}$ (J/mol*K^{-1})	$\Delta H_{App}^{\varepsilon,\ddagger}$ (kJ mol^{-1})
30 vol.% H_2O/NMP	22-50	169.3	75.0	116.5	59.7	-52.8	-15.3
H_2O	22-32	70.8	40.6	-17.6	14.2	-88.4	-26.4
	32-50			58.2	37.3	-12.6	-3.3

5. Conclusions

The presence of water enhances the nitrobenzene hydrogenation activity and lowers the activation energy barrier of the reaction, while the aprotic solvent NMP shows the opposite trend. We propose that high water concentrations increase the proton-electron transfer reaction, which is believed to facilitate the reduction of R-NO* surface species. Increasing the NMP concentration reduces proton mobility or proton shuttling, deaccelerating the reaction and increasing the apparent activation energy barriers. The presence of stimulus-responsive polymers provides an excess Gibbs free energy that lowers the enthalpy and entropy of the transition state in pure water, reducing the apparent activation energy barriers. Changing the solvent to NMP inhibits the stimulus-responsive behaviour of the p-NIPAM and thus its potential ability to enhance the activity of the catalyst. p-NIPAM stimulus-responsive polymers covalently bonded to the catalyst surface can excerpt drastic changes in the energy landscape of catalytic reactions if the solvent media consists primarily of water.

References

[1] C. Reichardt, Solvatochromic dyes as solvent polarity indicators, Chem. Rev. 94 (1994) 2319–2358.

[2] C. Reichardt, Solvents and Solvent effects in Organic Chemistry, 2nd edn, ch. 7, (1990).

[3] A.R. Katritzky, D.C. Fara, H. Yang, K. Tämm, T. Tamm, M. Karelson, Quantitative measures of solvent polarity, Chem. Rev. 104 (2004) 175–198.

[4] G. Li, B. Wang, D.E. Resasco, Water-Mediated Heterogeneously Catalyzed Reactions, ACS Catal. 10 (2020) 1294–1309. https://doi.org/10.1021/acscatal.9b04637.

[5] P. Lozano, T. Diego, J.L. Iborra, Effect of water-miscible aprotic solvents on kyotorphin synthesis catalyzed by immobilized α-chymotrypsin, Biotechnol. Lett. 17 (1995) 603–608.

[6] J. He, M. Liu, K. Huang, T.W. Walker, C.T. Maravelias, J.A. Dumesic, G.W. Huber, Production of levoglucosenone and 5-hydroxymethylfurfural from cellulose in polar aprotic solvent–water mixtures, Green Chem. 19 (2017) 3642–3653.

[7] M. Mohan, T. Banerjee, V. V Goud, Effect of protic and aprotic solvents on the mechanism of cellulose dissolution in Ionic liquids: A combined molecular dynamics and experimental insight, ChemistrySelect. 1 (2016) 4823–4832.

[8] B. Amini, S. Lowenkron, Aniline and its derivatives, Kirk-Othmer Encycl. Chem. Technol. (2000).

[9] C. V Rode, M.J. Vaidya, R. V Chaudhari, Synthesis of p-aminophenol by catalytic hydrogenation of nitrobenzene, Org. Process Res. Dev. 3 (1999) 465–470.

[10] F. Leng, I.C. Gerber, P. Lecante, S. Moldovan, M. Girleanu, M.R. Axet, P. Serp, Controlled and chemoselective hydrogenation of nitrobenzene over Ru@ C60 catalysts, ACS Catal. 6 (2016) 6018–6024.

[11] G. Quartarone, L. Ronchin, A. Tosetto, A. Vavasori, New insight on the mechanism of the catalytic hydrogenation of nitrobenzene to 4-aminophenol in CH3CN–H2O–CF3COOH as a reusable solvent system. Hydrogenation of nitrobenzene catalyzed by precious metals supported on carbon, Appl. Catal. A Gen. 475 (2014) 169–178.

[12] A. Deshpande, F. Figueras, M.L. Kantam, K.J. Ratnam, R.S. Reddy, N.S. Sekhar, Environmentally friendly hydrogenation of nitrobenzene to p-aminophenol using heterogeneous catalysts, J. Catal. 275 (2010) 250–256.

[13] P. Huang, Y. Yan, A. Banerjee, L. Lefferts, B. Wang, J.A.F. Albanese, Proton

Shuttling Flattens the Energy Landscape of Nitrite Catalytic Reduction, J. Catal. (2022).

[14] W. Stöber, A. Fink, E. Bohn, Controlled growth of monodisperse silica spheres in the micron size range, J. Colloid Interface Sci. 26 (1968) 62–69.

[15] C.A. Barbero, M. V Martínez, D.F. Acevedo, M.A. Molina, C.R. Rivarola, Cross-Linked Polymeric Gels and Nanocomposites: New Materials and Phenomena Enabling Technological Applications, Macromol. 2 (2022) 440–475.

[16] M. V Martinez, M. Molina, C.A. Barbero, Poly (N-isopropylacrylamide) cross-linked gels as intrinsic amphiphilic materials: swelling properties used to build novel interphases, J. Phys. Chem. B. 122 (2018) 9038–9048.

[17] M.J.E. da Silva, L. Lefferts, J.A. Faria Albanese, N-isopropylacrylamide polymer brushes alter the micro-solvation environment during aqueous nitrite hydrogenation on Pd/Al2O3 catalyst, J. Catal. 402 (2021) 114–124. https://doi.org/10.1016/j.jcat.2021.08.003.

[18] Y. Zhao, J.A. Baeza, N.K. Rao, L. Calvo, M.A. Gilarranz, Y.D. Li, L. Lefferts, Unsupported PVA-and PVP-stabilized Pd nanoparticles as catalyst for nitrite hydrogenation in aqueous phase, J. Catal. 318 (2014) 162–169.

[19] J. Panpranot, K. Phandinthong, P. Praserthdam, M. Hasegawa, S. Fujita, M. Arai, A comparative study of liquid-phase hydrogenation on Pd/SiO2 in organic solvents and under pressurized carbon dioxide: Activity change and metal leaching/sintering, J. Mol. Catal. A Chem. 253 (2006) 20–24.

[20] F. Zhao, M. Shirai, M. Arai, Palladium-catalyzed homogeneous and heterogeneous Heck reactions in NMP and water-mixed solvents using organic, inorganic and mixed bases, J. Mol. Catal. A Chem. 154 (2000) 39–44.

[21] Y. Yoon, R. Rousseau, R.S. Weber, D. Mei, J.A. Lercher, First-principles study of phenol hydrogenation on Pt and Ni catalysts in aqueous phase, J. Am. Chem. Soc. 136 (2014) 10287–10298.

[22] N. Kizhakevariam, X. Jiang, M.J. Weaver, Infrared spectroscopy of model electrochemical interfaces in ultrahigh vacuum: The archetypical case of carbon monoxide/water coadsorption on Pt (111), J. Chem. Phys. 100 (1994) 6750–6764.

[23] T. Yuzawa, T. Higashi, J. Kubota, J.N. Kondo, K. Domen, C. Hirose, CO coadsorption-induced recombination of surface hydroxyls to water on Ni (110) surface by IRAS and TPD, Surf. Sci. 325 (1995) 223–229.

[24] Y. Liu, Y. Fang, X. Lu, Z. Wei, X. Li, Hydrogenation of nitrobenzene to p-

aminophenol using Pt/C catalyst and carbon-based solid acid, Chem. Eng. J. 229 (2013) 105–110.

[25] L. Zhang, Z.-J. Shao, X.-M. Cao, P. Hu, Insights into different products of nitrosobenzene and nitrobenzene hydrogenation on Pd (111) under realistic reaction conditions, J. Phys. Chem. C. 122 (2018) 20337–20350.

[26] Z. Zhao, R. Bababrik, W. Xue, Y. Li, N.M. Briggs, D.-T. Nguyen, U. Nguyen, S.P. Crossley, S. Wang, B. Wang, Solvent-mediated charge separation drives alternative hydrogenation path of furanics in liquid water, Nat. Catal. 2 (2019) 431–436.

[27] T. von Grotthuß, Mémoire sur la décomposition de l'eau et des corps qu'elle tient en dissolution à l'aide de l'électricité galvanique, 1805.

[28] J. Hájek, N. Kumar, P. Mäki-Arvela, T. Salmi, D.Y. Murzin, Selective hydrogenation of cinnamaldehyde over Ru/Y zeolite, J. Mol. Catal. A Chem. 217 (2004) 145–154.

[29] M.A. Mellmer, C. Sanpitakseree, B. Demir, P. Bai, K. Ma, M. Neurock, J.A. Dumesic, Solvent-enabled control of reactivity for liquid-phase reactions of biomass-derived compounds, Nat. Catal. 1 (2018) 199–207. https://doi.org/10.1038/s41929-018-0027-3.

[30] D.S. Potts, D.T. Bregante, J.S. Adams, C. Torres, D.W. Flaherty, Influence of solvent structure and hydrogen bonding on catalysis at solid–liquid interfaces, Chem. Soc. Rev. 50 (2021) 12308–12337. https://doi.org/10.1039/d1cs00539a.

Supporting information

1. Nitrobenzene hydrogenation reaction

1.1 Selectivity of the reaction

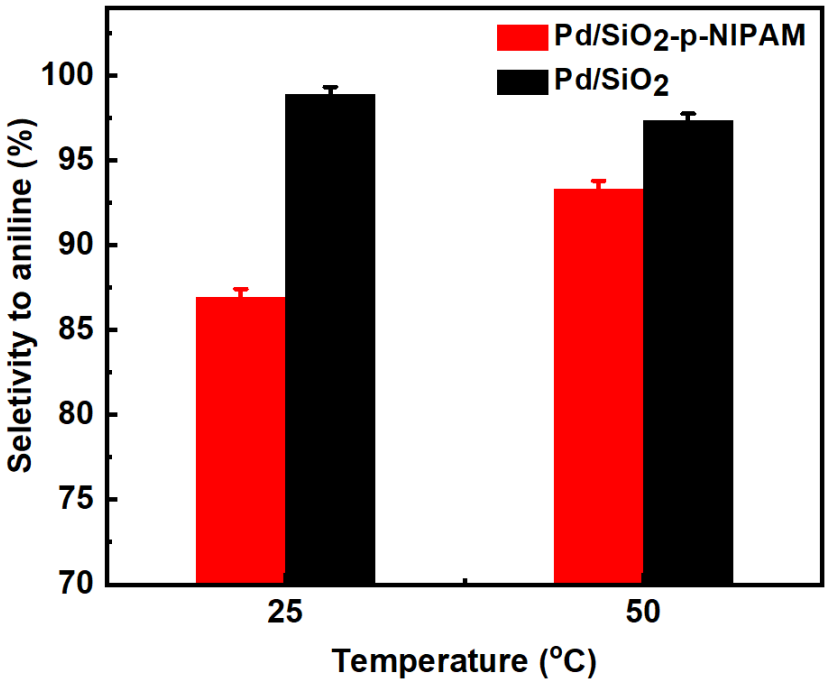

Figure S1. Selectivity to aniline at 10% conversion of nitrobenzene using 30 vol.% H_2O/NMP as solvent.

1.2 Reaction order

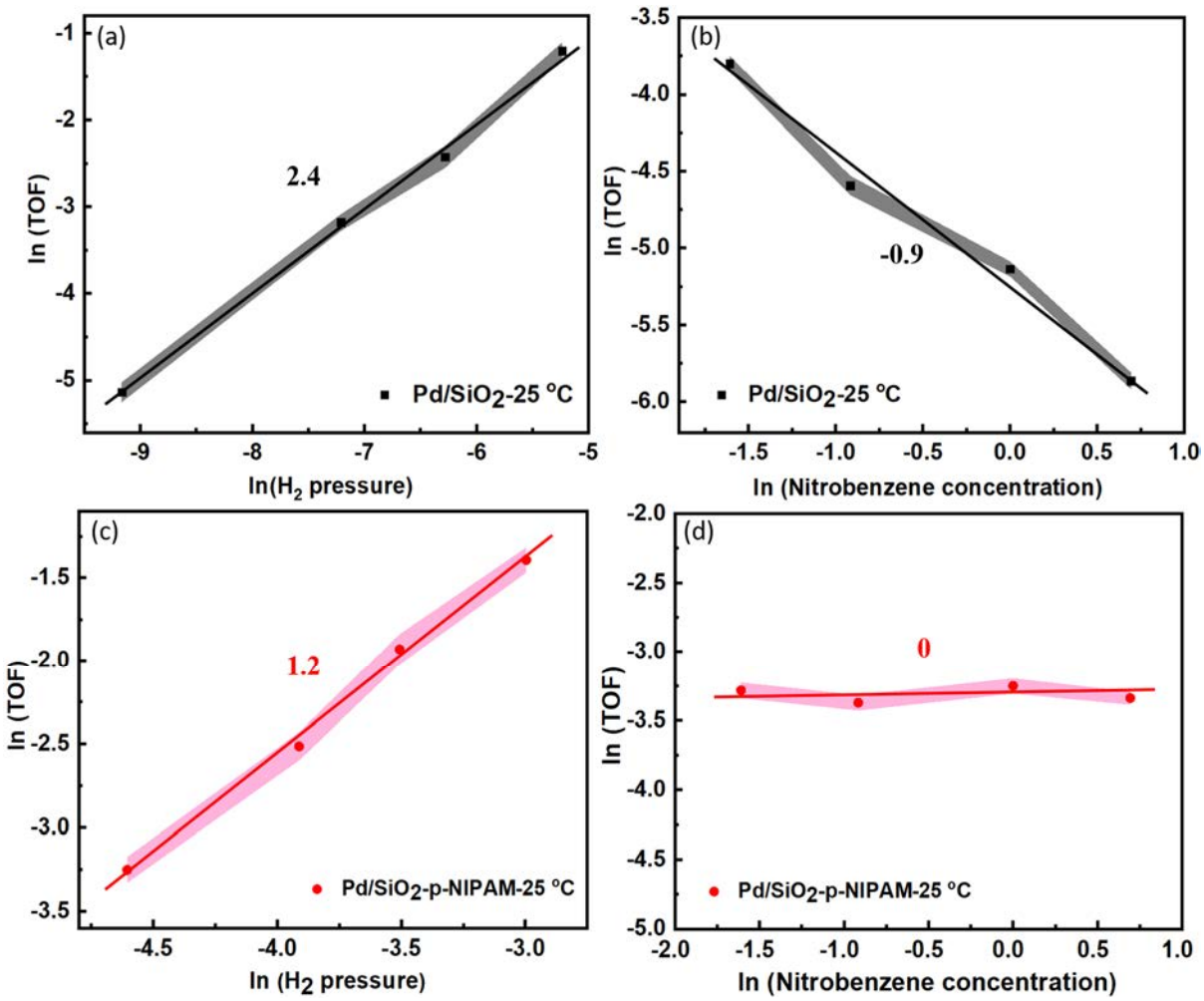

Figure S2. Pd/SiO_2 catalyst used for reaction order investigation using 30 vol.% H_2O/NMP as solvent:

(a) Hydrogen order investigation using 1mM nitrobenzene and (b) nitrobenzene order investigation using 0.01 bar H_2; Pd/SiO_2-p-NIPAM catalyst. used for reaction order investigation using 30 vol.% H2O/NMP as solvent: (c) Hydrogen order investigation using 1mM nitrobenzene and (d) nitrobenzene order investigation using 0.01 bar H_2.

1.3 Activation energy plot

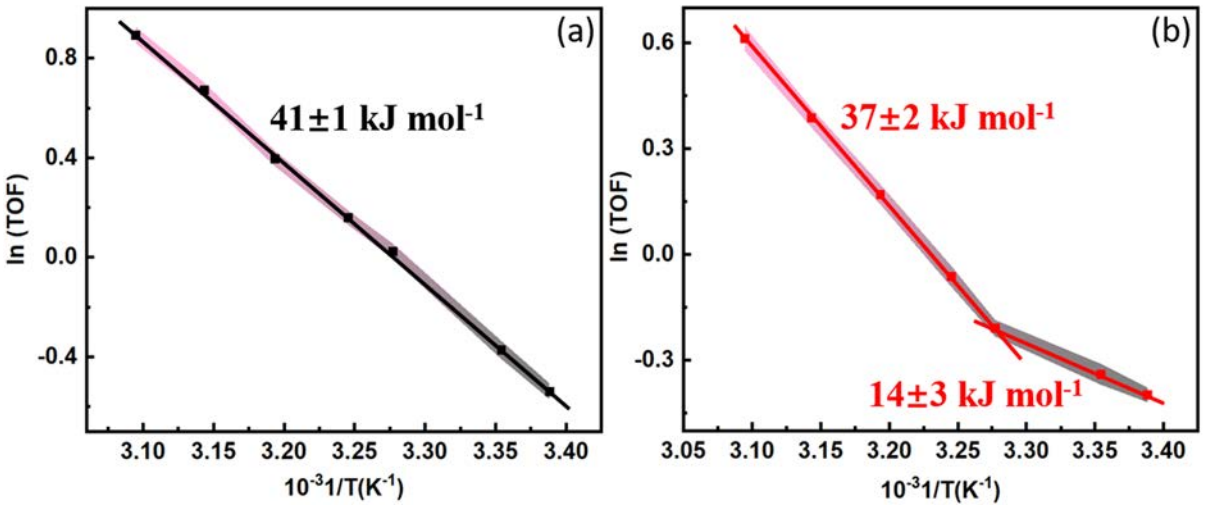

Figure S3. Temperature dependence of turn over frequency (TOF) at 0.03 bar hydrogen pressure using H_2O as solvent. (a) Pd/SiO_2 catalyst, (b) Pd/SiO_2-p-NIPAM catalyst

2. Derivation of the competitive adsorption on reaction rate

2.1 Formation of the product as RDS, with solvent adsorption on the catalyst surface.

According to the Langmuir–Hinshelwood-Hougen-Watson (LHHW) mechanism, two molecules A and B adsorb on neighboring sites and the adsorbed molecules undergo a bimolecular reaction.[1]

$A + * \rightleftharpoons A^*$ (S1)

$B + * \rightleftharpoons B^*$ (S2)

$S + * \rightleftharpoons S^*$ (S3)

$A^* + B^* \rightarrow C^* + *$ (S4)

The rate constants are now k_1, k_{-1}, k_2, k_{-2}, k_3 and , k_4, $k_{-4}$for adsorption/desorption of A, adsorption/desorption of B, and reaction to form product respectively, S represent the solvent. The rate law is: $r = k\theta_A\theta_B$

$\theta_A = K_1[A]\theta_v$ (S5)

$\theta_B = K_2[B]\theta_v$ (S6)

$\theta_S = K_4[S]\theta_v$ (S7)

$\theta_A + \theta_B + \theta_S + \theta_v = 1$ (S8)

$$\theta_v = \frac{1}{1+K_1[A]+K_2[B]+\mathrm{K}_S[S]} \quad \text{(S9)}$$

$$r = k_3\theta_\mathrm{A}\theta_\mathrm{B} = \frac{k_3\mathrm{K}_1\mathrm{K}_2[\mathrm{A}][\mathrm{B}]}{(1+K_1[A]+K_2[B]+\mathrm{K}_S[S])^2} \quad \text{(S10)}$$

When S has a high surface coverage

$$r = k_3\mathrm{K}_1\mathrm{K}_2{\mathrm{K}_S}^{-2}[\mathrm{A}][\mathrm{B}][\mathrm{S}]^{-2} = \frac{k_3\mathrm{K}_1\mathrm{K}_2[\mathrm{A}][\mathrm{B}]}{(\mathrm{K}_S[S])^2} \quad \text{(S11)}$$

When one considers that the concentration of nitrobenzene (1 mMol/L) in these experiments is three orders of magnitude lower than that of 25 vol.% NMP (2.6 Mol/L), then one can realize that the impact of surface competitive adsorption should rather large in this system. The fact that we do not see such a marked drop in the catalytic activity suggests that competitive adsorption is not the underlaying cause of the activity drop.

3. Derivation to calculate the entropy and enthalpy

The derivations to calculate the entropy, enthalpy and solvation effect are show in chapter 4 (Section 4 and section 5 of supporting information). Based on the reaction order investigation in Figure S2, when using 30 vol.% H_2O/NMP as solvent, the same reaction order was being obtained compared with the results obtained in pure water (Chapter 4). This implies that the reaction mechanism remains unaltered despite the high concentration of NMP. Hence, the $\Delta H_{app}^{\ddagger}$and $\Delta S_{app}^{\ddagger}$are being calculated for the Pd/SiO_2 and Pd/SiO_2-p-NIPAM catalyst from the slope and intercept as show in Figure S4, respectively.

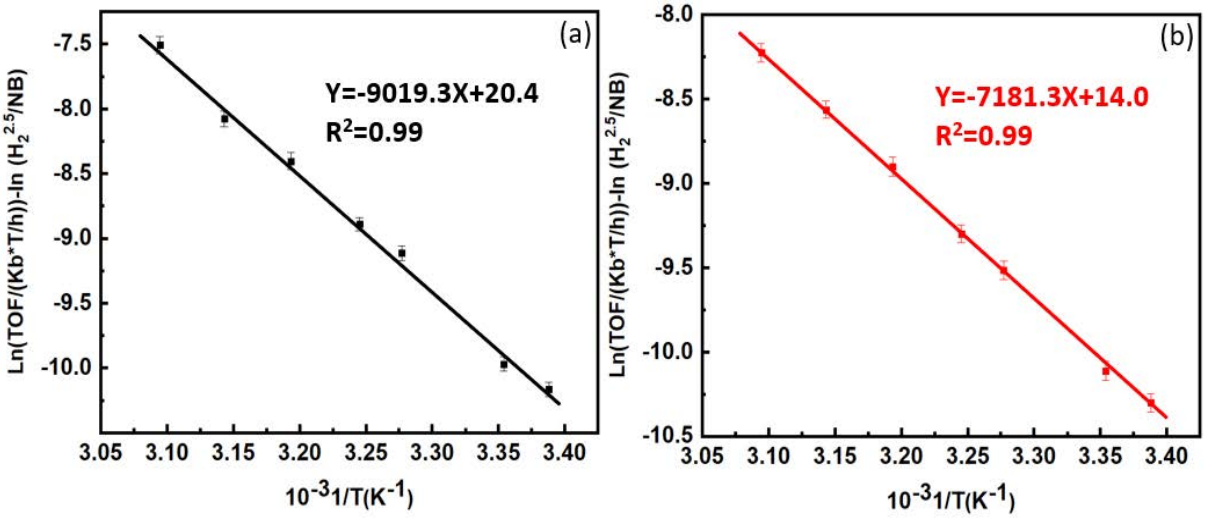

Figure S4. Transition state theory reaction rate vs temperature using 30 vol.% H_2O/NMP as solvent for the catalyst (a) Pd/SiO_2 ,(b)Pd/SiO_2-p-NIPAM.

References

[1] K.J. Laidler, J.H. Meiser, Physical Chemistry (1982), (n.d.).

Chapter 6

Conclusions and recommendations

The research work presented in this thesis is aimed at unraveling the complex interplay between the solvent environment near the active sites and the surface reaction intermediates to develop more stable, active, and selective heterogeneous catalysts. Broadly, this thesis can be subdivided into two subjects. In the first one, the so-called solvation effects are analyzed in the context of the metal-catalyzed reduction of toxic nitrites from drinking water and nitrobenzene reduction in the aqueous phase to anillin. Next, the impact of employing stimulus-responsive polymers as catalyst coatings was assessed on metal-supported catalysts for both reductive chemistries. Finally, we analyzed the impact of changing the proton affinity of the solvent on the reaction kinetics of Pd/SiO_2.

1. Nitrite hydrogenation and polymer induced solvation effects

Catalytic reduction of nitrite using Pd-based catalysts is considered as one of the most promising and efficient methods for the removal of nitrite and nitrate pollutants from drinking water. In this approach, hydrogen, nitrite, and nitrate react to either nitrogen or ammonia on a supported metal catalyst. Here, it is essential to control the selectivity towards dinitrogen with high precision as the toxicity of the nitrates and nitrites is lower than that of ammonia. As a result, achieving nearly stoichiometric conversion to nitrogen is essential for commercial deployment. To increase the selectivity to N_2 and suppress the formation of NH_4^+, one must understand in detail the reaction mechanism and the interdependence between surface coverages and the reaction kinetics.

For this reason, a detailed kinetic study was conducted in a broad range of hydrogen and nitrite concentrations at different temperatures (**Chapter 2**). Here, a negative order of -1 was obtained for nitrite, implying competitive adsorption of nitrite and hydrogen on the Pd surface. More importantly, previous work conducted by P. Xu et al. [1] using porous Al_2O_3 as a support reported hydrogen orders that varied from 1-2, which is line with the results herein obtained with values ranging from 0.5 to 1.5 using dense silica as support. These results suggested that the rate determining step was located late in the mechanism and that H-insertion was involved in the rate determining step.

By combining kinetic modeling and theoretical DFT calculations, performed in collaboration with Prof. B. Wang at the University of Oklahoma, it was demonstrated that the nitrite hydrogenation reaction in aqueous environments is controlled by a dual rate-determining step. The results indicated that the first hydrogenation of NO* to HNO* and the subsequent

hydrogenation of HNO* to HNOH* have a similar energy barrier (Blue line in Figure 1), which is consistent with the hydrogen reaction orders experimentally obtained. This flattening of the energy landscape was attributed to a new reaction pathway involving a proton-electron transfer through a network of water molecules near the active site so-called "*proton shuttling*" mechanism. In this process, the H atoms on the Pd surface give an electron to the Pd metal particle to form H^+, forming H_3O^+ by combining H^+ with an H_2O molecule. The resulting proton is transferred to adsorbed NO* via the water network according to the Grotthuss mechanism[2], while electrons are transferred to adsorbed NO* via the Pd metal particle (Figure 1).

Furthermore, the degree of rate control analysis showed that the balance between these two RDSs shifts with both the hydrogen concentration and reaction temperature, providing a new tool for the selection of the operating conditions of this catalyst. This quantitative agreement between experimental and theoretical results clearly demonstrates that it is essential to consider the molecular interaction of water in the reaction mechanism when nitrite reduction is conducted in aqueous environments.

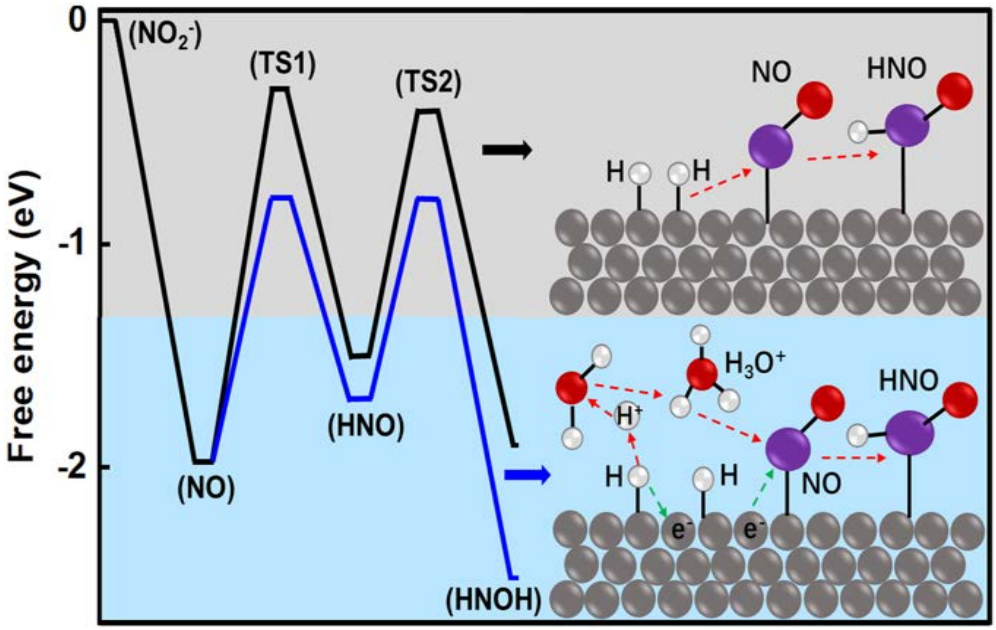

Figure 1. Free energy diagram of the nitrite hydrogenation reaction via direct reaction of adsorbed H atoms and NO (black line) and via proton shuttling (blue line).(**Chapter 2**)

In **Chapter 3**, the catalyst coated with thermally responsive polymer (p-NIPAM) was synthesized and applied to the nitrite hydrogenation reaction. The polymer was grown from the surface of the Pd/SiO_2 using atom transfer radical polymerization (ATRP), which leads to a well-controlled growth of polymer brushes with a thickness of c.a. 70 nm according to the

characterization results from Dynamic Light Scattering (DLS). This methodology leverages the -OH moieties of the silicon dioxide surface to covalently anchor the polymer brushes to the surface via silane chemistry. The beauty of this synthesis method is that no polymer brushes can be grown from the Pd surface as these nanoclusters are in the metallic state during the ATRP process, restricting the polymer growth to the -OH decorated silica surface. These materials were benchmarked against the parent catalyst consisting of Pd/SiO_2, without changing the metal cluster size or the catalyst accessibility as demonstrated by TEM characterization and mass transport studies. This allowed us to decouple the effects of particle size and mass transfer from the changes in the extent of solvation effects induced by the polymers at different temperatures near the active site. In short, we found that the p-NIPAM coated catalyst had a lower activation energy compared with the catalyst without polymer when the temperature of the reaction was below the LCST of the polymer (32 °C). Notably, increasing the temperature above the LCST led to an apparent barrier similar to those observed in the uncoated catalyst. By combining detailed reaction kinetic data, obtained in a wide window of experimental conditions, with transition state theory, we found that the polymer brushes of p-NIPAM enthalpically stabilize the transition state, leading to lower barriers. That is that the addition of the polymer provides the excess free energy of the transition state that decreases the apparent enthalpy of activation with the concomitant drop in the apparent entropy of activation, especially when the temperature is below the LCST. These effects vanished, however, as the temperature increased above the LCST. These results drastically change the current understanding of how stimulus-responsive catalysts operate as it shows that when the system is free of mass transport limitations and that the polymer-catalyst interactions via solvation effects create significant changes in the apparent activation energy barriers.

2. Nitrobenzene hydrogenation and polymer induced solvation effects

The nitrobenzene hydrogenation was studied in **Chapter 4** as a probe reaction to investigate the relationship between the chemistry of the reactants (NO_2^- vs $C_6H_5NO_2$) and the solvation effects induced by stimulus-responsive polymer brushes (p-NIPAM). After conducting detailed reaction kinetics on the nitrobenzene hydrogenation reaction, it was observed that, like in the case of nitrite, this reaction involves a dual-rate determining step where two subsequent hydrogen insertion processes are co-limiting the observed kinetics. When the polymer-coated catalyst was employed, the apparent activation energy barrier decreased by three-fold when the reaction was conducted below the LCST of the polymer. This phenomenon was also explained

in terms of changes in the excess free energy of the transition state upon the addition of the polymer at temperatures below and above the LCST, as explained for the nitrite hydrogenation. That is that at low temperatures the polymer coating decreases the apparent enthalpy of activation with the concomitant drop in the apparent enthalpy of activation of the transition state (Figure 2).

Furthermore, NMR spectroscopy showed that when using the polymer-coated catalyst, the presence of nitrobenzene reduces the self-diffusion coefficient of the amide protons in the p-NIPAM, which suggests that the interaction with the reactant can modify the mobility of the polymer molecules within the polymer layer.

Overall, these results demonstrate the universality of this concept as the effect of stimulus-responsive polymers via solvation effects near the active site is similar for surface intermediates formed from nitrite ions as well as uncharged nitrobenzene molecules.

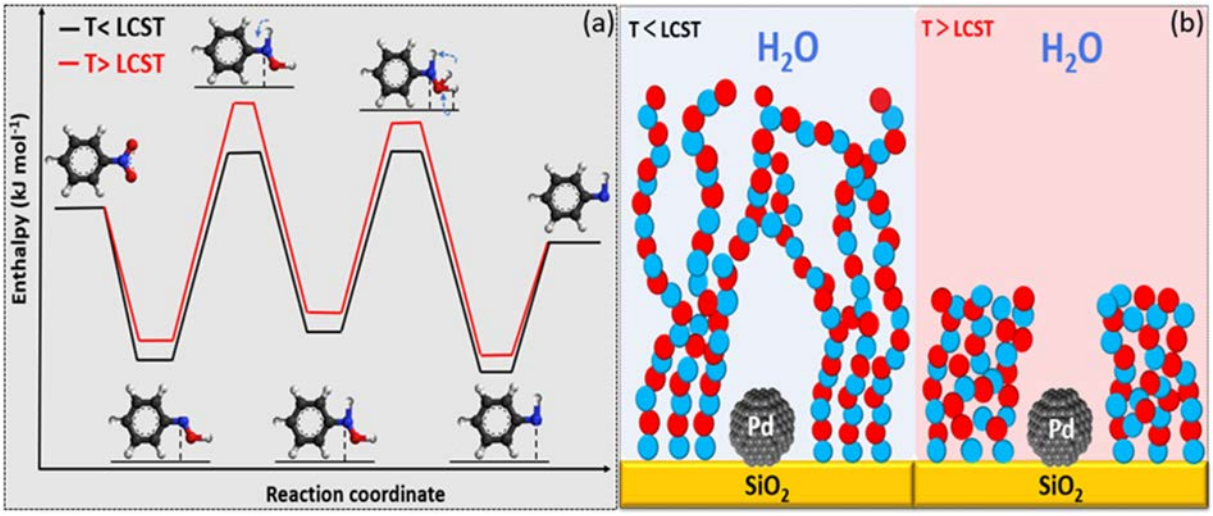

Figure 2. Illustrative representation of the change in the reaction energy diagram of the nitrobenzene hydrogenation as a function of the extent of solvation effects induced by stimulus-responsive polymer p-NIPAM. (**Chapter 4**).

Chapter 5 studied the effect of the solvent on the nitrobenzene reaction in the presence of polymer-coated catalysts. For this reason, we evaluated the impact of the solvent composition on the reaction rates and apparent activation barriers. This was accomplished by changing the solvent from pure water to mixtures with increasing concentrations of 1-methyl-2-pyrrolidone (NMP). When increasing the water content using the parent Pd/SiO_2, the reaction rate increases,

while the activation energy barrier decreased significantly. Notably, in pure NMP, the activity was negligible.

The reaction rate for nitrobenzene hydrogenation remains essentially unaltered when increasing the NMP concentration as high as 25 vol.%, indicating that competitive adsorption of reactants and NMP cannot explain the observed trends, especially if one considers that the concentration of nitrobenzene is three orders of magnitude lower than that of NMP. Alternatively, we proposed that high water concentrations enhance the proton-electron transfer reaction, which is believed to facilitate the reduction of R-NO* surface species. In contrast, high concentrations of NMP hinder proton diffusion and proton transfer to surface intermediate species, which reduces the apparent rates and increases the activation energy barriers.

Notably, the changes in the activation energy at temperatures above and below the LCST of the p-NIPAM initially observed in pure water vanish in 30 vol.% H_2O/NMP. This phenomenon was studied using the dynamic light scattering (DLS) characterization, revealing that the transition of the polymer from swollen to collapsed state at the lower critical solubility temperature (LCST) disappears almost completely in the case of high NMP concentration. This suggests that for the stimulus-responsive polymers covalently bonded to the catalyst surface, the polymer behaviour changes with the external environment (e.g. temperature and solvent), which can significantly alter the energy landscape of catalytic reactions.

Recommendations

The reaction kinetics, kinetic modeling, and degree of rate control analysis reveal that the RDS shifts with the reaction conditions (e.g. temperature and surface coverage of reactant) for nitrite hydrogenation reaction. Previous work in our group using ATR-IR spectroscopy conducted by S.D. Ebbesen et al.[3] investigated the intermediate species of nitrite hydrogenation starting from sodium nitrite. Here, it was found that NO* is the most important surface reaction intermediate. Unfortunately, the exact reaction pathway for the formation of N_2 and NH_4^+ after NO hydrogenation is still not clear yet. Therefore, it is recommended to conduct additional ATR-IR experiments starting from the hydrogenation of NO* in the aqueous phase over the Pd catalysts, to investigate the intermediate species. For the ATR-IR experiments, the Pd-based catalyst is firstly reduced with H_2, then, the saturated aqueous NO* solution flows through the ART-IR cell chamber, detecting surface intermediates with ATR-IR. In addition, additional DFT calculations are also recommended to determine the energy barrier for the formation of

intermediate species based on the observation from ATR-IR. Based on the previous research in chapter 2, the proton shuttling effect should be always considered in the DFT studies.[4]

Previous research has shown that the p-NIPAM coating on a Pd/Al_2O_3 catalyst causes a peak shift for the $Pd\text{-}NO_{X\,(ads)}^{-}$ and $NO_{(aq)}$ peaks during nitrite adsorption, which implies a solvation effect induced by the presence of polymer.[5] It is recommended to conduct ATR-IR at a temperatures above the LCST of the polymer to see how the peak position changes with the polymer behavior. This information may further explain the activation energy changes with the polymer behavior at different temperatures. In addition, it will important to expand the studies of the potential polymer-catalyst interactions using molecular dynamics simulations (MD) as there is only very limited information available in the literature.[6] So, here, it is recommended to conduct molecular dynamics calculations. This will help us to reveal the interaction between polymer and catalyst particles and the effect of polymers on the reactant binding energies and activation barriers.

For the NB hydrogenation reaction it is highly recommended to conduct ATR-IR spectroscopy to detect the intermediate species during the reaction and further unravel the reaction mechanism. Also, it is recommended to conduct ATR-IR at a temperature above the LCST. In this way, the effect of temperature on polymer behavior and the corresponding solvation effect can be studied for the NB reduction to anillin.

For the proton shuttling effect, previous research reported significantly higher activity when using a protic solvent compared to a dipolar aprotic solvent under the same reaction conditions.[7][8] Here, it is recommended to conduct DFT calculations considering the proton shuttling effect on the overall kinetics. In this way, the experimental results herein obtained can be further validated in a more comprehensive manner, and the effect of solvent on activation energy barrier and activity can be further explained. Also, it is recommended to investigate the reaction orders using a miscible liquid mixture of water and 1-methyl-2-pyrrolidone (NMP) as previous research showed that when doing the same reaction under a protic and aprotic solvent, different reaction orders can be obtained.[7] This reaction order investigation will help us to understand the effect of the solvent polarity on the nitrobenzene hydrogenation reaction mechanism.

Reference

[1] P. Xu, S. Agarwal, L. Lefferts, Mechanism of nitrite hydrogenation over Pd/γ-Al2O3 according a rigorous kinetic study, J. Catal. 383 (2020) 124–134. https://doi.org/10.1016/j.jcat.2020.01.003.

[2] T. von Grotthuß, Mémoire sur la décomposition de l'eau et des corps qu'elle tient en dissolution à l'aide de l'électricité galvanique, 1805.

[3] S.D. Ebbesen, B.L. Mojet, L. Lefferts, In situ ATR-IR study of nitrite hydrogenation over Pd/Al_2O_3, J. Catal. 256 (2008) 15–23. https://doi.org/10.1016/j.jcat.2008.02.013.

[4] P. Huang, Y. Yan, A. Banerjee, L. Lefferts, B. Wang, J.A.F. Albanese, Proton Shuttling Flattens the Energy Landscape of Nitrite Catalytic Reduction, J. Catal. (2022).

[5] M.J.E. da Silva, L. Lefferts, J.A. Faria Albanese, N-isopropylacrylamide polymer brushes alter the micro-solvation environment during aqueous nitrite hydrogenation on Pd/Al2O3 catalyst, J. Catal. 402 (2021) 114–124. https://doi.org/10.1016/j.jcat.2021.08.003.

[6] R.B. Venkatesh, T. Zhang, N. Manohar, K.J. Stebe, R.A. Riggleman, D. Lee, Effect of polymer–nanoparticle interactions on solvent-driven infiltration of polymer (SIP) into nanoparticle packings: a molecular dynamics study, Mol. Syst. Des. Eng. 5 (2020) 666–674.

[7] Z. Zhao, R. Bababrik, W. Xue, Y. Li, N.M. Briggs, D.-T. Nguyen, U. Nguyen, S.P. Crossley, S. Wang, B. Wang, Solvent-mediated charge separation drives alternative hydrogenation path of furanics in liquid water, Nat. Catal. 2 (2019) 431–436.

[8] J. Hájek, N. Kumar, P. Mäki-Arvela, T. Salmi, D.Y. Murzin, Selective hydrogenation of cinnamaldehyde over Ru/Y zeolite, J. Mol. Catal. A Chem. 217 (2004) 145–154.

Scientific contributions

List of publications

1. **Pengcheng Huang**†, Yu Yan†, Aayan Banerjee, Leon Lefferts, Bin Wang*, and Jimmy A. Faria Albanese*, Proton Shuttling Flattens the Energy Landscape of Nitrite Catalytic Reduction. **Journal of catalysis.** 413 (2022): 252-263.

2. **Pengcheng Huang**, Rick Baldenhofer, Ricardo P. Martinho, Leon Lefferts, Jimmy Faria Albanese*. Stimulus-Responsive Control of Transition States on Nanohybrid Polymer-Metal Catalysts. (Submitted to ACS catalysis)

3. **Pengcheng Huang**, Leon Lefferts, Jimmy Faria Albanese*, Modifying Reaction Rates and Stimulus-Responsive Behavior of Polymer-Coated Catalysts Using Aprotic Solvents. (Submitted to Journal of catalysis)

4. **Pengcheng Huang**†, Yu Yan†, Aayan Banerjee, Leon Lefferts, Bin Wang*, and Jimmy A. Faria Albanese*, Taming Solvation Effects in Pd-Catalyzed Nitrite Reduction in Water Using Stimulus-Responsive Polymer Coatings. (In preparation)

5. **Pengcheng Huang**, Leon Lefferts, Jimmy Faria Albanese*, Polymer-Modified Catalysts for Catalytic Reactions: A Tutorial Review (In preparation)

Oral presentations

1. Fine-Tuning of Solvation Environments in nitrobenzene hydrogenation Reactions Using Polymer-Modified Metal-Supported Catalysts (NANO2022, June 6-10th,2022. Sevilla, Spain)

2. Mechanistic Insights into Nitrite Hydrogenation over Palladium (The XXIII NCCC conference, May 9-11st, 2022, Noordwijkerhout, NL)

3. Fine-Tuning of Solvation Environments in nitrobenzene hydrogenation Reactions Using Polymer-Modified Metal-Supported Catalysts (Brightlands Polymer Day, November 7-9th, 2021, Veldhoven, NL)

4. Fine-Tuning of Solvation Environments in nitrite hydrogenation Reactions Using Polymer-Modified Metal-Supported Catalysts (ACS Fall conference, August 22-26th, 2021, Atlanta. USA.) Online

Poster presentations

1. Fine-Tuning Liquid Phase Reactions Using Polymer-Modified Metal-Supported Catalysts (The XXI NCCC conference, March 2-4th, 2020, Noordwijkerhout, NL)

Summary

The effect of the solvent environment is important for the activity and selectivity of a catalytic reaction conducted in the liquid phase. One must carefully consider the potential interactions between the solvent molecules and the reacting species as these interactions can alter mass transfer rates, reaction kinetics, product selectivity, and catalyst stability as well as the properties of the solvent including density and viscosity. As a result, these so-called solvation effects can induce a significant change in the catalytic performance. However, finding the perfect "marriage" between the solvent, reaction, and catalyst is difficult as only a few solvents can deliver the desired performance. Essentially, the best solvents to stabilize the reactants and products in the bulk might not be the optimal solvation environment for the catalyst. A promising approach could be to decouple the local reaction environment of the active sites from that of the solvent in the bulk. This can be achieved with a polymer coating that can induce a solvation effect near the active site. In this thesis, a thermal-responsive polymer (p-NIPAM) that has a lower critical solution temperature (LCST) has been employed as polymer coating on a model Pd/SiO_2 catalyst to validate this concept. The effect of the solvent and polymer-induced solvation effects on the reaction selectivity and activity have been studied using the nitrite and nitrobenzene hydrogenation reactions as probe chemistries.

In order to further increase the selectivity of nitrite to harmless N_2 by suppressing the formation of NH_4^+, it is essential to understand the Pd-catalyzed nitrite hydrogenation mechanism in detail. A rigorous kinetic study was conducted in a wide window of nitrite and hydrogen concentrations to interrogate the underlying surface chemistry. The results (**Chapter 2**) showed a negative NO_2^- reaction order when the H_2 pressure was low, which implies competitive adsorption of NO_2^- and H_2 on the catalyst surface. At the same time, the observed high H_2 reaction order (c.a. 1.5 at low concentrations of H_2) suggested that the rate-determining step (RDS) required several pre-equilibria involving hydrogen. Based on these observations, several RDS and reaction pathways have been analyzed. By combining kinetic modeling and density-functional theory (DFT) calculations, it was demonstrated that the reaction is co-limited by two consecutive surface elementary steps, involving the first and second hydrogenation of NO*. The degree of rate control (DRC) analysis suggested that the RDS can shift with the reaction conditions (temperature and reactant concentrations) from the first hydrogenation of NO* to the subsequent hydrogenation of HNO* to HNOH* species.

To study the effect of polymer on nitrite hydrogenation reaction, a thermal responsive polymer-coated catalyst has been synthesized via the atom transfer radical polymerization (ATRP) method and applied to nitrite hydrogenation (**Chapter 3**). The results showed that the presence of polymer lowers the apparent activation energy barrier of the reaction when the reaction is conducted below the LCST of p-NIPAM. Further analysis based on transition state theory showed that the polymer-coated catalyst provides an excess of Gibbs free energy that lowers the entropy and enthalpy of the nitrite hydrogenation reaction at low temperatures. Increasing the temperature above the LCST, at which the polymer collapsed, led to apparent barriers that were similar to those observed on the uncoated Pd/SiO_2 catalyst.

Chapter 4 studied the effect of polymer coated catalyst on nitrobenzene hydrogenation reaction. A detailed reaction kinetic study showed that the polymer-coated catalyst can improve the selectivity to aniline. More importantly, the presence of the polymer coating lowered the apparent activation energy barrier of the reaction especially when the temperature was below the LCST, resembling the behavior observed in the case of nitrite reduction (**Chapter 3**). This phenomenon was explained using the transition state theory treatments of the reaction kinetics. Here, it was demonstrated that the presence of polymer decreased the entropy and enthalpy of the nitrobenzene hydrogenation reaction. Further nuclear magnetic resonance spectroscopy (NMR) characterization was used to study the diffusion of the p-NIPAM coupled to Pd/SiO_2 in the presence of nitrobenzene and water at a temperature below and above the LCST. Here, we showed that the polymer-coated catalyst has a lower self-diffusion coefficient below the LCST than pure polymer in solution, while above the LCST, a higher self-diffusion coefficient was obtained due to the changes in surface wettability of the polymer-coated catalysts. This indicates that the hydrophilic and hydrophobic properties of the polymer will greatly affect the diffusion of the catalyst. Also, we showed that the presence of nitrobenzene reduces the self-diffusion coefficient of the polymer brush. These phenomena suggested that the presence of polymer not only modifies the diffusion of catalyst particles, but also the interaction with reactive species.

Solvent and corresponding solvation effects play a germane role in chemical conversion processes as they can greatly alter the reactivity, selectivity, and stability of catalytic materials. For this reason, we focused our attention on assessing the impact of polymer and solvent interactions on nitrobenzene hydrogenation (**Chapter 5)** as this probe reaction is rather sensitive to the operating conditions particularly when the catalyst is covered by thermo-

responsive polymers. This was accomplished by changing the solvent from pure water to mixtures with increasing concentrations of 1-methyl-2-pyrrolidone (NMP). Here, we observed that increasing the water content enhanced significantly the catalyst activity. The higher TOFs were accompanied by a decrease in the apparent activation energy barriers on the parent Pd/SiO_2. Notably, in pure NMP, the activity was negligible for this reduction reaction. This was attributed to the poor interaction of NMP with H^+, which is believed to be key for achieving high rates in the liquid phase. Dynamic light scattering (DLS) characterization revealed that as the NMP concentration increases, the transition of the polymer from swollen to collapse states at the LCST disappears completely. As a result, using 30 vol.% H_2O/NMP as solvent shows a constant activation energy barrier along with the temperature changes(i.e. non-thermal responsive behaviour). These results suggest that the solvent-polymer interaction is key to inducing the desired responsive-solvation effects at temperatures below and above the LCST. Also, it reveals that proton shuttling is essential in the hydrogenation of nitrobenzene in liquid environments.

Chapter 6 shows the highlight of this work and the conclusions. Also, a number of recommendations are proposed based on the main experimental observations and theoretical models herein reported.

Samenvatting

Het effect van het oplosmiddel op de reactieomgeving is belangrijk voor de activiteit en selectiviteit van een katalytische reactie die in de vloeibare fase wordt uitgevoerd. Men moet de mogelijke interacties tussen de oplosmiddelmoleculen en de reagerende moleculen zorgvuldig overwegen, aangezien deze interacties de massaoverdrachtssnelheden, reactiekinetiek, product selectiviteit en katalysator stabiliteit kunnen beïnvloeden , evenals de eigenschappen van het oplosmiddel, inclusief dichtheid en viscositeit. Als gevolg hiervan kunnen deze zogenaamde solvatatie-effecten een significante verandering in de katalytische prestatie veroorzaken. Het vinden van het perfecte "huwelijk" tussen het oplosmiddel, de reactie en de katalysator is echter moeilijk omdat slechts een paar oplosmiddelen de gewenste prestatie kunnen leveren. In wezen zijn de beste oplosmiddelen om de reactanten en producten in de bulk te stabiliseren mogelijk niet de optimale solvatatieomgeving voor de katalysator. Een veelbelovende benadering zou kunnen zijn om een variatie tussen de lokale omgeving van de actieve plaatsen en de omgeving van het oplosmiddel in de bulk te introduceren. Dit kan worden bereikt met een polymeercoating die leidt tot een solvatatie-effect in de buurt van de actieve plaats. Om dit concept te valideren is er in dit proefschrift een thermisch responsief polymeer (p-NIPAM) met een lagere kritische oplossingstemperatuur (lower critical solution temperature (LCST)) gebruikt als polymeercoating op een model Pd/SiO_2-katalysator. Het effect van het oplosmiddel en de polymeer-geïnduceerde solvatatie-effecten op de selectiviteit en activiteit van de reactie zijn bestudeerd met behulp van sondes chemie, door gebruik te maken van nitriet- en nitrobenzeen hydrogenerings reacties.

Om de selectiviteit van nitriet tot onschadelijk N_2 verder te verhogen door de vorming van NH_4^+ te onderdrukken, is het essentieel om het Pd-gekatalyseerde nitriet hydrogenerings mechanisme in detail te begrijpen. Een rigoureuze kinetische studie werd uitgevoerd in een breed venster van nitriet- en waterstofconcentraties om de onderliggende oppervlaktechemie te bestuderen. De resultaten (**Hoofdstuk 2**) lieten een negatieve NO_2^- reactieorde zien wanneer de H_2-druk laag was, wat een competitieve adsorptie van NO_2^- en H_2 op het katalysatoroppervlak impliceert. Tegelijkertijd suggereerde de waargenomen hoge H_2 reactieorde (ca. 1,5 bij lage concentraties H_2) dat de snelheidsbepalende stap (rate determining step (RDS)) verschillende pre-evenwichten met waterstof vereiste. Op basis van deze waarnemingen zijn verschillende RDS- en reactieroutes geanalyseerd. Door kinetische modellering en dichtheid functionele theorie (density functional theory (DFT)) berekeningen te combineren, werd aangetoond dat de reactie

wordt beperkt door twee opeenvolgende elementaire oppervlaktestappen, waarbij de eerste en tweede hydrogenering van NO* betrokken zijn. De analyse van de mate van snelheidscontrole (DRC) suggereerde dat de RDS kan verschuiven met de reactieomstandigheden (temperatuur en reactantconcentraties) van de eerste hydrogenering van NO* naar de daaropvolgende hydrogenering van HNO* tot HNOH*- species.

Om het effect van het polymeer op de nitriet hydrogenerings reactie te bestuderen, is een thermisch reagerende polymeer-gecoate katalysator gesynthetiseerd via de radicale polymerisatie van atoomoverdracht (atom transfer radical polymerization (ATRP)) methode en toegepast op nitriet hydrogenering (**Hoofdstuk 3**). De resultaten toonden aan dat de aanwezigheid van het polymeer de schijnbare activeringsenergiebarrière van de reactie verlaagt wanneer de reactie wordt uitgevoerd onder de LCST van p-NIPAM. Verdere analyse op basis van de overgangstoestand theorie toonde aan dat de met polymeer beklede katalysator een overmaat aan Gibbs-vrije energie levert die de entropie en enthalpie van de nitriet hydrogenerings reactie bij lage temperaturen verlaagt. Het verhogen van de temperatuur boven de LCST, waarbij het polymeer instortte, leidde tot schijnbare barrières die vergelijkbaar waren met die waargenomen op de onbeklede Pd/SiO_2-katalysator.

Hoofdstuk 4 bestudeerde het effect van een met polymeer beklede katalysator op de nitrobenzeen hydrogenerings reactie. Een gedetailleerde reactie kinetische studie toonde aan dat de met polymeer beklede katalysator de selectiviteit naar aniline kan verbeteren. Belangrijker was dat de aanwezigheid van de polymeercoating de schijnbare activeringsenergiebarrière van de reactie verlaagde, vooral wanneer de temperatuur lager was dan de LCST, wat lijkt op het gedrag dat werd waargenomen in het geval van nitrietreductie (**Hoofdstuk 3**). Dit fenomeen werd verklaard met behulp van de overgangstoestandentheorie behandelingen van de reactiekinetiek. Hier werd aangetoond dat de aanwezigheid van het polymeer de entropie en enthalpie van de nitrobenzeen hydrogenerings reactie verminderde. Verdere karakterisering door middel van kernmagnetische resonantiespectroscopie (nuclear magnetic resonance spectroscopy (NMR)) werd gebruikt om de diffusie van p-NIPAM gekoppeld aan Pd/SiO_2 in aanwezigheid van nitrobenzeen en water bij een temperatuur onder en boven de LCST te bestuderen. Hier toonden we aan dat de met polymeer beklede katalysator een lagere zelfdiffusiecoëfficiënt heeft onder de LCST dan zuiver polymeer in oplossing, terwijl boven de LCST een hogere zelfdiffusiecoëfficiënt werd verkregen als gevolg van de veranderingen in de bevochtigbaarheid van het oppervlak van het polymeer. Dit geeft aan dat

de hydrofiele en hydrofobe eigenschappen van het polymeer de diffusie van de katalysator sterk zullen beïnvloeden. We toonden ook aan dat de aanwezigheid van nitrobenzeen de zelfdiffusiecoëfficiënt van de polymeerborstel vermindert. Deze verschijnselen suggereerden dat de aanwezigheid van polymeer niet alleen de diffusie van katalysatordeeltjes modificeert, maar ook de interactie met reactieve species.

Het oplosmiddel en overeenkomstige solvatatie-effecten spelen een belangrijke rol bij chemische omzettingsprocessen omdat ze de reactiviteit, selectiviteit en stabiliteit van katalytische materialen sterk kunnen veranderen. Om deze reden hebben we onze aandacht gericht op het beoordelen van de impact van polymeer- en oplosmiddelinteracties op nitrobenzeen hydrogenering (**Hoofdstuk 5**), aangezien deze sonde reactie nogal gevoelig is voor de bedrijfsomstandigheden, vooral wanneer de katalysator bedekt is met thermo-responsieve polymeren. Dit werd bereikt door het oplosmiddel te veranderen van zuiver water naar mengsels met toenemende concentraties 1-methyl-2-pyrrolidon (NMP). Hier zagen we dat het verhogen van het watergehalte de katalysatoractiviteit aanzienlijk verhoogde. De hogere TOF's gingen gepaard met een afname van de schijnbare activeringsenergiebarrières op de ouder Pd/SiO_2. Met name in zuiver NMP was de activiteit verwaarloosbaar voor deze reductiereactie. Dit werd toegeschreven aan de slechte interactie van NMP met H+, waarvan wordt aangenomen dat het de sleutel is voor het bereiken van hoge snelheden in de vloeibare fase. Dynamische lichtverstrooiing (Dynamic light scattering (DLS)) karakterisering onthulde dat naarmate de NMP-concentratie toeneemt, de overgang van het polymeer van gezwollen naar instortingstoestanden bij de LCST volledig verdwijnt. Dientengevolge vertoont het gebruik van 30 vol.% H_2O/NMP als oplosmiddel een constante activeringsenergiebarrière samen met de temperatuurveranderingen (d.w.z. niet-thermisch responsief gedrag). Deze resultaten suggereren dat de interactie tussen het oplosmiddel en het polymeer de sleutel is tot het induceren van de gewenste responsieve solvatatie-effecten bij temperaturen onder en boven de LCST. Het laat ook zien dat een protonshuttle essentieel is bij de hydrogenering van nitrobenzeen in vloeibare omgevingen.

Hoofdstuk 6 toont het hoogtepunt van dit werk en de conclusies. Ook worden er een aantal aanbevelingen voorgesteld op basis van de belangrijkste experimentele waarnemingen en theoretische modellen die in deze studie worden gerapporteerd.

Acknowledgements

Now, it’s time to end my PhD study. I am very grateful that I made a choice to study abroad for my PhD study. Life at the University of Twente will be an unforgettable memory in my life. At the end of this thesis, I would like to acknowledge many people I met during my PhD journey.

First, I would first like to thank my daily supervisor, Jimmy, your temper is really good, very patient, kind to people, at the same time, serious at work, and very thoughtful. You are an enthusiastic person, and you always have some ideas. During the past four years, you really helped me a lot, from the daily follow-up meeting to the written and revision of the paper. Maybe, in the beginning, I didn’t really understand what we were going to do and achieve. However, in the end, I learned a lot and I was able to talk and argue with you about some of the questions. Thank you for your guidance and help over the past 4 years, I will benefit for life.

Then, I would like to thank my supervisor, Leon, who is a wise, respectable, and precisian person, your critical attitude on research and science is worth learning. I still remember the first interview with you and the second interview together with jimmy. Actually, still remember some of the questions. Fortunately, I can manage some of the questions. Thanks for giving me the great opportunity to do my PhD at CPM group. When I arrived, it felt very hard at the beginning to understand what people said. With your patience and encouragement, my English is improving. Maybe, when I was new here, I am not getting used to the life here. Sometimes I don't feel comfortable, and it caused some problems. However, everything went well in the end. Thanks for the understanding and humane care.

Next, I would like to thank the research collaborators. I had many collaborators during my PhD research. Aayan, thanks for the help on kinetic modeling and your treat during the NCCC conference. Bin and Yu, thanks for the DFT calculations, you did a lot of work and spent several years on it. The thickness of the thesis has a great contribution from you. Ricardo, thanks for the cooperation with NMR analysis, we have NMR analysis on nitrobenzene hydrogenation as well as nitrite hydrogenation. Sometimes, we are preparing the sample together, sometimes, I sent the sample to you. I can't remember how many times I sent you samples, the way to your lab, went from unfamiliar to familiar. Thanks for the great help.

Joel, you are the first bachelor student that I supervise, we did some catalyst synthesis together, and it was a good time that I can work with people together, hope you are doing well with your future study.

Jelle, you are a talented student with the ability to solve problems independently, I learned from you about kinetic modeling using Matlab. I wish all the best with your studies at UT.

Rick, I had a good time with you for your master's assignment. You are hardworking, friendly, and helpful. You help me a lot with some personal stuff. I wish you all the best in your PhD study at UT.

Pengyu, your help started before I came to UT. During the first two years of my PhD, sometimes, I needed your help with the translation, and sometimes, I needed your help with the experiments. You were always there and available. I really appreciate your help. I hope that you are doing well with your job in Shanghai.

Maria, you are the first PhD of jimmy in UT, you did some fundamental work for my PhD research. When I arrive, I already had the method for the synthesis of the catalyst. This provided me a good start for my research. I will remember the time that we are doing experiments, going to a conference, and taking exams together. I really appreciate the help from you.

Coen and Maaike, thanks for your help in the translation of the thesis summary into Dutch. I hope you guys can successfully complete your graduation experiments and thesis and I wish you all the best in your future careers.

During the last year of my PhD, I got new office roommates, namely fellow PhD candidates, Martim, Rem, and Janek. The three of you guys seemed to be handpicked, very hardworking PhD candidates. We had some nice discussions about research and life, especially, Martim, we talked a lot about international events, also, I would like to thank you for the help with the drawing of the thesis cover. Now, my PhD study has nearly come to an end at CPM. I am glad that there are people who can carry the torch. Janek, I wish you all the best with the nitrite/nitrate project.

There are group members, Jord, Fernando, Lola, Xinming, Suman and Song. I have been together with some of you for a long or short time. We had a great time during the borrel and coffee break. I wish you all the best with your research.

Bert, you are very helpful in the lab, even though it’s a bit tough at the beginning. However, after getting along with each other for a longer time, I can attest that you are kind and helpful. You helped me a lot with the use of HPLC, and I appreciate that. Tom and Ties, you helped me a lot with the XRF and elemental analysis, thanks for that, and I wish you all the best with your new job. Karin, you take care of the laboratory very well and keep things organized and clean.

I used a lot of filters for my research, and finally, I have finished all the experiments. Thanks a lot for the support.

Dorothy, you always give people a warm feeling, with patience and kindness to people. Especially, I have some trouble with English communication at the beginning. Your encouragement and guidance are very helpful to me, thank you very much. Anne, you were the secretary after Dorothy you are also a nice person. Always arrange things well and willing to help people. I wish you are doing well with your future job with more and more members joining the group.

There are many others who helped me during my PhD period, whom I might not have mentioned, but it does not mean you are not important. I want to thank you all for helping me during my PhD, and I wish you all the best in your future.

The last but not the least, I want to thank my family and my girlfriend. 感谢爷爷、奶奶，父母一直以来对我的支持与鼓励。

2022.11.02, Enschede

Pengcheng Huang (黄鹏程) was born in 1990, Xinyang, Henan province, China. He graduated from Shenyang University of technology with bachelor degree on polymer material and engineering in 2015. Then, he received his master degree in Industrial Catalysis from Shihezi University in 2018. After that, he started his PhD studies in the Catalytic processes and Materials (CPM) group at the University of Twente from 2018. The current thesis presents the outcome of his PhD research.

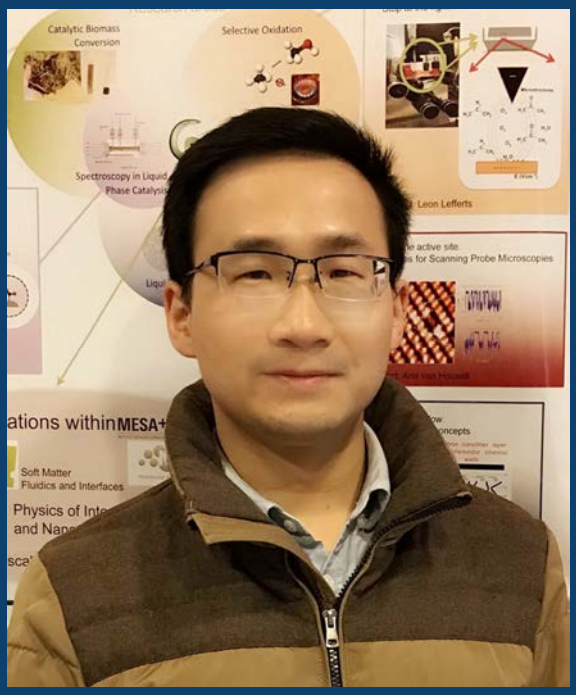

UNIVERSITY OF TWENTE.

9 789036 555012